HZDR-007

METAL NANOPARTICLES/NANOWIRES SELF-ASSEMBLY ON RIPPLE PATTERNED SUBSTRATE

- Mechanism, properties, and applications

Mukesh Ranjan

Wissenschaftlich-Technische Berichte
HZDR-007 · ISSN 1437-322X

WISSENSCHAFTLICH-
TECHNISCHE BERICHTE

HZDR
HELMHOLTZ
ZENTRUM DRESDEN
ROSSENDORF

Metal Nanoparticles/Nanowires Self-assembly on Ripple Patterned Substrate

-Mechanism, properties, and applications

Dissertationsschrift
zur Erlangung des akademischen Grades
Doctor rerum naturalium
(Dr. rer. nat.)

vorgelegt von

Mukesh Ranjan
geboren am 21.10.1978 in India

der Fakultät Mathematik und Naturwissenschaften
der Technischen Universität Dresden
2010

Gutachter:

1. Prof. Dr. W. Möller, FZ Dresden-Rossendorf / TU-Dresden

2. Prof. Dr. F. Buatier de Mongeot, Università degli Studi di Genova

Datum des Einreichens der Arbeit: 22 November 2010
Datum der Beendigung der Arbeiten: 6 Juni 2011

If it's green or wriggles, it's biology.
If it stinks, it's chemistry.
If it doesn't work, it's physics.
-Unknown

We see only what we know.
- *Johann Wolfgang von Goethe*

A little knowledge is a dangerous thing. So is a lot.
-Albert Einstein

Abstract

Plasmonic properties of self-assembled silver nanoparticles/nanowires array on periodically patterned Si (100) substrate are reported with special attention on the mechanism of nanoparticles self-assembly. The advantage of this bottom up approach over other self-assembling and lithographic methods is the flexibility to tune array periodicity down to 20 nm with interparticle gaps as low as 5 nm along the ripple.

Ripple pattern have shallow modulation (~2 nm) still particles self-assembly was observed in non-shadow deposition. Therefore adatoms diffusion and kinetics is important on ripple surface for the self-assembly. PVD e-beam evaporation method used for deposition has proven to be superior to sputter deposition due to lower incident flux and lower atom energy. It was found that particles self-assembly largely dependent on angle of incidence, substrate temperature, and deposition direction due to ripple asymmetric tilt. Ostwald ripening observed during annealing on ripples substrate has striking dependency on ripple periodicity and was found to be different compared to Ostwald ripening on flat Si surface.

In-situ RBS measurements of deposited silver on flat and rippled substrate confirmed different sticking of atoms on the two surfaces. The difference between maximum and minimum of the calculated local flux show a peak at an incidence angle of 70^{o} with respect to surface normal. This explains the best alignment of particles at this angle of incidence compare to others.

Self-assembled nanoparticles are optically anisotropic, i.e. they exhibit a direction dependent shift in LSPR. The reason of the observed anisotropy is a direction dependent plasmonic coupling. Different in plane and out of the plane dielectric coefficients calculated by modelling Jones matrix elements, confirms that nanoparticle/nanowire array are biaxial anisotropic ($\varepsilon_x \neq \varepsilon_y \neq \varepsilon_z$). The nanoparticles are predominantly insulating while nanowires are both metallic and insulating depending on the dimension.

Silver nanoparticles/nanowires self-aligned on pre-patterned rippled substrate are presented for the first time as an active SERS substrate. Anisotropic SERS response in such arrays is attributed to different field enhancement along and across the ripples. Strong plasmonic coupling in elongated nanoparticles chain results in significantly higher SERS intensity then spherical nanoparticles/nanowires and non-ordered nanoparticles. Higher SERS intensity across the nanowires array in comparison to along the array (bulk silver) confirms electromagnetic field enhancement (hot-junction) is responsible for SERS phenomenon.

Self-assembly of cobalt nanoparticle on ripple pattern substrate is also reported. Due to less adatom mobility and higher sticking cobalt self-assembly is possible only at much higher temperature. A strong uniaxial magnetic anisotropy was observed not observed for non ordered cobalt particles.

Table of contents

List of Abbreviations

SPP	Surface Plasmon Polariton
LSPR	Localised Surface Plasmon Resonance
SP	Surface Plasmon
SNOM	Scanning Near Field Optical Microscopy
SERS	Surface Enhanced Raman Scattering
EELS	Electron Energy Loss Spectroscopy
DDA	Discrete Dipole Approximation
FDTD	Finite Difference Time Domain
PVD	Physical Vapour Deposition
AFM	Atomic Force Microscopy
CSTEM	Cross Sectional Transmission Electron Microscopy
SEM	Scanning Electron Microscopy
RBS	Rutherford Backscattering Spectrometry
BH	Bradley-Harper
MCB	Makeev, Cuerno, and Barabasi
KS	Kuramoto-Sivashinsky
GCC	Garcia-Castro-Cuerno
ESD	Effective Surface Diffusion
IVF	Induced Viscous Flow
PSD	Power Spectral Density
rms	Root Mean Square
IBS	Ion Beam Sputtering
UHV	Ultra High Vacuum
FFT	Fast Fourier Transformation
RHEED	Reflection High Energy Electron Diffraction
STM	Scanning Tunnelling Microscopy
V-W	Volmer-Weber
ML	Monolayer
S-K	Stranski-Krastanov

GE	Generalized Ellipsometry
FWHM	Full Width Half Maximum
MSE	Mean Square Error
R6G	Rhodamine 6G (R6G)
MOKE	Magneto Optic Kerr Effect
SQUID	Superconducting QUantum Interference Device
FC	Field Cooling
ZFC	Zero Field Cooling
MR	Magnetic Reversal
RT	Room Temperature
3D-LKMCS	Three Dimensional Lattice Kinetic Monte Carlo Simulation
GISAXS	Grazing Incidence Small Angle X-ray Scattering

Chapter-1

Introduction

Sub-wavelength optics means interaction of light with structures comparable or much smaller then the wavelength of light. It is a topic of current research and important in the modern branch of physics called Plasmonics. The fascination about sub-wavelength optics started after Michael Faradayôs (1885) [1] discovery of ruby colour produce by colloidal gold nanoparticles. Soon after scientists like Lord Rayleigh (1899) [2], Ehrenhaft using Lorenz theory in (1903) [2], and J. C. Maxwell-Garnett (1906) [4] tried to find out the underlying physics with some success. Finally the German physicist Gustav Mie (1908) [5, 6] developed a theory known as Mie scattering theory by solving the Maxwellôs equations analytically for scattering of electromagnetic radiation by spherical particles. In his pioneering work he first proposed the collective electron excitation, and successfully explained the plasmon resonance absorption of gold colloids. His theory predict absorption bands dependency on the particle size and defines the change in colour that occurs as the size of the colloid nanoparticles is increased from 20 to 1600 nm.

Resonant interaction of collective electron oscillations frequency of metal nanoparticles with incident light frequency is known as Localized surface plasmon resonance (LSPR). It is associated with an enhanced near electric field at resonance frequency, which is localized at the nanoparticle and decays away from the nanoparticle/dielectric interface into the dielectric background [7-10]. Light intensity enhancement is a very important aspect of LSPR and localization means LSPR has very high spatial resolution (sub wavelength) limited only by the size of nanoparticles. The resonance frequency (absorption maxima) is characteristic of the type of metal (Au, Ag, Cu, Al, Pt) and are very sensitive to the size,

shape, arrangement and the host medium. For very small particles ($R/\lambda \leq 0.01$), the electric field of the incoming light is homogeneously distributed along the cluster and only dipolar plasmon excitations are present (quasi-static regime). If the clusters are larger, the inhomogeneous distribution of the electric field introduces additional multipole excitations.

In addition, the existence of surface plasmons (SP) in bulk metal was first predicted in 1957 by R.H. Ritchie [11]. In his pioneering treatment of characteristic energy losses of fast electrons passing through thin metal films, Ritchie predicted the existence of self-sustained collective excitations at metal surfaces. In the following two decades, SP were extensively studied by many scientists, the foremost of whom were H. Raether [12], E. Kretschmann [13, 14], and A. Otto [15]. Surface plasmons (SP) are coherent electron oscillations that exist at the interface between any two materials where the real part of the dielectric function changes sign across the interface (e.g. a metal-dielectric interface, such as a metal sheet in air) [7-9]. SP coupling with a photon results in hybridised excitation called surface plasmon polariton (SPP). This SPP can propagate along the surface of a metal until energy is lost either via absorption in the metal or radiation into free-space.

Although SP and LSPR known from decades, but only in recent last 10 year they have been thoroughly investigated due to advancement in near field characterisation techniques (SNOM, SERS, EELS etc.) and computational skill (DDA, FDTD,Wvase32). It is mentioned above that during LSPR near field enhanced at particle and its surrounding. Therefore two nanoparticles sitting in close proximity can produce a large field enhancement in between the particles gap due to dipolar field coupling. In recent years several theoretical as well as experimental research papers published about field enhancement between inter-particles gap [16-26]. Field enhancement in between two nanoparticles is even few order higher then single nanoparticle .This feature explain the large signal observed in surface enhance Raman scattering (SERS) and helped to detect even the single molecule [16,27,28]. Dipolar field coupling or field enhancement is strongly depend on inter-particle gap, and below 20 nm gap coupling is even much stronger [16-26]. Theoretical modelling predicts that field enhancement in an ordered particles chain is even higher then two particles system [16-26].

The unique properties of LSPR and the accompanied field enhancement opened new directions of research and have been utilised extensively in various plasmonic technologies. For instance, surface plasmon polaritons can serve as a basis for building nanoscale photonic circuits in the sub-100 nm size regime. Some of recent applications are plasmonic wave guides [29-31], plasmonic switching [32,33], optical modulators, photonic crystal [34-36], biological sensors[37], near field applications such as SNOM [38], Metamaterials [39],

Superlenses [40], photovoltaic [41,42], display and recording media [43,44], single molecule [16,27,28,45], proteins [45] and cancer tissue [46] detection by surface enhanced Raman scattering (SERS) etc.

Form a technological point of view the application of metal nanoparticles with plasmonic properties demands a fully control growth process. Sub wavelength optical devices demands miniaturization of optical components. Currently available approaches to grow ordered particles can be divided in two categories; top-down (lithographic methods) and bottom-up (self-assemble methods). The current limitation of lithography for making nanoparticles arrays with inter-particle gap down to 20 nm is problematic [47]. Whereas the field enhancement effects are prominent in this dimension or even lower dimensions. Another drawback of some of the lithographic approach is low area selection and time consuming process. Self-assemble and self-organisation methods have been successfully demonstrated using faceted alumina [48], anodized alumina [49, 50], and block co-polymers [51, 52] as substrates. Several chemical methods have also been presented [53, 54] with limited success. There are different flaws in these approaches, such as very little control on inter-particle gap and array periodicity. In the case of anodised alumina substrates only top surface of metal particles or wire are exposed therefore inter-particles coupling reduced. In chemical synthesis no control on ordering can be achieved. All these methods are lacking tunability.

Another approach which has been proposed recently is to use sputtered induced ripple pattern as template fallowed by oblique incidence PVD deposition to grow highly ordered nanoparticles and nanowires [55-59]. Knowledge base to produce rippled templates of different periodicity and on different substrate materials with full control is already available. The scaling laws to tune the ripple periodicity and amplitude have been investigated in detail for Si [60-65]. Therefore this approach appears to be very promising to develop highly ordered nanoparticles and wires for plasmonic applications. Different groups have successfully reported interesting plasmonic and magnetic properties produced by metal films deposited on such rippled templates [55, 56, 59, 66, 67]. Since this development is still in the beginning phase, we aimed the following objectives in this thesis work: effect of growth conditions on the self-assembly process, understanding of selectivity, and investigation of optical as well as magnetic properties of self-assembled silver /cobalt nanoparticles and nanowires respectively.

In **chapter-2** the theory and the scaling laws of ripple formation during ion beam sputtering will be discussed in brief and an overview of the developed experimental setup will be presented. Ripple pattern of small periodicity (~ 35 nm) were used in most of the

experiment to investigate plasmonic properties and coupling effects of closely sitting nanoparticles (< 20 nm) along the ripples and nanowires. The study was also extended for lower (~20 nm) and higher (~ 45 nm) ripples periodicity as well.

Different groups focused their attention to study the optical properties of self aligned silver or gold particles [55, 56, 59, 66]. However, none of the earlier works report the mechanism of self-assembly on ripple templates. The process of self-assembly is always reported briefly either using shadow deposition (angle of incident below 5^{o}) or at some other optimised angle with respect to substrate surface forming percolated chain of atoms on ripple substrates. In **chapter-3** the significance of angle of incidence for particle self-assembly on ripple surface along with theoretical understanding will be demonstrated. Different kinds of particles combinations (small, big + small, spread over complete surface) are formed depending on angle of incidence. The major outcome of this study reveals that local flux and sticking probability on ripple templates plays an important role for particle self-assembly. In-situ RBS measurements of sticking probabilities on normal and rippled substrate will be presented to validate this assumption.

Furthermore the influence of other process parameters such as substrate temperature, rate of deposition, deposition direction (due to ripple asymmetric tilt), and ripple periodicity will be shown in **chapter-3**. In earlier reported work sputter deposition was used mainly as the deposition method for silver film growth on rippled substrate. In our approach for the first time we have used *electron beam evaporation* deposition method and a brief comparative study was performed with magnetron sputtering method. Finally in this part we will show the optimised conditions to grow highly spherical ordered nanoparticles and nanowires. Ordered spherical nanoparticles can be produce by performing the post annealing. Ostwald ripening has been observed during annealing on ripples substrate. However, striking dependency on ripple periodicity was found compared to Ostwald ripening on flat Si surface. A systematic study of the same will also be shown in **chapter-3**. As mentioned earlier that other methods of self-assembly lack in tunability, it will be shown that by this method ordered nanoparticles of different periodicity and shapes and nanowires of different width can be produced.

Self-aligned nanoparticles are optically anisotropic, i.e. different plasmon resonances along and perpendicular to the ripple direction [55, 59]. In **chapter 4** detailed study of the effect of aspect ratio on localized surface plasmon resonance (LSPR) position is presented. LSPR position found to be deviated form Gans theory predicted LSPR position. This deviation attributed to the plasmonic coupling of the ordered nanoparticles that result in observed red-shift in the LSPR position. These results are inline with other reported

theoretical works [17, 18]. Plasmonic coupling also explains the reason of optical anisotropy of ordered particles on rippled substrate. The possibility of tuning the plasmon resonance by changing the interparticle distance or by varying the periodicity will also be demonstrated.

Optical properties of the silver nanowires of different width (fixed periodicity) and nanoparticles were studied with the help of generalised ellipsometry in **chapter-4**. First time we reported [68] that this system is biaxially optical anisotropic. Dielectric functions were calculated by fitting the Jones matrix elements with a biaxial layer model accounting for both metallic behaviour and localized surface plasmon resonances. The amplitude and wavelength maximum of the plasmon resonance perpendicular to the wires increases with increasing wire width and thickness. Similar model was implemented for extracting dielectric coefficients for nanoparticles of different periodicity and shapes.

Finally in **chapter-4** results of surface enhanced Raman scattering (SERS) study of Rhodamine 6 G (R6G) molecules on such ordered nanoparticles and wires will be presented. Conditions to obtain the maximum possible enhancement factor were investigated. These results also prove different plasmonic coupling along and perpendicular to the ripple direction inline with reflection results. Particles of different aspect ratios and wires were used for comparison. Also enhancement of gold nanowires was compared with silver nanowires.

Similar approach for making self-assemble nanoparticles was used for cobalt metal with an objective to study magnetic properties in **Chapter-5**. Cobalt nanowires array can also be formed by ion beam sputtering [69]. Cobalt nanowire and nanoparticles with different aspect ratio can also be grown on ripple pattern substrate. The growth behaviour of cobalt was found to be different then silver. Due to high sticking, low diffusion it was hard to implement the same parameters developed for silver. Therefore after failure of several experiments, successful self-assembling of cobalt nanoparticles was achieved. Later such samples were characterised with MOKE and SQUID characterisation methods. Very strong uniaxial magnetic anisotropy was observed not observed for non ordered cobalt particles.

Finally in **chapter-6** we will conclude with final remarks and will propose future directions

References

[1] M. Faraday, *Philos. Trans. R. Soc. (London)* 147 (**1857**) 145.

[2] L. Lorenz, *Wied. Ann.* 11 (**1880**) 70.

[3] L. Rayleigh, *Phil. Mag.* (5) 47 (**1899**) 379.

[4] J. C. Maxwell-Garnett, *Phil. Trans.* 203 (**1904**) 385, 205 (**1906**) 237.

[5] G. Mie, *Ann der Physik* 25 (**1908**) 377.

[6] G. Mie, *Royal Aircraft Establishment, Library English Translation* (**1976)** (*http://diogenes.iwt.uni-bremen.de/vt/laser/papers/RAE-LT1873-1976-Mie-1908-translation.pdf)*

[7] A. Otto, *Z. Phys.* 216 (**1968**) 398.

[8] W. L. Barnes, A. Dereux, T. W. Ebbesen, *Nature* 424 (**2003**) 824.

[9] J. M. Pitarke, V. M. Silkin, E. V. Chulkov, P. M. Echenique, *Rep. Prog. Phys.* 70 (**2007**) 1.

[10] S. A. Maiera, H. A. Atwater, *J. Appl. Phys.* 98 (**2005**) 011101.

[11] U. Kreibig, M. Vollmer, *Optical Properties of Metal Clusters* (Springer) (**1995**).

[12] R. H. Ritchie, *Phys. Rev.* 106 (**1957**) 874.

[13] E. Kretschmann, H. Raether, *Z. Naturf.* A 23 (**1968**) 2135.

[14] R. Bruns , H. Raether , *Z. Phys.* 237 (**1970**) 98.

[15] E. Kretschmann, *Z. Phys.* 241 (**1971**) 313.

[16] S. M. Nie, S. R. Emery, *Science* 275(**1997**) 1102.

[17] R. L. Chern, X. X. Liu, C. C. Chang, *Phys. Rev. E* 76 (**2007**) 016609.

[18] E. Hao ,G. C. Schatz, *J. Chem. Phys.* 120 (**2004**) 357.

[19] S. Zou, G. C. Schatz , *Chem. Phys. Lett.* 403 (**2005**) 62.

[20] A. S. Zelenina, R. Quidant, M. N. Vesperinas, *Optics Lett.* 32 (**2007**) 1156.

[21] D. A. Genov, A. K. Sarychev, V. M. Shalaev, A. Wei, *Nano Lett.* 4 (**2004**) 343710.

[22] K. Wang, E. Schonbrun, K. B. Crozier, *Nano Lett.* 9 (**2009**) 2623.

[23] J. R. Krenn, *Nature Materials* 2 (**2003**) 210.

[24] L. Aigouy, M. Mortier, J. Giérak, E. Bourhis, *J. App. Phys.* 97 (**2005**) 104322.

[25] A. L. Koh, K. Bao, I. Khan, W. E.Smith, G. Kothleitner, P. Nordlander, S. A. Maier, D. W. Mcomb, *ACS Nano* 3 (**2009**) 3015.

[26] H. Y. Lin, C. H. Huang, C. H. Chang, Y. C. Lan, H. C. Chui, *Optics Express* 18 (**2010**) 165.

[27] K. Kneipp, Y. Wang, H. Kneipp, L. T. Perelman, I. Itzkan, R. R. Dasari, M. S. Feld, *Phys. Rev. Lett.* 78 (**1997**) 1667.

[28] K. Kneipp, H. Kneipp, R. Manoharany, R. R. Dasari, M. S. Feld, *Bioimagin*g 6 (**1998**) 104.

[29] J. -C. Weeber, J. R. Krenn, A. Dereux, B. Lamprecht,Y. Lacroute, J. P. Goudonnet, *Phys. Rev. B* 64 (**2001**) 045411.

[30] J. R. Krenn, A. Dereux, E. Bourillot, J. P. Goudonnet, *Phys. Rev. Lett.* 82 (**1999**) 2590.

[31] H. Ditlbacher, *Phys. Rev. Lett.* 95 (**2005**) 257403.

[32] N. Large, M. Abb, J. Aizpurua, L. M.Otto, NanoLetters 10 (**2010**) 1741.

[33] V. K. S. Hsiao, Y. B. Zheng, B. K. Juluri, T. J. Huang, *Adv. Mater.* 20 (**2008**) 3528.

[34] R. F. Cregan, *Science* 285 (**1999**) 1537.

[35] A.V. Krasavin, N. I. Zheludev, *Appl. Phys. Lett.* 84 (**2004**) 1416.

[36] A.V. Krasavin, A.V. Zayats, N. I. Zheludev, *J. Opt. A: Pure Appl. Opt.* 7 (**2005**) S85.

[37] S. S. Yee, *Sens. Actuators B* 54 (**1999**) 1.

[38] G. P. Wiederrecht, *Eur. Phys. J. Appl. Phys.* 28 (**2004**) 3.

[39] P. Nagpal, *Science* 325 (**2009**) 594.

[40] T. Taubner , D. Korobkin , Y. Urzhumov , R. Hillenbrand , *Science* 313 (**2006**) 1595.

[41] H. A. Atwater, A. Polman, *Nature materials* 9 (**2010**) 205.

[42] V. E. Ferry, L. A. Sweatlock, D. Pacifici, H. A. Atwater, *Nano Lett.* 8 (**2008**) 12.

[43] S. Park, J. W. Hahn, *Optics Express* 17 (**2009**) 20203.

[44] C. Z. Xin, W. U. L. Nan, *Chinese Science Bulletin* 53 (**2008**) 2257.

[45] X. X. Han, B. Zhao, Y. Ozaki, *Anal. Bioanal. Chem.* 394 (**2009**) 1719.

[46] T. V. Dinh, L. R. Allain, D. L. Stokes, *J. Raman Spectrosc.*33 (***2002***) 511.

[47] R. Lloyd, Harriott, *Proceed. of The IEEE* 89 (**2001**) 366.

[48] S. Camelio, D. Babonneau, D. Lantiat, L. Simonot, *Eur. Phys. Lett.* 79 (**2007**) 47002.

[49] G. Riveros, S. Green, A. Cortes, H. G´omez, R.E.Marotti, E. A. Dalchiele, *Nanotechnology* 17 (**2006**) 561.

[50] C. T. Wu, F. H. Ko, H. Yen, Hwang, Microeletronic Engineering 83 (**2006**) 1567.

[51] C. Mendoza, T. Pietsch, J.S. Gutmann, D. Jehnichen, N. Gindy, A. Fahmi, *Macromolecules* 42 (**2009**) 1203.

[52] J. Y. Cheng, H. I. Smith, E. L. Thomas, *Adv.Mater.18* (**2006**) 2505.

[53] H. Schmidt, *Appl. Organ. Chem.* 15 (**2001**) 331.

[54] Q. Liu, Y. Cui, D. Gardner, X. Li, S.He, I.I.Smalyukh, *Nano Lett.* 10 (**2010**) 1347.

[55] T.W. H. Oates, A. Keller, S.Facsko, A.Mücklich, *Plasmonics* 2 (**2007**) 47.

[56] A. Toma, D. Chiappe, D. Massabo, C. Boragno, F. B. Mongeot, *Appl. Phys. Lett*. 93 (**2008**) 163104.

[57] T.W. H.Oates, A.Keller, S.Noda, S.Facsko, *Appl. Phys. Lett.* 93 (**2008**) 063106.

[58] Y. F. Guan, A. J. Pedraza, *Nanotechnology* 16 (**2005**) 1612.

[59] S. Camelio, D. Babonneau, L. Simonot, *Eur. Phys. Lett.*79 (**2007**) 47002.

[60] A. Keller, S. Facsko, W. Möller, *New J. Phys.* 10 (**2008**) 063004.

[61] W. L. Chan, E. Chason, *Appl. Phys. Lett*. 101 (**2007**)121301.

[62] A. Keller, S. Roßbach, S. Facsko, W. Möller, *Nanotechnology* 19 (**2008**) 135303.

[63] A. D. Brown, J. Erlebacher, *Phys. Rev. Lett.* (**2005**) 056101.

[64] B. Ziberi, F. Frost, T .Höche, B. Rauschenbach, *Phys. Rev. B* 72 (**2005**) 235310.

[65] S. Facsko, T. Dekorsy, C. Koerdt, H. Kurz, A. Vogt, H. Hartnagel, *Science* 285 (**1999**) 1551.

[66] S. Camelio, D. Babonneau, D. Lantiat, L. Simonot, F. Pailloux, *Phys. Rev. B* 80 **(2009)** 155434.

[67] O. M.Liedke, B. Liedke, A. Keller, B. Hillebrands, A. Mucklich, S. Facsko, J. Fassbender, *Phys. Rev. B* 75 (**2007**) 220407.

[68] M. Ranjan, T. W. H. Oates, S. Facsko, W. Möller, *Optics Letter* 35 (**2010**) 2576.

[69] R. Moroni, D. Sekiba, F. Buatier de Mongeot, G. Gonella,C. Boragno, L. Mattera, U.Valbusa, *Phys. Rev. Lett*. 91 (**2003**) 167207-1.

Chapter-2

Rippling Theory and Experiments

This chapter introduces briefly to the physics of sputtering and pattern formation and describes the features of developed experimental setup, used ion-source and deposition systems (e-beam evaporation, magnetron sputtering). Fundamentals of used characterization techniques (AFM, TEM, SEM, RBS) for both template preparation and after metal deposition will also be discussed briefly. Finally, scaling laws applicable in ripple substrate production used in our study and useful for plasmonic application will be reported.

2.1 Sputtering induced surface rippling

The phenomenon of removing surface atoms by energetic ion bombardment is known as sputtering (Originated from the Latin verb *sputare,* to emit saliva with noise). It was first discovered by J. J. Thompson in 1897 to describe the use of energetic ions to remove material from a substrate surface via momentum transfer. However, Grove is generally credited as the first individual to observe the phenomenon in a laboratory setting in 1853[1]. Several applications were discovered later based on sputtering process, such as sputter deposition from a target material to substrate and cleaning of surfaces with atomic precision. Ion beams can be focused and scanned across a sample surface using magnetic or electric fields, making it possible to ñwriteò nanometer scale features. Additionally, certain ñreactiveò ionized gases can be used to selectively etch a particular chemical species. Therefore, these two features have made this etching technique crucial to current microelectronic device fabrication.

A unique feature associated with material removal during ion sputtering is a surface instability, i.e., the surface roughness *increases* upon sputtering. This feature is unique because, in contrast to wet chemical etching, where regions of positive surface curvature are etched less quickly than regions of negative curvature, leading to surface smoothening, ion sputtering results in regions of positive curvature being etched far more quickly than regions of negative curvature. The surface instability associated with ion sputtering can be exploited to create regular arrays of ripples, bumps, or dots [2, 3] possessing submicron length scales (Fig. 2.1). These *sputter* induced *ripples* are formed as a result of a competition between roughening by ion sputtering and surface smoothing mechanisms such as surface diffusion [4]. The ion beam stochastically roughens the surface whereas smoothing mechanism wash out perturbations; this combination acts to promote the formation of a *regular* array of surface features.

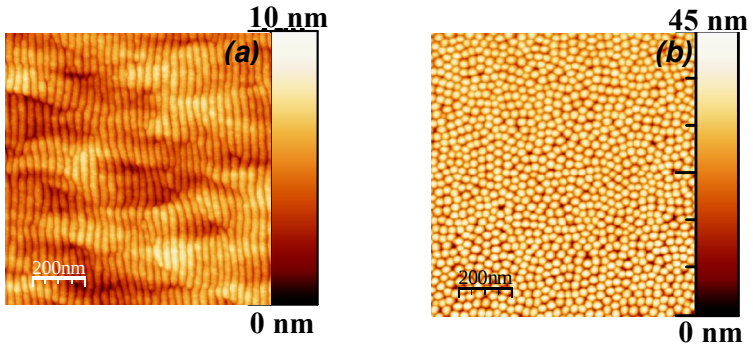

Fig. 2.1: *(a) Ripple pattern produced on Si (100) surface by oblique incidence of 500 eV ions beam with 35 nm periodicity and 2 nm amplitude of modulation .*
(b) Hexagonally ordered nanodots on GaSb surface produced by 800 eV ions at normal incidence.

Sputter ripples were first observed on uranium surfaces etched with energetic (3-15 keV) Ar^+ ions directed at glancing incidence [5]. Upon sample ion bombardment with ions directed at a fixed direction, an electron micrograph shows the formation of elongated and irregular channels. However, when this sample was rotated by 90 degrees and subsequently sputtered again, the formation of highly regular ripples possessing amplitude of 10-15 nm was observed. One year later, the first example of sputter ripples produced on surfaces simultaneously heated and ion etched was observed on polycrystalline Al [6]. After this formation of ripple on various substrate materials semiconductors (Si, Ge, SiGe, GaSb, InP etc.), Metals (Ag, Cu, Pt, Co etc.), insulators (Quartz glass, Al_2O_3, MgO etc.) were studied with time both experimentally and theoretically [2].

The first analysis to address the existence of a surface instability during ion sputtering was conducted by Sigmund [7], who studied the surface erosion rate for different surface topographies and zero surface curvature. However, Sigmund pointed out that an instability exists for curved surfaces. Bradley and Harper (BH) [4] extended this formalism to account for the effect of a small surface curvature upon the sputtering yield. BH also incorporated surface relaxation due to surface diffusion in their model, and it remains the most successful theory for explaining sputter induced rippling. Makeev, Cuerno, and Barabasi (MCB) [8] extended the BH theory with the inclusion of non-linear terms in their analysis of the morphological evolution of ion sputtered surfaces. In the fallowing section we will briefly address only the existing models describing ripple pattern formation and scaling laws based on previously conducted experiments [9-12]. After the theoretical treatment experimentally observed scaling laws (Energy, angle of incidence, fluence dependency on ripple wavelength) will be shown, they were used in this work to produce ripple templates.

2.1.1 Sigmund sputtering theory

To clarify the physical basis of the processes which rule the formation of such nanopatterns, we need to understand first the basics of sputtering. The bombardment of solid targets with energetic particles can give rise to many different processes. Incident ions can be backscattered or implanted into the target, and different particles like atoms, electrons and photons can be emitted from it. Moreover, an ion penetrating a solid will undergo many collisions with target atoms, transferring them its kinetic energy and momentum. This may lead to displacement of atoms with consequent creation of lattice defects like vacancies and interstitials. When target atoms receive enough kinetic energy they will induce additional collisions with other target atoms and so additional atomic displacements. This process is known as ó*collision cascade*ô[13-15]. In case of small number of atoms placed in motion and isotropic distribution of the collision density the process is called *'linear collision cascade'*. The cascade is described in terms of binary collisions between moving ions and stationary atoms. When target atoms travelling towards the surface (due to momentum reversal) gain enough energy, they can overcome the surface binding energy barrier and be emitted in vacuum. This process will lead to material erosion (sputtering). Incident ions can loose their kinetic energy in both elastic (nuclear collisions) and inelastic (electronic excitation) processes. However, for the low energy range ion energy loss is mainly due to nuclear collision processes, which determine the energy deposition and the range of ions in the target.

The amount of ion energy deposited by an ion and the ion range depend on the material properties and the ion mass and energy. Furthermore, the increasing number of ions will induce additional defects in the crystalline structure which may lead to surface amorphization in case of high defect density. The erosion rate of a surface under ion bombardment is determined by the sputtering yield Y, defined as the average number of atoms leaving the surface of a solid per incident particle [14, 16, 17]. Most of the sputtered atoms come from the surface. However, the scattering events take place within a certain layer of average depth ά*a'* which is the average energy deposition depth. Usually the number of sputtered atoms is orders of magnitude smaller than the total number of atoms participating in the collision cascade. A well accepted description of ion sputtering has been developed by Sigmund [16,17]. He derived a set of transport equations describing the energy transfer during the sputtering process in case of amorphous targets. In Sigmundôs theory of sputtering the rate at which material is sputtered from a point on an arbitrary surface $z = h(x,y)$ is proportional to the power deposited there by the random slowing down of ions. The average energy deposited at a point $\mathbf{r} = (x,y,z)$ in the solid by an ion which travels along the z-axis until striking the surface has the following Gaussian distribution:

$$E(\vec{r}) = \frac{\varepsilon}{(2\pi)^{3/2}\sigma\mu^2}\exp\left(-\frac{(z-h(0,0)+a)^2}{2\sigma^2}-\frac{x^2+y^2}{2\mu^2}\right) \tag{2.1}$$

In eq. 2.1 ε indicates the total energy carried by the ion and σ and μ are the widths of the distribution in the directions parallel and perpendicular to the incoming ion beam, respectively. A schematic illustration of the ion energy distribution is shown in Fig. 2.2.

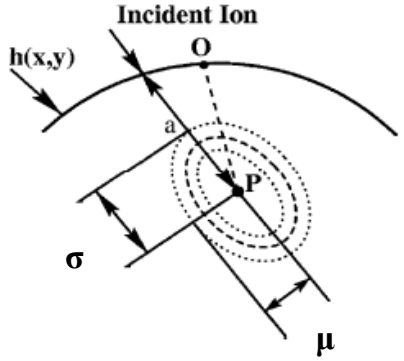

Fig. 2.2: *Schematic illustration of the energy distributed by an incident ion. While the collision process induced by an ion is rather complex, according to Sigmund it can be reduced to the following effective process: the ion penetrates the bulk of the material and stops at point P, where all its kinetic energy is released and spread out to the neighbouring sites following a Gaussian form with widths σ and μ.*

Monte Carlo simulations of the sputtering process have shown that the deposited energy distribution can be well approximated by a Gaussian function for intermediate and high energies [18]. The mean energy deposition depth of an ion travelling inside the bulk is usually comparable to the penetration depth and is proportional to the ion energy according to this relation:

$$a(\varepsilon) = \frac{1-m}{2m}\gamma^{m-1}\frac{\varepsilon^{2m}}{NC_m} \tag{2.2}$$

N represents the target atomic density, γ is equal to $\frac{4M_1M_2}{(M_1+M_2)^2}$ (M_1, M_2 are the mass of ion and target atom, respectively), C_m is a constant dependent on the inter-atomic potential and the exponent $m = m(\varepsilon)$ varies from $m = 1$ at high energies to $m \sim 0$ at low energies. For intermediate energies (10-100 keV) $m \sim ½$ and the energy deposition depth becomes $a(\varepsilon) \sim \varepsilon$. Eq. 2.1 describes what happens in case of a single ion hitting the solid. Actually the sample is irradiated by a uniform flux f of bombarding ions, which penetrate the solid at different points simultaneously. Therefore erosion velocity at an arbitrary point O depends on the total power given by all the ions entering within the range of the distribution (Eq. 2.1). The normal erosion velocity at a point O is calculated as [17]:

$$v(O) = \Lambda\int_Q \Phi(\bar{r})E(\bar{r})d\bar{r} \tag{2.3}$$

The integral is calculated over the region Q of all points at which the deposited energy contributes to the total power. $\Phi(\mathbf{r})$ is a local correction to the uniform flux f due to the variation of the local slopes, and Λ is a constant which depends on the material, according to binding energy and scattering cross-section:

$$\Lambda = \frac{3}{4\pi^2}\frac{1}{NU_0C_0} \tag{2.4}$$

U_0 is the surface binding energy and C_0 a constant proportional to the square of the effective radius of the inter-atomic potential. eq. 2.3 is only valid when shadowing effects and re-deposition of sputtered material are ignored. Sigmundôs theory offers a very detailed description of ion bombardment but it is not able to provide direct information about the morphology of ion sputtered surfaces. The equation for the erosion velocity in the given form

can not be used to make analytical predictions about the dynamical properties of surface evolution.

2.1.2 Bradley-Harper model for sputter induced rippling

The first and rather successful model able to explain the evolution of surface morphology under ion irradiation with subsequent ripple formation has been proposed by Bradley and Harper (BH model) in 1988 [4]. Starting from Sigmundôs theory of sputtering, they demonstrated for the first time that the dependence of the sputtering yield on the surface curvature induces an instability which leads to the formation of periodically modulated surfaces. Many theoretical studies about surface erosion by ion irradiation consider the sputtering yield independent from the local curvature of the surface. Nevertheless, such assumption is a good approximation only if the radius of curvature at an arbitrary point on the surface is much larger than the ion range (R>> a). Bradley and Harper notified that it is impossible to predict the formation of wave-like structures on a surface without considering such effect. To determine the dependence of the sputtering yield on the curvature, they calculated from eq. 2.3 the normal component of the surface velocity $v(\phi,R)$ at a point O when an uniform flux f is incident at angle ϕ, measured relative to the z-axis (z-axis is normal to the surface). The coordinate system is defined like this that axis x and y lie parallel and perpendicular to the projection of the ion beam on the surface, respectively. They treated the system as a two dimensional one, but this does not affect the result since it can be easily generalized to the three dimensional case. Moreover, they assumed that the surface height $h(x)$ varies slowly enough so that R, the radius of curvature at point O, is much larger than the ion range a. The final result obtained from their calculation has the form:

$$v(\phi,R) \approx \frac{\Lambda \varepsilon f a}{\sqrt{2\pi}\sigma\mu} B_1^{-1/2} \exp\left(-\frac{a^2}{2\sigma^2}+\frac{A^2}{2B_1}\right)\left[\cos\phi+\Gamma_1(\phi)\frac{a}{R}\right] \tag{2.5}$$

where

$$\Gamma_1(\phi) \equiv \frac{A}{B_1}\sin\phi - \frac{B_2}{2B_1}\left(1+\frac{A^2}{B_1}\right)\cos\phi - \frac{AC}{B_1^2}\left(3+\frac{A^2}{B_1}\right)\cos\phi \tag{2.6}$$

Λ is a constant of proportionality relating the power deposited at O to the rate of erosion there, and the coefficients A, B_1, B_2 and C depend on the parameters σ, μ and the angle ϕ[4]. Considering first the limit of a flat surface (R=∞), using $Y_0(\phi) = Nv(\phi, R=\infty)/f\cos\phi$, the yield results to be equal to:

$$Y_0(\phi) \approx \frac{\Lambda \varepsilon N a}{\sqrt{2\pi}\sigma\mu} B_1^{-1/2}(\phi) \exp\left(-\frac{a^2}{2\sigma^2} + \frac{A^2(\phi)}{2B_1(\phi)} \right) \tag{2.7}$$

where $$B_1^{-1}(\phi) = \left(\frac{\sigma}{a}\right)^2 \left\{ 1 + \left[\left(\frac{\sigma}{\mu}\right)^2 - 1 \right] \cos^2\phi \right\}^{-1} \quad Since(\sigma > \mu)$$

N is number of atoms per unit volume in amorphous volume. eq. 2.7 shows that sputtering Yield is an increasing function of the incident angle ϕ, which is a reliable result except of course for cases of grazing incidence where the model is not valid anymore. eq. 2.5 contains the dependence of the sputtering yield on the surface curvature. The coefficient of a/R, Γ_1, is negative for $\phi = 0$. This means that when the ion beam is normally incident on a periodic disturbance, the valleys are eroded more rapidly than the crests, being the radius of curvature R negative in a valley. The result is that sputtering increases the amplitude of the perturbation and so leads to an instability and roughening of the surface. The process is well understandable looking at Fig. 2.3.

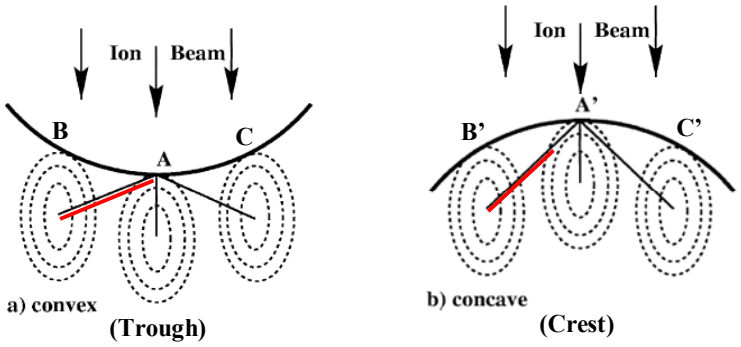

Fig. 2.3: *Schematic illustration of the physical origin of the instability during ion erosion of non-planar surfaces. A surface element with convex geometry (a) is eroded faster than that with a concave geometry (b), due to the smaller distances (solid lines) the energy has to travel from the impact point to the surface (A or A' points).*

The energy deposited at the point A by ions hitting the surface at A is the same as that deposited at Aô by ions hitting the surface there. However, the average energy deposited at A by an ion which hits the surface at B is higher than that deposited at Aô by an ion incident at Bô and the same is true for C and Cô respectively. This leads to a higher rate of erosion in A compared to Aô. Starting from the equation for the erosion velocity generalized for the three dimensional case and combining the smoothing effect due to thermally activated surface

diffusion, Bradley and Harper derived a linear equation for the surface morphology evolution under ion sputtering [4]:

$$\frac{\partial h}{\partial t} = -v_0(\phi) + v_0^{'}(\phi)\partial_x h + S_x(\phi)\partial_x^2 h + S_y(\phi)\partial_y^2 h - K\nabla^4 h \tag{2.8}$$

Here K is thermally activated surface diffusion, S_x, S_y coefficient depend on experimental parameters describe later. This equation describes the temporal evolution of the surface height $h(x, y, t)$ during sputtering under an incident angle ϕ considered respect to the normal of the initial flat surface. The general meaning of this equation is the competition between two mechanisms: the roughening of the surface, due to the curvature dependent sputtering yield, and smoothing effects for thermal diffusion of target atoms. The first term on the right side represents the angle dependent erosion velocity of a flat surface. The second term is related to the lateral movement of the structures on the surface. These first two terms do not affect the characteristics of the final topography (wavelength and amplitude). The third and fourth terms describe the curvature dependent erosion rate and are responsible for the roughening of the surface while the last one is the contribution of surface relaxation due to material transport on the surface. The two coefficients S_x and S_y depend on the ion energy, ion incident angle and material properties:

$$S_{x,y} = \frac{fa}{N} Y_0(\phi)\Gamma_{1,2}(\phi) \tag{2.9}$$

The two coefficients $\Gamma_{1,2}(\vartheta)$ account for the local variation of the sputtering yield and are equal to:

$$\Gamma_1(\phi) \text{ (see eq. 2.6)}$$
$$\Gamma_2(\phi) = -\frac{\mu^2}{a^2}\left(\frac{1}{2}B^2 + \frac{AC}{B_1}\right)\cos\phi \tag{2.10}$$

They depend on the ion incident angle and on the parameters which characterize the distribution of the deposited energy. Which they calculated using the SRIM code [18]. The coefficient K describes the thermally activated surface diffusion related with material transport on the surface:

$$K = \frac{D_s \gamma \Omega^2 N}{k_B T}\exp\left(\frac{-\Delta E}{k_B T}\right) \tag{2.11}$$

Here D_s is the surface diffusion constant, γ the surface free energy per unit area, Ω the atomic volume, n the number of atoms per unit volume on the surface, ΔE the activation energy for surface diffusion, k_B the Boltzmann constant and T the surface temperature. Only by adding a smoothing term eq. 2.8 predicts the formation of ripple structures on the surface; the roughening terms alone are not enough. To practically see how the periodic solution comes out it is useful to take the Fourier transform of eq. 2.8, with $\mathbf{q} \equiv (q_x, q_y)$ the wave vector. eq. 2.8 becomes:

$$\frac{dh(q_x,q_y,t)}{dt} = [-S_x q_x^2 - S_y q_y^2 - K(q_x^4 + q_y^4)]h(q_x,q_y,t) \tag{2.12}$$

The solution of such equation is:

$$h(q_x,q_y,t) = h(q_x,q_y,0)\exp[r(q)t] \tag{2.13}$$

where $h(q_x,q_y,0)$ is the initial amplitude spectrum of the Fourier transform with growth factor:

$$r(q_x,q_y) = -S_x q_x^2 - S_y q_y^2 - K(q_x^4 + q_y^4) \tag{2.14}$$

Eq. 2.13 describes the time evolution of the amplitude of the Fourier components and it increases exponentially for positive $r(q)$ values. According to the sign of the growth factor, the surface can roughen or smoothen. The function $r(q)$ has a maximum at $q^* = (\max|S_{x,y}|/2K)^{1/2}$, where $\max|S_{x,y}|$ is the largest in absolute value between $-S_x$ and $-S_y$. The diffusion coefficient K is always positive, so that the sign of $r(q)$ depends on the coefficients S_x and S_y, which means on the parameters $\Gamma_1(\phi)$ and $\Gamma_2(\phi)$. The amplitude with wavenumber q^* will grow faster than the others, resulting in a periodicity with wavenumber q^* which will dominate the surface topography. The corresponding wavelength of ripples can be written as:

$$\lambda = \frac{2\pi}{q^*} = 2\pi\left(\frac{2K}{\max|S_{x,y}|}\right)^{1/2} \tag{2.15}$$

The direction of the wavevector of the periodicities depends on the values of S_x and S_y. The model can actually predict the dependence of the wavelengths λ_x, λ_y on the ion incidence angle. An example for the case $a = 3$ nm, $\sigma = 0.9$ nm, $\mu = 0.7$ nm is shown in Fig. 2.4 [9] : At an incident angle around 70° a change from $S_x<S_y$ to $S_x>S_y$ is observed, this implies the rotation of the ripple pattern from normal to parallel with respect to the projected direction of the ion beam. This fact has been seen in various experiments [9,10]. For normal incidence, $\Gamma_1(\vartheta)$ is equal to $\Gamma_2(\vartheta)$ and the direction of the selected wavevector is arbitrary. In this case

several ripple orientations will be selected by surface imperfections and a grid of hillocks and depressions will result on the surface, which is in agreement with experimental observation [3,9,10]. It is possible to derive some simple conclusions based on the BH theory, i.e. the dependence of the ripple wavelength λ on sputtering parameters:

- The amplitude of the ripples should grow exponentially without saturation.
- λ decreases with increasing ion energy according to the relation $\lambda \approx \frac{1}{E^{1/2}}$;
- λ is a decreasing function of the ion flux of the form $\lambda \approx \frac{1}{f^{1/2}}$;
- λ does not depend on the ion fluence.
- λ is a decreasing function of the temperature ,i.e. $\lambda \approx \frac{1}{T^{1/2}}$

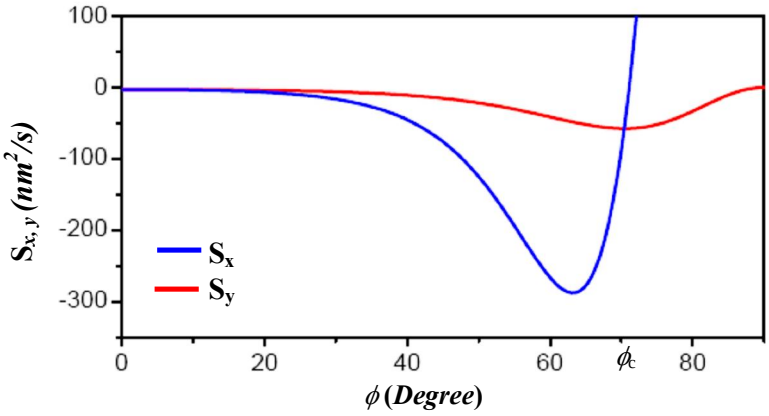

Fig. 2.4: *$S_{x,y}$ against angle of incidence ϕ, calculated for 500 eV Ar^+ bombardment on Si with a flux of 5x10^{15} cm^{-2}s^{-1} for a= 3 nm , σ = 0.9 nm, μ = 0.7 nm and Y=3[9].*

BH model does not take into account any other possible smoothing mechanism except thermal diffusion. Nevertheless this mechanism is active on the surface and becomes the dominating relaxation process only at high temperatures. To explain ripple formation at low temperature it is necessary to consider other smoothing effects. Makeev et al. [19] introduced the ion-induced effective surface diffusion (EDS) as the main relaxation mechanism at low temperatures. It does not imply a real mass transport along the surface, but it results from the local variation of erosion of the target during ion beam sputtering. Considering the EDS term as the main smoothing term eq. 2.8 becomes:

$$\partial_t h = -v_0 + v_0' \partial_x h + S_x \partial_x^2 h + S_y \partial_y^2 h - D_{xx} \partial_x^4 h - D_{yy} \partial_y^4 h - D_{xy} \partial_x^2 \partial_y^2 h \qquad (2.16)$$

The terms with the coefficients $(D)_{xx,yy,xy}$ enter eq. 2.16 in the form of diffusion-like terms proportional to the fourth derivative of the height function and thus lead to an additional anisotropic smoothing of the surface. Therefore, this relaxation mechanism is usually called effective or ion-induced surface diffusion (ESD). However, it is important to note that ESD results from preferential erosion during the sputtering which appears as a reorganization of the surface and does not involve any mass transport along the surface. Thus, ESD is strictly speaking no diffusion mechanism. This is also displayed by the fact that the coefficient D_{xx} might even become negative at large incident angles, leading to an additional instability of the surface. The three coefficients D_{xx}, D_{yy}, D_{xy}, depend on the parameters which determine the distribution of the deposited energy, ion flux, and incidence angle. If ESD is the main relaxation mechanism then the ripple wavelength can be calculated as follows :

$$\lambda_{x,y} = \frac{2\pi}{q^*} = 2\pi\left(\frac{2D_{xx,yy}}{\max\left|S_{x,y}\right|}\right)^{1/2} \tag{2.17}$$

- In this case λ is increasing with ion energy: $\lambda \approx a \approx E^{2m}$;
- λ is independent of ion flux and fluence.

Another relaxation mechanism which can contribute to surface smoothing is the ion-induced viscous flow (IVF), which is related to material transport along the surface and depends on the concentration of defects created during the cascade[20, 21]. In this case the wavelength is independent from the ion flux and fluence and is increasing with the ion energy.

2.1.3 Anisotropic Kuramoto-Sivashinsky equation

The BH model was very successful in explaining the mechanism which leads to ripple formation as well as their amplitude, wavelength and orientation with respect to the ion beam direction, in good agreement with experimental results. Nevertheless, this is a linear model unable to explain the long term behaviour of the surface evolution (like the appearance of kinetic roughening [22]) and to describe the stochastic nature of the sputtering process. For example, according to the linear model the ripple amplitude should increase exponentially in time, but in experiments amplitude saturation has always been observed [23]. The addition of non linear terms, which are depending on higher order powers of the surface height or its derivatives, modifying drastically the long term behaviour of the surface evolution. Cuerno et al. [24, 25] included non- linear terms in the BH model by expanding the basic sputtering

mechanism to include higher order effects. Performing the integral of the normal erosion velocity at a generic point *O* of the surface, they derived the equation of motion for the height profile:

$$\partial_t h(x,y,t) \cong -v(\varphi, R_x, R_y)\sqrt{1+(\nabla h)^2} \tag{2.18}$$

where φ is the angle of the beam direction with the local normal to the surface at $h(x,y)$ and R_x, R_y the radii of curvature at *O*. To take into account the stochastic arrival of ions on the surface a Gaussian white noise $\eta(x,y,t)$ with zero mean has been added to the equation. Expanding eq. 2.18 they obtained an anisotropic noisy Kuramoto-Sivashinsky equation (AKS) :

$$\partial_t h = -v_0 + v_0^{'}\partial_x h + S_x\partial_x^2 h + S_y\partial_y^2 h + \frac{\ell_x}{2}\left(\partial_x h\right)^2 + \frac{\ell_y}{2}\left(\partial_y h\right)^2 - D\nabla^4 h + \eta(x,y,t) \tag{2.19}$$

The coefficients of the non linear terms, ℓ_x and ℓ_y, depend on the ion beam parameters and energy distribution parameters *a*, σ, μ. They describe the tilt-dependent erosion rate, proportional to the ratio between ion flux and penetration depth *f*/*a*. ℓ_y is negative for all incidence angles, ℓ_x can have both positive and negative values. Unlike the linear expression, the nonlinear surface evolution equation can not be solved analytically, but it can be calculated numerically. Integration of such equation has been performed by Park et al. [26]. They showed that for short sputtering times the non linear effects are negligible and the system evolution is well described by the linear instability mechanism. However, after a crossover time, which depends on the coefficients of eq. 2.19, the surface morphology is completely determined by the non-linear terms. The crossover time τ can be written as:

$$\tau \cong \frac{D}{S_{\max}^2}\ln\left(\frac{S_{\max}}{\ell_{\max}}\right) \tag{2.20}$$

$\ell_{\max}$ is in the same direction of $S_{\max}$ for crossover time τ . The amplitude at the crossover time is predicted to be proportional to the ratio $S_{\max}/\ell_{\max}$ [26]. Two cases can be distinguished according to the signs of ℓ_x and ℓ_y. For $\ell_x \cdot \ell_y > 0$ the non-linear terms destroy the ripple morphology and lead to kinetic roughening. In case of $\ell_x \cdot \ell_y < 0$, ripple formation is followed by a long transient rough regime which ends in a new morphology of rotated ripples. The ripple wavelength and orientation are also correctly described by the linear

theory. Beyond the crossover time the non linear terms become effective and as a consequence the surface width saturates. Moreover, the ripple pattern generated in the linear regime disappears and the surface exhibits kinetic roughening [26].

2.1.4 GCC hydrodynamic model

The anisotropic generalization of the Kuramoto-Sivashinky (KS) equation has been very successful in predicting some of the non-linear effects observed in experiments of ripple formation, but still has some limitations. For example, it is not able to predict the increase of the ripple wavelength in time known as coarsening. It has actually been observed many times in experiments [27-30], but models introduced so far can not take it into account. A new model for ion beam sputtering (IBS) ripple formation at off-normal incidence has been proposed by Garcia-Castro-Cuerno (GCC model) [31-33]. It is called ôhydrodynamic modelô since it is based on the hydrodynamic description of pattern formation in Aeolian sand dunes and ion sputtered systems. Starting from this general model, a single height equation in which coefficients can be related to experimental parameters has been derived. This equation contains both the AKS equation and the hydrodynamic theory and generalizes those obtained by previous continuum models. Moreover it is able to predict many experimental features of pattern formation by IBS at oblique incidence, like transverse ripple motion with non-uniform velocity, onset of kinetic roughening and ripple coarsening. They considered two coupled fields: the thickness of the mobile surface adatoms layer and the height of the bombarded surface. The main difference between this model and previous ones is that in the present model not all the near-surface atoms which break their bonds with the surface will be eroded, but most of them will be re-deposited locally, giving raise to an implicit viscous flow in the amorphized layer. The model is basically a generalized AKS equation but with the presence of new nonlinear terms depending on the fraction of eroded atoms that become mobile. This continuum equation is able to describe much richer pattern dynamics. Numerical integrations of this model show that in the linear regime all the features predicted by the BH model are reproduced. Entering the non-linear regime the main role is played by the second non linearity. The first non linearity always leads to the saturation of the pattern with constant wavelength and amplitude [31-33]. Finally the GCC model is one of the very successful models about ripple formation, it can account for many non-linear effects which take place on the surface during ion irradiation. A detail description of complete model equations can be found in the cited reference [31-33].

2.2 Experimental setup

In this section the developed experimental setup used in the present work including details about the used ion-source and deposition methods are presented. This section is mainly divided in the following parts: description of vacuum chamber, ion source, and deposition systems.

2.2.1 Vacuum chamber

An ultra high vacuum (UHV) chamber was designed to fulfil two objectives in a single chamber, first to produce templates using ion beam sputtering and second metal film deposition using e-beam and magnetron sputter deposition. The chamber is equipped with a turbo-molecular pump and a cryogenics-pump to achieve vacuum down to $1x10^{-8}$ mbar. A Kaufman type ion source and an e-beam evaporator are mounted at two different levels and in opposite direction as shown in Fig. 2.5. In the centre there is a hanging water cooled sample holder which can be adjusted to the desired height and rotation. The sample holder offers the possibility of rotating at the desired angle and prevented from thermal effects on sample due to water cooling arrangement. During sputtering the temperature is maintained at 15^{o}C. A Faraday cup is also mounted on the shaft of sample holder facing the ion-source. This helps to achieve the position of maximum flux, which can be changed time to time due to some maintenance work (change of ion source filament, Grid misalignment etc.) and also used for flux calculations at different angle of beam incidence. One side of the chamber is connected with a transfer chamber (load-lock). Due to the much smaller volume of transfer chamber it can be pumped down very fast and a sample transfer can be done. The sample mounted on an Omicron plate can be transferred in main chamber with the help of a wobble stick (not shown in the Fig. 2.5). During Ar gas insertion the pressure raise to $2x10^{-4}$ mbar. The distance between the sample holder and the ion source (acceleration grid) amounts around 200 mm, and is much smaller than the mean free path length of ions of around 1 m for the working pressure given above. Therefore the extracted ions will reach the sample without collisions that could affect their kinetic energy and lead to a broad beam. There are two thermocouple connections (k-type), one directly connected backside of the sample holder and another mounted on one flange with a movable arrangement, to observe the temperature directly at the sample surface. Main features of the experimental setup are shown in Fig. 2.5. Due to different requirements

of sample orientation for sputtering and deposition, it was not possible to finish the entire experiment in-situ without breaking the vacuum.

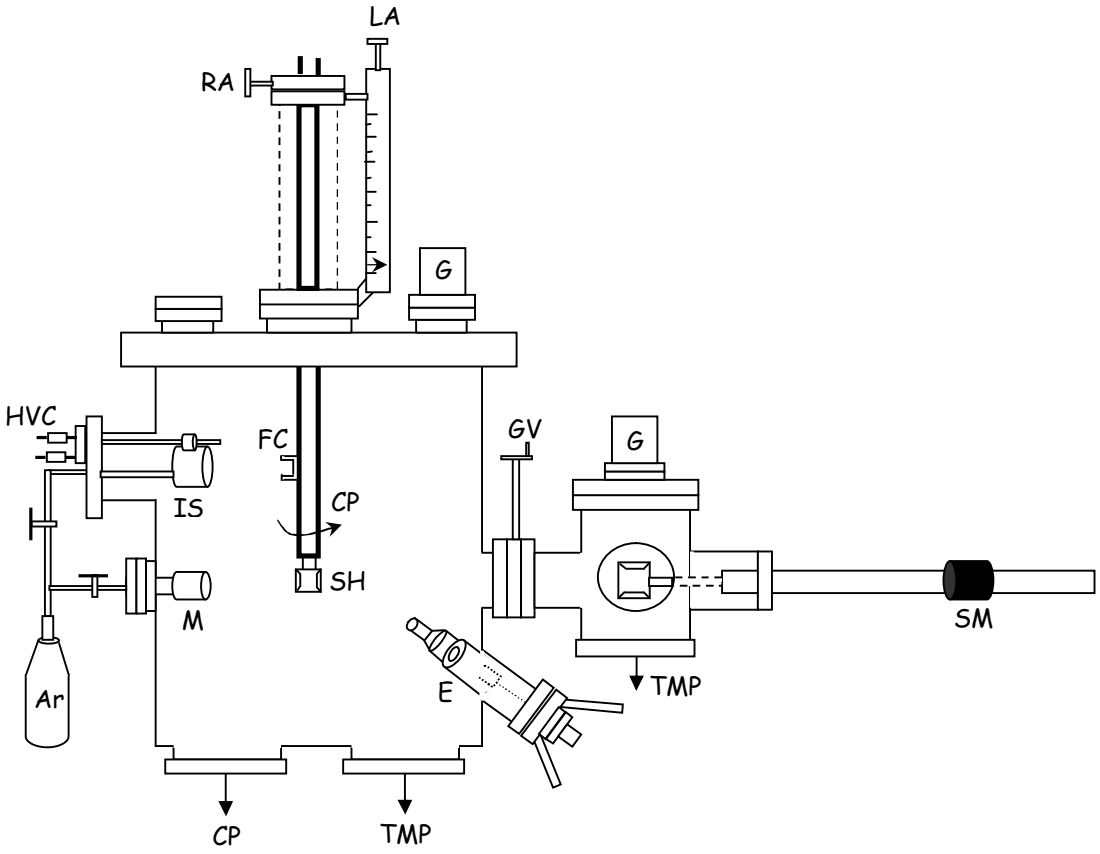

Fig. 2.5: *Schematic diagram of the experimental chamber. Abbreviations used above are defined like this.* ***IS****-Ion source,* ***M****-Magnetron,* ***E****- Evaporation system,* ***SH****-Sample holder,* ***CP****-Cooling pipe,* ***FC****-Faraday cup,* ***CP****-Cryogenic pump,* ***TMP****-Turbo molecular pump,* ***HVC****-High voltage connector,* ***G****-Vacuum gauge,* ***GV****-gate valve,* ***SM****-Sample mover,* ***RA****-Rotating arrangement,* ***LA****-Lifting arrangement.*

2.2.2 Ion-source

A Kaufman type ion source [9, 34, 35,] of beam energy maximum up to 1.2 keV was used for the ripple substrate preparation. Initially such sources were produced for space applications for providing thrust to satellites but due to life time of used filament and grids they were replaced by grid-less plasma thrusters. In laboratory and industry they are still favoured due to their simple design and operation. Some of the known applications are in ion beam assisted deposition [36] or surface smoothing [37]. Schematic of the typical Kaufman ion source is shown in Fig. 2.6.

A thoriated tungsten filament is mounted inside a ceramic discharge vessel. This vessel provides local higher pressure to ignite the discharge and also prevents the excessive heating of the source body that can damage the permanent magnets. Just in front of the hot filament a graphite anode ring is mounted. Emitted electrons from the filament are attracted towards the ring shaped anode and hit the available gas neutrals. The applied voltage between filament and the anode is called discharge voltage (V_{dis}).Hence this filamentary discharge concept creates the plasma. Since electron can easily be lost through source grounded body and anode, it will be difficult to sustain the discharge.

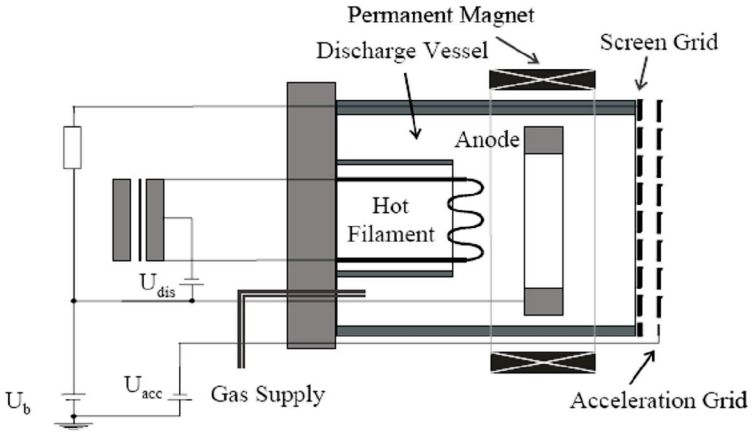

Fig. 2.6: *Schematics diagram of the Kaufmann type ion source.*

Therefore a magnetic cusp is used around the source body, with field lines such that the electrons are confined within the discharge vessel region and therefore their mean life time is increased. Using two grids system consisting of screen and accelerating grids, ions are extracted from plasma and accelerated in the form of a beam. The grids and anode ring are made of graphite. Each grid consists of hexagonally ordered holes for higher transparency of 1 mm diameter and has an opening aperture of two inches in diameter. Anode ring and grids are separated either with small ceramic balls or by circular washers. These spacers need to be cleaned after several experiments due to deposition of sputtered graphite from grids to avoid short-cuts between grids.

The energy of the extracted ion beam (represented by the so-called beam voltage V_b) is determined by the sum of V_{dis} and the voltage V_{scr} applied to the screen grid, $V_b = V_{dis} + V_{scr}$. By applying a negative voltage V_{acc} to the accelerator grid, ions get extracted from the plasma and are accelerated towards this grid. The value of V_{acc} affects the shape and the divergence of the ion beam. The potential distribution graph in different region is shown in

Fig. 2.7. However, in the current experiments, no influence of V_{acc} on the surface morphology has been observed. The same holds also for the discharge voltage V_{dis}. Therefore, in the experiments of this work, V_{acc} was fixed at ī 200 V and V_{dis} at 70 V. The working pressure in the vacuum chamber during operation was 2 $\times 10^{-4}$ mbar. The applied ion flux was determined by measuring the ion current on the sample and ranged from 3.5×10^{14} to 3.5×10^{15} $cm^{-2}s^{-1}$. Within this range, no influence of the flux on the surface morphology was observed.

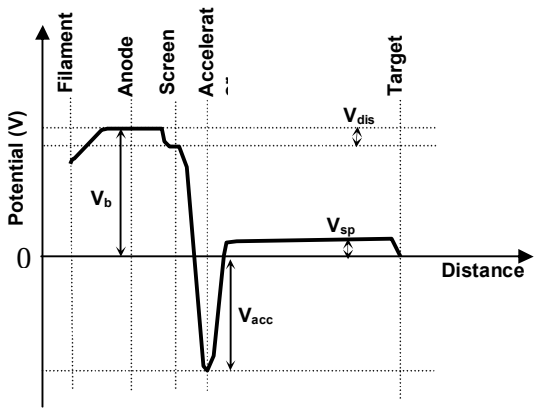

Fig. 2.7: *Potential diagram across the different parts of the ion source and outside, up to the sample holder.*

2.2.3 E-beam evaporation system

Film growth on prepared rippled templates was performed mainly using an e-beam evaporator system. This method gives a very precise control on deposited metal flux and is capable to work at very low pressure (~10^{-8} mbar in our work) unlike sputter deposition which provide very high atomic flux and operates at substantially higher pressure (10^{-3}-10^{-2} mbar). During our investigation it was found that incident atom flux is crucial for nanoparticle self-assembly. Therefore this method is the preferred choice. Schematic diagram and actual-view of the inner-view of commercially available e-beam evaporator (EFM3) from Omicron is shown in Fig. 2.8(a, b). Rod of evaporant or some amount inside a proper crucible is mounted with a metal shaft connected with high voltage (600-1000 V). In front of crucible at some distance there is a thoriated tungsten filament Fig. 2.8(a, c) [39, 40]. Under operating condition filaments throws the electrons, which are attracted towards crucible due to high voltage. Sufficient temperature rising due to electron heating leads to evaporation of material. Some part of evaporated material is ionised which is monitored with flux monitor connected close to exit. Choice of proper crucible is very important; it should have evaporating or melting temperature much higher then evaporant. Mo crucible for silver and Al_2O_3 core inside Mo crucible was used for cobalt deposition respectively (Fig. 2.8(d)).

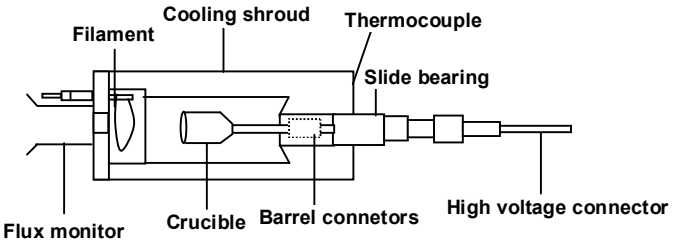

***(a)* Schematic diagram of e-beam evaporator**

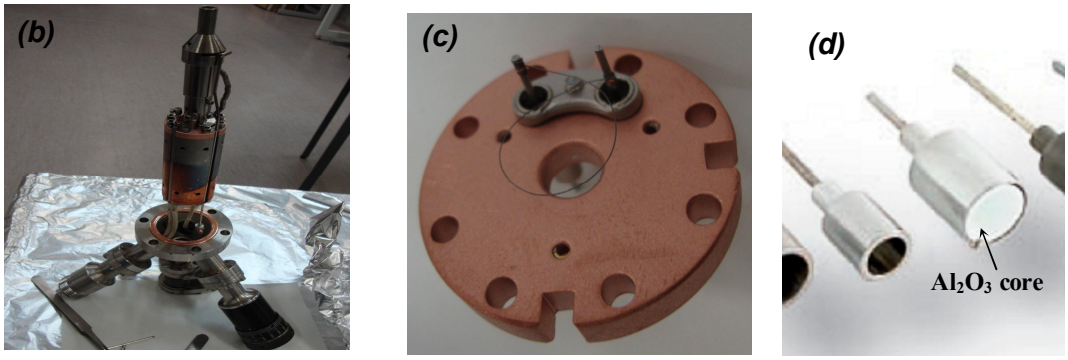

Fig. 2.8: *(a)Schematic diagram of e-beam evaporator,(b)E-beam evaporator, (c)Used filament, (d)Used crucible for silver (left) and cobalt deposition (right).*

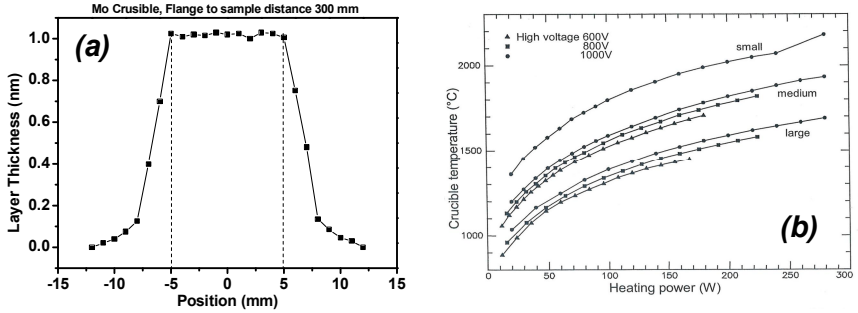

Fig. 2.9: *(a) Spot diameter at a distance of 300 mm for 8.0 mm Mo crucible.*
(b) Mo crucible temperature of different crucible size for different e-beam energies [39].

Due to low pressure (~10^{-8} mbar) operation (less collision, higher mean free path) the evaporated material can be used for deposition at fairly large distance (270 mm in our case) with small divergence. As shown in Fig. 2.9(a) at a distance 300 mm the deposition is almost constant within 10 mm , which is actually the sample size always used for this study. Mo crucible temperature varied depending on the applied high voltage and can reach upto 2000^{o}C (Fig. 2.9(b)) [39], while for silver 900^{o}C is sufficient for evaporation. For Silver at 800 V beam energy and with filament current of 1.9 A deposition rate of 0.15 nm/minute could be achieved.

2.2.4 Magnetron sputtering system

Magnetron sputtering deposition method was also used for a comparative study with e-beam deposition in a few experiments. Magnetron sputtering is another very popular method to grow thin and thick films with a fast deposition rate. As on today several type of magnetron designs exist and can be divided into two configurations, planar (more commonly used) magnetron and cylindrical magnetron. Conceptual diagram of planar magnetron functioning is shown in Fig. 2.10. Target material in the disc form is mounted at the centre and isolated with ground with a few mm gap. This gap is adjusted according to Paschenôs law of discharge, which tells that for an optimum combination of pressure (p) and electrode gap (d) there exists a minimum voltage V at which discharge can be start. Special design of magnet as shown in Fig. 2.10 is used to confine the electrons near target region using (ExB) drift [40]. Permanent magnets are placed at the back side of the cathode target generates magnetic field lines that enter and leave through the cathode plate. During operation magnetron require continuous water cooling to avoid damage of permanent magnets Ar gas is usually used for non reactive experiments. Ar ion hits the target material and releases the secondary electrons and target atoms. Secondary electrons sustain the discharge and sputtered atoms used for deposition on a substrate close to magnetron. Due to high pressure operation ($1x10^{-2}$ m.bar) neutral face large collisions and can not move very far from magnetron like in the case of evaporation. DC as well as pulsed DC or RF power can be applied to cathode depending upon the type of target material used. 2ò silver and cobalt targets were used in our experiments with a DC voltage connection operating around 300 V.

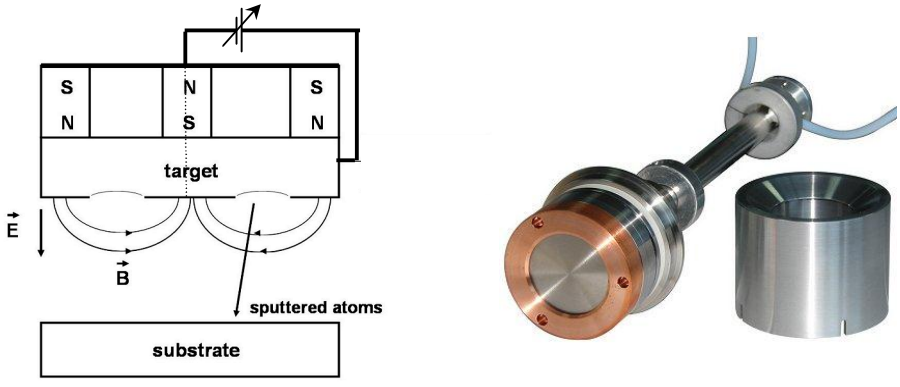

Fig. 2.10: *Schematic diagram of working principle of magnetron is shown left side and actual target mounted magnetron is shown right side.*

2.3 Characterisation techniques

Different characterisation techniques were used in the different fabrication stages (starting from growth stage) and application of self-assembled nanoparticle and nanowires. Ripple topography was characterised mainly by ex-situ tapping mode AFM. After silver and cobalt deposition the samples were characterised using ex-situ SEM, since in AFM the particle chain appear much closer and particle appear to be bigger due to tip art effects. It was also difficult to see silver cluster each time using AFM due to some unknown reasons (Silver particle mobility or plasmon interaction). TEM study was performed for a few samples in the cross-sectional view of deposited nanoparticles. This gave useful information about their location, shape and alignment. Film growth was calibrated using RBS measurements. Optical properties were accessed using ellipsometry and Raman spectroscopy. Details of these optical techniques will be given in the corresponding sections.

2.3.1 Atomic force microscope (AFM)

Atomic force microscopy is part of a microscopy group called scanning probe microscopy (SPM). With this technique, a sample is analyzed by probing the surface with a tip and the interaction between tip and sample is measured by tracking the deflected laser from a cantilever [41]. Physical topography, charge density, magnetic field, plasmon coupling and other surface properties can be discerned in different mode of operation like AFM, SSRM, MFM, SNOM etc.

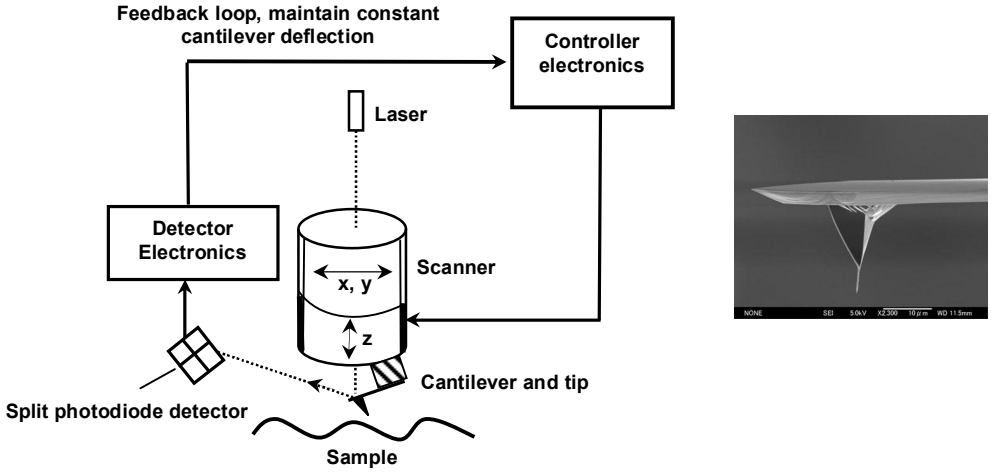

Fig. 2.11: *Schematic of the functioning of AFM and an actual view of AFM tip.*

Different probing methods are available in AFM, *contact mode* (Probe having direct physical contact with the sample), *non-contact mode* (Tip oscillating at a constant amplitude above the sample surface), *tapping mode* (Oscillating tip touches the sample with low forces).Fig. 2.11 shows the basic components of an atomic force microscope. Piezoelectric tripod scanner is used to provide sub-nanometer motion measurements with one stationary pivot point and three discrete piezoelectric mounted orthogonal for individual X, Y, Z control. This provides a large scanning area X and Y. Piezo scan across the sample surface while vertical motion is done by Z-piezo scan. Fig. 2.11 also shows probe tip mounted on a cantilever. Basically used cantilever tip are of silicon nitride (Fig. 2.11) and cantilever with spring constant less than inter-atomic bond strength is available. The probe motion sensor senses the spacing between the probe and the cantilever and provides correction signal to the piezo scanner to keep the height constant. The optic lever system consists of a diode laser and a position sensitive photo-detector.

All the AFM measurements of this work have been performed using a Multi-Mode™ scanning probe microscope with a NanoScope IV controller from Veeco Instruments in tapping mode. Images were usually taken with 512 points per scan line. Point Probe Plus tips (PPP-NCLR) for non-contact and tapping mode operation from NANOSENSORS™ have been used. These tips are shaped like polygon based pyramids of 10 to 15 εm height. The tip apex has a radius typically smaller than 7 nm and a half cone angle of less then 10^{o}. The cantilevers are made of highly doped silicon with a reflective aluminium coating on the detector side and have a nominal length of 225 εm. Sometimes the tip-sample interaction may lead to a deterioration of the tip. If the tip radius is too large to access the structure inter-distance, then the measured topography will be determined by the tip shape. Such a situation is visualized in Fig. 2.12. Therefore proper choice of tip is important to minimize the tip artifacts.

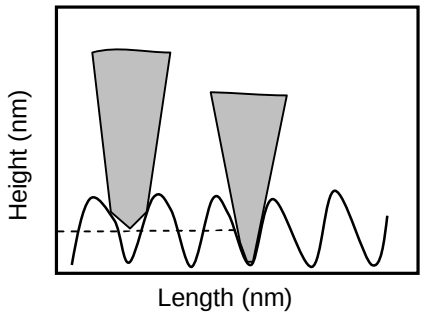

Fig. 2.12: *Schematic of how tip of two different sizes approach the rippled surface and consequently affect the surface topography.*

In the present study the objective of using the tapping mode AFM is to access the quality, i.e. long range lateral ordering, the wavelength, and the amplitude of the ripple pattern. Line scans provide the amplitude height information while the wavelength was determined via *FFT* (Fast Fourier Transformation) of the surface topography. Performing the discrete two dimensional *FFT* of the height profile of AFM images, it is possible to deduce the dominating spatial frequencies present on the surface and the amplitude of the roughness. The *FFT* for the discrete case is given by eq. 2.22 for a square image $L \times L$ with N and d equal in x and y directions, fx, and fy are the spatial frequency coordinates along the x-axis and y-axis, respectively.

$$FFT(f_x, f_y) = \frac{1}{N^2} \sum_{x=1}^{N} \sum_{x=1}^{N} h(x, y) e^{-i2\pi L / N(xf_x + yf_y)} \tag{2.22}$$

Two representative examples for ripple and dot structures are given in Fig. 2.13. *FFT* images give information about spatial frequencies (f_x, f_y), the spatial frequency has a minimum value at the center of the image and increases by moving out. Due to the preferred orientation of the ripples spots are visible in the *FFT* image (Fig. 2.13(a)). The direction of spots gives the direction of the wave vector of ripples. Ripple quality can be compared with Fig. 2.13(b) where *FFT* show only two dim peaks. The AFM image in Fig. 2.13(c), shows dot structures emerging on the surface. The image reveals the short range ordering of dots building domains with hexagonal ordering. However, these domains are randomly distributed in between them, therefore, a ring is visible in the corresponding *FFT* spectra (Fig. 2.13(c)).

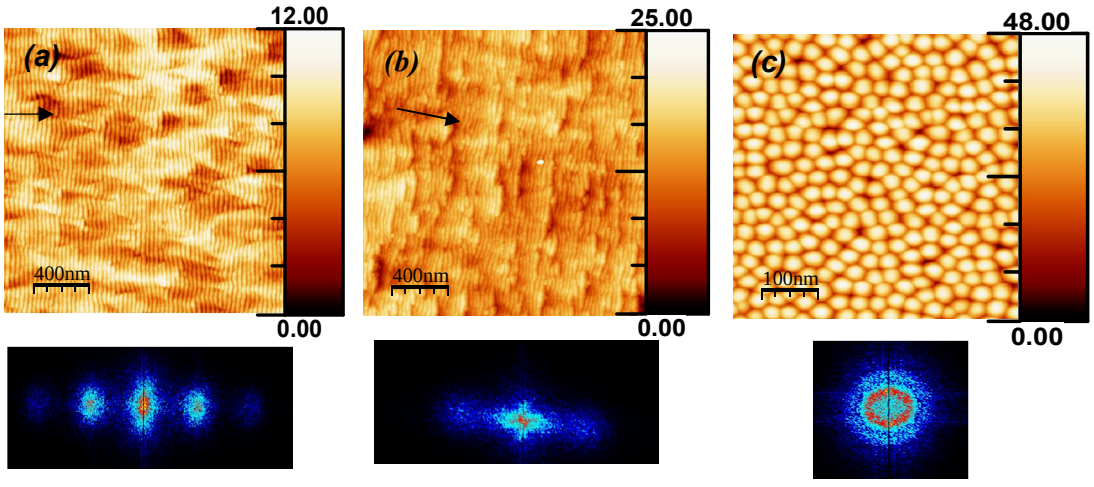

Fig. 2.13: *(a) Highly ordered ripple prepared at Si(100) surface, showing second order peak in FFT below,(b)Poorly ordered ripple prepared at SiO2 surface, FFT also show poor lateral correlation,(c) Hexagonally ordered dots prepared on GaSb surface, below is FFT showing the circular ring.*

The position of the spot (ring) determines the characteristic spatial frequency of ripples (dots), i. e. the wavelength of structures in the real space. From the width of the spot ring information about the homogeneity and spatial correlation of periodicities can be deduced. Additional spots (rings), are multiples of the first one, and are related to the high lateral ordering of structures. The higher the number of spots the better is lateral ordering. In fact the position of the first spot (ring) gives the mean separation between structures. For the ripples, it is assumed that the separation between ripple equal to ripple size. Due to the wavelike form of ripple the term ripple wavelength will be used to describe their size. This will be done with the supposition, that the separation in between ripples is equal to their size. For dots, the mean separation is equal to the mean lateral size by supposing that the dots are close packed to each other.

2.3.2 Transmission electron microscopy (TEM)

The first TEM was built by Max Knoll and Ernst Ruska in 1931[42]. Transmission electron microscopy (TEM) is a microscopy technique whereby a beam of electrons is transmitted through an ultra thin specimen, interacting with the specimen as it passes through. An image is formed from the interaction of the electrons transmitted through the specimen; the image is magnified and focused onto an imaging device, such as a fluorescent screen, on a layer of photographic film, or to be detected by a sensor such as a CCD camera. TEMs are capable of imaging at a significantly higher resolution than light microscopes, owing to the small de Broglie wavelength of electrons (0.0037 nm at 100 kV). This enables the instrumentôs user to examine fine details, even as small as a single column of atoms, which is tens of thousands times smaller than the smallest resolvable object in a light microscope. TEM is based on the absorption and scattering of transmitting electrons. In Fig. 2.14 the principle construction of a TEM is shown. An electron gun in the illumination system emits electrons that are then focussed and imaged onto the specimen by electromagnetic lenses. When penetrating the specimen, the electrons are scattered elastically and inelastically. The objective lens determines the limit of the image resolution. Finally the electronic signals are magnificated and recorded. EDS and EELS measurements are possible with a TEM. [42].

TEM from FEI Pvt. Ltd (Model: Titan, Energy range upto 300kV) was used in the present study. For preparing the TEM cross sections, two 5 x 4 mm^2 pieces of the sample have to be glued with the faces together. Furthermore, the sample has to be thinned mechanically by using different cutting and sanding techniques. Afterwards a valley is sanded

in the middle of the sample slice (dimpler). The final preparation step, the ion milling, is the sputtering with Ar ions of 3-5 kV at an angle of incidence of 4^{o}-5^{o}.

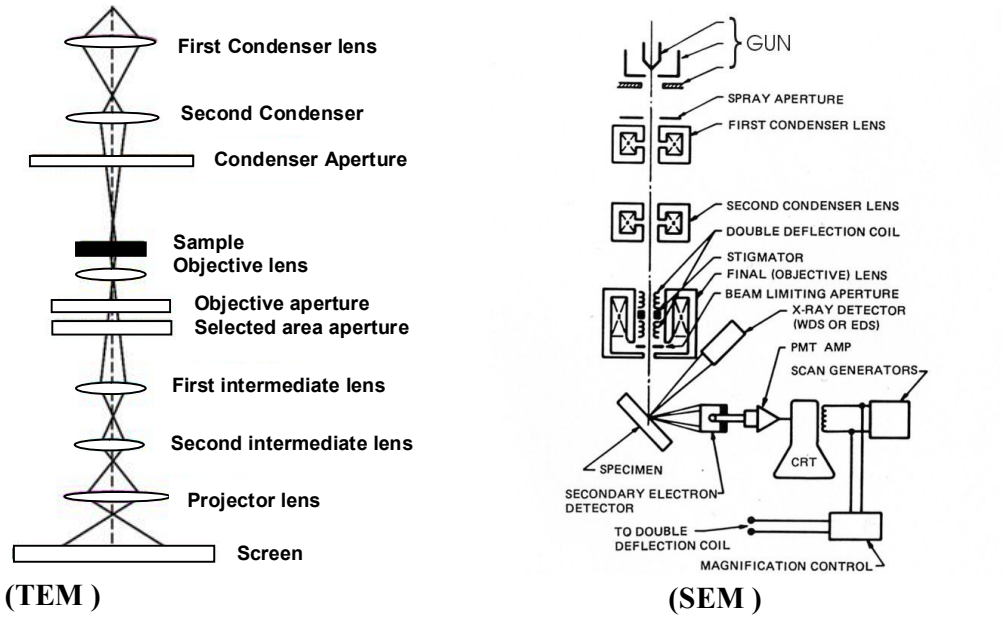

Fig. 2.14: *Schematic diagram of Transmission Electron Microscope (TEM)left and scanning electron microscope (SEM)right .*

2.3.3 Scanning Electron Microscope (SEM)

The first SEM image was obtained by Max Knoll, who in 1935 obtained an image of silicon steel showing electron channeling contrast. The scanning electron microscope (SEM) is a type of electron microscope that images the sample surface by scanning it with a high-energy beam of electrons in a raster scan pattern. The electrons interact with the atoms that make up the sample producing signals that contain information about the sample's surface topography, and composition. The types of signals produced by an SEM include secondary electrons, back-scattered electrons (BSE), characteristic X-rays, light (cathodoluminescence), specimen current and transmitted electrons. The electron beam, which typically has an energy ranging from 0.5 keV to 40 keV, is focused by one or two condenser lenses to a spot about 0.4 nm to 5 nm in diameter (Fig. 2.14). When the primary electron beam interacts with the sample, the electrons loose energy by repeated random scattering and absorption within a teardrop-shaped volume of the specimen known as the interaction volume, which extends from less than 100 nm to around 5 µm into the surface. The size of the interaction volume depends on the electron's landing energy, the atomic number of the specimen and the specimen's density. The

energy exchange between the electron beam and the sample results in the reflection of high-energy electrons by elastic scattering, emission of secondary electrons by inelastic scattering and the emission of electromagnetic radiation, each of which can be detected by specialized detectors.

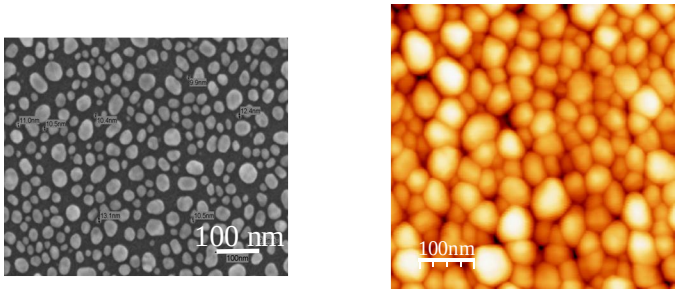

Fig. 2.15: *Surface topography of silver nanoparticles grown on flat Si surface. Left and right images were captured using SEM and AFM respectively. In SEM picture they look separated, while in AFM appear to be closely packed.*

Two different SEM (Nvision 40 and Hitachi S-4800, Energy upto 40 keV) were used for characterization. There black and white contrast of the shown SEM results will be different some time depending on the type of the SEM used. SEM was used as a main characterization method to analyze the samples immediately after metal deposition in the present study. Only topographical information collected by SEM sufficient to provide information about lateral ordering of nanoparticles , their shape, inter-particle gap, average diameter with the help of SPIP software. AFM is not the proper choice for this purpose, a comparison of similar sample measured in SEM and AFM is shown in Fig. 2.15. Since the AFM tip is not capable to resolve closer nanoparticles, all the particles appear closely packed. In SEM particles are clearly separated and more information about their shape and better statistics can be obtained. Therefore all samples were characterized mainly by SEM after deposition.

2.3.4 Rutherford backscattering Spectrometry (RBS)

Rutherford Backscattering Spectrometry (RBS) was used at two stages of this work; firstly RBS for calibrating deposition rates for e-beam evaporation system and second in-situ RBS measurements performed for determination of sticking probability on rippled surface. Originally E. Rutherford used the backscattering of alpha particles from a gold film in 1911 to

determine the fine structure of the atom, resulting in the discovery of the atomic nucleus. RBS as a method for materials analysis was firstly described in 1957 by Rubin et al. [43]. Rutherford Backscattering Spectrometry (RBS) is a widely used nuclear method for the near surface layer analysis of solids. A target is bombarded with light ions at an energy in the MeV-range (typically 0.5ï 4 MeV), and the energy of the backscattered projectiles is recorded with an energy sensitive detector, typically a solid state detector (Fig. 2.16). The energy of the backscattered particles depends both on the mass of the scattering nucleus and the depth of the collision in material [44, 45].

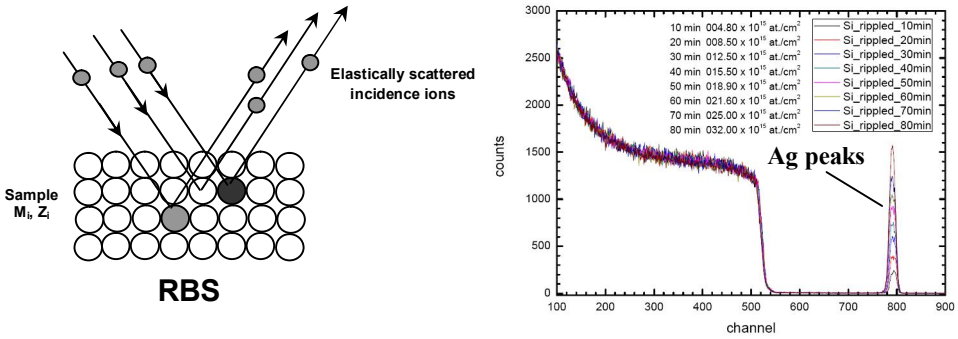

Fig. 2.16: *Schematic diagram of RBS working principle. RBS spectrum of Ag growth (in atoms/cm^2) on Si rippled with time with 2 MeV ^{4}He, 165^o scattering angle.*

The ions penetrate into the matter and lose their kinetic energy, at the beginning mainly in collisions with electrons until they come to rest in a depth of several micrometers. Only near the end of the range nuclear stopping dominates. Near the surface a very small fraction of the ions approach atomic nuclei near enough to be scattered at large angles. RBS allows the quantitative determination of the composition of a material and depth profiling of individual elements. RBS is quantitative without the need for reference samples, non-destructive, has a good depth resolution of the order of several nm, and a very good sensitivity for heavy elements of the order of parts-per-million (ppm). The analyzed depth is typically about 2 εm for incident He-ions and about 20 εm for incident protons. Several computer codes were developed with time incorporating all the technical details about detector sensitivity, beam energy, incident angle and other theoretical scattering equations. Such codes are capable to do direct elemental analysis, atomic density at surface and depth analysis. Some of the well known codes are RUMP [46], SIMNRA [47], and RBS etc. A typical RBS spectrum is shown in Fig. 2.16 measure for continuous silver deposition in a in-situ measurement on Si rippled surface in Rossendorf RBS facility. More detail information about this facility is available at ñhttp://www.fzd.de/dbò.

2.4 Scaling laws for plasmonic application

In this chapter we have discussed about physics of ripple formation, experimental facilities and used characterization methods. It has been already mentioned that a large ripple wavelength range from 20 nm to several 100 nm can be produced depending on ion energy and incident fluence. The incident angle can also influence the lateral ordering and the coarsening of ripples. Our objective is to produce ordered particles/wire array with a very low periodicity to enhance the plasmonic field effects. Large numbers of recent publications are available demonstrating experimentally as well as theoretically the inter-particle near field coupling effects [48, 49]. The plasmonic coupling was found to decay exponentially with inter-particle as shown in Fig. 2.17. Plasmonic coupling is also increases with increase in particles aspect ratio (Fig. 2.17). Both these two parameters: aspect ratio and interparticle gap can be varied easily using the rippled templates.

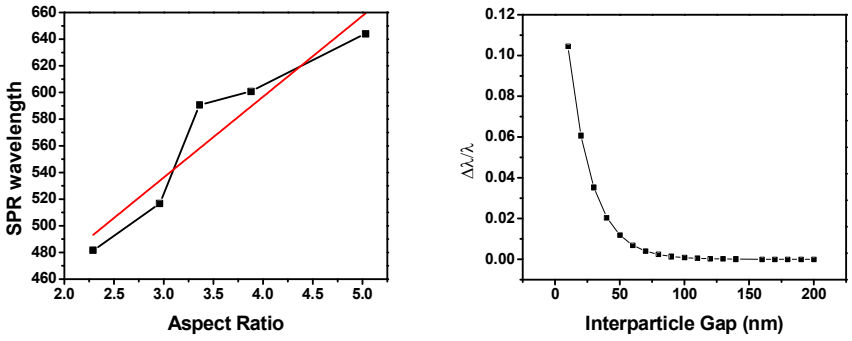

Fig. 2.17: *Variation in plasmon resonance with particle size and inter-particle distance both experimentally and simulated as stated in [49].*

Below 25 nm the coupling is increases drastically, consequently a large plasmon resonant shift arise. These examples are shown in literature usually for lithographically produced particles, where particle size (~100 nm) and inter-particle gap (~Minimum 20 nm) is large. Therefore special interest in this work was to go below limit of lithographic approach. With the present approach nanoparticles self-assembled along ripple length with much shorter inter-particle gap (~ 5 nm) have been produced. Ripple pattern of narrow wavelength in the range 20-50 nm maximum were chosen as templates for the deposition. Therefore, in this section only those ion energy scaling for ripple formation are reported which fulfill above requirement. The Experimental parameters for the production of ripple templates presented here are adopted from previous work in our lab by Keller et al. [9, 11, 12, 50].

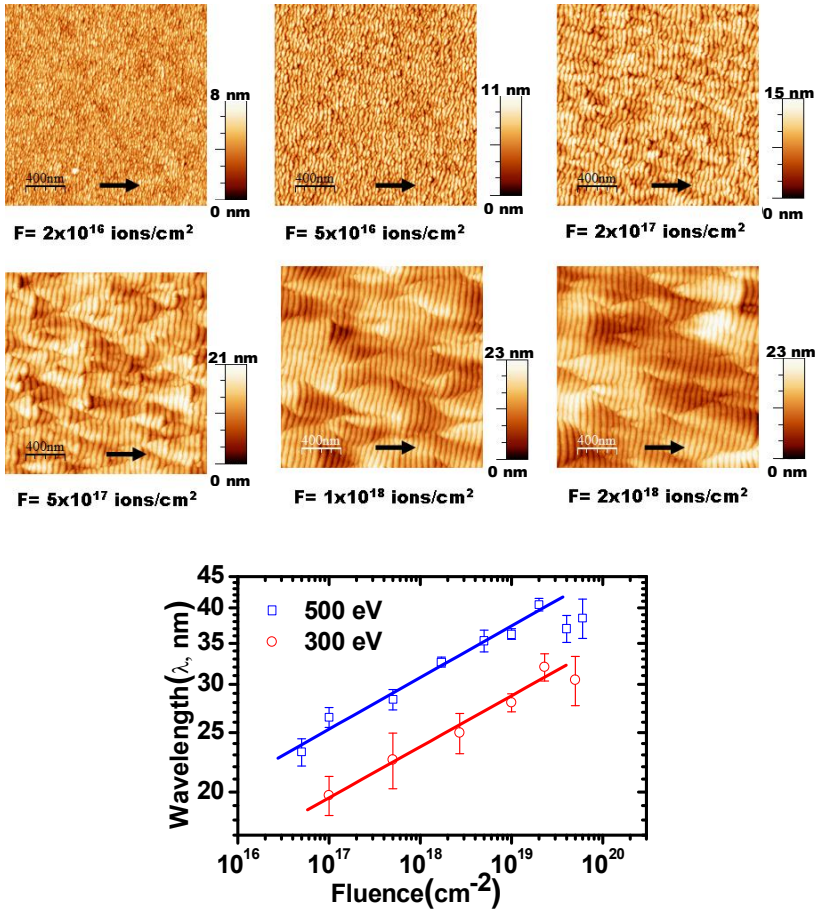

Fig. 2.18: *AFM topography of samples prepared at difference fluence in increasing order irradiating with 500 eV Ar+ ion and fixed angle of incidence 67°(Top AFM Images). Corresponding plotted values are shown right side for two different ion energies.*

The templates are produced by bombardment of 500 eV kinetic energy Ar+ ions broad beam on an epi-polished Si (100) substrate. The initial rms roughness of Si wafer is below 0.1 nm. The Si sample is maintained at a constant temperature of 15°C and chamber vacuum at $2x10^{-4}$ mbar during ion irradiation. Morphological changes for an ion incident angle 67° with respect to surface normal for different fluences and ion energies 300eV and 500 eV are shown in Fig. 2.18, respectively. At low fluence (~ 10^{16} cm^{-2}) shallow ripples appear. With increasing fluence wavelength coarsening is observed resulting in larger wavelength ripples. Summary of ripple periodicity of these images is shown in Fig. 2.18. The ripple wavelength can be tune from 20 nm to around 45 nm at 500 eV by simply varying the fluence in the range from 10^{16} to 10^{19} cm^{-2}. At the higher fluence wavelength get saturates. The solid lines in plot shown in Fig. 2.18 represent power law fits, $\lambda \alpha \phi^{n}$, with a coarsening exponent n ~ 0.08. In addition, λ is increases with ion energy, indicating that ion-induced diffusion is the dominating smoothing process [9,11].

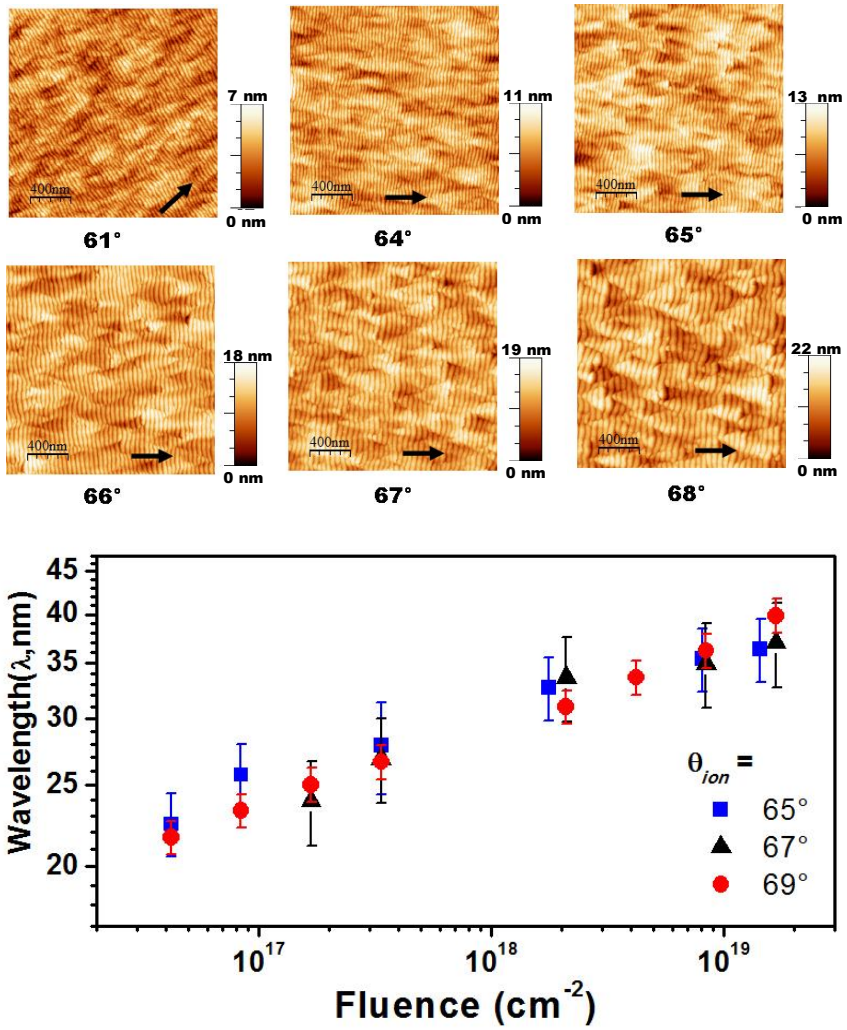

Fig. 2.19: *Ion incidence angle variation at constant fluence and energy and corresponding plot for different fluences.*

The influence of the ions incident angle at constant energy of 500 eV and fluence of $1x10^{17}cm^{-2}$ is presented in Fig. 2.19. Ion incidence angle can change surface morphology significantly. In the range of 65^{o}-69^{o} well ordered ripple are observed and deteriorate at larger angles. Therefore in this study an incidence angle of 67^{o} was always used. Within our range of experimental parameters the ripple amplitude was found to be 1.5 nm-3.0 nm. However, such small modulations are sufficient for the nanoparticles self-assembling on surface without using shadow deposition: this will be discussed in detail in chapter-3. Line scan of well ordered ripple pattern is presented in Fig. 2.20, showing the ripple modulation and corresponding amplitude. It can be seen that peak to peak amplitude is around within 3.0 nm.

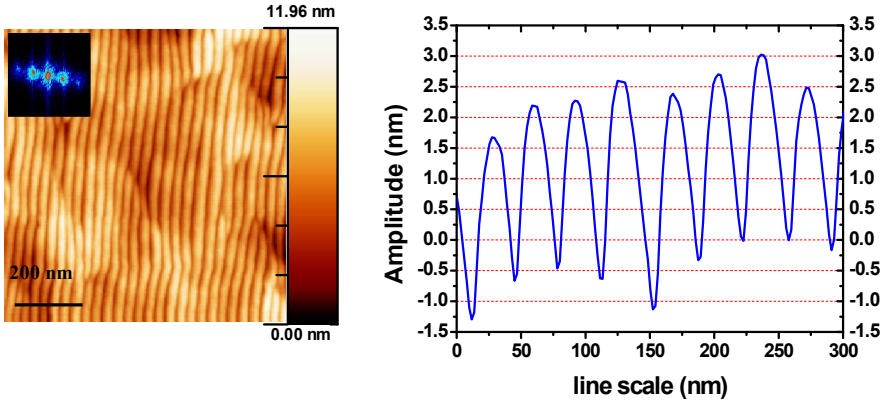

Fig. 2.20: *Line scan of ripple modulation for amplitude information is shown below.*

AFM images of ripple pattern with periodicity of 22, 28, 35, 35, 41, 44 and 51 nm along with their rms roughness prepared on Si (100) surfaces are shown in Fig. 2.21. The rms roughness increases with ripple periodicity. Ripples of periodicity range 30-35 found to be superior in terms of ordering (Fig. 2.21) compare to 20 nm (some what disconnected ripples) and 45-50 nm (slight inhomogeneous). A higher lateral ordering of the 28 nm and 35 nm ripple patterns is reflected by the second order peak appearing in the FFT (inset of Fig. 2.21). Above 40 nm a parallel ripple mode with much higher wavelength appears [9,12], which dominates the roughness at higher fluences .This quasi periodic pattern is visible in the AFM as high bumps perpendicular to ripple direction. Well ordered ripple pattern with wavelength below 20 nm could not be achieved so far. Therefore in most of our experiments ripple with periodicity around 35 nm was use as a template.

The quality of the ripple pattern directly affects the self-alignment of nanoparticle. During irradiation top few nanometers of the Si surface is amorphized and oxidizes (2-3 nm thick) immediately after exposing to atmosphere. Oxide layer formation is a favorable condition for both silver and cobalt cluster formation due to larger surface free energy differences and this also prevent silicide formation. An interesting property of the rippled templates is their asymmetry observed in cross-sectional TEM (Fig. 2.21). Ripples are tilted in the direction of incident ion beam, it is also a favorable condition provide much larger ridge portion in one side and smaller steep portion on the other. Length of ripple ridge varies for the ripples of different wavelength. Hence nanoparticle of very small to larger sizes (< ridge size) can be aligned on ripple surface.

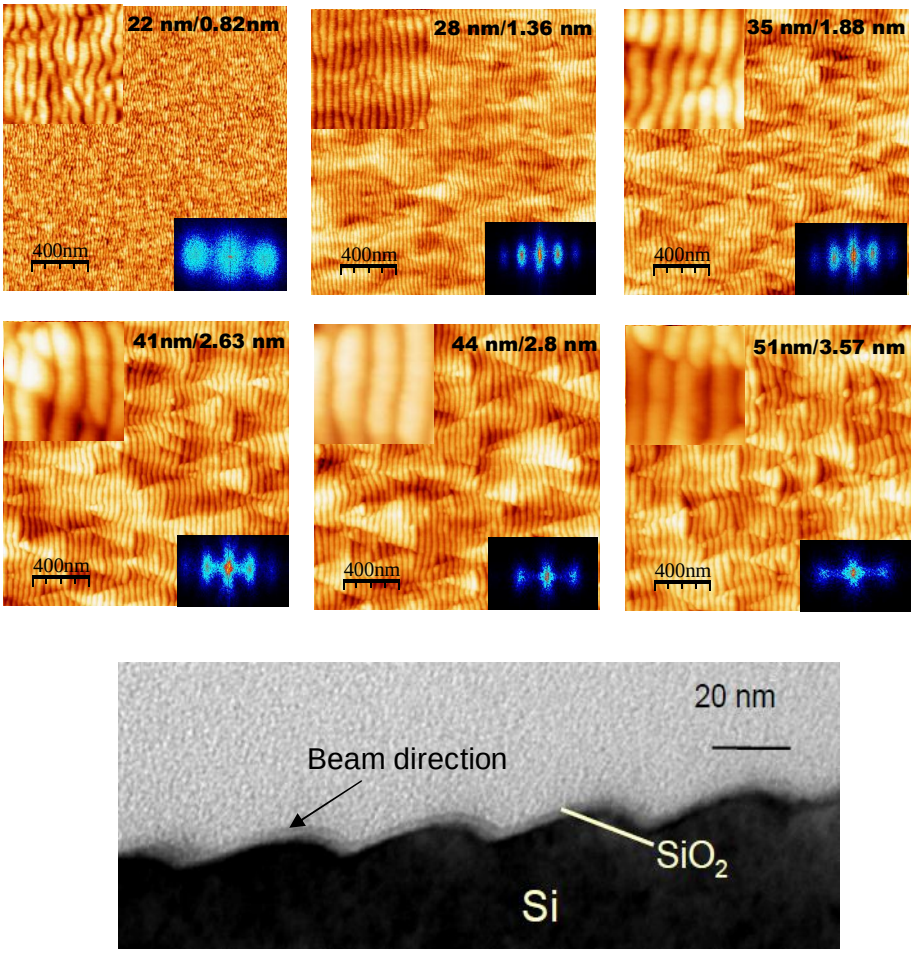

Fig. 2.21: *Sample of different periodicity ripple used in present study with their RMS roughness and FFT (Top 6 images). Cross-sectional TEM image showing ripple asymmetry and formed oxide layer on top.*

References

[1] W. R. Grove, *Philos. Mag*. 5 (**1853**) 203.

[2] W. L. Chan, E. Chason, *J. Appl. Phys*. 101 (**2007**) 121301.

[3] S. Facsko, T. Dekorsy, C. Koerdt, C. Trappe, H. Kurz, A. Vogt, H. L. Hartnagel**,** *Science* 285 (1999) 1551.

[4] R. M. Bradley, J. M. E. Harper, *J. Vac. Sci. Technol*. A 6 (**1988**) 2390.

[5] P. Haymann, J. J. Trillat, *Comp. Rend*. 248 (**1959**) 2472.

[6] R. L. Cunningham, P. Haymann, C. Lecomte, W. J. Moore, J. J. Trillat, *J. Appl. Phys*. 11 (**1960**) 839.

[7] P. Sigmund, *J. Mater. Sci*. 8 (**1973**) 1545.

[8] M. A. Makeev, R. Cuerno, A.ï L. Barabasi, *Nucl. Instr. and Meth. in Phys. Res. B* 197 (**2002**) 185.

[9] A. Keller, PhD. Thesis, *Evolution of ion-induced ripple patterns– Anisotropy, nonlinearity, and scaling*, FZD, Dresden (**2009**).

[10] B. Ziberi, F. Frost, T.Höche, B. Rauschenbach, *Phys. Rev*. *B* 72 (**2005**) 235310.

[11] A. Keller, S. Facsko, W. Möller, *New J. Phys*. 10 (**2008**) 063004.

[12] A. Keller, S. Roßbach, S. Facsko, W. Möller, *Nanotechnology* 19 (**2008**) 135303.

[13] P. Sigmund, A. Oliva, *Alloy sputtering at high fluence: Preferential sputtering and competing effects*, (**1992**). (*http://www.osti.gov/energycitations/servlets/purl/10141417-EsXvVB/native/)*

[14] R. Behrisch*, Sputtering by Particle Bombardment*, Springer, Heidelberg (1981).

[15] H. Gnaser, Low-Energy Ion Irradiation of Solid Surfaces*,* Springer, Berlin (1999).

[16] P. Sigmund, *Phys. Rev*. 184 (**1969**) 383.

[17] P. Sigmund, *J. Mat. Sci*. 8 (**1973**) 1545.

[18] J. F. Ziegler, J. B. Biersack, U. Littmark, *The Stopping and Range of Ions in Solids (Pergamon* New York) (**1985**).

[19] M. A. Makeev , A. L. Barabasi, *Appl. Phys. Lett*. 71 (**1997**) 2800.

[20] C. Herring, *J. Appl. Phys*. 21 (**1950**) 301.

[21] T. M. Mayer, E. Chason, A. J. Howard, *J. Appl. Phys*. 76 (3), (**1994**) 1633.

[22] S. Habenicht, W. Bolse, K. Reimann, U. Geyer, *Phys. Rev. B* 60 (**1999**) 2200.

[23] J. Erlebacher, M. J. Aziz, E. Chason, M. B. Sinclair, J. A. Floro, *Phys. Rev. Lett*. 82 (**1999**) 2330.

[24] R. Cuerno and A. L. Barabasi, *Phys. Rev. Lett*. 74 (**1995**) 4746.

[25] R. Cuerno, H. A. Makse, S. Tomassone, S. T. Harrington, H. E. Stanley, *Phys. Rev. Lett*. 75 (**1995**) 4464.

[26] S. Park, B. Kahng, H. Jeong, A. L. Barabasi, *Phys. Rev. Lett*. 83 (**1999**) 3486.

[27] G. Carter ,V. Vishnyakov, *Phys. Rev. B* 54 (**1996**) 17647.

[28] D.P. Datta , T.K. Chini, *Phys. Rev. B* 69 (**2004**) 235313.

[29] A.D. Brown , J. Erlebacher, *Phys. Rev*. B 72 (**2005**) 075350.

[30] A. Keller, S. Rossbach, S. Facsko,W. Moeller, *Nano. Techn*. 19 (**2008**) 135303.

[31] M. Castro, R. Cuerno, L. Vazquez, R. Gago, *Phys. Rev. Lett*. 94 (**2005**) 016102.

[32] J. Munoz-Garcia, M. Castro, R. Cuerno. *Phys. Rev. Lett*. 96 (**2006**) 086101.

[33] J. Munoz-Garcia, R. Cuerno, M. Castro, *Phys. Rev. B* 78 (**2008**) 205408.

[34] H. R. Kaufman, *J. Vac. Sci. Technol*. 15(2) (**1978**) 272.

[35] B. Wolf, *Handbook of Ion Sources*. *CRC Press*, (**1995**).

[36] G. K.Wolf, K.Zucholl, W.Ensinger, Nucl. Inst. Meth. *Phys. Res. B* 21 (**1987**) 570.

[37] F. Frost, R. Fechner, B. Ziberi, A. Flamm, *Thin Solid Films* 459 (**2004**) 100.

[38] J. Kirschner, H. Engelhard, D. Hartung, *Rev. Sci. Instrum.* 73(11) (**2002**) 3853.

[39] Instruction Manual for UHV evaporator, *Omicron Technology*, Version 3.7

[40] M. A. Lieberman, A. J. Lichtenberg, *Principle of Plasma discharges ad material processing* , *John Wiley & Sons, Inc*. (**1994**).

[41] G. Binnig, C. F. Quate, C. Gerber, *Phys. Rev. Lett*. 56 (**1986**) 930.

[42] J. A. Venables, *Introduction to surface and thin film processes*, Cambridge University press (**2000**).

[43] S. Rubin, T. O. Passell, E. Bailey, *Analytical Chemistry* 29 (**1957**)736.

[44] R. Grötzschel, *Rutherford backscattering Spectrometry (RBS)*, Web-article *(http://www.scitopics.com/Rutherford_Backscattering_Spectrometry_RBS.html)*

[45] M. Mayer, *Rutherford backscattering Spectrometry (RBS)*, Web-article *(http://users.ictp.it/~pub_off/lectures/lns022/Mayer_1/Mayer_1.pdf)*

[46] M. Thompson, *RUMP: Rutherford backscattering spectroscopy analysis package*. *(http://www.genplot.com.)*

[47] M. Mayer, SIMNRA: *Simulation of RBS, ERD and NRA spectra*. *(http://www.rzg.mpg.de/_mam/.)*

[48] K. H. Su, Q. H.Wei, X. Zhang, *Nano Letters* 3 (**2003**) 1087.

[49] P. K. Jain, W. Huang, M. A. El-Sayed, *Nano Letters* 7 (**2007**) 2080.

[50] A. Keller, R. Cuerno, S. Facsko, W. Möller, *Phys. Rev. B* 79 (**2009**) 115437.

Chapter-3

Nanoparticles/nanowires Self-assembly

In this chapter models of thin film growth will be presented followed by the results of silver deposition on Si (100) and rippled Si (100) substrates, respectively. Silver film growth on Si (100) and (111) substrates have widely been studied at atomic scale using different techniques like RHEED [1], STM [2, 3], and others. Silver atoms were found to be very mobile even at room temperature and follow island formation growth mode on Si and SiO_2 substrate. Different models were proposed based on thermodynamic and kinetic theories, giving insight into such a growth mode [4-6]. Silver growth on rippled Si substrate is expected to be more complicated and has not been studied so far in this respect. In order to develop an understanding of the growth of silver on rippled Si substrate a basic summary of various growth models will be present which are generally applicable for flat surfaces. However, no attempt is made to develop a detailed diffusion and rate equation for this system.

Afterwards the experimental results of silver film growth performed on flat Si substrate under different process parameters will be presented and discussed. Finally results of the studies on rippled Si substrate will be presented that were carried out varying several process parameters, i.e. angle of incidence, deposition rate, substrate temperature, deposition direction etc. We investigated what angle of incidence is appropriate to form highly ordered and bigger nanoparticles along the ripples. Deposition rate is very important to form well connected long nanowires. Substrate temperature was found to be crucial for making spherical nanoparticles chain. Due to ripple asymmetric tilt deposition from two different

direction results in different results under similar growth conditions. Main motivation of these studies was the understanding of the mechanism leading to silver nanoparticles and nanowires self-assembly on rippled Si substrate and to optimise the self-alignment process. In the end of this chapter we will be able to show under what experimental conditions nicely ordered nanoparticles / nanowires can be formed for plasmonic applications.

3.1 Thin film growth models

It is generally accepted that there are three main modes of film growth on surfaces [4-5], which are illustrated schematically in Fig. 3.1. Bauer first time described these growth models in terms of surface energies [4-6]. In hetero-epitaxy the nucleation of atoms is strongly influenced by the surface free energy of the substrate (γ_s), the film free energy (γ_f), and the interfacial energy (γ_i). Assuming that there is enough surface diffusion so that depositing material can rearrange itself to minimise γ, that means nucleation is not kinetically limited and reach to a equilibrium. In the island, or Volmer-Weber (V-W) growth mode (Fig. 3.1(a)), small clusters nucleate directly on the substrate surface and subsequently grow into islands of the condensed phase. This happens when the atoms (or molecules) of the deposit are more strongly bound to each other than to the substrate ($\gamma_i + \gamma_f > \gamma_s$). This mode is displayed by many systems of metals growing on insulators, including many metals on alkali halides, graphite, and other layer compounds such as mica [4-5].

The layer by layer, or Frank-van der Merwe growth mode (Fig. 3.1(b)), displays the opposite characteristics. Because the atoms are more strongly bound to the substrate than to each other, the first atoms condense and form a complete monolayer on the surface, which is then covered with a somewhat less tightly bound second layer. The film spreads across or wets since ($\gamma_i + \gamma_f < \gamma_s$), this means total surface energy is lower for the wetted substrate than for the bare one. Provided the decrease in binding is monotonic towards the value for a bulk crystal of the deposit, layer by layer growth mode is obtained. This growth mode is observed in the case of adsorbed gases, such as several rare gases on graphite and on several metals, in some metal-metal systems, and in semiconductor growth on semiconductors [4-5].

The layer plus island, or Stranski-Krastanov (S-K), growth mode (Fig. 3.l (c)) is an intermediate case. After forming the first monolayer (ML) or a few ML, subsequent layer growth is unfavourable and islands are formed on top of this ‘intermediate’ layer. There are many possible reasons for this mode to occur, and almost any factor which disturbs the monotonic decrease in binding energy, characteristic of layer growth, may be the cause. Such

a change in energy is shown by (γ_{fo}). For example, the lattice parameter or the symmetry of the intermediate layer may not be able to be continued into the bulk crystal of the deposit. This results in a high free energy of the deposit- intermediate-layer interface which favours subsequent island formation. There are many examples of its occurrence in metal-metal, metal-semiconductor, gas-metal and gas-layer compound systems [4-5].

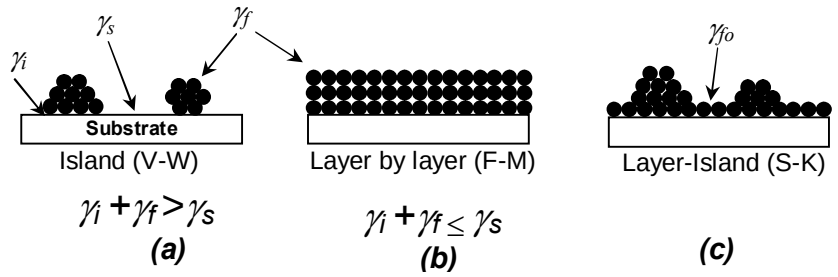

Fig. 3.1: *Schematics of three growth mode V-W, F-M and S-K are shown in a sequence of (a), (b) and (c).*

Another approach to understand these growth modes is to plot surface energy ratio (*W*) and lattice mismatch (*f*), which is possible by minimising volume free energy equation (ΔG_S). The net free energy change for the nucleation of a hemispherical island on top of a growing, strained epitaxial layer of thickness *h* is given by [4-6],

$$\Delta G = \frac{2\pi r^3}{3}\Delta G_V + \pi r^2 \gamma + \Delta G_s \tag{3.1}$$

$\Delta G_V, \gamma, \Delta G_S,$ are the volume free energy of the island and interfacial and strain energy interaction between the island and epitaxial layer respectively. ΔG_S is defined as difference in epilayer strain energy per unit area after the island nucleates ($Y\varepsilon^2 h/2$) relative to that in the epilayer prior to island nucleation($Yf^2 h/2$).therefore

$$\Delta G_s = \frac{1}{2}\left(\varepsilon^2 - f^2\right)YhA \tag{3.2}$$

where ε is the strain in film, *Y* is the elastic modulus of the layer and *A* (πr^2) is the area affected by strain. *f* is lattice mismatch strain or simply misfit , defined like this $f = \frac{[a_o(s) - a_o(f)]}{a_o(f)}$ where a_o is the lattice parameter and *f* and *s* refer to the film and substrate respectively. Thermodynamic equilibrium is achieved when $d\Delta G/dr = 0$[5], this occurs at a critical nucleus size $r = r_c$ given by

$$r_c = -\frac{\left(\gamma - \frac{1}{2}\left(\varepsilon^2 - f^2\right)Yh\right)}{\Delta G_V} \tag{3.3}$$

In the limit when $r_c=0$ The critical film thickness h_c for the onset of the rough island morphology (S-K growth) is

$$h_c = \frac{2\gamma}{\left(\varepsilon^2 - f^2\right)Y} \tag{3.4}$$

This relation implies that h_c varies approximately as f^{-2}. With this we may better understand the three film growth modes in terms of surface energy ratio $W = (\gamma_s - \gamma_f)/\gamma_s$ and f (Fig. 3.2).

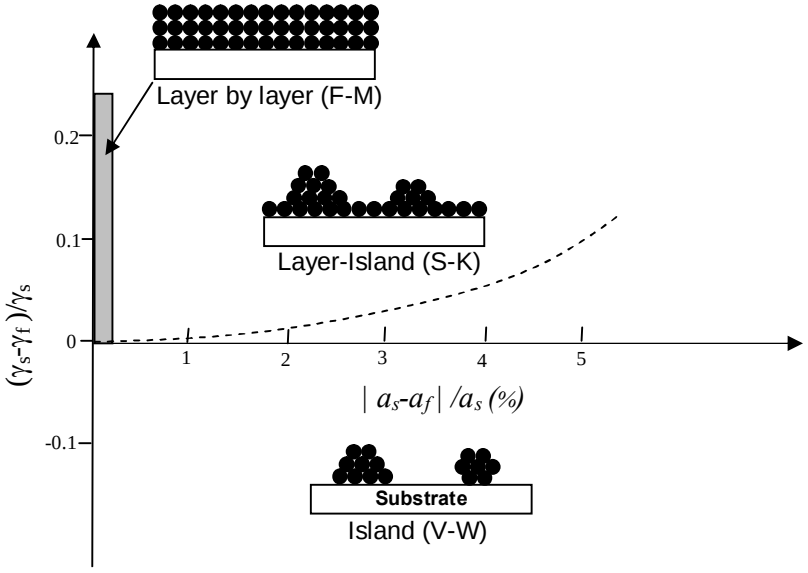

Fig. 3.2: *Stability regions of the three film growth modes in coordinates of surface energy difference between films and substrate and lattice misfit.*

When W<0 island growth dominate, but its range expands when there is additional misfit present. Layer growth is possible only when W>0; this growth mechanism can bear a small amount of misfit, that makes strained layer epitaxy feasible. In between island and layer film morphologies and competing with them, S-K growth mode adopted.

Silver growth on SiO_2 is a nice example of V-W or island like growth. Such behaviour of silver growth can be observed in cross-sectional (CS) TEM [7] shown in Fig. 3.3(a). Silver-silver atom interaction is so strong that atoms prefer to stick to each other rather than to the substrate. γ_f is very important, which is the deciding contribution for island like growth mode. Without mentioning the details about film deposition on rippled surface at this stage, one

qualitative example for the γ_i variation is shown in Fig. 3.3(b, c). Sample (b) and (c) were prepared under similar conditions except that sample (b) was prepared completely inside the vacuum chamber (in-situ), i.e. sputtering and then deposition of the same amount of silver. Sample (c) was sputtered and then taken out (Oxide layer formation) and remounted into the vacuum chamber. In case (b) substrate is amorphous Si as a result film appear to be more wetted (more surface coverage) and elongated wire like clusters can be observed, while in case (c) due to oxidation substrate top layer is become SiO_2 (Higher γ_i value then Si) well separated small clusters are formed.

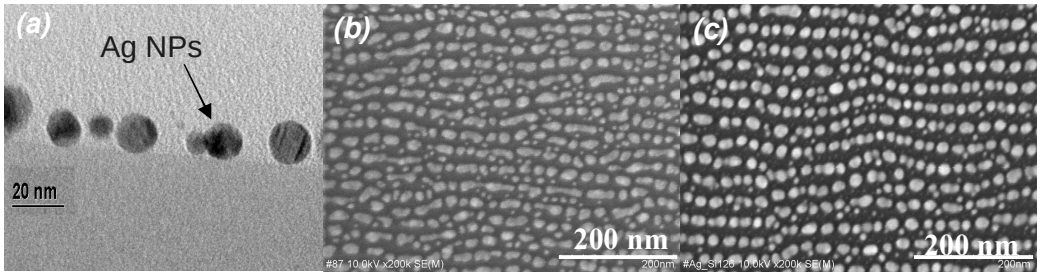

Fig. 3.3: *Image (a) reprinted with permission from [7] copyright © Institute of physics is a CS-TEM of silver nanoparticle showing the island growth at SiO_2 substrate, (b) and (c) showing affect of different interfacial energies γ_i as explained in the text above.*

We now go into the details of the processes occurring when an atom reaches the substrate surface after evaporation. The individual atomic processes responsible for film growth are illustrated in Fig. 3.4. Incoming single atom on the substrate may diffuse over the surface until they are lost by one of several processes. These processes include re-evaporation, nucleation, capture by existing clusters, dissolution into the substrate, and capture at special (defect) sites such as steps. Each of these processes will be governed by characteristic times, and energies which themselves will depend on the single-atom concentration and/or coverage. If such processes are thermally activated, then these times will in turn be controlled by activation energies and frequency factors. Some of the important energies are indicated in Fig. 3.4. In addition to re-evaporation, there are diffusion energies (E_d), binding energies of small clusters of size (E_j), upto the so-called ócriticalô size of nucleus *(E_i).* Large clusters can decay as well as grow, as is the case close to equilibrium conditions. Then the corresponding free energies of evaporation (latent heats) in *2D* (onto the substrate) and *3D* (into the vapour) can also be important. So far, Fig. 3.4 indicates that we are concerned with two independent experimental variables, growth rate and temperature, which together form the main way that chemical potential can be influenced for a given system. But we also need three essentially

independent types of material parameters (E_a, E_d, E_{ji},) shown in Fig. 3.4 to describe the behaviour of the early stages of nucleation and growth, even on a perfect substrate.

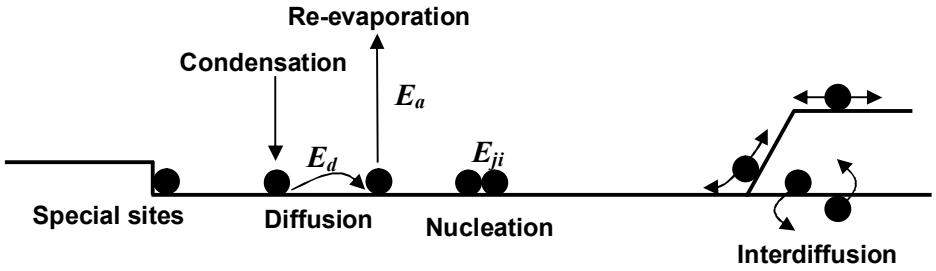

Fig. 3.4: *Schematic diagram of processes and characteristic energies in nucleation and growth on surfaces.*

Real surfaces, however, may be far from perfect, containing a distribution of ledges, kinks, dislocations and point defects, in addition to perfect terraces. These imperfections can influence the binding of single atoms and small clusters to the substrate and therefore can strongly influence adsorption, diffusion and nucleation. This is especially so if there is a high nucleation barrier (i.e. a low concentration of critical nuclei) on a perfect terrace. Then the barrier will often be by-passed on a real surface by the agency of special sites, shown schematically in Fig. 3.4 by a ledge.

The final sets of processes illustrated schematically in Fig. 3.4 are re-arrangement processes. The clusters which initially form, at defect sites or on perfect terraces, are not necessarily in their most stable form and can re-arrange in many different ways. Such processes can include mixing of species (alloying), shape changes caused by (surface) diffusion and/or coalescence, annealing of defects, etc. Diffusion processes thus occur at several stages of thin film formation: the motion of single atoms in forming small clusters, the mobility of these clusters themselves and the re arrangement of larger clusters (islands) after coalescence. All these features of nucleation and growth are applicable to silver film growth at ripple surface as well.

3.2 Metal film growth on a flat Si surface

3.2.1 Time evolution of film growth

With this brief understanding about film growth mechanisms experimental results obtained at flat silicon substrate are shown in this section. Time evolution of the silver cluster growth on Si substrate is shown in Fig. 3.5 performed at room temperature and with a deposition rate of 0.53 ML/min. Ex-situ SEM measurements were performed after each experiment. Deposition

rate of e-beam evaporator was calibrated using both RBS (Section 2.3.4 of chapter 2) and ellipsometry (section 4. chapter 4). We will always mention deposition rate in terms of monolayer/minute (ML/min.) in entire discussion. One monolayer of silver contains ~$1.2x10^{15}$ atoms/cm^2 (FCC crystal structure). Pressure during deposition was always kept constant at $2x10^{-8}$ mbar in all the experiments. In Fig. 3.5(a) SEM of the film deposited for 35 min is shown, particles look like bimodally distributed, i.e. combination of small and big particles of random shape mixed together. After 60 min (Fig. 3.5(b) these particles coalesce and make more homogeneously distributed particles dimmers, and the process of coalescence is continue as shown in Fig. 3.5(c) after 75 min. Until the very last stage of growth coalescence is dominant, and the island ï like particles do not form a closed film.

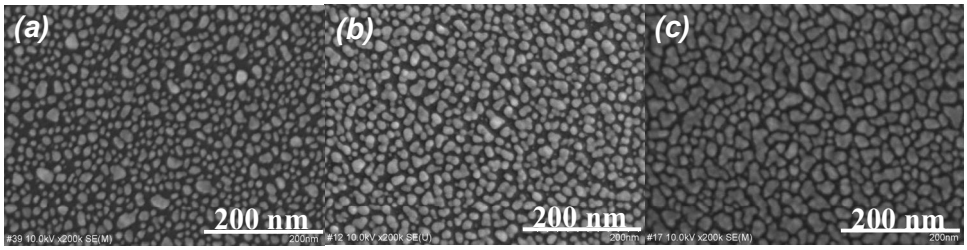

Fig. 3.5: *Silver growth on Si (111) substrate at fixed deposition rate of 0.53 ML/min for three different time 35 min, 60 min and 75 min respectively.*

3.2.2 Influence of deposition flux on film growth

Atoms nucleation and nuclei density are decided by incoming incident flux. This limits their diffusion or migration on surface. Less incoming flux will generate fewer nucleation sites and results in lower particle coalescence and vice-versa. Therefore within same time of deposition film produced at lower flux should appear to be denser than at higher flux. Results of very slow deposition rate 0.01 ML to 0.5 ML / min are shown in Fig. 3.6. In 35 min. of time very tiny particles even much smaller than 5 nm are formed at lower rate of 0.01 ML/min. and 0.05 ML/min., which are not even clearly visible in SEM image. Main difference can be seen for Fig. 3.6(d and e) where the deposition rate is 0.1ML/min and 0.53 ML/min, respectively. As expected, particles are more closely packed at lower deposition rate and not close enough to coalesce but for higher deposition rate this happens in much faster time scale i.e. at higher deposition rate at *t=0* there are more nucleation sites for adatoms. Eventually they coalesce and make bigger clusters in the same time although at lower deposition rate it takes time to reach this stage. Due to this in our actual work about silver deposition on rippled substrate we

always used the higher flux of 0.53 ML/min or even higher to make bigger separated nanoparticles in a shorter time.

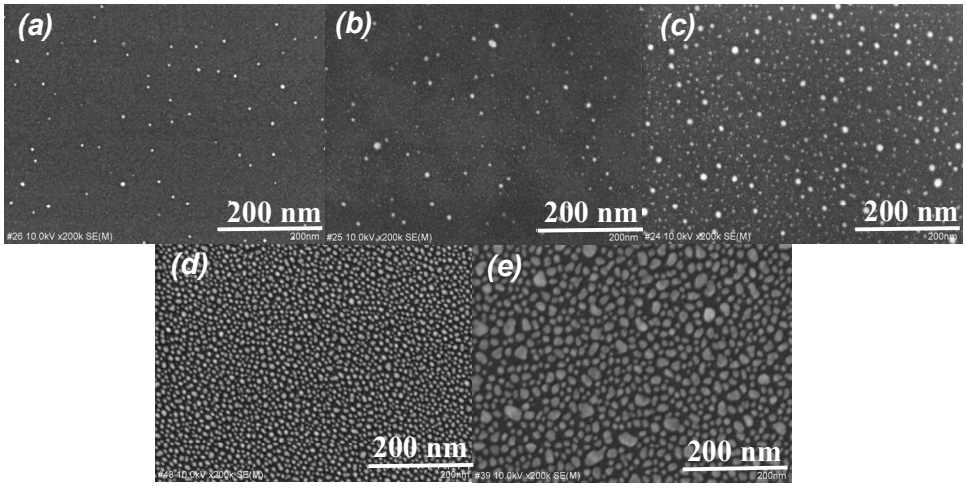

Fig. 3.6: *For a fixed time of deposition 35 min effect of the different deposition rates of 0.01, 0.05, 0.1, 0.2,0 .53 ML/min are shown, respectively.*

3.2.3 Effect of substrate temperature

Temperature plays a crucial role during film growth, since it directly affects the diffusion of adatoms. SEM images of silver films prepared at room as well as 300^{o}C substrate temperature during growth are shown in Fig. 3.7(a, b). Amount of deposition is the same in both cases but still we observe slightly bigger, flatter and closely sitting random shape clusters for the film growth at heated substrate. The rapid spreading of the islands accelerated the coalescing with the islandsô density decreasing, which promoted the formation of closed silver films [8]. In another experiment, when sample (a) is post-annealed at the same temperature (300^{o}C) particles change the shape drastically as shown in Fig. 3.7(c) to get the equilibrium shape. In this case they no longer spread over the surface and rather makes separated particles. Even though sample (b and c) are heated at same temperature but there is a difference in sample (b) and (c). In first case atoms diffused due to temperature and they can also be buried under another adtoms during growth but in second case growth process is over, clusters just have to reshape to minimise surface free energy and approach equilibrium shape.

During annealing the silver film undergo Ostwald ripening process [4-6, 9-11] resulting in bigger particle size. According to Wulff theorem [4, 5], the shape of particle will try to minimize total surface energy such that,

$$\gamma_j . A_j = constant \text{ and } \gamma_j / r_j = constant \tag{3.5}$$

Where γ_j ,A_j, r_j, are the surface free energy , area and distance from centre of the jth facet, respectively (Fig. 3.7(d)). Similar shapes can be observed in Fig. 3.7(c) after annealing.

There is a step during this annealing process which is important to be emphasised here, that is for annealing purpose samples are taken out from vacuum and exposed to atmosphere. Physisorption of oxygen at silver surface due to atmosphere exposure reduces surface free energy of silver particles. Reduction in surface free energy implies reduction in surface tension. Such decrease will induce lattice expansion and rise of thermal expansion coefficient relative to the particles in vacuum [12]. Hence when such sample is annealed inside vacuum, lattice constant can further expand upto three times higher [12] and in a process can minimise surface energy by reshaping in spherical shape. Otherwise such a reshaping was not possible after post annealing immediately after deposition without breaking vacuum (without oxygen physisorption). However, the adsorbed oxygen will leave the surface at higher temperature [12, 13]. In the further discussion annealing will always mean as defined here; exposing nanoparticles to atmosphere and then heating inside low vacuum.

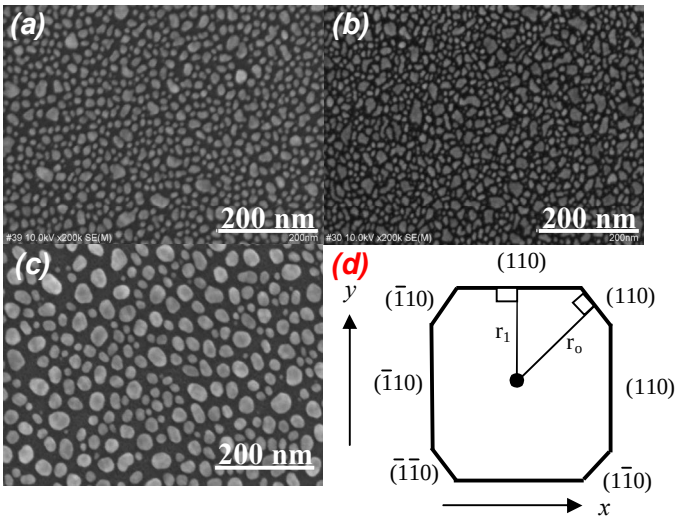

Fig. 3.7: *(a) films deposited at room temperature, (b) at 300^{o}C temperature and (c) post annealed at 300^{o}C at constant deposition rate and time .Wulff construction (d) for a needle crystallite oriented along the z axis (Perpendicular to plane of paper.*

3.3 Metal film growth on rippled surface

3.3.1 Experimental procedure

To establish the process of producing well ordered nanoparticles using pre-patterned ripple Si substrates various experiments were performed in order to optimize the deposition process.

Angle of incidence of silver atoms, deposition time, rate of deposition, substrate heating, and proper direction of deposition were varied. A sketch of developed two step process is shown in Fig. 3.8(a), which shows that in the first step ripple substrate is produced with low energy ion irradiation (Chapter-2) and then silver atoms are deposited at an oblique incidence normal to the ripples direction. Self-aligned silver nanoparticles are shown in the ridge portion along the ripples. The important fact to be noticed in this figure is the direction of deposition which is opposite to the direction of incident ion beam. Due to the ripple asymmetry (Fig. 2.20) different results are obtained depending on the direction of deposition. This difference will be discussed in a separate section, but all the experimental results shown below are based on the direction of deposition shown in Fig. 3.8(a). In Fig. 3.8(b) different regions of ripples surfaces are shown along with their nomenclatures as used in the discussion further on.

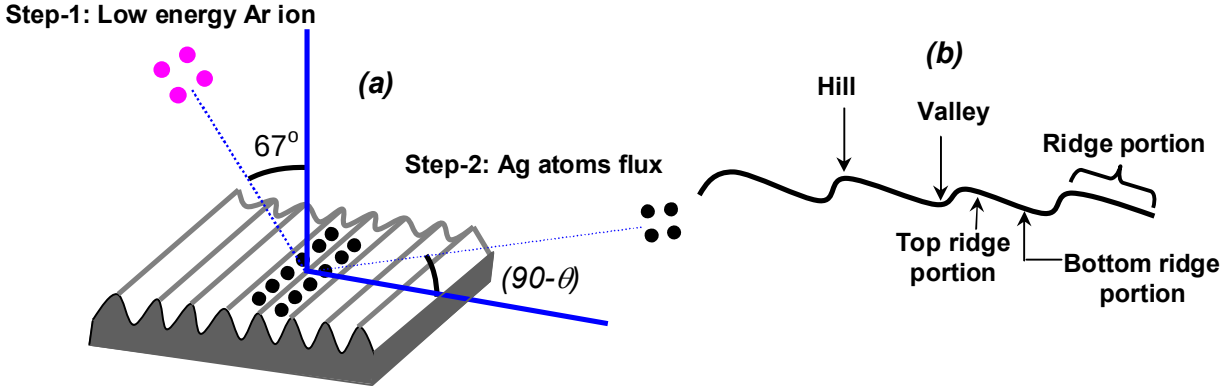

Fig. 3.8: (a) *Schematic diagram of the two step process to produce self aligned particles. Ripples produced in first step and self-aligned particles and wire in second step.(b)Nomenclature of the different regions of ripple surface used during discussion.*

3.3.2 Effect of angle of deposition

In a first approach the evaporated silver atom flux was incident normal to the ripple surface with 0.53 ML/min for 35 min at room temperature. This results in normal cluster growth similar to the one observed on the non rippled Si substrate (Fig. 3.9(a) and Fig. 3.7(a)). Small and big clusters spread over entire surface no selectivity or influence of substrate can be observed. Similar behaviour was observed for other angles of incidence (Not shown here) until the angle of incidence becomes greater than 60^{o}. At 60^{o} incidence from normal to surface the ripple topography and some particle alignment is observed (Fig. 3.9(b)). Several small particles are spread over the ripple ridge portion. At 70^{o} incidence single bigger particles near top ridge portion are formed with some small particles on the down slope (Fig. 3.9(c)). This is a very important clue that even at 70^{o} which is actually outside of shadow

deposition regime (Fig. 3.10) perfect self-alignment of nanoparticles could be achieved, in contradiction to other reported work [14,15] showing self-alignment only in shadow deposition (Angle of incidence 85^o). Depending on the direction of deposition, angle of incidence greater then 72^o and 77^o will come under shadow deposition regime (Fig. 3.10). Angle of shadow deposition will change according to the ripple tilt and amplitude. Example shown here is for 35 nm periodic ripples. Therefore at 80^o incidence (Under shadow deposition regime) alignment is still observed but very tiny particles are formed in the same time of deposition (Fig. 3.9(d)). Due to shadowing only the part of the ridge receive flux. With this study we could conclude that even in non shadow deposition at 70^o incidence well ordered nanoparticle can be produced on the rippled templates. Therefore this angle was fixed for all other experimental results shown in this chapter.

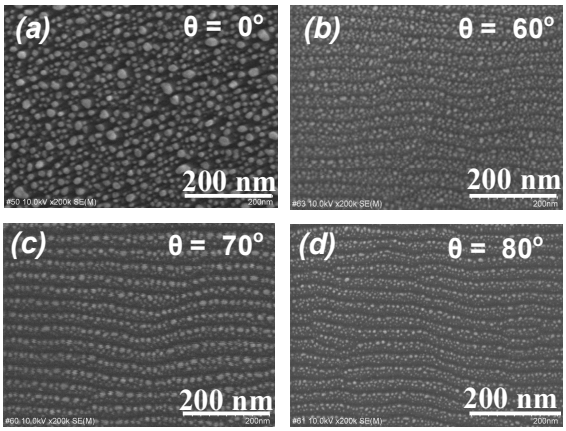

Fig. 3.9(a-d): *SEM images of silver nanoparticles on rippled Si substrate at different angle of deposition at a constant rate , time and at room temperature.*

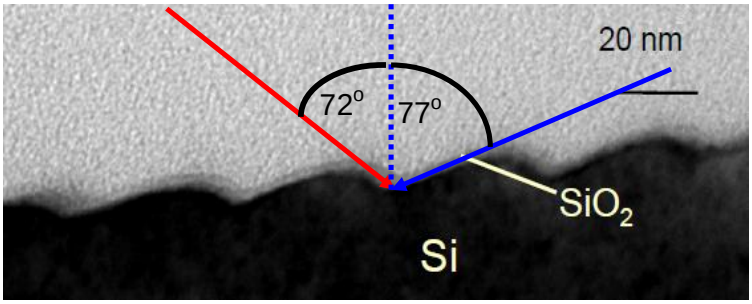

Fig. 3.10: *Cross-sectional TEM of rippled substrate, blue and red lines are corresponding to the directions of ion beam and deposition, respectively. Maximum values of the angles that can be used for non shadow depositions from two different directions are also shown.*

The difference in results obtained at 70^o and 80^o angle of incidence is clear based on shadow or non shadow deposition but what causes the difference in between 60^o and 70^o? To

clarify it, similar experiment was performed in a computer simulation using 3DLKMCS (Three Dimensional Kinetic Lattice Monte Carlo simulation). A mathematical function mimicking the ripple structure was first determined (Fig. 3.11). The homogeneous diffusion and no defects induced growth was considered for the adatoms at this simulated ripple like surface. All other energies, adsorption (0.26 eV) and migration barrier (0.2 eV), taken from literature [4-6] and surface diffusion equations and nucleation theory was applied. Simulated deposition was performed at the same angle and direction like in real experiments. This simulation work was performed in a collaborative work with theory group at FZD, deeper details about simulation are outside the scope of this thesis work and are published elsewhere [16]. Only outcome of the simulation is included to understand our results.

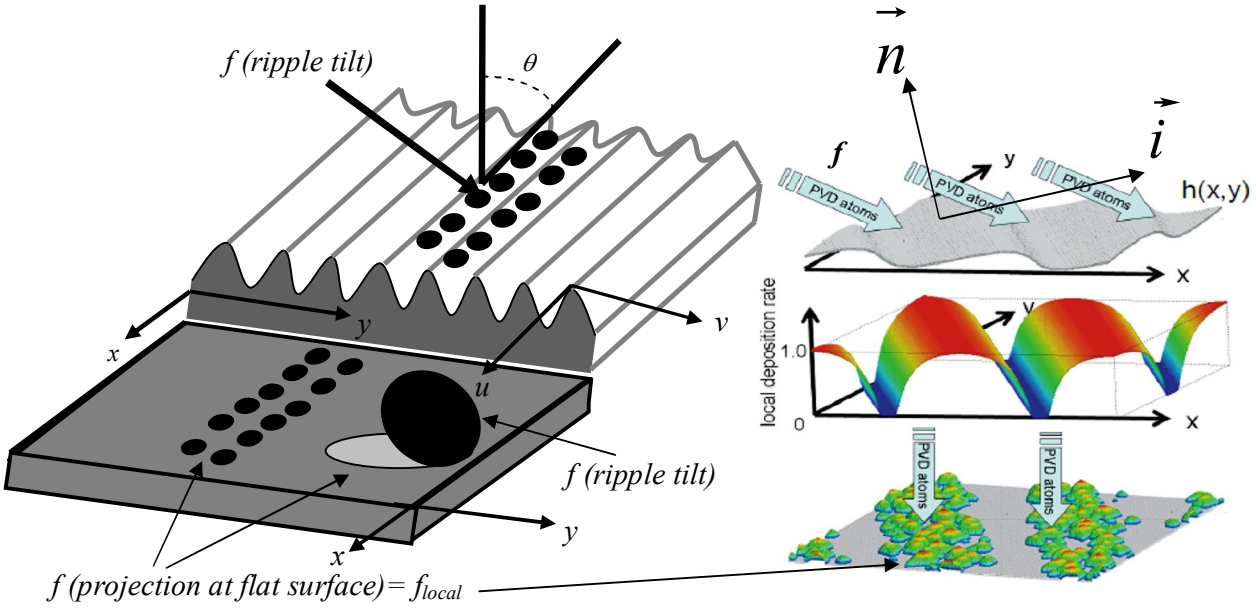

Fig. 3.11: *Concept of local flux shown on left side and inhomogeneous local flux distribution obtained in simulation shown on the right side.*

The projection of the deposited flux on ripple surface to the corresponding flat surface is inhomogeneous i.e. spatial variation of deposited amount of material, while it is homogeneous for deposition at non-rippled substrate (Fig. 3.11 and 3.7(a)). This variation in surface coverage gave us the indication that sticking probability of silver atom is different for rippled and for the flat surface. Uneven coverage or sticking is due to the differences in available local fluxes at ripple and normal Si surface. Local flux is a function of angle of incident and ripples aspect ratio (Eq. 3.6)[16], therefore it is very specific to the ripple surface. The local flux can be calculated with the coordinate system as shown in Fig. 3.11, in the following way.

$$f_{local} = f_{ripple}(\vec{i}.\vec{n}) \qquad (3.6)$$

f is the Ag flux from the evaporator, $\vec{n}$ is the surface normal and $\vec{i}$ is the flux vector oriented to the evaporation source. The second term takes into account the effect of ripple aspect ratio. Thermally activated adatom diffusion and morphology depends on the local flux. The higher the local flux is the higher the sticking probability of adatoms is. Fig. 3.12(a) shows the distribution of local flux on ripple surface at all the angles mentioned above, i.e. normal incidence, 60°, 70° and 80°, respectively. It can be clearly seen that local flux distribution is not the same for all the cases. For the normal incidence it is homogeneously distributed with a slight variation near ripple valley. In the case of 80° shadow region is also reflected in the calculated results.

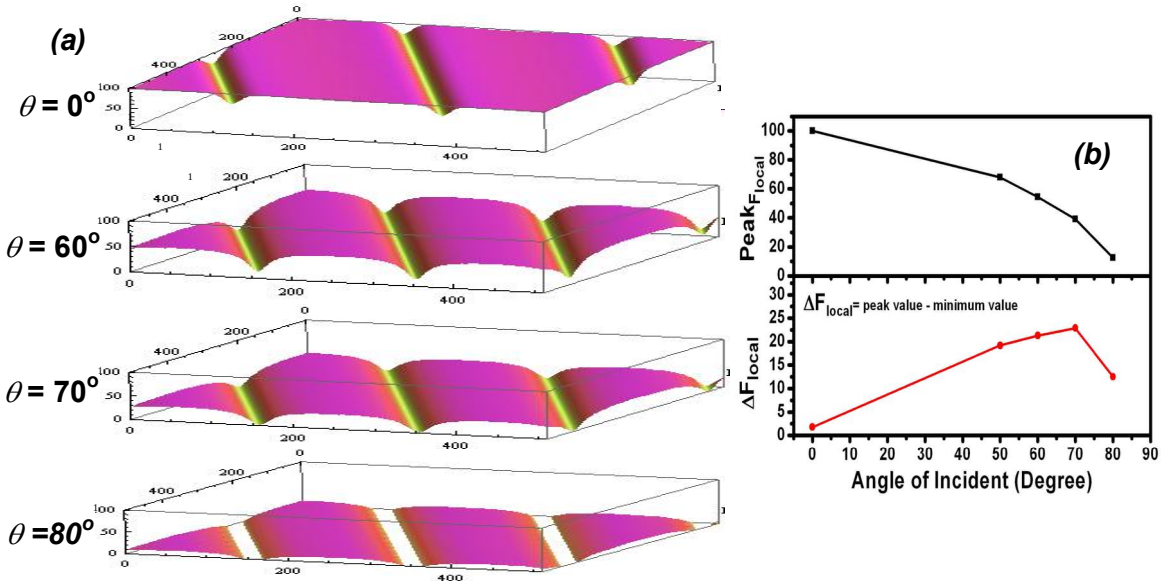

Fig. 3.12: *Local flux variation at different angle of incidence shown on left side, while peak value and difference with minimum value is plotted against incident angle shown on right side. Values of local flux are plotted in scale of 0-100 %.*

To see the difference between 60° and 70°, the peak value of local flux and its difference with minimum values of local flux are plotted as a function of angle of incident (Fig. 3.12(b)). These values are taken from the calculated values of Fig. 12(a). At normal incidence peak values of local flux is almost 100 % of total flux and decreases drastically with increase in angle of incidence. However, the difference between maximum and minimum values of local flux is increasing below the shadowing angle and decreases again thereafter. Thus in the case of 60° angle of incidence, almost equally sized particles are spread over a large area. While at 70° angle of incidence, larger particles are formed near the top ridge portion and very small near bottom ridge due to minimum and maximum local flux variation.

3.3.3 Deposition from different directions

Under similar deposition conditions, deposition from two different directions i.e. left and right sides normal to ripples, respectively (Fig. 3.8 and Fig. 3.10) results in different morphologies. An example of the same is shown in Fig. 3.13, Nanowires and elongated nanoparticles are formed for a 75 min deposition depending on deposition direction. This result can also be explained by the local flux variation. Local flux distribution in one case is very steep (Fig. 3.13(a)), that means sticking probability is maximum only on the top ridge portion. Hence the majority of atom sticks there and easily cover this relatively small portion to form nanowires (Fig. 3.13(d). While in another case (Fig. 3.13(b)) local flux distribution is broader which support particle formation for the given amount of deposit (Fig. 3.13(c). CS-TEM shown below also shows clearly the different preferred location of particles deposited from two different directions (Fig. 3.13(e, f)). This is another very useful finding of this work, which explains which side of deposition is appropriate for particle or wire like structure formation.

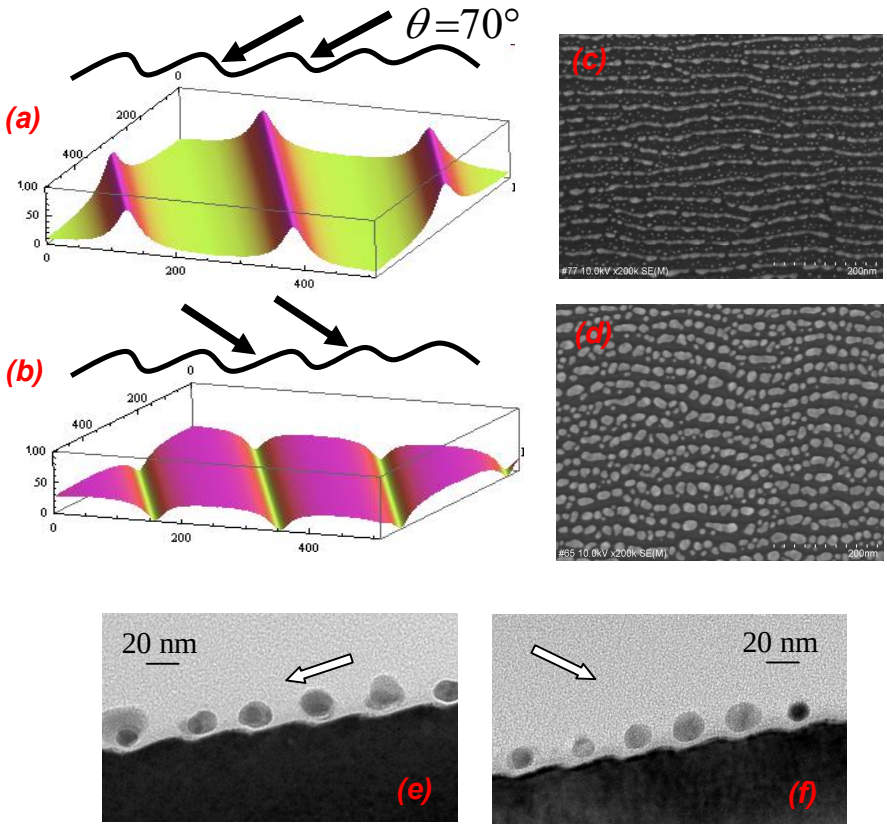

Fig. 3.13: *Film deposited from two different direction of ripple tilt with corresponding local flux distribution and SEM images. CS-TEM shown in the bottom is showing different preferred location depending on deposition direction.*

Deposition parallel to ripple direction does not lead to self-alignment. Particles grow everywhere on the rippled surface (Fig. 3.14). Trace of local flux was found to be similar like in the case of normal incidence, i.e. homogeneously distributed. So choice of deposition parallel to ripple can be discarded for making ordered particles.

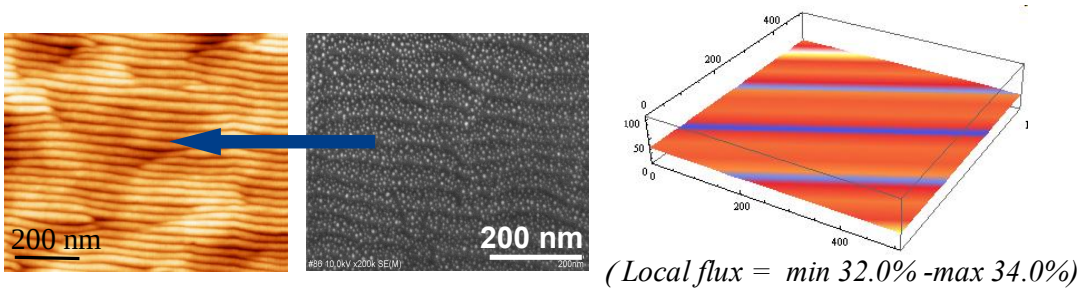

Fig. 3.14: *Deposition parallel to ripple showing no alignment and homogeneous local flux variation.*

3.3.4 Evidence of different sticking probability

Earlier it was mentioned that local flux variation is inhomogeneous on rippled surface and homogeneous on a flat surface. Consequently the sticking probability of atoms should be different on rippled and flat substrates. To validate this result experimentally, an in-situ RBS measurement was planned (This facility is newly developed in Forschungszentrum Dresden-Rossendorf (FZD)). For this purpose e-beam evaporator was directly mounted on the RBS measurement chamber (Fig. 3.15) at 70^{o} angle of incidence using an axis rotator. To avoid any difference (such as flux variation) caused due to two separate experiments i.e. mounting flat and rippled Si sample separately in two different experiments. A special sample which is half rippled and half flat was prepared. AFM topography of both sides of such a sample is shown in Fig. 3.16(a).

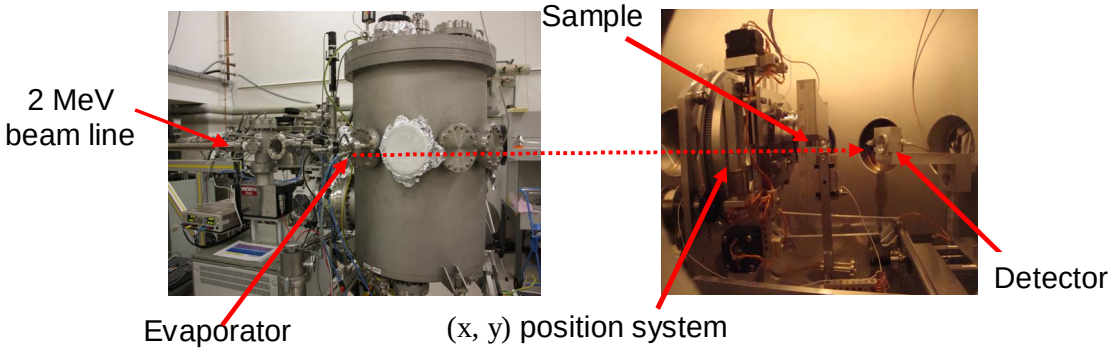

Fig. 3.15: *In-Situ RBS facility at FZD connected with 2MeV He ion beam line (Left), inner view showing location of evaporator, sample and the detector.*

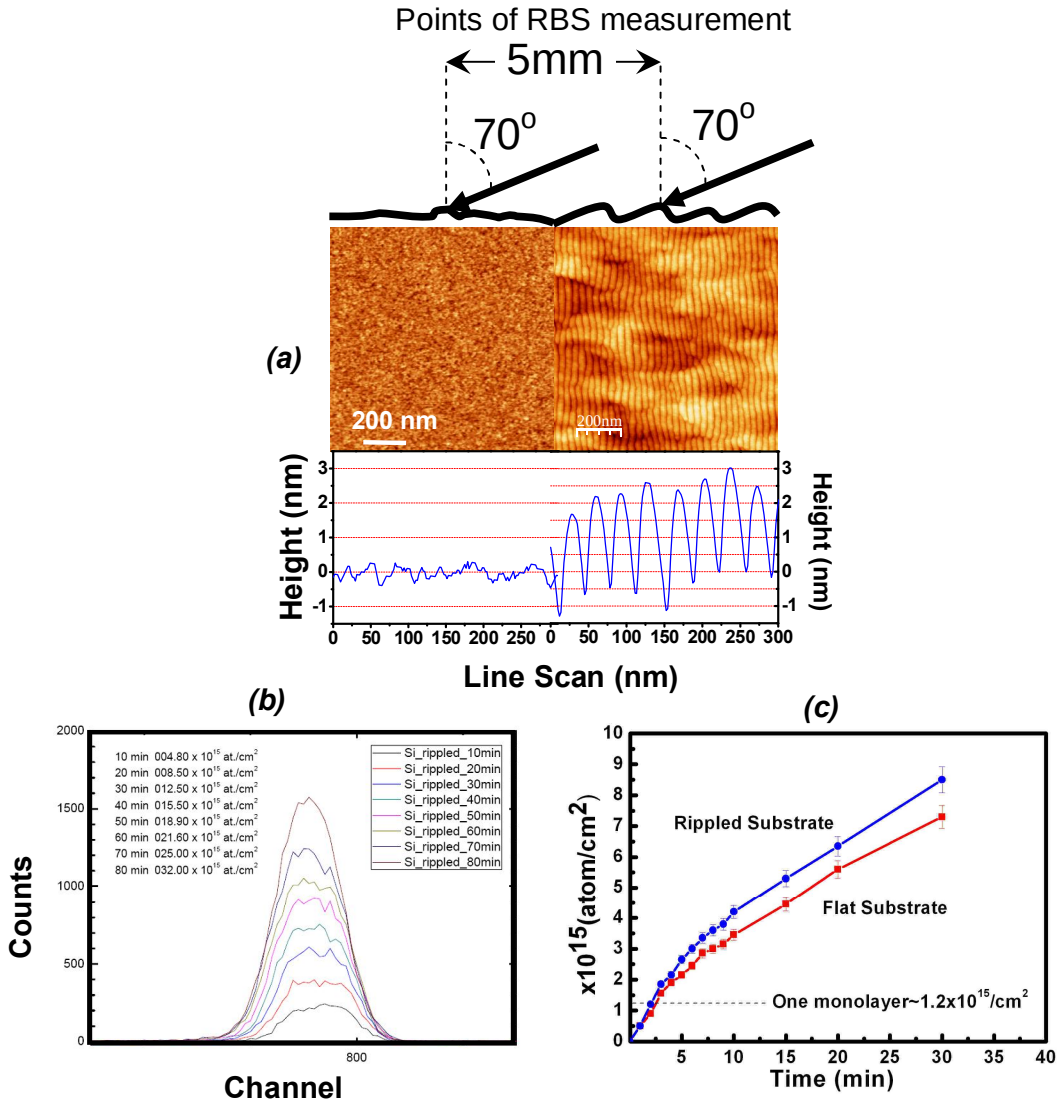

Fig. 3.16: *(a) Sample prepared for RBS measurement showing the deposition direction and distance between the spots of RBS measurements. (b) Shows the RBS spectrum of continuous silver growth. (c) The comparison of deposited amount on rippled and flat Si substrate.*

The deposition started at a deposition rate of 0.5 ML/min. The RBS spectra was taken after every 1.0 min. of deposition for both rippled and flat silicon surface. The measurement spots were just 5 mm apart. To avoid channeling the detector was moved for different angles from 0-5 degree in steps of 0.5 degree and spectra was captured for each angle to generate the better statistics. 20 mF charge was collected for each measurement. Therefore every measurement took around 15 min and in this way it took a complete day to measure 10 MLs.

Fig. 3.16(b) presents the RBS spectra of deposited silver, showing the increasing amount of silver with time. Fig. 3.16(c) shows the increase in atomic density with deposition time calculated using SIMNRA simulation software. Change in sticking behavior with

monolayer coverage can be understood with this plot. Slope of first ML coverage is very steep, that means sticking also increases rapidly in this growth regime and then between 2-4 ML slope decreases and after 4-5 ML it moves towards saturation reducing the slope even further. Coverage on both surfaces (Rippled and Non-rippled) is initially very close but then it increases in the case of rippled substrate. Although it is not an actual sticking probability measurement and there is a possibility that He ions of RBS measurement can also influence the results upto some extent but it is a relative study. Since all the deposition and RBS measurement conditions are same for both rippled and flat surface but coverage is found to be different in a given time, indicates the different sticking probabilities. It was very hard to fully cover the sample even after longer deposition time as self-shadowing of bigger silver clusters at this oblique angle deposition prevents complete layer formation. Therefore the plot still shows an increasing trend, under complete coverage condition perfect saturation should observed corresponding to sticking coefficient equal to one. This experiment has future scope for details investigation of absolute sticking probability measurement and to perform it for different aspect ratios ripples and direction. But it demands continuous beam time of several days. Due to lack of time we had to leave it as future scope.

3.3.5 Growth evolution with time

Nucleation and coalescence behavior of particles grown on rippled substrate is similar to that of normal Si surface, but due to selectivity it remains uniaxial along the ripples. As mentioned above the local flux variation is inhomogeneous on ripple surface and it has a peak on the top ridge portion that causes this selectivity. In the initial phase several small clusters form and those eventually coalesce and make elongated particles. This process continues to form nanowires. Fig. 3.17 demonstrates this behavior, three ex-situ SEM images taken after time step of 30 minutes for deposition of 45 min., 75 min. and 105 min., respectively. Plot of the statistics of the particles number and size (Fig. 3.17) show an exponential decay in number of particle and increase in average number of particle length.

According to Campbell [17, 18] particle density (n) is given by

$$n = n_0 exp\ (-\alpha n_o^{1/3} d^{2/3}) \qquad (3.2)$$

n_o is the island density at the very beginning of the deposition, d is the average thickness, α is a constant which depends on the shape of the islands . This indicates that the island density decreases with the growth of the film because of the islands coalescence. Saturation is reached

in nuclei density n_0 when the deposited atoms move towards existing nuclei before making new nuclei with other migrating atoms. After that, the nuclei grow larger and higher until they connect to each other and the island density decreases. On a rippled surface nucleation mechanism follows a similar law, however with different dynamics in the direction parallel and perpendicular to the ripple. Ripple periodicity and amplitude prevents the coalescence of two adjacent particles sitting on two consecutive ripples. Therefore coalescence is possible only along the ripples axis not perpendicular to this upto the very last stage of surface coverage (Fig. 3.18). We have examined this uniaxial growth for ripple periodicity as low as 20 nm. So the higher is the ripple amplitude and periodicity, the lower is the possibility of coalescence of the particles lying on two adjacent ripples.

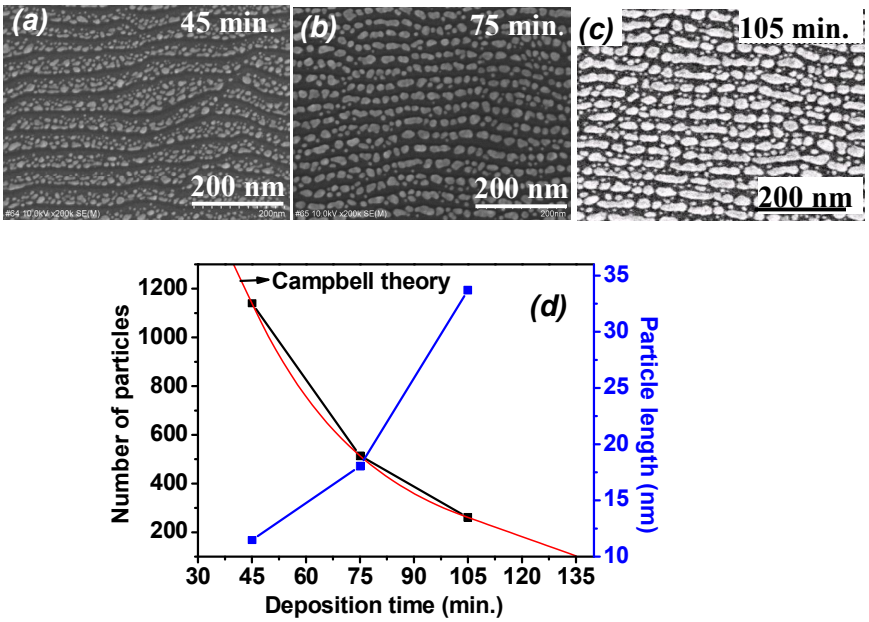

Fig. 3.17: *SEM images of the samples deposited for 45 min.(a),75min.(b) and 105 min. (c) respectively. Plot summaries the average number of particle and their length along the ripple. Red line is corresponding model fit.*

It can be seen more clearly in a shadowed region of a dirt particle that growth is preferentially along the ripples (Fig. 3.18) even though the layer is almost fully covered. A comparison of growth structures on normal surface and on the rippled surface are also shown in Fig. 3.18. It can be seen that on a flat surface the particle coalescence goes in all directions while on a rippled surface they maintain the order until the film is fully closed. These experiments demonstrate that the particles aspect ratios and interparticle gaps can be tuned. Analysis of Fig. 3.17 shows that the average particle length increases from 11 nm to 34 nm, and the number of clusters decreased from 1140 to 261 in the given time range. The results also very well match when compared with equation (3.2).

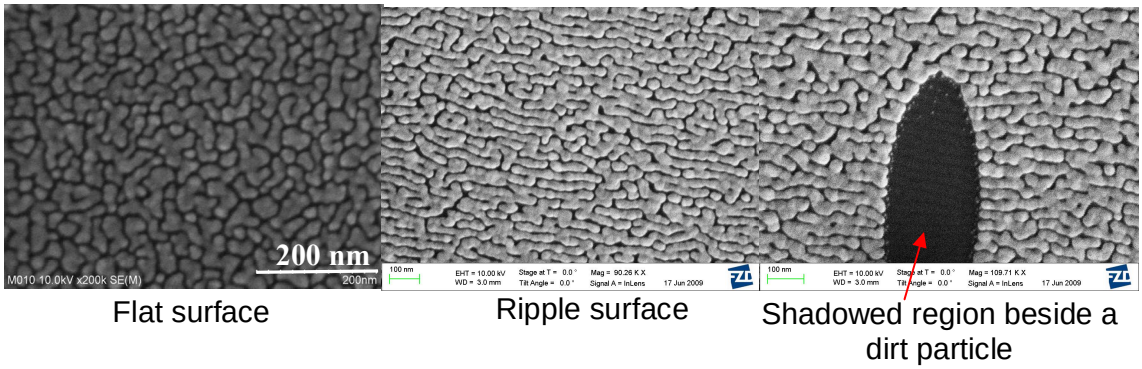

Fig. 3.18: *Growth on flat Si and rippled Si substrate for a very large surface coverage. Still it fallows the ripples pattern. Shadowed region in a dirt particle showing uncoated ripples portion.*

3.3.6 Effect of deposition rate

The influence of flux on the growth of nanoparticles is already discussed for the case of flat Si substrate. Incident flux was found to be crucial to tune aspect ratio of particles or wires on rippled substrate. Increase in flux results in fast and denser coalescence along the ripple. An example of the same is shown in Fig. 3.19. Nanowires of larger length could be produced instead of elongated clusters (Fig. 3.19) by increasing the deposition rate three times higher from 0.53 ML/min. to 1.6 ML/min keeping amount of deposition the same. Higher flux will make higher nucleation density of small particles which eventually coalesce faster in comparison to the lower flux case. It can be observed that at lower flux even if the experiment conducted for longer time still the particles are well separated. Results of thicker wire formation at a higher atomic flux also support eq. 3.2, that means the higher the initial flux (n_o) the faster the coalescence process.

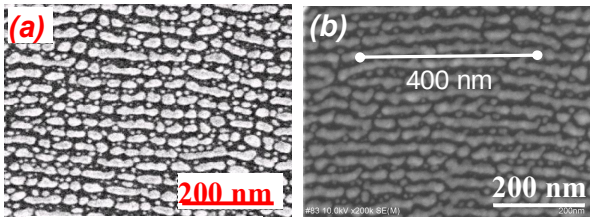

Fig. 3.19: *Effect of fast deposition rate results in nanowire formation.*

3.3.7 Effect of substrate temperature

Much emphasis was given in section 3.2.3 on the discussion of substrate temperature, since substrate heated under different conditions (substrate heating during deposition, post-

annealing etc.) may lead to completely different results. Fig. 3.20 summarises the results of three experiments conducted at same temperature but under different conditions: substrate heating during deposition, annealing immediately after deposition, and exposing to atmosphere and then vacuum annealing, respectively. Fig. 3.20(a) show the film grown on rippled substrate at 300^{o}C temperature, as mentioned earlier that due to higher surface diffusion of silver adatoms on surface coalescence is enhanced. Clusters patch covering more surface area on the ripples are developed, though at room temperature there are only well separated clusters are formed under similar deposition condition. The rapid spreading of the islands accelerated the coalescing with the islandsô density decreasing, which promoted the formation of such patch like clusters. This behavior is similar like growth at normal Si substrate; in this case surface coverage can be seen at ripple ridge portion.

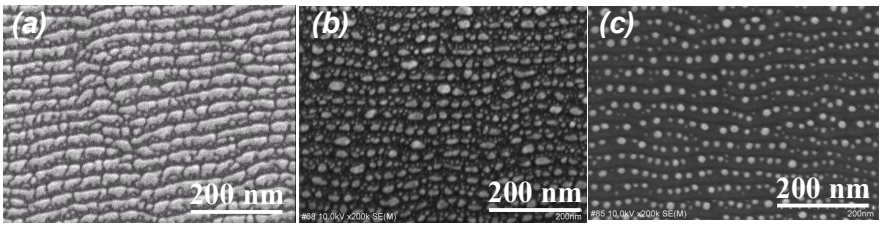

Fig. 3.20: *SEM images corresponding to deposition at heated substrate (a), annealing without breaking vacuum (b) and annealing after breaking vacuum and exposing to atmosphere then again vacuum annealing (c). Substrate temperature was 300^{o} C in all cases.*

Effect of annealing, inside the vacuum, just after completing deposition does not affect much to the particle shape at same 300^{o}C temperature. We always found aligned particles of random shapes (Fig. 13.20(b)). The reason of this probably as discussed in [19] that particles do not get sufficient driving force from surface energy to reshape the particles, since thermal expansion coefficient of silver is relatively low in vacuum compared to that in atmosphere [20]. So this way of annealing is not helpful either to make ordered spherical particles or wires.

Finally particles grown under similar deposition conditions (Flux, time, incidence angle) used in the case of Fig. 20(a, b) were exposed to atmosphere for some time and then annealed at 300^{o}C in vacuum at lower pressure of 1x10^{-7} mbar. Very well ordered spherical particles are formed not reported so far using the present method. Due to the surface free energy minimization, which is lowered due to physisorption of oxygen on the silver surface, the particles achieve such a spherical shape (already discussed in section 3.2.3). This is also a very useful result of this work; in this way very well ordered spherical nanoparticles aligned along the ripple can be produced with different aspect ratios. So we have found that under

three different temperature experiments surface coverage (~27 %) was maximum for Fig. 20(a) compare to the other two temperature experiments (Fig. 3.20(b, c)) (~ 11-12 %).

3.3.8 Preferred location of particles

Until now we have shown and discussed results obtained at different operating parameters and different direction of deposition. But one question is still left whether particles are on hills, ridges or in valleys? Based on a comparison of AFM, SEM, and TEM images (Fig. 3.21) and simulation results, it can be concluded that in the beginning particles start nucleating near the hill region (region of maximum local flux) of the ripples substrate. A schematic diagram of the nanoparticles growth on rippled substrate is shown in Fig. 3.21 (a). The growing mechanism can be understood like this. First small particles form on the top ridge region but since atomic flux continuously coming at certain angle, particle size will be become larger with time. Larger particle have lower surface energy and hence the contact angle is also reduces [21]. Therefore increase in particle size reduces interfacial energy, hence

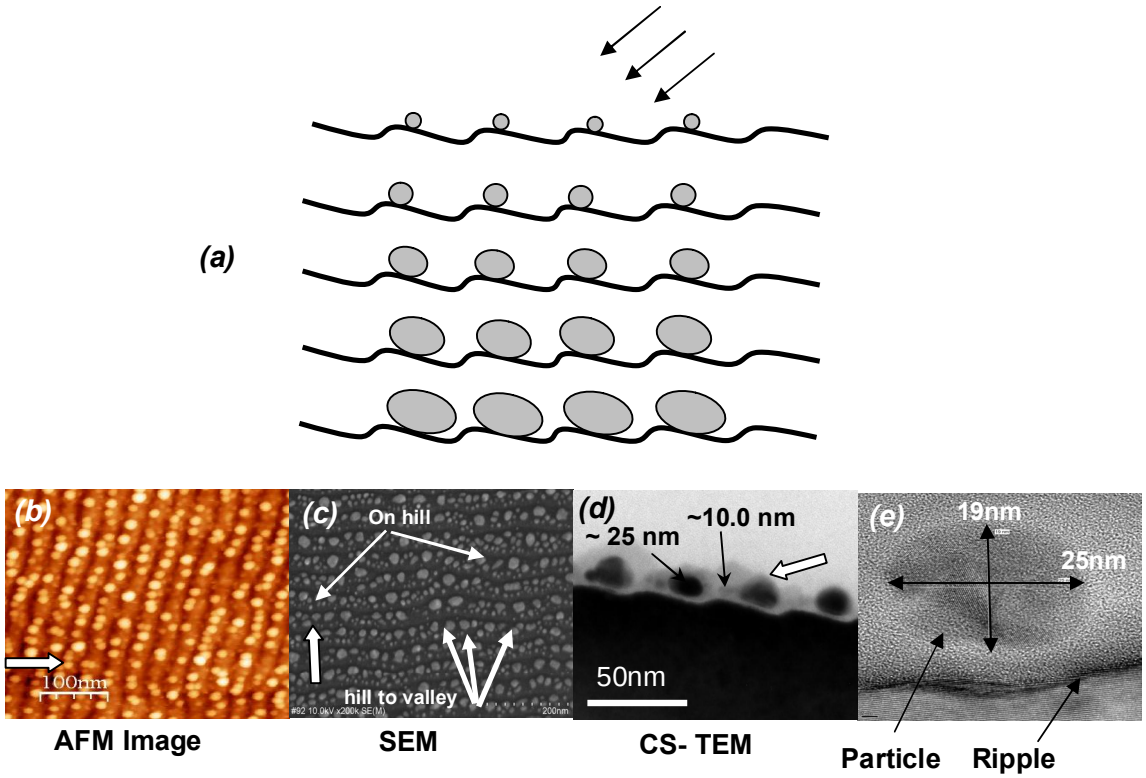

Fig. 3.21(a-e): *(a)Schematic of the nanoparticles growth. AFM image (a), (b) SEM image to show some particles are on hill and some expended from hill to valley. (c) is the cross-section TEM to show that particles less then 17.5 nm are on hill and larger elongated hill to valley. White vector is the direction of incoming flux. (d) TEM image of the single particle sitting in ripple valley.*

the particles reshape again along the ripple slope to rebalance the energies. Continuous deposition will increase the particle diameter towards the valley. Finally, particles become elongated on the ripple slope towards the valley. When the particle diameter is above a certain length (~ 17.5 nm in the case of 35 nm periodicity) they start tilting in the direction of thee valley. It is very clear from the shown SEM and TEM images (Fig. 3.21(c, d)), that some small particles are still on the hill (< 17.5 nm) whereas others are located on the slope from hill to valley (> 17.5 nm). Condition described here is applicable only for the deposition direction shown in Fig. 3.21(a). For the case when deposition is performed from another direction (section 3.3.3) the situation is different, in this case particles already start growing from the valley region and further reshaping or readjustment of particle is restricted.

3.3.9 Tunability for plasmonic application

We have shown that the ripple template based approach can be utilised to form highly ordered nanoparticles and nanowires with suitable process parameters. In first chapter it was proposed that this method is superior in terms of tunability of size and interparticle gap. Actually to tune the plasmon resonance this capability is crucial. Before showing the tunability lets first show that the particles are really ordered as they appear in SEM and TEM images. Furthermore, lets investigate if there is any long range correlation between the ripples period and the ordered clusters ?

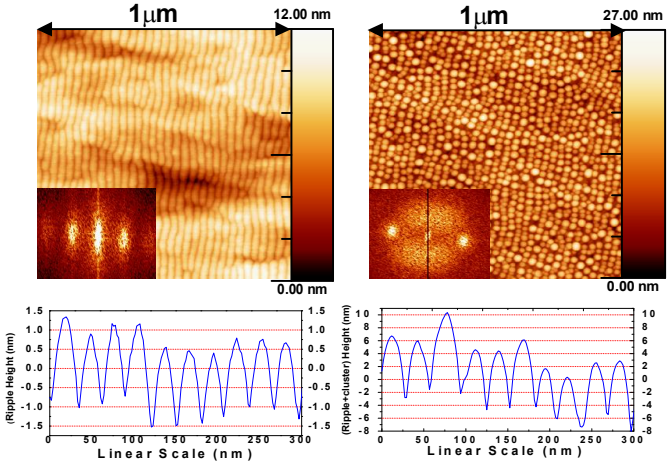

Fig. 3.22: *Ordered ripples obtained after first step and ordered silver particles after deposition in second step. Inset show the FFT of the images, two peaks clearly display that ripples as well as particles are ordered. Below are the plots of height and periodicity.*

FFT of the AFM images taken from the substrate before and after deposition is shown in inset of Fig. 3.22. Even after silver deposition two pronounced peaks appear like in the bare rippled case. This confirms high degree of nanoparticles ordering. Two broader peaks also appear in the perpendicular direction indicating an ordering in this direction too. Line scan at a random position of sample (Fig. 3.22) also shows same number of ripple bumps before and after deposition but with increased amplitude due to silver particles.

Since particles follow ripple wavelength we can make ordered particle arrays of desired periodicity. An example of this is shown in Fig. 3.23 demonstrating ordered nanoparticles of 20 nm, 35 nm and 45 nm periodicity, respectively. Average inter-particle gap along the ripple can also be changed by annealing for different temperatures and time. Similarly parallel nanowires of different width can also be formed by precisely controlling the deposition time and deposition rate as shown in Fig. 3.23. So there are several process parameters can be varied to tune : ripple periodicity by ion energy and fluence, the silver growth (Flux, time, direction of deposition, temperature) which provide lots of flexibility of tuning aspect ratios. Study on the optical properties of such samples will be shown in next chapter in terms of tuning the plasmonic properties.

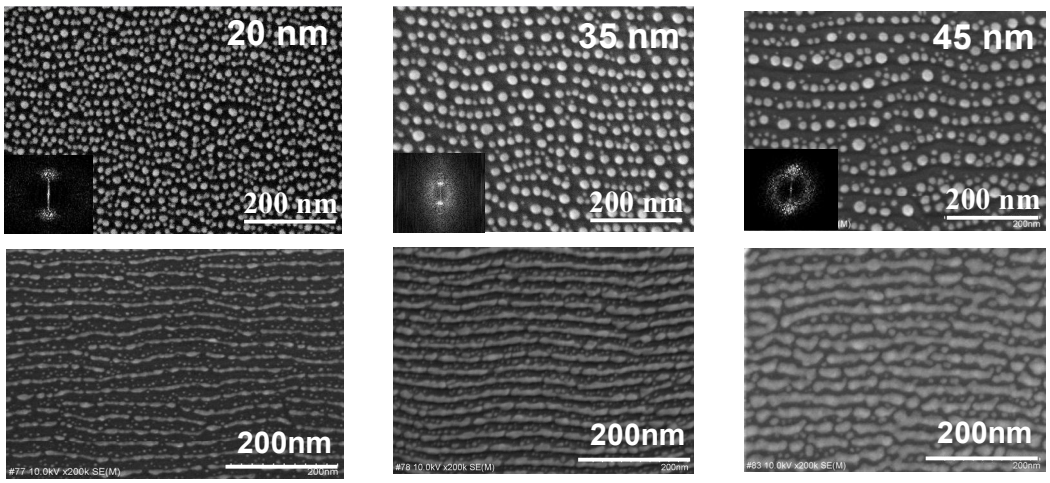

Fig. 3.23: *Ordered nanoparticles of 20, 35 and 45 nm periodicity produced after annealing (Top SEM images). Nanowires of different width 10, 12.5 and 15 nm ,repectively produced on 35 nm ripple substrate (Bottom three images).*

3.3.10 Comparison with magnetron sputtering deposition

To the best of our knowledge another groups involved in similar experimental work [14, 15, 22, and 23] used sputtering processes (magnetron or ion-beam) for the deposition purpose. Therefore it is worth to compare results of e-beam evaporation with magnetron sputter deposition. Magnetron sputtering works at very low vacuum typically in the range of 10^{-2}-10^{-3}

mbar. Deposition rate of magnetron sputtering is almost two order of magnitude higher and also energy of sputtered atoms is much higher (1-10 eV). Due to this reason adatom life time is much shorter and nucleation is much faster leading to a high density of particles at the beginning. Due to these differences nucleation kinetics in magnetron sputter deposition is very different from e-beam deposition.

In Fig. 3.24(a, c) films deposited on flat Si substrates using e-beam evaporation and Fig. 3.24(b, d) using magnetron sputtering (MS) at room temperature (RT) as well as at 300^{o}C substrate temperature are shown, respectively. Image (b) and (c) look similar that means in MS more surface is covered at RT due to higher flux and high mobility of adatoms, which is the case in e-beam evaporation at high temperature. In image (d) particles shown are grown at heated substrate of 300^{o}C, which look similar to annealing results of evaporated particles. The possible reason for this is maybe the high pressure operation provides some oxygen content to the particle surface and they get spherical in energy minimization process. Any role of plasma environment is not clear in this case. But the difference in the two deposition processes can be clearly observed.

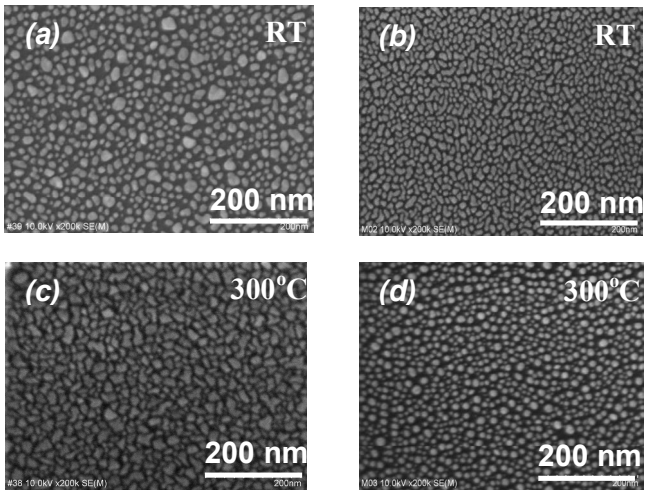

Fig. 3.24: *Comparison between samples prepared using evaporation (a, c) and magnetron sputtering (b, d) at room temperature and 300^{o}C, respectively.*

Therefore to produce ordered spherical nanoparticles we have used magnetron sputtering at heated substrate of 300^{o}C temperature. Deposition was tried from both directions of ripple at similar angle of incidence (70^{o} from normal). In the case of deposition from the long ridge side no alignment was observed (Fig. 3.25(a)), whereas in another case very few particles appeared in ordered form (Fig. 3.25(b)). The second case gives the possibility for

particle alignment if the process runs for sufficiently longer time. This means MS is not able to provide particle self-alignment due to high flux and nucleation density of particles. Even atoms seem to be so energetic that migrate over the ripples amplitude and nucleate everywhere randomly. Oates et al. [23] produced ordered nanoparticles using MS with limited success and no other group reported silver nanowire formation using magnetron sputtering so far.

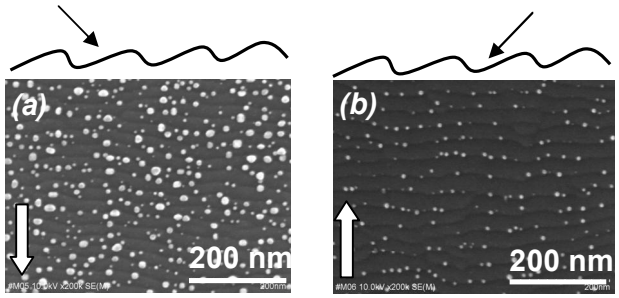

Fig. 3.25: *Cluster growth using magnetron sputtering from two different directions at 300°C, white arrow shows the direction of deposition.*

3.3.11 Uniaxial Ostwald ripening

Before proceeding to show Ostwald ripening results, we need to differentiate between different coalescence processes; Ostwald ripening, sintering and cluster migration. All the processes are very important to understand uniaxial Ostwald ripening on ripple surface. In the initial phase of nanoparticles growth, either on flat or rippled Si substrate, several small and big particles develop on the surface. With time larger particles grow or ripen at the expense of the smaller ones. This process is known as Ostwald ripening. Driving force is to minimize surface free energy of particles. This behavior can be understood in terms of the chemical potential ($\mu=2\Omega\gamma/r$) of the particles, where Ω, γ, r are the atomic volume, surface tension and radius considering spherical particles, respectively. Effective atomic concentration is large where μ is large, forcing them to escape to where μ is small. This is the case just outside very small particles. If there are two particles of different radii r_1, r_2 ($r_1 > r_2$) with chemical potentials $\mu_1, \mu_2 (\mu_1 < \mu_2)$ respectively, atoms will diffuse from particle 2 (shrink) to particle 1 which grow at the expense of another (Fig. 3.26(a)). A mechanism has thus been established for coalescence even if the particles were not in direct contact.

In the sintering process two adjacent particles coalescence and make a final shape minimizing surface energy (Fig. 3.26(b)). Coalescence occurs due to the collision of migrating particles (Fig. 3.26(c)). Clusters of size <10 nm can easily migrate at sufficiently

high temperature. This case is more common for Ag and Au , and the diffusion coefficient was found to be a function of particle radius and thermal activation energy [4].

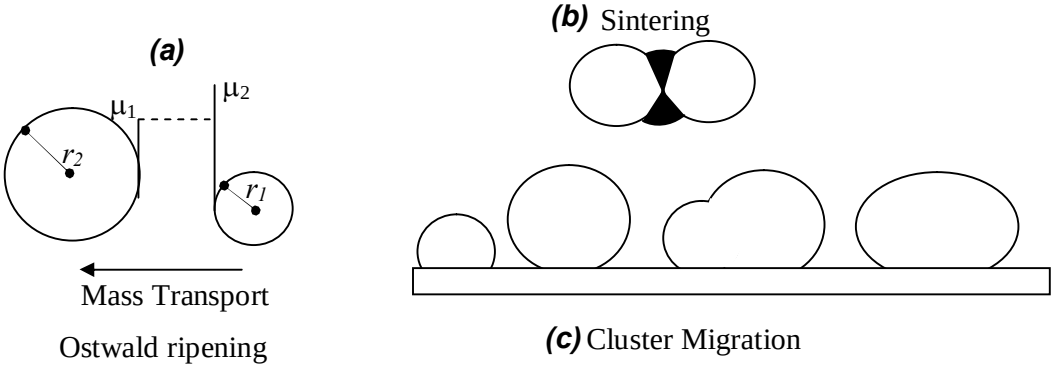

Fig. 3.26: *Representation of different coalescence processes: Ostwald ripening, Sintering and cluster migration.*

On ripple surface before annealing process there are several clusters of random shape and size arranged along the ripples (Fig. 3.27(a)). In our understanding during growth sintering process is dominating leading to elongated particles formation. But during annealing substrate temperature is increased enhancing the surface migration of smaller particles. Due to this migration they either colloid with bigger particles or undergo Ostwald ripening. But after some time when particle size is large enough they can not migrate anymore on the surface and only then particles size increases with decreasing density by Ostwald ripening. Since in all of our experiments we performed annealing at 300^{o}C for 1.0 h, we believe that under these conditions finally it is the Ostwald ripening which is still working in the long time scale.

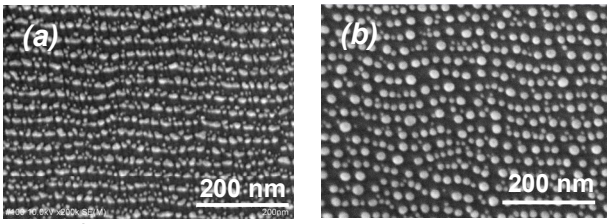

Fig. 3.27: *SEM image of the sample before and after annealing.*

In Fig. 3.27(b) it can be seen clearly that Ostwald ripening is only uniaxial along the ripples. We performed annealing for 20 nm and 45 nm periodicity ripples as well for comparing them for the case of 35 nm period ripples substrate. Since region of ripening is the ridge portion of the ripples, ridge portion gets narrower for the lower periodicity ripples.

When annealing was performed for a lower periodicity of 20 nm, the ripening occurs like on flat surface homogeneously in all the directions (Fig. 3.28). Comparison of particles deposited on flat and 20 nm ripple substrate before and after annealing is shown in Fig. 3.28. After annealing a bimodal particles distribution can be observed that will still be promote further Ostwald ripening. We observe that the Ostwald ripening is not uniaxial as in the case of 35 nm ripples. This means in 20 nm ripple coalescence is possible in all the directions.

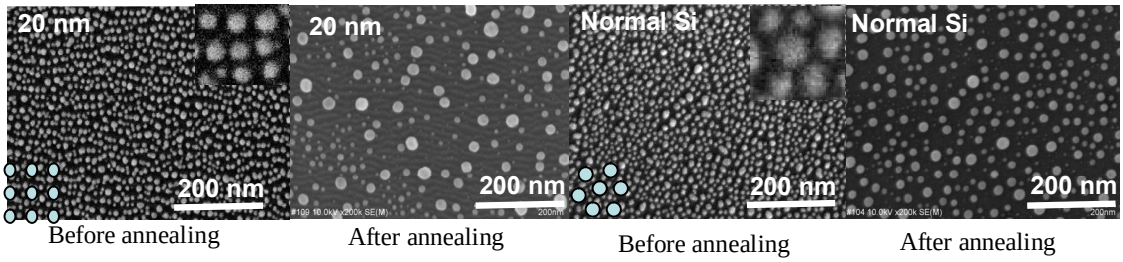

Fig. 3.28: *Ostwald ripening process on 20 nm periodic particle array and on normal substrate. Inset shows the zoomed portion at some random places of the image.*

Annealing performed at 45 nm ripple periodicity for 1.0 hour and longer time for 4 hour is shown in Fig. 3.29. The ripening process is still found to be uniaxial for this sample. This indicates that only at low periodicity of 20 nm it can happen that the uniaxial ripening is lost. Another interesting feature appears while plotting the statistics of the particle size and number after annealing for all set of samples (Flat surface, 20, 35, and 45 nm) ripples shown in Fig. 3.29. Number of particles in the case of 20 nm periodic array found to be much less as compared to others, and the average particle radius is even higher. This can be understood based on the inset of Fig. 3.28, nearest neighbor in case of 20 nm periodic particles are more compared to that of normal substrate , this give a larger possibility to perform Ostwald ripening and consequently making bigger particles and loosing smaller particles. Uniaxial Ostwald ripening observed in higher periodicity ripple indicates that there exists a minimum distance between particles across the ripple where this ripening is possible.

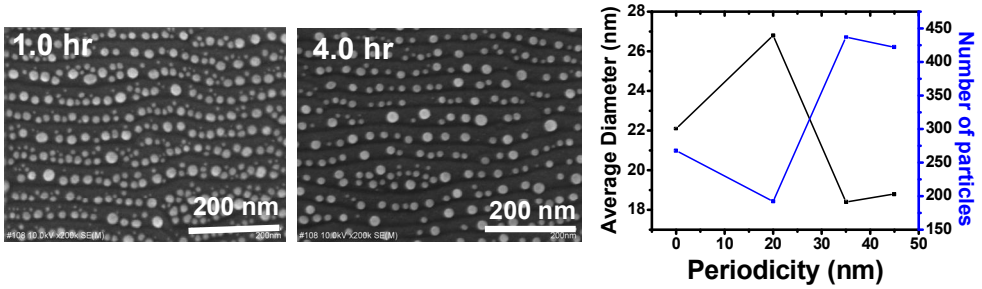

Fig. 3.29: *Ostwald ripening process run for 1.0 hr and 4.0 hr for 45 nm periodicity particles. Statistics of particles size and number in the case of normal substrate, 20 nm, 35 nm and 45nm particle array is shown in the last plot.*

We have also studied this uniaxial Ostwald ripening at different temperatures to find out exactly in what temperature range particles change their shape and loose the periodicity for 20 nm periodic particles. In Fig. 3.30 series of SEM results of one sample (20 nm ripple period with high silver amount) annealed at different temperatures starting from 55^{o}C to 458^{o}C are shown. Between 50-150^{o}C particles maintain the ordering and very little change in shape appears. But suddenly between 157-200 ^{o}C they become spherical in shape and loose the periodicity. Thus even if we annealed the sample upto 407^{o}C particles shape remains spherical and only their size keep on increasing due to Ostwald ripening. Lost of ordering at this temperature will also be shown in optical measurement results in next chapter.

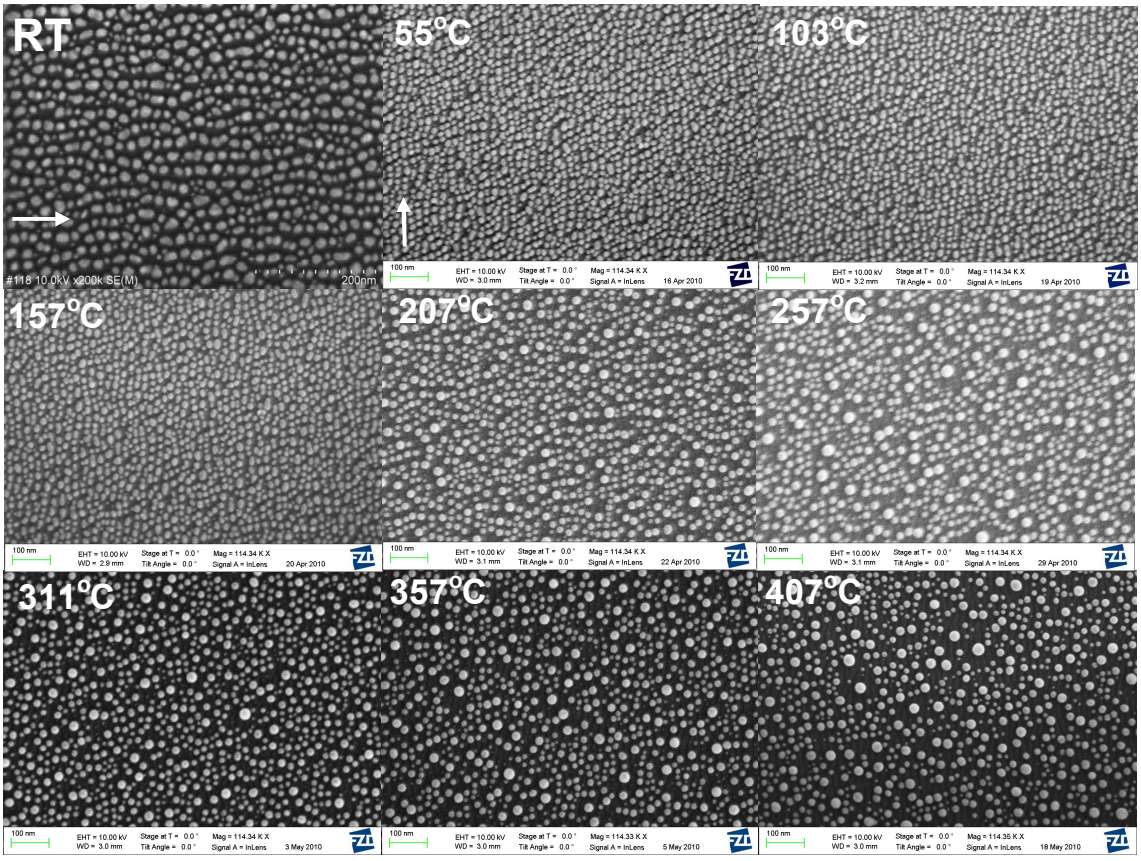

Fig. 3.30: *Annealing steps of silver particles deposited at 20 nm periods ripples for various temperature ranges. Red arrow is drawn parallel to ripples.*

3.3.12 Weak self-assembling at normal incidence

One question arises after finding the uniaxial Ostwald ripening: What will occur if silver is deposited on rippled substrate at normal incidence and then annealed? In previous section we have seen that closer particles coalescence or smaller particles migrates and then coalescence during annealing. Finally to minimize surface free energy they prefer spherical shape. During

annealing particles did not coalesce across the ripples for higher wavelength ripples. We can conclude that migration length of particles is not large enough so that particle can travel this distance from one ripple to another ripple. Particle size keeps on increasing due to Ostwald ripening. If precise amount of silver is deposited at normal incidence and the annealing is performed, then after all kinetically govern coalescence particle will becomes spherical. If the particle size is smaller then the ridge portion then they should be separated by ripple periodicity.

Exactly same result was observed in experiment as shown in Fig. 3.31. For this experiment silver was deposited on 45 nm and 20 nm rippled substrate at a normal incidence. SEM images of 12 nm silver deposited on 45 nm ripple at normal incidence before and after annealing are shown in Fig. 3.31(a, b), respectively. Before annealing there is no ordering of particle as should be the case of normal incidence growth discussed earlier but particles appear to be weakly ordered after annealing. That means ripple modulations promote the uniaxial ripening and separate the particles and do not allow further coalescence across the ripple.

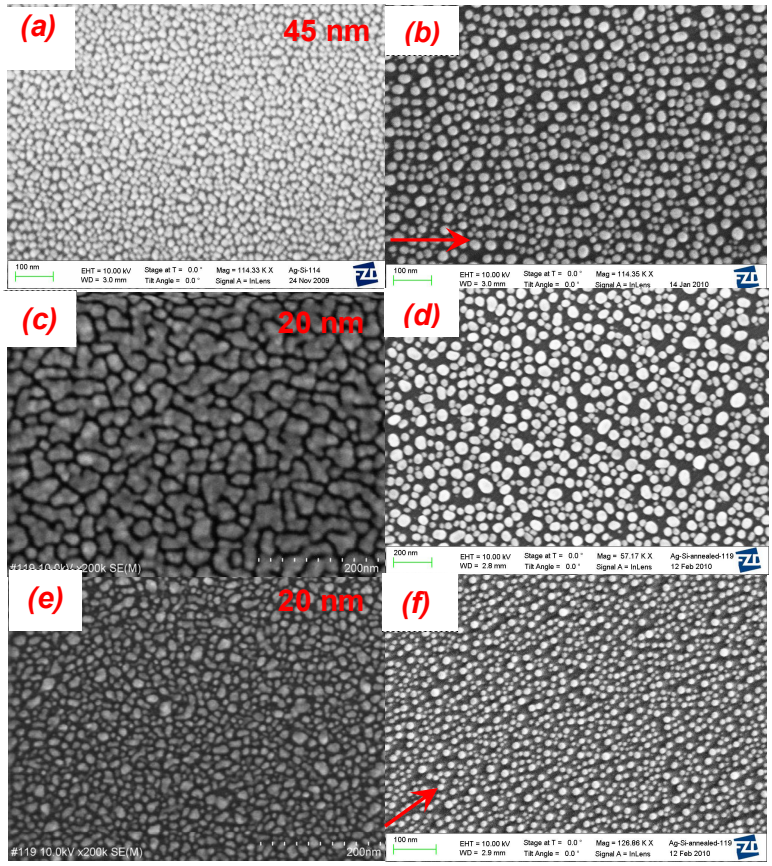

Fig. 3.31: *Normal incidence growth of silver on 45 nm (a, b) and 20 nm (c, d, e, f) wavelength ripple with a precise amount 12 (a, b c, d) nm and 6 nm (e, f) cases. Results for both before and after annealing are shown.*

Similar experiments were performed for 20 nm (12 nm silver) ripples and there was no ordering observed in this case (Fig. 3.31(c, d)). The phrase ñprecise amountò used above is important, as if after annealing particle size is lager then ripple ridge portion it can easily coalesce with adjacent particles across the ripple. So deposited amount should be such that Ostwald ripening should remain uniaxial. Therefore using slightly lower amount of deposition (6 nm) we could even align the particle in case of 20 nm ripple as well (Fig. 3.31(e, f)).In conclusion to this part, we could say both kinetics and thermodynamics are important during the silver growth on ripple substrate and to form ordered spherical silver nanoparticles even at normal incidence.

Reference:

[1] G. Lelay, M. Mammeville, R. Kern, *Surface Science* 72 (**1978**) 405.

[2] M. S. Ho, C. C. Su, T. T. Tsong, *J. J. Appl. Phys*. 45 (**2006**) 2382.

[3] J. R. Osiecki, K. Takusari, H. Kato, A. Kasuya, S. Suto, *J. Phys.: Conference Series* 61 (**2007**) 1107.

[4] M. Ohring, *Material science of thin films* (Academic Press) (**2002**).

[5] D. L. Smith, *Thin-Film deposition principle and practise* (McGraw-Hill) (**1995**).

[6] J. A. Venables, *Introduction to surface and thin film process* (Cambridge University Press) (**2000**).

[7] T. W. H. Oates, A. Mücklich, *Nanotechnology* 16 (**2005**) 2606.

[8] T. C. Zhang, Z. X. Mei, Y. Guo, Q. K. Xue, X. L. Du**,***J. Phys. D: Appl. Phys*. 42 (**2009**) 065303.

[9] R. Finsy, *Langmuir* 20 (**2004)** 2975.

[10] L. R. Houk, S. R. Challa, B. Grayson, P. Fanson, A. K. Datye, *Langmuir* 25 (**2009**) 11225

[11] M. Strobel, K. H. Heinig,W. Möller, *Phys. Rev B*, 64 (**2001**) 245422.

[12] J. Hu, W. Cai, C. Li, Y. Gan, L. Chen, *Appl. Phys. Lett*. 86 (**2005**) 151915.

[13] K. Chatterjee, S. Banerjee, D. Chakravorty, *Phys. Rev. B* 66 (**2002**) 085421.

[14] A. Toma, D. Chiappe, D. Massabo, C. Boragno, F.B.Mongeot, *Appl. Phys. Lett*. 93(**2008**) 163104.

[15] S. Camelio, D. Babonneau, D. Lantiat, L. Simonot, F. Pailloux, *Phys. Rev. B* 80 (**2009**) 155434.

[16] S. Numanzawa, M. Ranjan, K. -H. Heinig, S. Facsko et al., J. Phys.: Condens. Matter **23** (2011) 222203.

[17] T. C. Zhang, Z. X. Mei, Y. Guo, et al. ,*J. Phys. D: Appl. Phys*. 42 (**2009**) 065303.

[18] C. T. Campbell, *Surf. Sci. Rep.* (**1997**) 271.

[19] Y. F. Guan, A. J. Pedraza, *Nanotechnology* 16 (**2005**) 1612.

[20] H. Jinlian, C. Weiping, L. Cuncheng, G.Yanjie, L. Chen, *Appl. Phys. Lett.* 86 (**2005**) 151915.

[21] K. K. Nanda, A. Maisels, F. E. Kruis, *J. Phys. C* 112 (**2008**) 13488.

[22] T. W. H. Oates, A. Keller, S. Noda, S. Facsko, *Appl. Phys. Lett*. 93(**2008**) 063106.

[23] T. W. H. Oates, A. Keller, S. Facsko, A. Mücklich, *Plasmonics* 2 (**2007**) 47

Chapter-4

Optical Properties of Self-aligned Nanoparticles/nanowires

In chapter-1 we have introduced briefly that light interaction with bulk metal and metal nanoparticles excites surface plasmon polaritons (SPP) and localised surface plasmon resonances (LSPR), respectively. The understanding of LSPR using the case of a metal sphere in a simple electrostatics approach within the quasi static limit ($R<<\lambda$) will be presented here. Later we will show resonances in much larger particles in the preview of Mie-scattering theory [1, 2]. Modified dielectric functions due to size, shape etc. of the metal nanoparticles are the key factors that affects the resonance conditions. Therefore we will begin with the classical description of the dielectric function of bulk metals, which is later modified due to particle size in the Mie treatment. Mie theory is applicable to explain LSPR only in single isolated nanoparticle and does not consider the effect of plasmonic field coupling for closely sitting particles. In reality we need to deal with collection of such nanoparticles. Therefore discussion will also be extented to multi-particle system. LSPR has been extensively studied for disordered nanoparticles of different shapes, sizes, and interparticle gaps [1-15]. A literature overview of the LSPR variation with different factors will also be presented.

Nanoparticles film can produce anisotropic LSPR response due to various reasons, such as non spherical shape of nanoparticles, special geometrical arrangement of nanoparticles, etc. Shape anisotropy means that the plasmon resonance is shifted for the excitation along two different axis (long and short) of the nanoparticle. This shift changes further with the change in particle aspect ratio. Gans first reported anisotropy induced by the

non-spherical shape of nanoparticles [1-3]. His work is mainly the extension of Mie theory incorporating the particle shape effect. Since our particles are mainly elongated in shape and expected to have some shape anisotropy a description of Gans theory will also be presented following the Mie theory.

It has been reported previously that self-aligned nanoparticles/nanowires produced on ripple patterned templates are optically anisotropic [16, 17]. The plasmon resonance of these nanoparticles is blue shifted if the direction of incident polarised light changes from along the ripples to across the ripple. However, the type and cause of the optical anisotropy was not clearly discussed. Self-aligned nanoparticles on rippled surfaces are mainly non-spherical and are arranged in a row. Therefore the optical anisotropy may results from both shape and ordering of the nanoparticles. We have first conducted a reflection measurement study to find out the LSPR positions along and across the ripple for various aspect ratio particles arrays. These LSPR positions were compared with values predicted by Gans theory. This study show convincingly which factor (shape or arrangement) is dominating in our system to cause the optical anisotropy. It will be demonstrated that the plasmonic field coupling of ordered particles is a much stronger effect then the shape anisotropy.

As mentioned earlier the modified dielectric properties in the transition from bulk to nanoparticles plays a key role in the occurrence of LSPR. Anisotropy of a system can be classified to uniaxial or biaxial based on the dielectric tensor of the system. We will introduce such anisotropies in brief. Therefore to investigate the type of anisotropy calculation of dielectric properties of our particle/wire array system using Generalised ellipsometry (GE) will be presented. For this purpose we apply a rigorous 4x4 matrix formalism method [18, 19] in a biaxial layer model implementing both metallic and LSPR resonance behaviour. Different in plane and out of plane values of dielectric coefficients confirms the reason of anisotropy observed in reflection measurement.

Finally in the last section to use self-aligned nanoparticles and nanowires as an active surface enhanced Raman scattering (SERS) substrate is demonstrated. This system found to be superior for SERS compared to randomly distributed particles with a high enhancement factor. Higher SERS signal in between two nanowires and nanoparticles compare to along wire long axis indicates the large field enhancement between two nanowires and nanoparticles. The effect of inter-particle distance and aspect ratio on the strength of field enhancement is demonstrated. Enhancement factor is found to be one order higher along the ordered chain of elongated particles compare to randomly distributed nanoparticles. Elongated nanoparticles shows significantly higher SERS signal compare to long wires.

Enhancement factor of ~10^8 was found for 10^{-6} M concentrated R6G molecule for the vibrational mode Raman peak at 1509 cm^{-1}.

4.1. Theory for LSPR and experimental evidences

4.1.1 Dielectric functions of bulk metal

Metals have completely filled valence bands and a partially filled conduction band. The optical properties of metals can be explained by a plasma model, where a gas of free electrons of number density *n* moves against a fixed background of positive ion cores [1, 2]. For free electron metals, like the alkali metal, the dielectric function is governed mainly by transitions within the conduction band, whereas in other metals substantial contributions of interband transitions from lower-lying bands into the conduction band or from the conduction band into higher unoccupied levels are present. Noble metals (Au, Ag, Cu) show both types of transitions.

Drude-Lorentz-Sommerfeld presented a simple approach to calculate the optical response of free-electron metals. The electrons oscillate in response to the applied electromagnetic field and their motion is damped via collisions occurring with a characteristic collision frequency ($\Gamma=1/\tau$), τ is known as relaxation time of free electron gas. So one can solve a simple equation of motion for an electron in the external field $E=E_o e^{-i\omega t}$:

$$m_e \frac{\partial^2 x}{\partial t^2} + m_e \Gamma \frac{\partial x}{\partial t} = -eE \tag{4.1}$$

The solution of this equation describing the oscillation of the electron is $x(t)=x_o e^{-i\omega t}$. The complex amplitude x_o incorporates any phase shifts between driving field and response via

$$x(t) = \frac{e}{m_e\left(\omega^2 + i\Gamma\omega\right)} E(t) \tag{4.2}$$

Displaced electrons contribute to the macroscopic polarization $P = -nex.$ According to the relation of polarisation *P*, *E* and displacement field D:

$$D = \varepsilon_o E + P = \varepsilon_o\left(1 - \frac{\omega_P^2}{\omega^2 + i\Gamma\omega}\right)E, \text{where} \qquad \omega_p = \frac{ne^2}{\varepsilon_o m_e} \tag{4.3}$$

ω_p is the Drude plasma frequency of free electron gas. The dielectric function of the free electron gas reads then :

$$\varepsilon(\omega) = \left(1 - \frac{\omega_P^2}{\omega^2 + i\Gamma\omega}\right) \tag{4.4}$$

The real and imaginary components of this complex dielectric function $\varepsilon(\omega) = \varepsilon_1(\omega) + i\varepsilon_2(\omega)$ are given by

$$\begin{aligned} \varepsilon_1(\omega) &= 1 - \frac{\omega_P^2}{\Gamma^2 + \omega^2} \\ \varepsilon_2(\omega) &= \frac{\omega_P^2\Gamma}{\omega(\Gamma^2 + \omega^2)} \end{aligned} \tag{4.5}$$

For $\omega >> \Gamma$ the real and imaginary part of $\varepsilon(\omega)$ for free electron metals can be written as

$$\begin{aligned} \varepsilon_1(\omega) &\approx 1 - \frac{\omega_P^2}{\omega^2} \\ \varepsilon_2(\omega) &= \frac{\omega_P^2\Gamma}{\omega^3} \end{aligned} \tag{4.6}$$

Under this condition $\varepsilon_2(\omega)$ is very small and therefore $\varepsilon(\omega)$ is predominantly real. This can be considered as the dielectric function of an undamped free electron plasma. Note that the behaviour of noble metals in this frequency region is completely altered by interband transitions, leading to increase in ε_2. In the region of very low frequencies, where $\omega << \Gamma$, $\varepsilon_2 >> \varepsilon_1$, real and the imaginary part of the complex refractive index are of comparable magnitude and metals are mainly absorbing [1,2].

In the free electron model $\varepsilon \to 1$ at $\omega >> \omega_p$. Noble metals (Au, Ag, Cu) have completely filled *d* shells and just one electron in the s band. Therefore extension of this model is needed in the region $\omega >> \omega_p$ (where response is dominated by free s electrons), since the filled *d* band close to Fermi surface causes a highly polarised environment. This residual polarisation can be incorporated by modifying the value of *P* in eq. 4.3. This effect is therefore described by a dielectric constant ε_∞ (varies between 1 to 10). The modified dielectric function is

$$\varepsilon(\omega) = \varepsilon_\infty - \frac{\omega_P^2}{\omega^2 + i\Gamma\omega} \tag{4.7}$$

Fig. 4.1 [19] shows ε_1 for silver for the wide range between 2.0-11.0 eV. Black line is the experimentally measured dielectric function while the dotted line is calculated values showing contribution of free electrons (ε_{FCA}) and bound electrons (ε_{bound}). E_p (at $\omega = \omega_p$

$\varepsilon_1 \rightarrow 0$) is the energy at plasma frequency. It can be seen that the bound electron contribution increases the overall value of ε_1 and shifts the E_p from 9.2 eV to 3.9 eV.

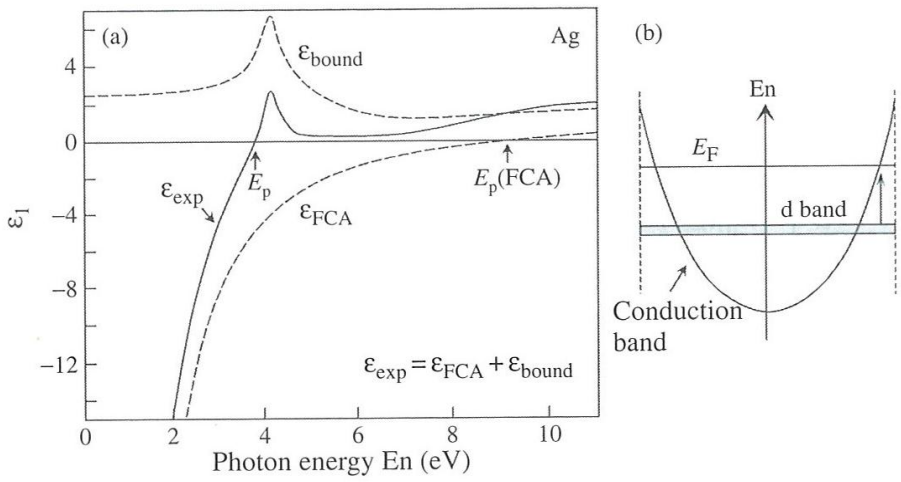

Fig. 4.1: *Experimentally measured value of ε_1 for bulk silver compare with model with the contribution of free and bound electrons. Right side is sketch of the filled d band just below the Fermi level[19].*

4.1.2 Response of small metal sphere to an electric field

The interaction of a particle of size R with an electromagnetic field can be analyzed using the simple quasi-static approximation provided that $R << \lambda$, i.e. particle size is much smaller than wavelength of light in the surrounding medium (Fig. 4.2).

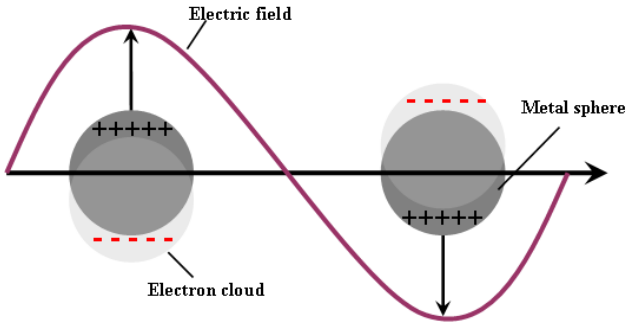

Fig. 4.2: *Schematic of plasmon oscillation for a sphere, showing the displacement of the conduction electron charge cloud relative to the nuclei.*

The positive charge in a particle is assumed to be immobile and negative charge (conduction electrons) is allowed to move under the influence of an external electric field. Using the proper boundary conditions at the surface of the sphere the resulting polarization can be calculated. In this case internal field comes out to be :

$$E_i = E_o \frac{3\varepsilon_m}{\varepsilon + 2\varepsilon_m} \tag{4.8}$$

ε_m is the dielectric constant of the embedding medium. The static polarizability of the sphere is comes out to be

$$\alpha = 4\pi\varepsilon_o R^3 \frac{\varepsilon - \varepsilon_m}{\varepsilon + 2\varepsilon_m} \tag{4.9}$$

Both internal field and polarizability show resonance behaviour when

$$\begin{aligned} &\left|\varepsilon + 2\varepsilon_m\right| = Minimum \\ &i.e.\left[\varepsilon_1(\omega) + 2\varepsilon_m\right]^2 + \left[\varepsilon_2(\omega)\right]^2 = Minimum \end{aligned} \tag{4.10}$$

Apparently that the polarizability experiences a resonant enhancement under the condition that $\left|\varepsilon + 2\varepsilon_m\right|$ is minimum, which is for the case of small or slowly ï varying ε_2 around the resonance simplifies to;

$$\varepsilon_1 = -2\varepsilon_m \tag{4.11}$$

This relationship is called the *Fröhlich condition* and the associated mode is the dipole surface plasmon of the metal nanoparticle. For a sphere consisting of a Drude metal with a dielectric function as in Eq. 4.4 located in air, the Fröhlich criterion is met at the frequency $\omega = \omega_p / \sqrt{3}$. This express the strong dependence of the resonance frequency on the dielectric environment: the resonance red shifts as ε_m is increased

4.1.3 Mie-Scattering theory

The above discussion of the quasi-static regime holds only for sufficiently small particles. Mie presented a more general solution of the diffraction problem of a single sphere of arbitrary material in the frame of electrodynamics. He applied Maxwellôs equations with appropriate boundary conditions in spherical coordinates using multipole expansion of the incoming electric and magnetic fields. He divided the problem into two parts: electromagnetic and material. He introduced a phenomenological dielectric function $\varepsilon(\omega, R)$, which can be taken either from experiment or from model calculations [1-3]. $\varepsilon(\omega, R)$ may be different from bulk since intrinsic size effects influence damping (Γ). Wide use and importance of Mie

theory is due to this phenomenological dielectric function $\varepsilon(\omega, R)$ as it incorporates all important nanoparticles effects. In this consent $\varepsilon(\omega, R)$ of some particles are those which satisfied Mie theory, i.e produce the same spectral response observed experimentally.
Mie calculated the total extinction cross section (σ_{ext}) due to absorption and scattering from a particle surface, which are given by eq. 4.12.

$$\begin{aligned} \sigma_{ext} &= \frac{2\pi}{|k|^2}\sum_{L=1}^{\infty}(2L+1)\,\mathrm{Re}\left\{a_L + b_L\right\} \\ \sigma_{sca} &= \frac{2\pi}{|k|^2}\sum_{L=1}^{\infty}(2L+1)\left(|a_L|^2 + |b_L|^2\right) \\ \sigma_{abs} &= \sigma_{ext} - \sigma_{sca} \end{aligned} \tag{4.12}$$

k is the wave vector, L give information about type of mode (L=1 for dipole, L=2 for quadrupole, etc.) and a_L and b_L complex equations of Riccati-Bessel cylindrical functions [1].

When applied to a spherical particle in the Quasi-static regime ($R<<\lambda$) neglecting the higher order multipoles excitations and phase retardation scattering cross-section of Mie theory is comes out to be :

$$\sigma_{ext}(\omega) = 9\frac{\omega}{c}\varepsilon_m^{3/2}V\frac{\varepsilon_2(\omega)}{\left[\varepsilon_1(\omega)+2\varepsilon_m\right]^2+\varepsilon_2(\omega)^2} \tag{4.13}$$

where V denotes the particle volume. It can be seen that this equation provides the same condition for resonance as in Eq. 4.10. The spectral features of eq. 4.13 such as position and shape of the resonance do not directly depend on the particle radius R but only indirectly due to size the dependence of $\varepsilon_{1,2}(\omega)$. Therefore the resonance position, height, and width offer a suitable experimental tool to study the size dependence of the dielectric functions.

The above equation has been used extensively to explain the absorption spectra of small metallic nanoparticles in a qualitative as well as quantitative manner .However, for larger nanoparticles where the dipole approximation is no longer valid the plasmon resonance depends explicitly on the particle size. The larger the particles become, the more important are the higher-order modes as the light can no longer polarize the nanoparticles homogeneously. These higher-order modes peak at lower energies and therefore the plasmon band red shifts with increasing particle size. At the same time, the plasmon bandwidth increases with increasing particle size. It also follows from the Mie theory. As the optical absorption spectra depend directly on the size of the nanoparticles, this is regarded as an extrinsic size effect [1, 2].

In one of the early approaches, Kreibig and von Fragstein [1-3] proposed that electron-surface scattering must be enhanced in small particles since the mean free path of the conduction electrons is limited by the physical dimension of the nanoparticle. The mean free path of the electrons in silver and gold is of the order of 40-50 nm [1,3, 27]. If the electrons scatter with the surface in an elastic but totally random way, the coherence of the overall plasmon oscillation is lost. Inelastic electron- surface collisions would also change the phase. The smaller the particles, the faster the electrons reach the surface of the particles. The electrons can then scatter at the surface and lose the coherence more quickly than in a larger nanoparticle. As a consequence the plasmon band width increases with decreasing nanoparticle radius. The damping constant Γ is related to the lifetimes of all electron scattering processes which are mainly electron-electron, electron-phonon and electron-defect scattering in the bulk material. An additional term accounting for electron-surface scattering is added to Γ and then becomes a function of the particle radius R as follows [1-3] :

$$\Gamma = \Gamma_o + \frac{Av_F}{R} \tag{4.13}$$

Γ_o is the bulk damping constant. A is a theory-dependent parameter which is dependent on the details of the scattering process (e.g. isotropic or diffuse scattering) and v_F (1.39×10^8 cm.sec^{-1}) is the velocity of the electrons at the Fermi energy. This size effect is considered an intrinsic size effect, since the material dielectric function itself is size dependent, in contrast with the extrinsic size effect in large particles (i.e. R >20 nm). This model gives the correct $1/R$ dependence of the plasmon band width as a function of size for nanoparticles described by the dipole approximation in the intrinsic size region (R <20 nm). However, the best advantage of this theory is probably the fact that it provides a very good description for the dependence of the particle dielectric constant on size. The modification of the dielectric constant is done in a straightforward manner.

4.1.4 Shape anisotropy: Gans theory

For non spherical particles electrodynamics calculations of scattering are much more tedious. The plasmon resonance absorption band splits into two bands as the particles become more elongated along one axis. With increasing aspect ratio the energy separation between the resonance frequencies of the two plasmon bands increases [1-3]. The high-energy band corresponds to the oscillation of the electrons perpendicular to the major (long) axis and is

referred to as the transverse plasmon absorption. This absorption band is relatively insensitive to the nanorod aspect ratio and coincides spectrally with the surface plasmon oscillation of the nanoparticles. The other absorption band at lower energies is caused by the oscillation of the free electrons along the major (long) rod axis and is known as the longitudinal surface plasmon absorption.

Fig. 4.3 shows the absorption spectra of two nanorod samples having aspect ratios of 2.7 and 3.3 [3]. The short-wavelength absorption band is due to the oscillation of the electrons perpendicular to the major axis of the nanorod while the long-wavelength band is caused by the oscillation along the major axis. The former is rather insensitive towards the nanorod aspect ratio in contrast with the longitudinal surface plasmon band which red shifts with increasing aspect ratio. This is illustrated in the inset where the two band maxima ((□), transverse mode; (O), longitudinal mode) are plotted against the nanorod aspect ratio R. The optical absorption spectrum of nanorods with aspect ratio can be modelled using an extension of the Mie theory known as Gans theory. Within the dipole approximation according to the Gans treatment, the extinction cross-section for elongated ellipsoids is given by eq. (4.14). Gans added a geometrical factor in the real part of dielectric function in the denominator of scattering equation.

$$\sigma_{ext}(\omega) = \frac{\omega}{3c}\varepsilon_m^{3/2} V \frac{\left(1/p_i^2\right)\varepsilon_2(\omega)}{\left[\varepsilon_1(\omega) + \frac{(1-p_i)}{p_i}\varepsilon_m\right]^2 + \varepsilon_2(\omega)^2} \qquad (4.14)$$

$$\sigma_{ext}(\omega) = \frac{\omega}{3c}\varepsilon_m^{3/2} V \frac{\left(1/p_i^2\right)\varepsilon_2(\omega)}{\left[\varepsilon_1(\omega) + k_i\varepsilon_m\right]^2 + \varepsilon_2(\omega)^2}$$

Where $i = x, y, z$

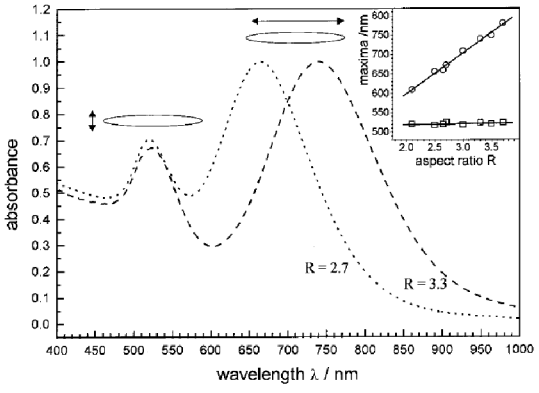

Fig. 4.3: *Size-dependent surface plasmon absorption of gold nanorods. Optical absorption spectra of gold nanorods with mean aspect ratios of 2.7 and 3.3 are shown Reprinted with permission from [3] copyright © 2000 Taylor & Francis.*

Peak wavelength maxima in both cases (longitudinal and transverse) can be very easily calculated under quasi static dipole approximation using Gans theory, if dielectric coefficients of surrounding and bulk metal are known as shown in eq. 4.15. For metal nanorods, the relationship between the aspect ratio and the optical absorption peak can be described by Gans theory, which introduced a geometrical factor k_i for different dimensions. The x and y axes of the nanorod are nearly identical and correspond to the nanorod diameter (d), whereas the z axis represents the nanorod length (l).

$$\varepsilon_{1(meteal)} = -k_i \varepsilon_m \tag{4.15}$$

ε_m is the dielectric coefficient of surrounding media which is air in our case. k_i is the space dependent screening geometrical factor given by

$$k_i = (1 - p_i)/p_i \quad i=x,y,z \tag{4.16}$$

$$p_x = p_y = (1 - p_z)/2 \tag{4.17}$$

$$p_z = (1 - e^2)\left[\ln\left(((1-e))/(1+e)\right) - 2e\right]/2e^3 \tag{4.18}$$

$$e = \left[\left(l^2 - d^2\right)/d^2\right]^{1/2} \quad l/d \text{ is aspect ratio} \tag{4.19}$$

Here l is length and d is diameter of the nanoparticle.

4.1.5 Effective dielectric function: Maxwell-Garnett theory

As mentioned earlier Mie-theory is only applicable to the scattering of a single particle. It is assumed that the individual particles are non-interacting and separated from each other. Therefore, the electric field created around one particle by the excitation of a surface plasmon resonance is not felt by the other surrounding particles. If the interparticle distances become smaller than the particle dimension the plasmon resonance red shifts and often a second absorption peak at a longer wavelength is observed. In the case of composite materials such as densely packed nanoparticles in a transparent host medium, the effective-medium theories are better suited to explain their optical properties [1-3].

The Maxwell-Garnett theory (Eq. 4.20) is an effective-medium theory. It treats the metal- dielectric composite material in which the particles are embedded and isolated from each other. The particle dimension and interparticle distances are considered to be infinitely small compared with the wavelength of the interacting light. The Maxwell-Garnett theory is based on the Clausius-Masotti equation and it assumes that it is justified to describe the

composite material containing metal nanoparticles embedded in an inert host medium by an effective complex dielectric constant ε_c such as

$$\frac{\varepsilon_c - \varepsilon_m}{\varepsilon_c + k\varepsilon_m} = f_m \frac{\varepsilon - \varepsilon_m}{\varepsilon + k\varepsilon_m} \tag{4.20}$$

Where ε and ε_m are the dielectric constants of the metal nanoparticles and the host medium respectively. In contrast with the Mie theory, ε_m is also a complex function depending on the frequency of light. f_{m} is the volume fraction of the metal nanoparticles in the composite material and k is a screening parameter. The latter is related to the shape of the nanoparticles.

4.1.6 Optical anisotropy

During Gans theory treatment we have discussed only longitudinal or transverse plasmon modes. These modes are due to different dielectric properties along long and short axis of the particles. In the case when the optical response of the material changes with orientation in any direction it is said to be optically anisotropic in general. In this case the optical constants are described by a three dimensional dielectric tensor. Anisotropic material can be classified broadly in two categories, uniaxial and biaxial material. In uniaxial material two dielectric coefficients are the same and only one direction has different dielectric coefficient ($\varepsilon_x = \varepsilon_y \neq \varepsilon_z$). In biaxial material, on the other hand, all the dielectric tensors are different ($\varepsilon_x \neq \varepsilon_y \neq \varepsilon_z$).

The propagation of light in anisotropic media can be described in a more systematically forming a dielectric ellipsoid. Light having electric field E propagating in dielectric media will have energy density given by:

$$\begin{aligned} U_d &= \frac{1}{2} E.D = \frac{1}{2\varepsilon_o \varepsilon} D.D = \frac{1}{2\varepsilon_o}\left(\frac{D_x^2}{\varepsilon_x} + \frac{D_y^2}{\varepsilon_y} + \frac{D_z^2}{\varepsilon_z}\right) \\ if\ i &= \frac{D_i}{\sqrt{2\varepsilon_o U_d}}, \quad i = x, y, z \\ \frac{x^2}{\varepsilon_x} &+ \frac{y^2}{\varepsilon_y} + \frac{z^2}{\varepsilon_z} = 1 \end{aligned} \tag{4.21}$$

Final equation in (4.21) represents an ellipsoid in (x, y, z) coordinates. Now we can understand anisotropy by drawing a dielectric ellipsoid. Fig. 4.4(a) corresponds to an isotropic media, where the ellipsoid becomes sphere, and the dielectric functions are independent of the

propagation direction of light. In other two cases Fig. 4.4(b) and Fig. 4.4(c) one and all semi-axis are different corresponding to uniaxial and biaxial anisotropy, respectively.

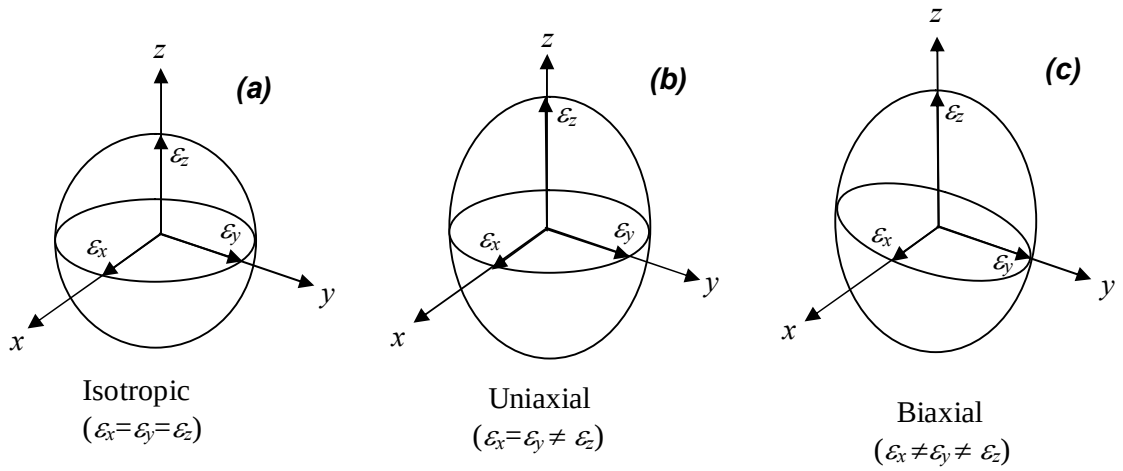

Fig. 4.4: *Dielectric ellipsoid of (a) isotropic material, (b) uniaxial material, and (c) biaxial material, respectively.*

4.1.7 Literature overview of LSPR

Different techniques are available now a day for the measurement of localised surface plasmon resonance even for single nanoparticles such as SPR spectroscopy, dark-field spectroscopy, absorption spectroscopy, extinction spectroscopy, reflection and transmission spectroscopy, ellipsometry etc. Also a wide range of software (DDR, FDTD, T-matrix, MEEP, WVASE32, SCOUT etc.) are available based on the theories describe above to model experimentally measured LSPR. LSPR have been extensively studied for particles of different size, shapes, different inter-particles gaps and host medium. We present a summary of such effects based on selected results from references [1, 3, 7, 12, 15, 21, 25]. The examples within the quasi static limit based on eq. 4.9 are presented first and later for particles of bigger size.

In Fig. 4.5 different cases are discussed with respect to the reference parameters of an oblate truncated ellipsoid on a supporting substrate of dielectric function ε_m = 1.33, truncation parameter t = 0.605, aspect ratio s = 1.06545, short cluster axis a= 2.75 nm, long cluster axis *b* = 2.93 nm and filling fraction *f* = 0.19 [1]. The spectra in Fig. 4.5 (a) depict the effect of the particle size on the volume reduced imaginary part of the polarizability (4π Im(α))/V (Eq. 4.9). While the particle size has no significant influence on the resonance position for particle with radius below 10 nm, the resonance amplitude is enhanced and the FWHM is

significantly reduced when increasing the particle radius from 3 nm to 10 nm. When particles are deposited on a supporting substrate with dielectric coefficient > 1, the particles dipoles

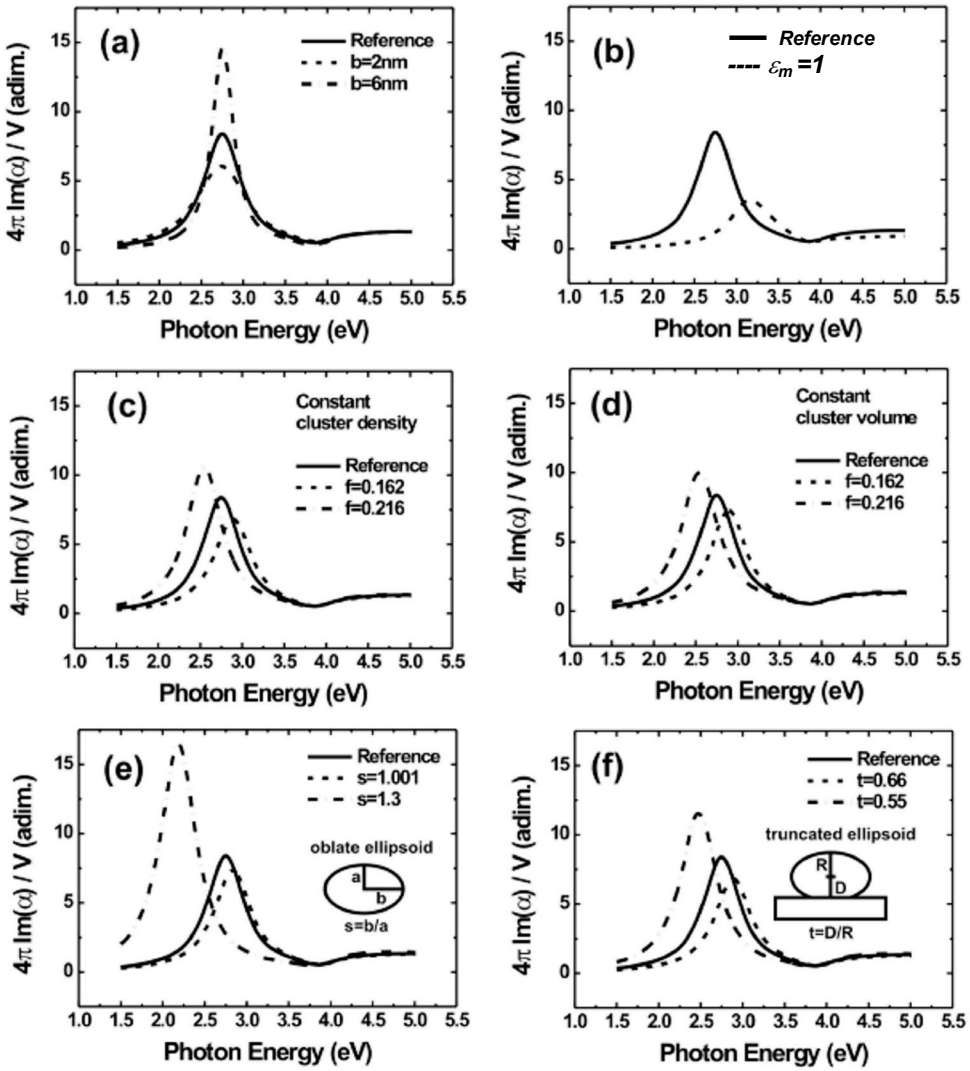

Fig. 4.5: *Dependence of cluster polarizabilites on cluster size (a), surrounding medium (b), cluster arrangement (c)+(d) and cluster shape (e)+(f)[1]. All the cases are compared with respect to a reference sample of oblate truncated ellipsoid on a supporting substrate of dielectric function ε_m=1.33 and aspect ratio s=1.06545.*

induce an image dipole in the substrate material. Since these image dipoles are oriented in the opposite direction of the cluster dipoles, an additional damping factor is introduced which moves the plasmon resonance to lower energies as can be seen in Fig. 4.5(b). A similar red shift occurs upon embedding metal clusters in a host material with dielectric coefficient > 1. The increase in the resonance amplitude can be attributed to the influence of an ensemble of particles on the resonance, because in previous calculations for a single cluster no such behaviour was found. Another factor with a large impact on the particles resonance is the

particle-particle interaction which becomes stronger with decreasing separation between the particles.

For a random distribution of metal particles the particle-particle distance is described by the so called filling fraction *f*, which gives the area or volume fraction of clusters on a surface or in an embedding medium, respectively. A smaller gap between individual clusters introduces a larger particle-particle coupling which leads to a red shift of the resonance peak and an increase of the resonance amplitude as seen in Fig. 4.5(c, d). This can be achieved in two different ways: (1) varying the volume of individual particle when holding the particle density constant ((Fig. 4.5(c)) and (2) varying the particle density when holding the volume of individual particle constant (Fig. 4.5(d)).

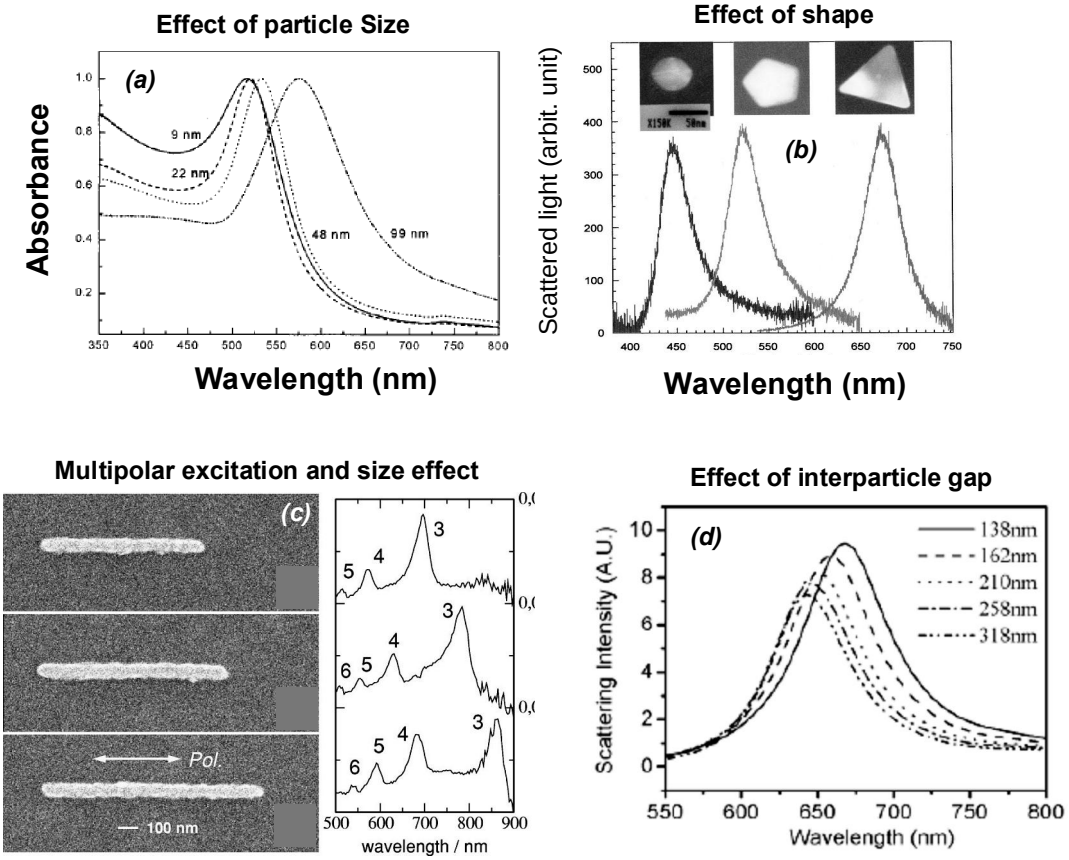

Fig. 4.6: *(a) LSPR red shifted with increase in particles size [3], Reprinted with permission from [15] copyright © 2000 Taylor & Francis. (b) Particles of different shape reflect the different SPR position [7,12], Reprinted with permission from [7] copyright © [2002], American Institute of Physics.(c) SPR red shifted with particles size and also higher order resonance also appear with increase size [21],Reprinted with permission from [21] copyright © [2000], American Institute of Physics. (d) SPR red shifted with reduction in interparticle gap [25], Reprinted with permission from [25] copyright © [2003], American Chemical Society.*

The particle shape also plays an important role: Fig. 4.5(e) and Fig. 4.5(f) show the effects of particle geometry and particle truncation, respectively, while keeping the particle

volume constant. In this case the particle geometry is that of an oblate ellipsoid of aspect ratio $s = b/a$ between the long cluster axis b and the short axis a, which gives the deviation from spherical shape. The particle plasmon resonance experiences a larger red shift and amplitude increase as the particle shapes become more aspherical. A similar behaviour can be observed when particles are truncated which usually happens when metal particles are grown on hard substrate materials. The relevant parameter in this case is the so called truncation parameter $t = D/R$ with D being the distance between particle center and substrate surface and R the particle radius perpendicular to the substrate plane. With increasing truncation, the particle resonance moves to lower energies and the resonance amplitude increases.

Fig. 4.6(a) shows the measured absorption spectra for various sizes particle [3]. LSPR is clearly red shifted with increase in particle size. LSPR of different types of particles shapes are shown in Fig. 4.6(b) [7, 12]. For triangular shape particles plasmon shift is maximum compared to spherical. Fig. 4.6(c) shows an example of extinction spectra of gold nanowires of various lengths [21]. Wire length is comparable or greater than incident light in this case. Several resonances due to excitation of higher order oscillation modes are visible. Also LSPR red shifted with nanowire length. In the last example (Fig. 4.6(d)) effect of interparticle gap is shown. LSPR red shifted with reducing the interparticle gap reflecting that plasmonic coupling is getting stronger with gap reduction [25].

4.2 Reflection measurement and plasmon tunability

With this overview of the theory of LSPR and various parameters affecting it, we now present the optical properties of our aligned silver nanoparticles using reflection measurements and their understanding based on Gans theory.

4.2.1 Optical anisotropy in self-aligned nanoparticles

Ellipsometry is one of the best available methods to characterise the optical properties of thin films and nanostructures materials [19]. Modern ellipsometers are capable of measuring reflection, transmission and reflection ratios of incident p- and s- polarised light (ψ, Δ), Muller Matrix elements and several other features [19]. Details of the use of ellipsometry for anisotropic sample measurements will be described in section 4.2.2. We have used ellipsometry for reflection measurement to study the variation in LSPR positions of our nanoparticles arrays of different aspect ratios and periodicities. Working principle of reflection measurement is shown in Fig. 4.7. Linearly p- and s- polarised lights are simultaneously or independently incident near normal, at 15^o to the surface normal. Reflected

light is captured in a detector and the intensity ratio of the incident (I_i) and reflected (I_r) light is measured as a function of the light wavelengths. Reflectance for p- and s- polarised light is expresses by :

$$R_p = \frac{I_{rp}}{I_{ip}} = \frac{\left|E_{rp}\right|^2}{\left|E_{ip}\right|^2}, R_s = \frac{I_{rs}}{I_{is}} = \frac{\left|E_{rs}\right|^2}{\left|E_{is}\right|^2}, \quad (4.22)$$

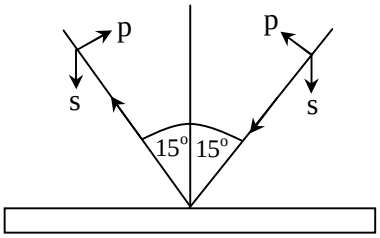

Fig. 4.7: *Schematics diagram of reflection measurement.*

Here E represents the light electric field before and after reflection, corresponding subscripts stand for incident and reflected p- and s- polarised light, respectively. A comparison of reflection measurements conducted for bulk silver and for randomly distributed nanoparticles is shown in Fig. 4.8(a, b), respectively. For bulk silver reflectance is almost constant for the entire visible range but for nanoparticles it exhibits a peak at plasmon resonance wavelength. The combined effects of the free electrons and the bound d-electrons influence the reflectance properties of the metal film. For silver the highly polarisable d-band electrons reduce the electric field that provides the restoring force for the free electron oscillations. This leads to a reduced oscillation frequency as mentioned in section 4.1.1 about bulk metal properties. Hence the d-band contribution makes the threshold energy of interband transitions decrease to 3.9 eV(about 320 nm) shown as the sharp reflectance edge in Fig. 4.8 [19,20].

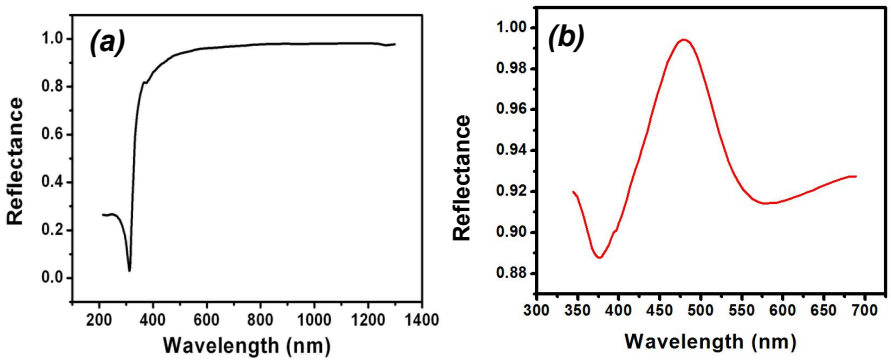

Fig. 4.8: *Reflectance of bulk silver (a) and nanoparticles (b).*

The reason of the resonance observed in Fig. 4.8(b) has already been discussed in previous sections. Reflection measurements performed for both non-ordered and ordered nanoparticles by incident p- and s- polarised light show different behaviour. For clarity please

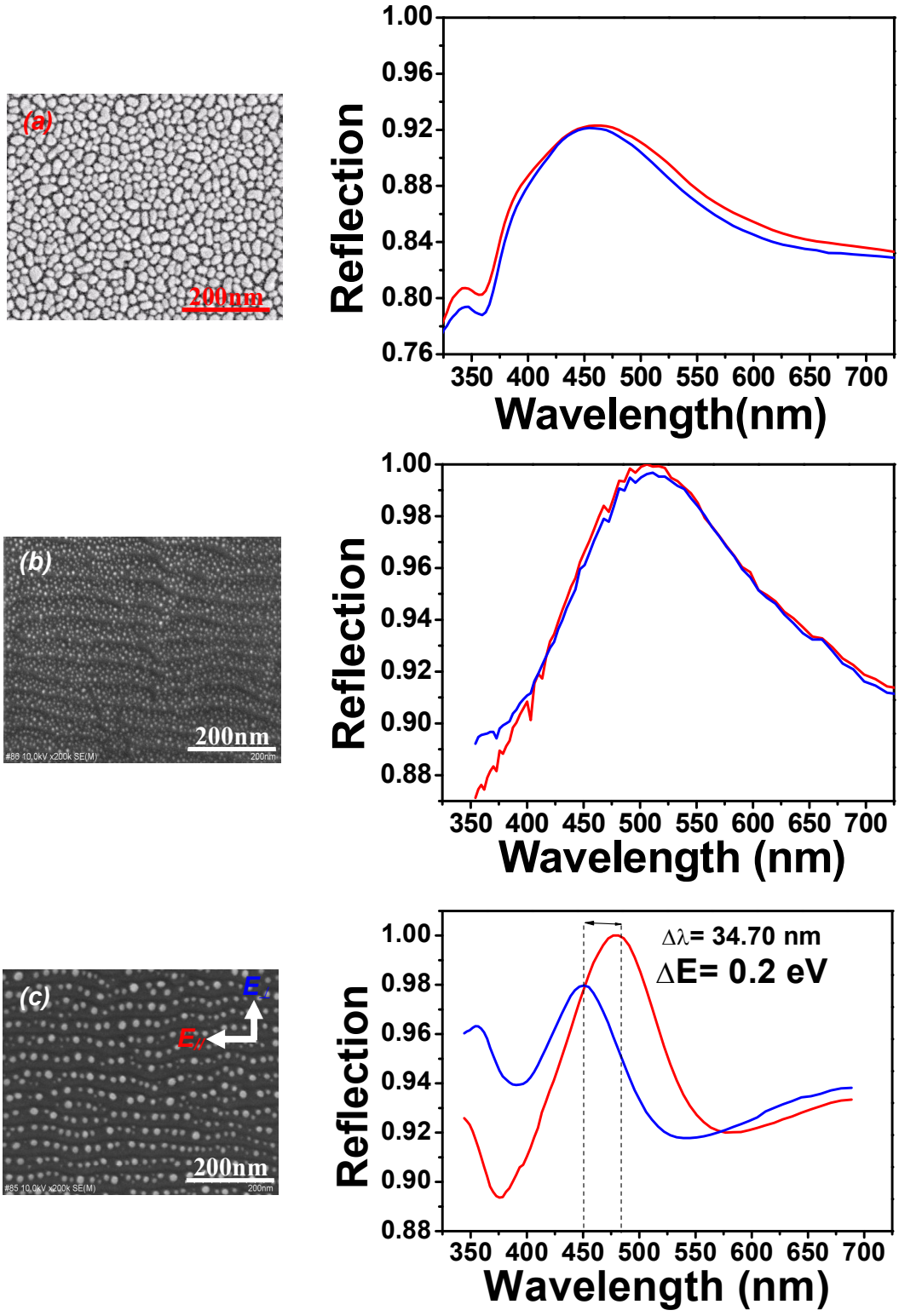

Fig. 4.9: *Reflection measurements corresponding to non-ordered particles on normal Si, rippled Si substrate and for ordered nanoparticles are shown in plot (a), (b) and (c) respectively. Red and blue lines are corresponding to p-polarisation and s-polarisation respectively.*

note that p-polarisation means light electric field vector is parallel to ripples ($E_{//}$) and s-polarisation means it is perpendicular to ripples ($E_{\perp}$) thoughtout in this discussion as shown in

Fig. 4.9(c). In Fig. 4.9(a, b) particles are non-ordered deposited on flat Si substrate and on rippled Si substrate, respectively. In both cases the plasmon resonance occurs at the same wavelength for both p- and s- polarized light. Only for the case of ordered particles shown in Fig. 4.9(c) a red shift of the plasmon resonance appears from s- to p- direction [19, 20] indicating an anisotropy. Comparing Fig. 4.9(a, d and c) the following observation can be made: particles of random shape and size shows a broader resonance (Fig. 4.9(a, b)), while annealed spherical particles produce a much sharper resonance peak with low broadening (Fig. 4.9(c)). It can be concluded that aligned particles of lower size distribution can be produced with annealing with a tuneable optical anisotropy. For non-ordered particles there is no direction dependent change in LSPR observed. Particles are close enough so that their near field can be coupled but coupling is isotropic not directional to cause any optical anisotropy. The anisotropy due to single particle shape is minor effect and averaged out for several particles in a far field measurement like reflection.

Particles shown in Fig. 4.9(c) are rather spherical in shape so no large shape anisotropy is expected. However, a shift as high as 0.2 eV is observed in the measurements. Therefore, this anisotropy can not be attributed to the shape of particles. The reason for this anisotropy is attributed to different near field coupling between the particles along and perpendicular to the ripple direction (Fig. 4.10(b)). Along the ripples particles are more closely arranged at ~10 nm interparticle distance, while parallel to ripples they are separated by the ripple wavelength of ~ 35 nm (Fig. 4.10(a)).

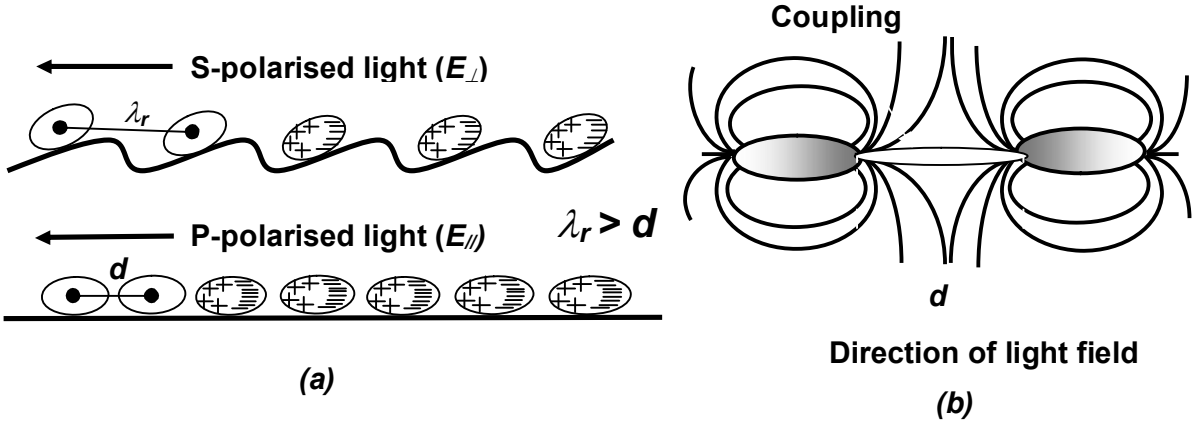

Fig. 4.10: (a) *Schematics of nanoparticles arranged along and perpendicular to the ripples. (b) Dipole field coupling representation.*

It is has been found experimentally as well as theoretically that the coupling field vanishes exponentially with interparticle gap [25, 26]. It is also visible in Fig. 4.9(c) that the resonance strength perpendicular to ripple direction is weaker than parallel to it.

Correspondingly the number of aligned particles is higher along the ripple compare to the perpendicular direction. The light scattering theory by Chern et al. [23] showed that the shift in LSPR increases with number of particles arranged in a row. More number of particles couple field more strongly and consequently make a larger red-shift. Therefore the number of particles and accordingly different inter-particle gap along and perpendicular to ripple direction is responsible for the observed optical anisotropy of aligned Ag nanoparticles.

4.2.2 Evidence of plasmonic coupling

In the previous section, it has been shown that ordered nanoparticles array show different LSPR along and across the ripple. A noticeable energy shift of the plasmon resonances in two directions appears. We attributed this optical anisotropy to different plasmonic coupling along and across the ripple direction. This discussion concluded that self-aligned nanoparticles are optically anisotropic. Similar study was performed for nanoparticles array of different aspect ratios. The aspect ratio was varied between 2 to 5 in our experiments (Fig. 4.11). Particles become elongated in shape with increasing aspect ratio.

Elongated particles have different length and width. Therefore plasmon resonances can be excited in two directions, parallel to particle long axis (longitudinal plasmon) and perpendicular to particles long axis (transverse plasmon) respectively. Plasmons excited in the longitudinal direction also excite weak plasmon in the transverse direction, but this appears only for very high aspect of the particles (Fig. 4.6(c)). In our measurements we did not see two LSPR peaks for any aspect ratio used in this study. Therefore plasmons are independently excited using p- and s- polarised light. Wavelengths of plasmon resonance in both cases (p- and s-) were calculated under quasi static dipole approximation using Gans theory (Eq. 4.15) [3, 28, 29]. For this purpose we first calculated the dielectric function in both longitudinal and transverse plasmon resonance mode and then compared the results with existing silver metal data base [1, 30, 31]. This means under resonance condition using eq. 4.15 ($\varepsilon_{metal} = -k_i\ \varepsilon_m$), the dielectric functions depends on geometrical function (k_i) and embedding medium (ε_m). Since k_i depends on particles aspect ratio, dielectric functions are easy to calculate. Dielectric functions provide the corresponding wavelength that can be read easily obtain from silver metal data base. Calculated peak wavelength is then compared with the experimentally obtained values as shown in Fig. 4.11(a, b).

It is worth to note that the wavelength of longitudinal plasmon resonance follow the trend like Gans theory i.e. wavelength increases with aspect ratio and differ within 25 nm

(Fig. 4.11(a)). However, in transverse plasmon mode this difference is more than 100 nm (Fig. 4.11(b)). As discussed in previous sections the dipole field of ordered particles couples both along and perpendicular to the ripples. With increase in the particles length along the ripples direction, the number of particles and their interparticle gap is reduces. Therefore, with increasing aspect ratio deviation between experimentally observed longitudinal LSPR peaks and predicted by Gans theory is also reduced (Fig. 4.11(a)). Gans theory is valid for single particle only treatment and we are comparing it for particle chain. Therefore, when the number of particles is reduced deviation between theory and experimental values also reduce. With increase in length more particle coalescence and move towards single particle behaviour i.e. for single particle case theory and experiment should coincide.

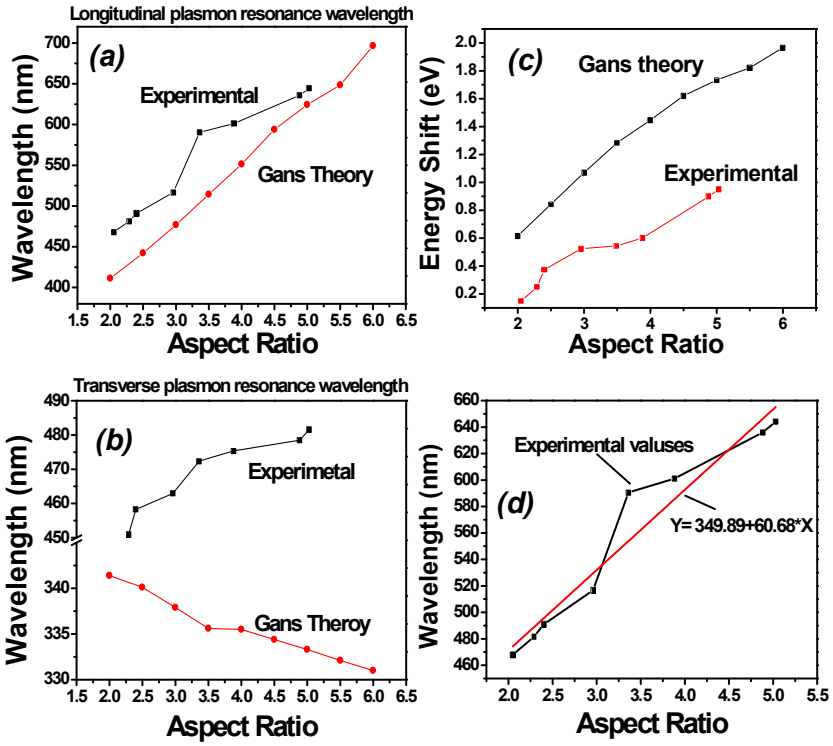

Fig. 4.11: *Comparison of experimentally observed longitudinal and transverse plasmon resonance with predicted by Gans theory (a, b). Corresponding energy shift and linear fit are shown in (c, d).*

In the case of single particle Gans theory predicts a blue shift in the transverse mode plasmon resonance with increase in aspect ratio. But in our measurements a red shift is observed in the case of transverse plasmon resonance variation with aspect ratio. This red shift even increases with aspect ratio like in the case of longitudinal plasmon. This trend can be explained with the following argumentation, Gans theory predicts blue shift in the transverse direction due to different shape. In our samples as well, particles shape is changing

across the ripple but as compared to shape effect, plasmonic coupling in between the particles is much stronger. With aspect ratio the width of particles is also increasing, which reduces the interparticle gap across the ripple. Thus coupling in between two adjacent particles appears to be dominating than the size effect and hence we observed a red shift in LSPR even in transverse plasmon resonance.

A very important observation is that when the aspect ratio changes from 2 to 5, the red-shift in longitudinal direction is very high (~150 nm) while in transverse direction it is only ~ 40 nm. This also confirms the prediction of other reported work that coupling is stronger along the particle long axis and is distance dependent [26]. Due to this reason in Fig. 4.11(c) we observe a larger difference in energy shift in compared to Gans theory.

Finally the calculated energy shift of LSPR from p- to s- direction is found to be increasing with aspect ratio (Fig .4.11 (c)). Due to preferential growth along the ripple mainly the length of the particles is changed and the width is almost constant. Therefore the resonance peak wavelength corresponding to p-polarization is more strongly red-shifted compare to s-polarization with increase in particle length. This increases the energy shift with increasing aspect ratio. But again there is a large difference with the values predicted by Gans theory due to the reasons describe above.

So Gans theory is only in qualitative agreement to our results. Due to plasmonic field coupling as mentioned above there are discrepancies. Therefore it can be concluded that self-aligned nanoparticles exhibits plasmonic coupling in both directions. In Fig. 4.11(d) the variation in peak longitudinal wavelength is plotted against aspect ratio and a straight line is fitted to the plot. Usually in literature LSPR peak wavelength is reported with a straight line fit to express the tunability of LSPR with aspects ratio [32, 33]. So for the sake of completeness straight line fitted (Eq. 4.23) in our case is also shown here, which is quite similar as compare to other reported work of similar nature [32, 33]. This straight line fitting actually give the tunability of plasmon resonance with aspect ratio.

$$(\text{Peak Wavelength}) = (60.68)^* (\text{Aspect ratio}) + 349.89 \qquad (4.23)$$

4.2.3 LSPR tunability with ripple periodicity

One of the objective of this work was to show that ripple pattern templates are suitable for plasmonics studies. This point will be validated if we actually capable to show LSPR tunability. In the previous chapter we have shown that with the sputtering parameter ripple of different periodicities can be produced. Using these surfaces with appropriate growth

parameters silver particles of different aspects ratios can be produced along the ripples. These two factors provide a high degree of flexibility to tune the plasmon resonance. Examples of tuning the LSPR using self-aligned nanoparticles on pre-pattern ripple surface are shown in Fig. 4.12(b, c). Aligned particles chains of 20 nm, 30 nm, 35 nm, and 45 nm periodicity, respectively were prepared for this purpose (Fig. 4.12 (a)).

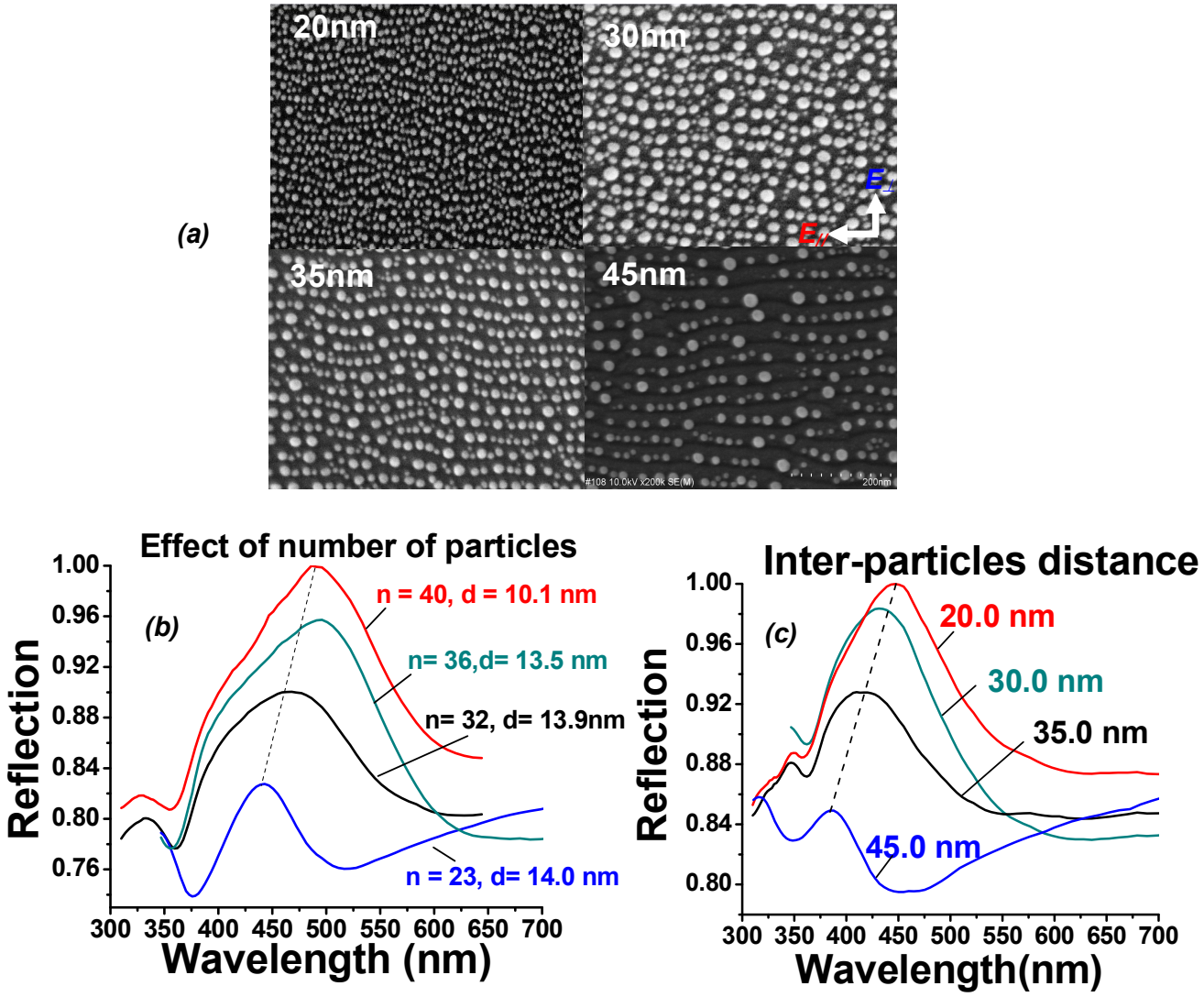

Fig. 4.12: *SPR tunability with ripple periodicity and by varying number of particles with changing annealing temperature. (a)Present the effect of number of particles along the ripples (b) present the effect of interparticle gap.*

In addition, performing the annealing at different temperature and time inter-particles gap can be adjusted. During annealing not only the interparticle gap is changed but the number of particles is also changed. Therefore LSPR along the ripples can also be tune by changing the number of particles. Across the ripples the interparticle gap is mainly determined by the ripple wavelength. In this direction it can be varied only by changing the

ripple periodicity. In Fig. 4.12(a) SEM images of the prepared samples are shown. Based on the statistics of SEM images, the average particles size and the average number of particles along the ripple in a given image were calculated and are written in Fig. 4.12(b, c). The number of particles is changing along the ripples and the interparticle gap across the ripples.

The effect of number of particles on plasmon resonance is shown in Fig. 4.12 (b). With increasing number of particles in the chain the LSPR is shifted to higher wavelength. Near field of particles sitting in a row couple strongly and changes with number of particles [27]. Even though the average particle size is slightly smaller in the case of 20 nm periodic array they show the strongest coupling along the ripples. This is clear evidence showing the effect of number of particles on plasmonic coupling. In the direction perpendicular the ripples interparticle distance is changing with the ripple periodicity. Therefore we observed a blue shift in the LSPR positions in Fig. 4.12(c). Both the effect reported here i.e. number of particles and interparticle gap are important and change the coupling substantially. In this way the LSPR can be tuned with several available parameters.

4.3 Biaxial optical anisotropy in aligned nanoparticles/nanowires

4.3.1 Generalised ellipsometry measurement

Generalised ellipsometry (GE) is a special form of ellipsometry in which the light is polarised at different angles and more information about the sample is collected after reflection compare to single polarisation state used in reflection or transmission measurements. To learn the details about GE, we need to understand the working principle of normal ellipsometry. In ellipsometry p- and s- polarised light are irradiated onto a sample at Brewster angle [15]. At Brewster angle the sensitivity is increased as the difference between the two reflection coefficients of p- and s- polarised light is maximised. The polarisation state of the light is measured after reflection from the sample. Due to difference in electric dipole radiation from p- to s- direction the amplitude of reflection coefficients is also different significantly. After reflection a change in amplitude and phase is observed. Ellipsometry measures two values (Ψ, Δ), that represent amplitude ratio and phase difference before and after reflection between p- and s- polarisation, respectively. For a homogeneous sample refractive index and extinction coefficients can directly be calculated with measured (Ψ, Δ) values by using Fresnelôs equations [19]. (Ψ, Δ) are represented together in the form of a third parameter ρ like this,

$$\rho \equiv \tan(\psi)\exp(i\Delta) \equiv \frac{r_p}{r_s} \equiv \left(\frac{E_{rp}/E_{ip}}{E_{rs}/E_{is}}\right) \tag{4.24}$$

r_p and r_s are the reflection of p- and s- polarised light, respectively. To analyse the measured ellipsometric data generally a physical model is defined for the dielectric function ε. Then (Ψ, Δ) are calculated with the help of the physical model by introducing known bulk dielectric functions as the starting point. Then calculated and measured values of (Ψ, Δ) are compared. A mean-square error (MSE) minimization algorithm is used to get the best fitting between model and measured values. Once the best fit is achieved (MSE < 10 %) other optical parameter like (n, k) or dielectric coefficients can be calculated. For an isotropic sample light reflection of a linearly polarised light can be expressed as :

$$\begin{pmatrix} E_{rp} \\ E_{rs} \end{pmatrix} = S\begin{pmatrix} E_{ip} \\ E_{is} \end{pmatrix} = \begin{bmatrix} r_p & 0 \\ 0 & r_s \end{bmatrix}\begin{pmatrix} E_{ip} \\ E_{is} \end{pmatrix} \tag{4.25(a)}$$

The matrix S is called Jones matrix and for an isotropic sample the off-diagonal elements are zero. However, for optically anisotropic samples part of the incident p-polarised light is converted into s-polarised light and part of the s-polarised light is converted into p-polarised light as shown in Fig. 4.13. Equation (4.25 (a)) can be rewritten as

$$\begin{pmatrix} E_{rp} \\ E_{rs} \end{pmatrix} = \begin{bmatrix} r_{pp} & r_{ps} \\ r_{sp} & r_{ss} \end{bmatrix}\begin{pmatrix} E_{ip} \\ E_{is} \end{pmatrix} \tag{4.25(b)}$$

Here (r_{pp}, r_{ss}) corresponds to r_p and r_s of the isotropic sample and (r_{ps}, r_{sp}) corresponds to converted p- and s- polarised light into s- and p- respectively. Jones matrix for anisotropic sample can be readjusted as shown in eq. (4.26) [18, 19].

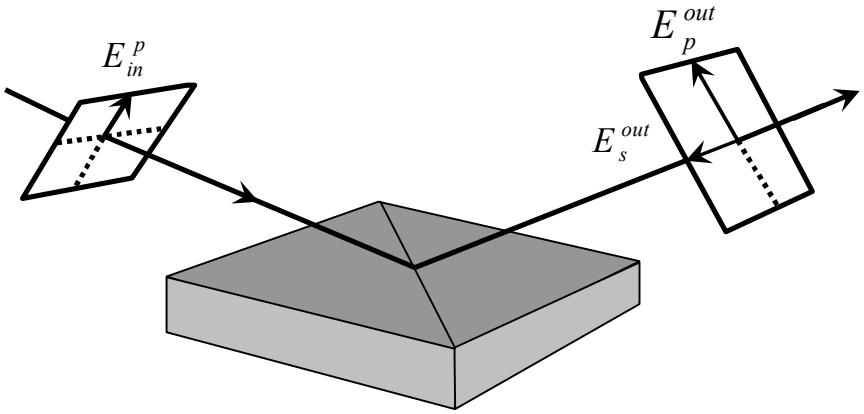

Fig. 4.13: *Schematic of the anisotropic sample, showing the generation of p - and s- polarisation after reflection of a incident p-polarised light.*

$$S_{ani} = \begin{bmatrix} r_{pp} & r_{ps} \\ r_{sp} & r_{ss} \end{bmatrix} = r_{ss} \begin{bmatrix} r_{pp}/r_{ss} & r_{ps}/r_{ss} \\ r_{sp}/r_{ss} & 1 \end{bmatrix} = r_{ss} \begin{bmatrix} \rho_{pp} & \rho_{ps} \\ \rho_{sp} & 1 \end{bmatrix}$$

Where

$$\begin{aligned} \frac{r_{pp}}{r_{ss}} &\equiv \rho_{pp} = \tan\Psi_{pp} \exp(i\Delta_{pp}) \\ \frac{r_{ps}}{r_{ss}} &\equiv \rho_{ps} = \tan\Psi_{ps} \exp(i\Delta_{ps}) \\ \frac{r_{sp}}{r_{ss}} &\equiv \rho_{sp} = \tan\Psi_{sp} \exp(i\Delta_{sp}) \end{aligned} \qquad (4.26)$$

For an anisotropic material the Jones matrix has 6 independent parameters $(\Psi,\Delta)_{pp,ps,sp}$, instead of two parameters for isotropic samples. GE is capable of measuring all Jones matrix elements by rotating and analysing various polarisation states for an anisotropic sample. Extracting dielectric functions from the Jones matrix is much more complicated with the inclusion of more parameters. To overcome this problem Schubert [18, 19] developed a transfer matrix approach known as 4x4 matrix method. Using this approach the dielectric tensor can directly be calculated with the help of a suitable model. A complete description of this method is given in ([19] , Chapter 6), This rigorous mathematical treatment converts the 3x3 dielectric tensor matrix into 2x2 Jones matrix of anisotropic sample. Our commercially available rotating compensator ellipsometer (J. A. Woollam Co. M2000) used in this study measures the polarized reflection states at multiple polarizer settings and uses linear regression analysis to extract the Jones matrix elements.

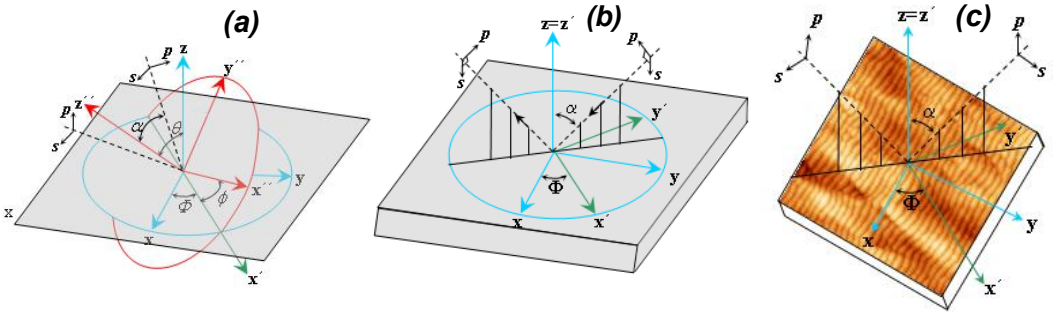

Fig. 4.14: *GE axis rotation with respect to lab coordinates with three Euler angles (Φ,θ,ϕ). Second image is corresponding to (Φ, 0, 0) and third implementing same coordinate system on ripples substrate.*

In GE measurements the sample orientation and the knowledge of various axis is very important. It is assumed that initially the dielectric function tensor is oriented arbitrarily (Fig.

4.14(a)) .The rotation angles of the tensor with respect to lab coordinate system are known as Euler angles (Φ, θ, ϕ). These three angles are considered as the model fit parameters and used to transform random rotation into the lab coordinate system using a transpose matrix [19]. In the reflection measurement we have seen that there is an obvious in plane anisotropy present in our samples. Therefore in our case other two angles (θ, ϕ) are zero, since we could easily observed the anisotropy during in plane rotation (Φ) of the sample . No other anisotropy was observed by the changing angle of incidence. In this case Fig. 4.14(a) becomes like Fig. 4.14(b, c). That means in our sample an azimuthal in plane anisotropy is found. We did not observe any optical anisotropy in rippled Si substrate; All off-diagonal elements of Jones matrix were found to be zero in this case.

4.3.2 Biaxial layer modelling of Jones matrix elements

In the previous section we have already shown that a system of self-aligned nanoparticles is optically anisotropic. Without specifying whether it is biaxial or uniaxial. This information can be concluded only if the dielectric functions of the system are known. For this purpose GE measurement were performed and measured data were modelled using a biaxial layer model. The modelling started with the assumption that the system is bi-axially anisotropic. After proper modelling if the dielectric functions come out to be of the form $\varepsilon_x = \varepsilon_y \neq \varepsilon_z$ then it will be a uniaxial anisotropy or biaxial for $\varepsilon_x \neq \varepsilon_y \neq \varepsilon_z$, respectively.

An example of measured Jones matrix elements is shown in Fig. 4.15(a. b) for the sample shown in Fig. 4.15(c). All the six elements $(\Psi, \Delta)_{pp,\ ps,\ sp}$ are non zero in this case. This measurement was performed for a fixed azimuthal angle, i.e. the light plane of incidence makes 45^o with respect to ripple long axis (Fig. 4.15(c)). For such an anisotropic sample, the sample azimuthal rotation gives different values for $(\Psi, \Delta)_{ps,sp}$. $(\Psi, \Delta)_{ps,sp}$ are generated due to the cross polarization and are highly direction dependent, while $(\Psi, \Delta)_{pp}$ are correspondingly isotropic sample values. The $(\Psi)_{ps,sp}$ shown in Fig. 4.16(a, b) are corresponding to different azimuthal angles. It can be seen that the values of $(\Psi)_{ps,\ sp}$ are highest at 45^o orientation. The reason of this is that the resultant in plane light electric field component from both p- and s-polarised light is maximum at 45^o. At other azimuthal angle it will reduced, for example if the light plane of incident is along the ripple it will excite less plasmon across the ripple and negligible cross polarisation. So the component that excites the plasmon from both directions parallel and perpendicular to the ripple simultaneously can cause the maximum anisotropy.

Therefore, in all the measurements of nanoparticles and nanowires the sample azimuthal orientation was chosen as 45° (Fig. 4.15(c)).

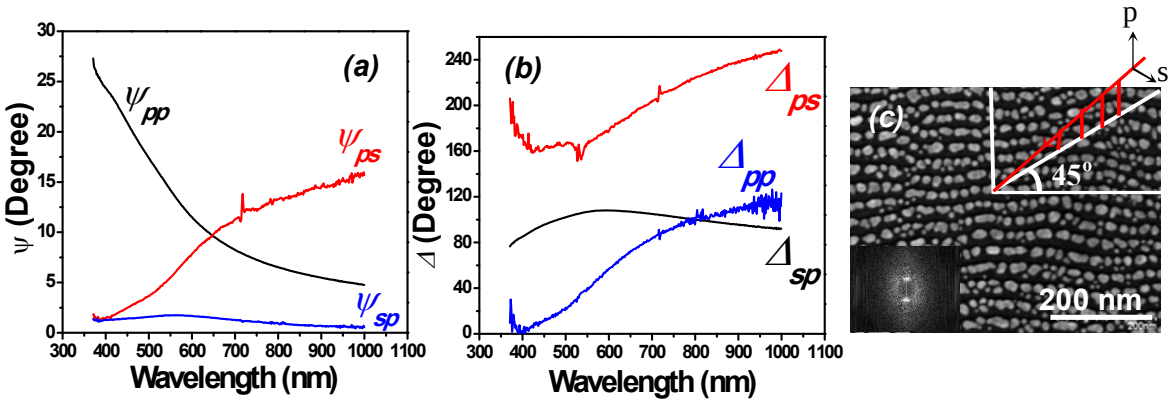

Fig. 4.15: *Jones matrix elements measured using GE in corresponding to the sample orientation shown in SEM image.*

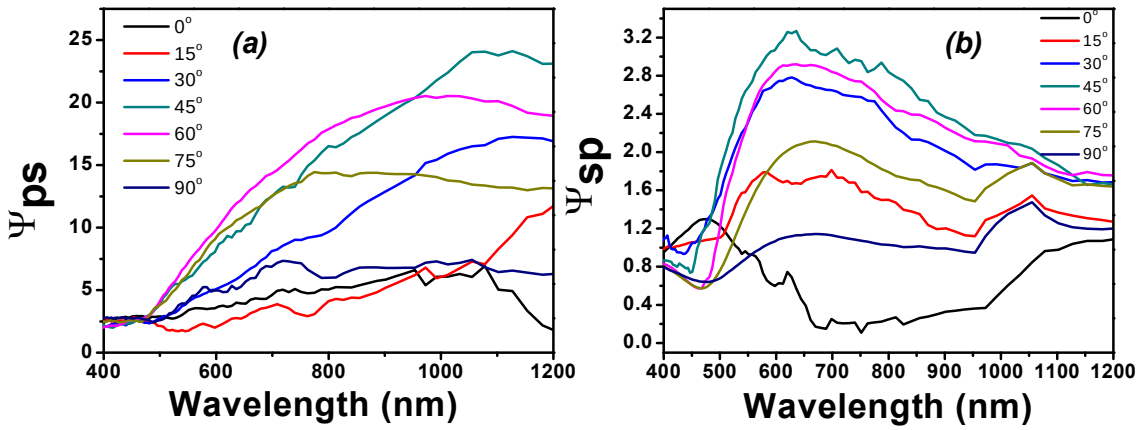

Fig. 4.16: *Variation in $(\Psi)_{ps,sp}$ values at different azimuthal angles.*

In Fig. 4.17 schematic of the used biaxial model is shown. Lorentz model was used for the axes along and perpendicular to the ripples (along x, y axis) and Drude model was used perpendicular to the surface (z-axis). As mentioned in previous section that in metals (Silver in our case) the Fermi level lies within the conduction band and the conduction band is filled with electrons. In the case of silver, however, the d band is located 4 eV below E_F and optical transitions occur from the d band to Fermi level. These excited d electrons are highly localised on atomic sites, accordingly, the bound electron in the d state can be considered as electric dipoles. Therefore, the optically properties of Ag can be accounted considering both free carrier absorption and bound electron. Due to this reason the Lorentz oscillator model [8, 9, 19, 20] is best known to describe the dielectric properties of silver nanoparticles and was used along *x* and *y* and Drude model [1, 19] used for bulk metals along z-direction.

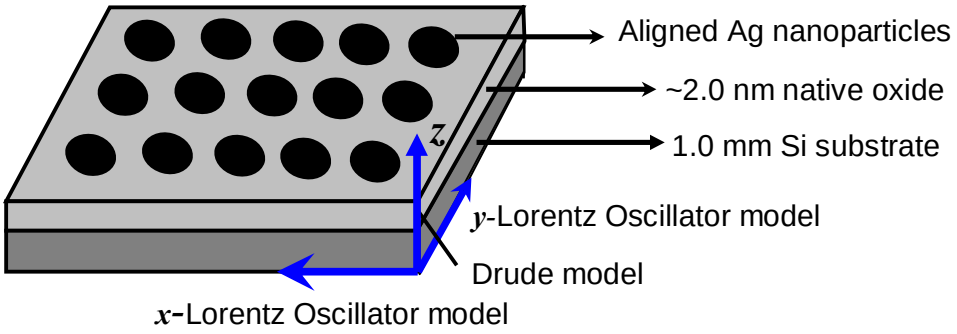

Fig. 4.17: *Schematic of chosen biaxial layer for modelling Jones matrix element with Lorentz oscillator models along x and y direction and Drude for z direction respectively.*

Silver dielectric functions from the literature [30, 31] are used as a basis for the three orthogonal dielectric functions (ε_x, ε_y, ε_z). Inside the biaxial model described above the bulk dielectric functions are modified to fit the measured Jones matrix elements. The Drude component (Eq. 4.27) is characterised by the metal plasma frequency, ω_p, which is proportional to the free electron concentration, and the broadening parameter, Γ, which is dominated by electron scattering from surfaces and crystal defects.

$$\varepsilon_z = \varepsilon_\infty - \frac{\omega_p^2}{\left(\omega^2 + i\Gamma\omega\right)} \tag{4.27}$$

ε_∞ is the interband transition contribution. ε_z (normal to the surface), both ω_p and Γ are set as fitting parameters in the biaxial model along z-direction. For bulk silver $\omega_p = 1.4\text{x}10^{16}$ s^{-1} and $\Gamma = 3.2\text{x}10^{13}$ s^{-1}. ω_p is expected to be below that of bulk silver since in both directions there is a large void content. Γ is expected to increase due to increased surface scattering. For nanoparticles smaller than or equal to the mean free path of the conduction electrons (52 nm for silver) [27], electron-surface scattering is believed to be important as well. An additional term accounting for electron-surface scattering is added that depends on the particle radius and then Γ becomes a function of the particle radius R as follows [1-3] :

$$\Gamma = \Gamma_o + \frac{Av_F}{R} \tag{4.28}$$

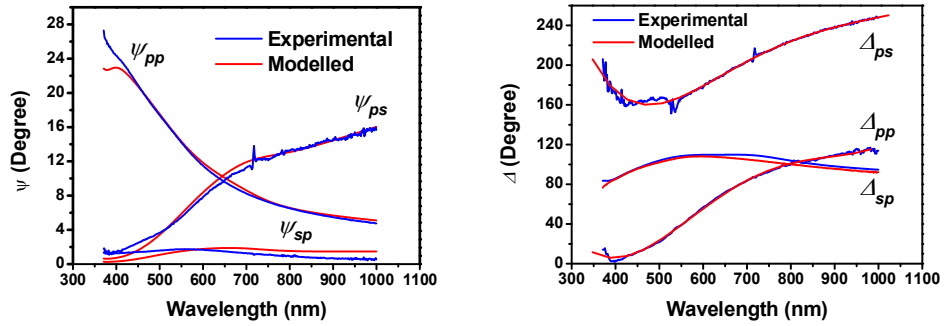

Fig. 4.18: *Modelled Jones matrix elements using biaxial layer model.*

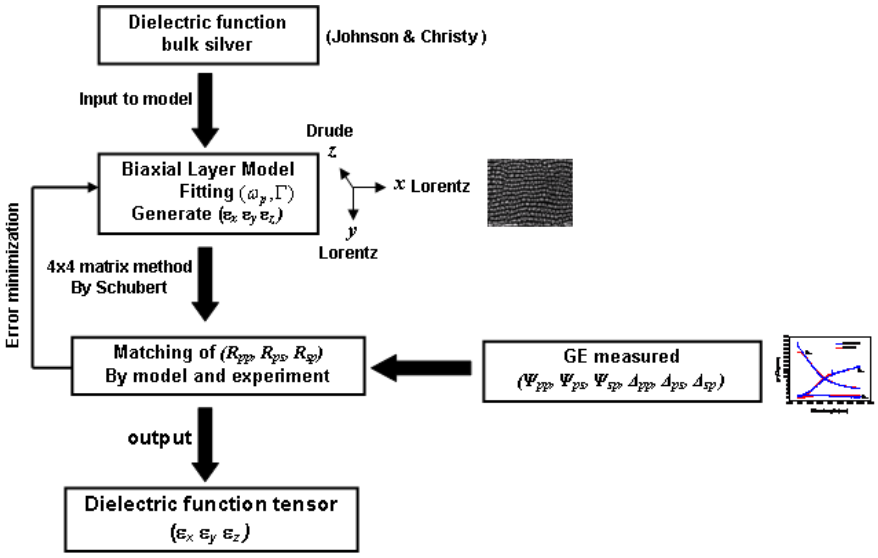

Fig. 4.19: *Flowchart of the complete modelling steps of using a biaxial layer model for extracting dielectric function tensor of the aligned particles.*

where Γ_o is the bulk damping constant. A is a theory-dependent parameter which is dependent on the details of the scattering process (e.g. isotropic or diffuse scattering) and v_F (1.39×10^8 cm.s^{-1}) is the velocity of the electrons at the Fermi energy.

For ε_x and ε_y the Drude component is replaced by a Lorentzian function (Eq. 4.29) in the biaxial layer, which accounts for the LSPR.

$$\varepsilon_{x,y} = \varepsilon_\infty - \frac{\omega_p^2}{\left(\omega_o^2 - \omega^2 - i\Gamma\omega\right)} \tag{4.29}$$

ω_o is the resonance frequency. The model described is constructed using the ellipsometry software WVASE32 in which a mean-square error (MSE) minimization algorithm is used to fit the model parameters to the measured elements of the Jones matrix. Although the model ignores ripple substrate effect or particles tilt on ripple, the results of the fitting (see Fig. 4.18) provide physically meaningful results with low parameter correlation and acceptable MSE

values, which test the reliability of the model. Under best fitted condition the dielectric functions of the material can be extracted from the model. A flowchart describing the modelling steps is shown in Fig. 4.19.

4.3.3 Dielectric functions of nanoparticles array

The dielectric functions extracted from the Jones matrix elements of Fig. 4.18 corresponding to the sample of Fig. 4.15 (c) are shown in Fig. 4.20. Both (ε_1, ε_2) along x and y directions deviate strongly from the bulk silver dielectric function behaviour as shown in Fig. 4.20. Along z axis the dielectric function is resembling the bulk silver behaviour. However, $(\varepsilon_1)_{x,y}$ shows transition from metal to insulator, i.e. $(\varepsilon_1)_y$ becomes positive above 450 nm and $(\varepsilon_1)_x$ above 725 nm. This shows that the insulating behaviour is more prominent along the short axis of the nanoparticle compare to the long axis. $(\varepsilon_2)_{x,y}$ shows a different plasmon resonances around 725 nm and 525 nm, respectively, as observed in reflection measurements as well. *With these results we can conclude that system of self-aligned nanoparticles is biaxially anisotropic, since values of all the extracted dielectric function are different.*

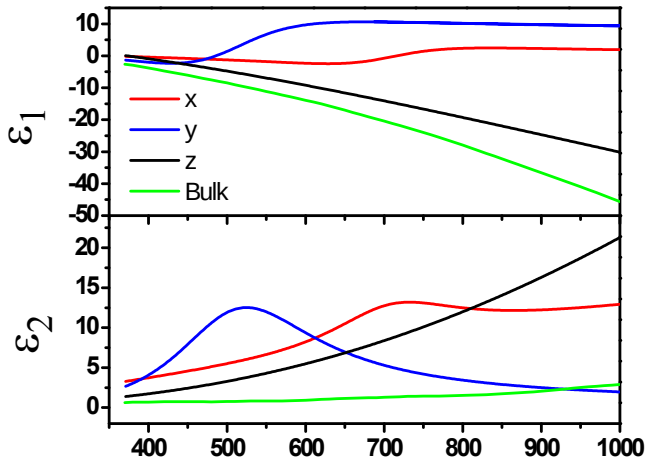

Fig. 4.20: *Dielectric function extracted using biaxial layer model for the sample shown in Fig. 4.15(c).*

4.3.4 Dielectric functions of annealed samples

The same modelling was used for different aligned silver nanoparticles prepared under different experimental conditions. A comparison of the dielectric functions of a sample before and after annealing are shown in Fig. 4.21 along with their SEM images. Before annealing particles are mostly elongated and after annealing they become spherical in shape. This effect

can be seen in $(\varepsilon_2)_x$, along x-axis where a large blue shift is observed after annealing . Since particles long axis shrinks and inter-particle distance increases, the field coupling is reduced and the resonance shifts back to higher energies.

In addition, small nanoparticles vanish during annealing; reducing the number of particles. Therefore, broadening of the plasmon resonance is reduced after annealing indicating a smaller distribution of particles size, also visible in SEM image. Along y-axis the average inter-particle gap decreases. Therefore in $(\varepsilon_2)_y$ the resonance becomes sharper but relatively weak after annealing. $(\varepsilon_1)_x$ exhibits both metallic and insulating behaviour. After annealing however, insulating behaviour is predominant. This indicates that a critical size of the particle may exist below which it behave like insulator [38]. In y-direction the dielectric function is insulating before and after annealing, whereas in z-direction ε_z shows bulk silver like behaviour.

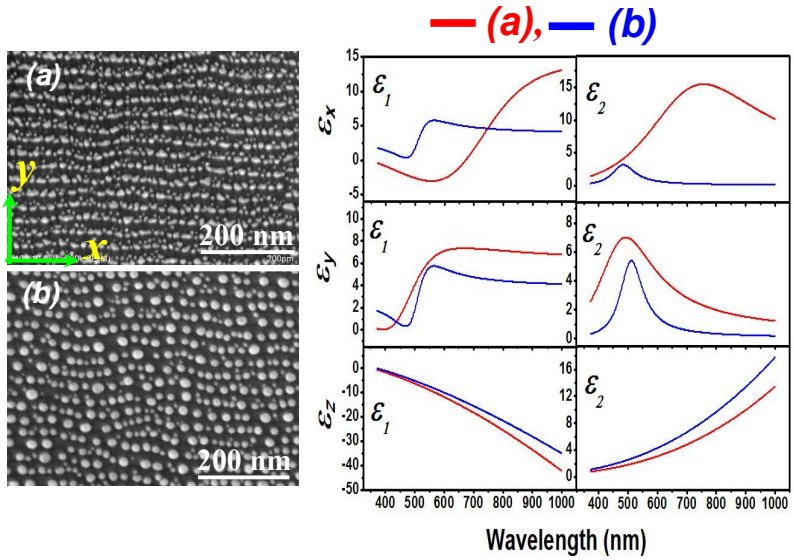

Fig. 4.21: *Dielectric functions before and after annealing, respectively. (a) before annealing and (b) after annealing.*

4.3.5 Measurement of lost of anisotropy

In chapter 3 we had shown that particles arranged in 20 nm periodic array loose periodicity when annealed at sufficiently high temperature. It was also shown that around 200°C particle suddenly change their shape and loose their ordering. This phenomenon can also be observed in reflection and in GE measurements. Initially, when the particles are not annealed a red-shift in LSPR from s- to p- direction is measured. During annealing when the particles shrink a blue shift along the ripple is observed, since the interparticle gap is also increased and aspect

ratio reduces (Fig. 4.22). On the other hand LSPR position is red shifted due to slight increase in aspect ratio perpendicular to ripples. This behaviour is maintained at 103°C and 157°C temperature. But at 207°C when the particles are losing ordering the optical anisotropy is also lost. The blue shift along the ripple is less while red-shift perpendicular to the ripple is large. At a higher temperature the particles takes random places on the rippled surface. Finally, non-ordered particles show no shift in LSPR position in any direction. Similar behaviour is found for one of the element of Jones matrix . ψ_{ps} has a large non zero value at room temperature (Fig. 4.22) and it sustains even upto annealing at 157°C. However, at 207°C this element vanishes. The advantage of this experiment is to produce nanoparticle array of around 20 nm, in-situ measurement can be performed to check that particles are ordered or not.

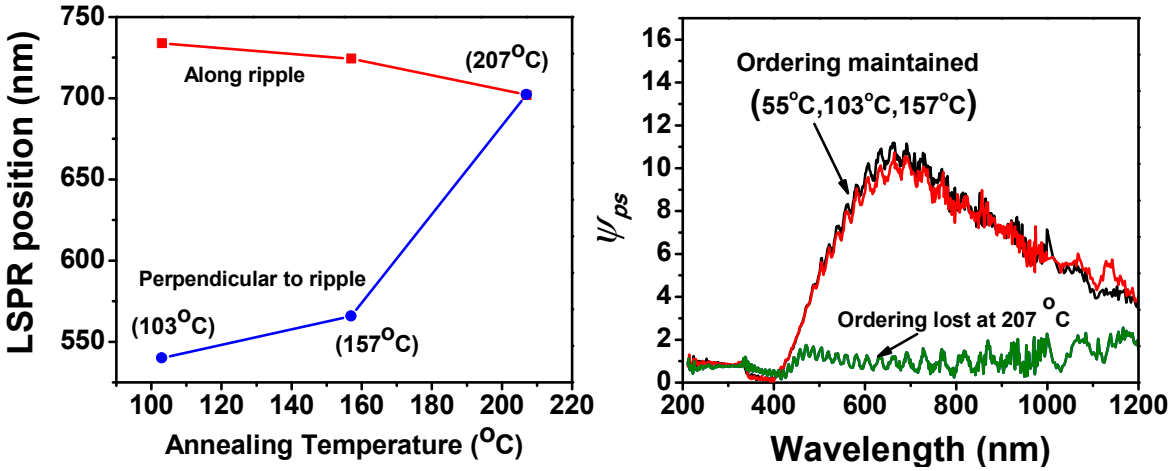

Fig. 4.22: *Change in SPR position during annealing of 20 nm periodic array of nanoparticles at different temperature. Simultaneously one of the Jones matrix element also vanishes once the periodicity is lost.*

4.3.6 Optical property of film growth on heated substrate

In this example film produced on heated substrate exhibits different dielectric properties compare to the one prepared at room temperature. Film prepared at heated substrate (Fig. 4.23(b)) covers more surface than the film prepared at room temperature (Fig. 4.23(a)). It means in the case of sample Fig. 4.23(b), distance between the wires is reduces across the ripple due to enhanced diffusion at heated substrate. Therefore we observe a red-shift in the plasmon resonance in $\varepsilon_2(y)$ (Fig. 4.23) due to more surface coverage [1,7-9], but since film is more flatten on the surface the strength of resonance is less compared to the other film. Also $\varepsilon_1(y)$ is positive in entire region for sample of Fig. 4.23(b). Since at heated substrate mainly

discontinuous wires are formed along the ripple therefore $\varepsilon_1(x)$ is positive in entire measurement range while in other case it is negative showing bulk silver like behaviour. In z-direction, the wires still show bulk silver like behaviour in both cases. Since now a days ellipsometry is also used for in-situ measurements, our developed optical model can be utilized for tuning the dielectric function for the nanoparticles and wire system. Also especially one can judge perfect wire formation along the x-axis during growth if bulk metal behaviour is observed and perpendicular to it LSPR.

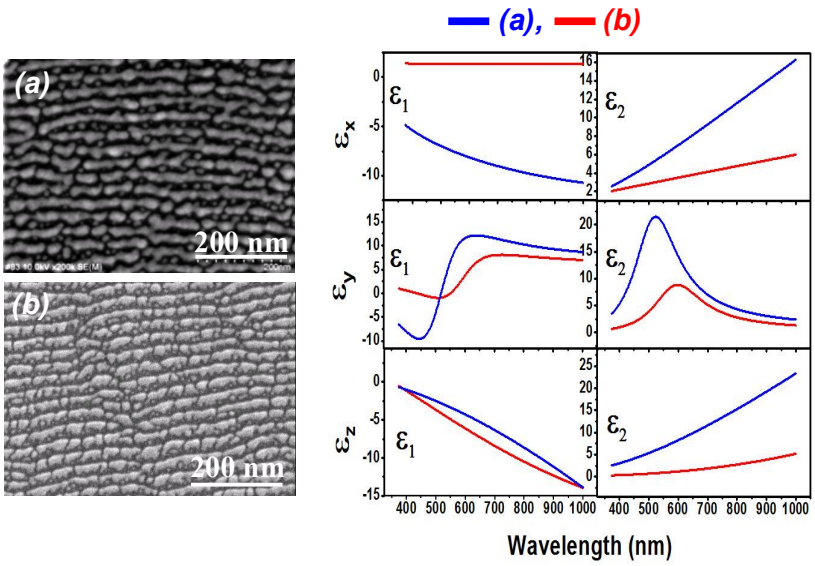

Fig. 4.23: *SEM images (a) and (b) of nanowires grown at room and 450°C temperature, respectively. Corresponding dielectric functions blue colour is corresponding to (a) and red corresponding to (b) are shown in the right side.*

4.3.7 Dielectric functions of different periodicity particles arrays

Dielectric functions for particle arrays of different periodicity with 20, 35, and 45 nm, respectively are shown in Fig. 4.24. $(\varepsilon_1)_{x,y}$ is predominantly positive in entire range showing the insulating nature once again as shown above . In this case the average particle size is around 11 nm for 20 nm ripple periodicity and 14 nm for 35 nm and 45 nm periodicities. The plasmon resonance red shifted when the number of particles increases along the ripple as shown in $(\varepsilon_2)_x$. This reflects the clear trend of effect of number of particles in a row as shown in a simulation work in [27,37] and observed in our reflection measurement. In the case of 20 nm periodicity number of particles is higher compared to other two cases. Therefore a stronger resonance and larger red-shift is observed even though the particle size is relatively

smaller. The only difference is during reflection measurement p- and s-polarized lights incidents along and perpendicular to the ripples at an angle of 15°, but in GE measurement sample is orientated at 45° azimuthally and light incident at an angle of 75° with respect to surface normal. Therefore plasmon resonance positions are different in reflection measurements but the observed trend is similar. Normal to the ripple direction particles are more closely arranged hence the resonant coupling reflected in $(\varepsilon_2)_y$, is also stronger for 20 nm particles. It weakens with increase in ripple periodicity and produces a blue shift. Large distribution in particle size is also visible for the broader resonance in case of 45 nm ripples.

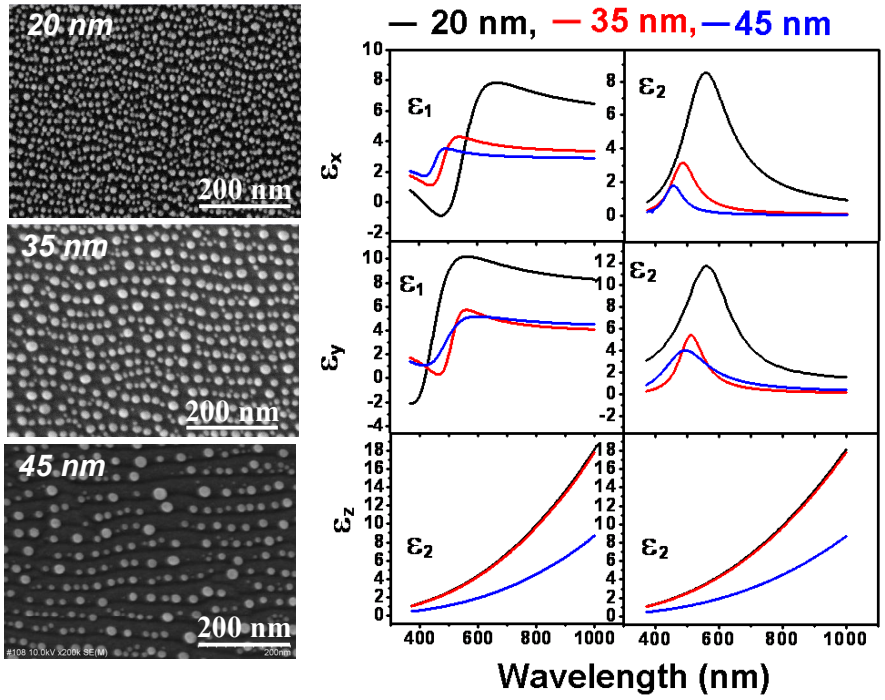

Fig. 4.24: *SEM images of three different arrays of nanoparticles (Left side) with 20 nm, 35 nm, and 45 nm periodicity and their corresponding dielectric functions (right side) are shown.*

4.3.8 Dielectric functions of nanowire array of 35 nm period

Nanowires arrays of different width with the same periodicity as 35 nm have been prepared. Dielectric functions of nanowire array were calculated using model describe before. Most part of this section has been taken from our published work [34]. Along the wire length nanowires are like bulk silver metal but perpendicular to wire length they behave like nanoparticles and exhibit a LSPR. Therefore in the biaxial layer model, Lorentz oscillator is replaced by Drude function along the wire long axis. The model was tested for three nanowire array of fixed

periodicity of 35 nm but of different width 10 nm, 12.5nm and 15 nm, respectively. Measured and modelled Jones matrix elements are shown in Fig. 4.25. In this case as well the model gives a good agreement with measurements.

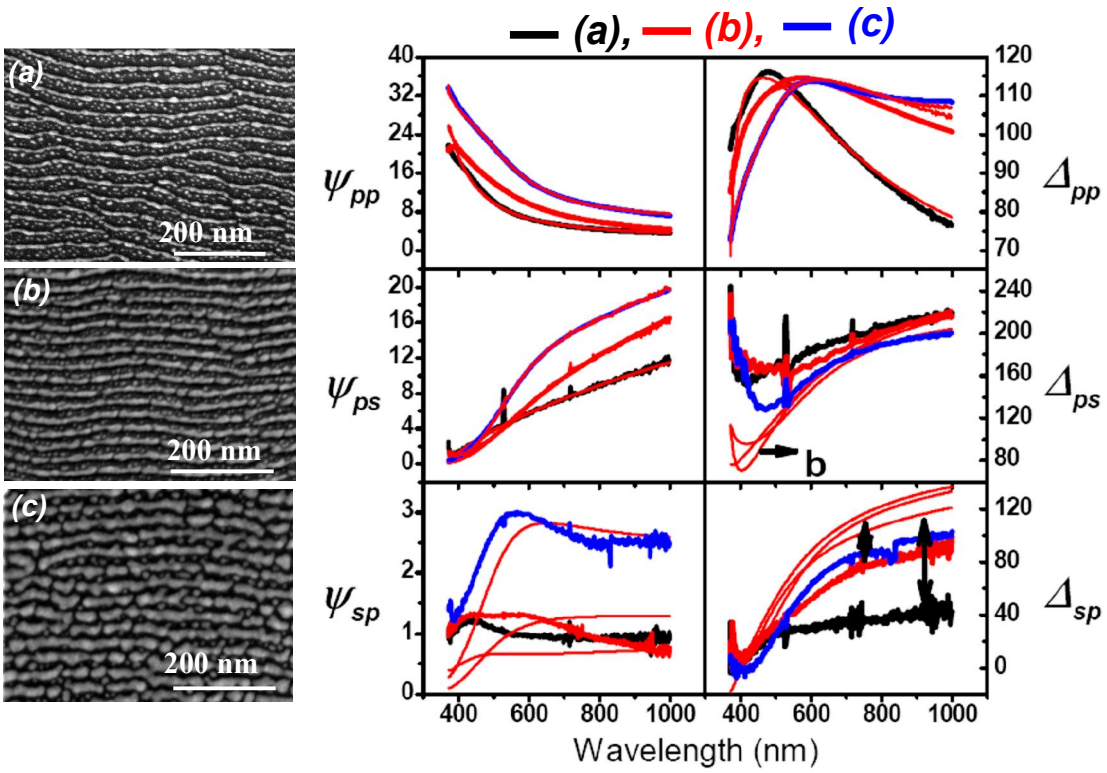

Fig. 4.25: *(a-c) silver nanowires of different width decorating the ridges of the ripple patterns. Measured (thick lines) values of the GE parameters, corresponding to Figs. (a) (black), 1(b) (red) and 1(c) (blue). The thin red lines represent the respective model results.*

The modelled dielectric functions are shown in Fig. 4.26. ε_x and ε_z display predominantly metallic behaviour, although ε_x of sample Fig. 4.26(a) is positive in the UV indicating an insulating nature, while at wavelengths higher than 550 nm it becomes negative. ε_z very close to the dielectric functions of bulk silver. Note the strong resonance in the imaginary parts of ε_y due to the LSPR. The amplitude and wavelength maximum of the resonance increase with increasing wire thickness, both due to the increased proportion of silver in the volume content of the layer [35]. Also the maximum values of the imaginary part of ε_y located at 520 nm are consistently higher than those of the imaginary part of ε_x across the measurement range. This illustrates the strength of the absorption cross section of the LSPR.

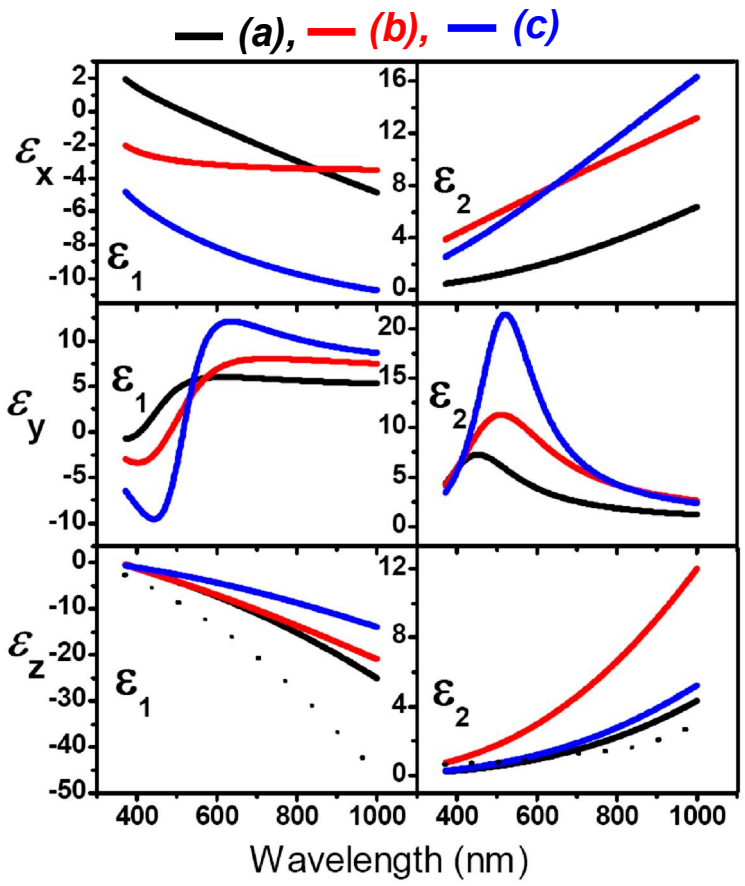

Fig. 4.26: *Biaxial dielectric functions of the nanowire arrays shown in Fig. 4.16((a) black line, (b) red line, (c) blue line) determined by fitting Generalized Ellipsometry measurements .*

Matching of the modelled values with the measured Jones matrix elements demonstrates the validity of the model. However, an additional test was performed to validate the model. Based on the modelled dielectric function the reflection and transmission of the nanowire array can be predicted. In the case of correct modelling predicted values should match with the experimentally measured values. Ellipsometry used for the study was not capable to measure the absolute reflection as presented in previous sections. Therefore to perform the transmission measurement silver wires were grown on SiO_2 rippled substrate. In the transmission measurement electric field component parallel to wire long axis transmitted while perpendicular to it shows LSPR. To simulate these measured transmissions using our model bottom layer was replaced with SiO_2 in the layer stack used in the model. Perfect matching of the both results can be observed in Fig. 4.27(ii).

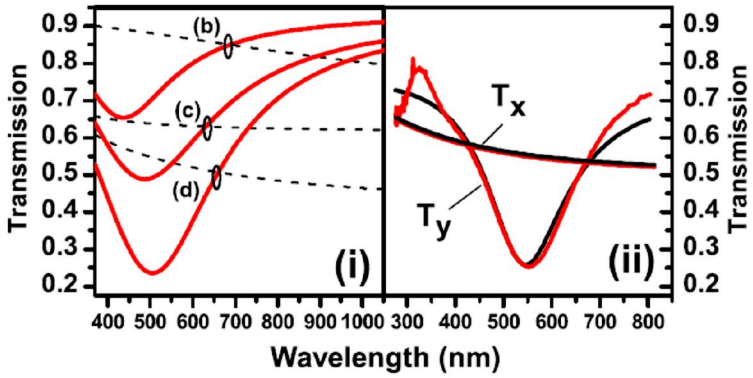

Fig. 4.27: *(i) Simulated transmission spectra using the dielectric functions of three wires shown above on a SiO_2 layer. (ii) Comparison of modelled (black) and measured (red) transmission spectra of silver wires grown on rippled SiO_2 substrate.*

Armed with the biaxial dielectric functions of the layers, we may simulate the expected transmission properties of nanowire arrays produced on transparent substrates. Fig. 4.27(i) shows the simulated transmission of the three arrays shown in Fig. 4.25(a-c) on a 0.1mm thick silicon dioxide substrate. Light is incident normal to the substrate surface, with electric field vectors parallel (dashed black line) and perpendicular (solid red line) to the direction of the wires. The main message from the curves is that for all three samples the extinction ratio is highly wavelength dependent. Transmission of parallel polarization is relatively constant across the range, the difference in magnitude being primarily dependent on the layer thickness of the silver. Light polarized perpendicular to the wires is weakly transmitted in the visible near the LSPR maximum. However in the IR transmission is above 80% for all three materials.

The unusual plasmonic properties of such dense nanowire array lead us to speculate on their application in photovoltaics. A desirable goal in this field is to utilize ultrathin metal films as the transparent conductive electrode (TCE). The materials considered here would function not only as the TCE with transparencies above 80% over most of the measured spectral range (sample a) with bulk silver like dielectric functions (high electrical conductivity), but also as a plasmonic scatterer to improve the light trapping in the absorption layer [36]. By combining the two elements into a single layer, the compactness can be increased.

4.4 Anisotropic SERS in self-assembled nanoparticles

4.4.1 Introduction

Surface enhanced Raman scattering (SERS) has emerged as a highly sensitive technique for molecules detection in recent years [39-41]. Advancement in this field now reached to single molecule detection level [39-41] and has established SERS for molecular sensing [42,43]. Detection of proteins and cancer tissues using SERS are promising applications for medical science [44, 45]. Due to the much lower scattering cross-sections (10^{-30} cm^2) standard Raman spectroscopy was limited to very high concentration of molecules only. Tremendous increase in scattering cross-section (maximum reported upto $10^{-16}cm^2$) makes SERS a superior method for molecular sensing [40, 41]. In SERS process, molecules to be detected are brought in contact with a roughened metal (Ag, Au, Cu etc.) surface [46] or near metal nanoparticles (Fig. 4.28) [47]. SERS phenomenon has been attributed to two possible mechanisms, i.e. electromagnetic (electric field enhancement) and chemical enhancement (charge transfer) [48-50]. According to electromagnetic theory, SERS is the result of double resonant phenomenon: both incident light field and Raman scattered field (Stokes /anti-Stokes) are resonantly enhanced by the surface plasmons [48].This means that metal nanoparticle can scatter light at the Raman shifted wavelength. Therefore the intensity of Raman scattering by molecules close to metal or nanoparticle surface is enhanced by a factor of $\left|E_{local}(\omega_{exc})/E_{incident}(\omega_{exc})\right|^4$ [47, 48, 50]. Here ω_{exc} is the excitation frequency. The enhancement factor of Stokes signal power is reported to be of the order of 10^4-10^{15} under normal to exceptional experimental conditions [39, 46]. Large field enhancement observed in SERS between two metallic particles is a contribution of plasmonic coupling [47, 50-53]. Molecules sitting in between the particles feel much stronger enhanced near field and contribute to larger SERS signal. Therefore such a zone is called as ñhot-junctionò. Recently, it has been predicted theoretically that in a nanoparticles chain or array the field enhancement is even larger compared to two particles. Therefore SERS is expected to be even higher in this case [54-56]. Since SERS intensity linked with near field enhancement, therefore any reason affecting the near field will directly change the SERS signal. The field enhancement decays exponentially with interparticle gap [57-59]. It also depends on the size of nanoparticles [52, 54, 59-61] and the wavelength of incident light [52]. For anisotropic substrate polarisation of light also plays an important role. The electromagnetic field is greatly enhanced if the polarisation is parallel ($E_{//}$) to the long

axis of particle dimmer and reduced for perpendicular polarisation ($E_{\perp}$) [39, 47, 62]. Higher aspect ratio silver nanoparticles are reported to more SERS active then spherical silver particles [63, 64]. SERS intensity also found to be higher with increase in molar concentration of the molecule under investigation and get saturates above certain concentration level [59].

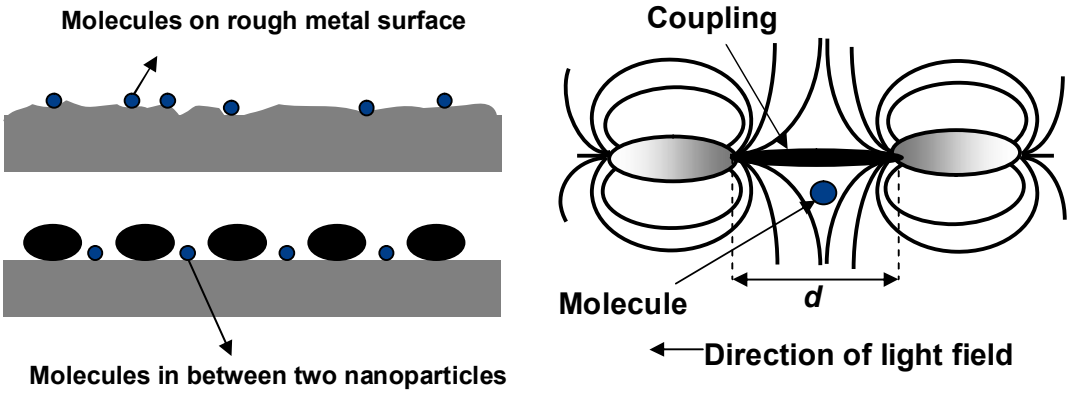

Fig. 4.28: *Representation of two type of SERS phenomenon, molecule lie on rough metal surface or in between two nanoparticles. Right image is the sketch of near field coupling of two nanoparticles and molecule lies in that region.*

In the present study we aimed to investigate the suitability of self-aligned nanoparticles/nanowires as an effective SERS substrate for Rhodamin 6G (R6G) molecule detection. From our experiments, it can been be concluded that hot-junction formation (Electromagnetic effect) is responsible for the large enhancement in SERS. The effect of inter-particle gap on field enhancement is demonstrated. SERS measurements indicate different electromagnetic coupling in the self-aligned nanoparticles and nanowires along and perpendicular to the ripples, respectively. These results are inline with the observed anisotropy in reflection measurement. Comparison of ordered array of nanoparticles and nanowires of 35 nm periodicity with different aspect ratios will also be presented. SERS signal of silver nanowires is also compared with gold nanowires.

4.4.2 Electromagnetic theory of SERS

Although exact theory of the SERS effect is still on debate, but most of the experimental observation could be explained based on the electromagnetic theory. To understand this theory we need to understand the fundamental of Raman scattering of a molecule, later it will be discussed how field of Raman scattered photon is enhanced for a molecule sitting in the

close proximity of the metal nanoparticle. According to quantum mechanical explanation of Raman effect, when an incident photon of energy *hv* collides with a scatterer molecule initially in a stationary state E_1, Total energy E_1+hv remain conserved [65,66]. If the collision is elastic then molecule remain in its initial energy estate and the photon is scattered without change in its energy, giving rise to the Rayleigh scattering at same frequency. The collision however can also be inelastic as well when there is an exchange of energy between the photon and the molecule. Molecule in initial energy range E_1 takes energy and from the photon and goes to a higher energy state E_2 and consequently incident photon is scattered with a smaller energy $hv-\Delta E$, where ($\Delta E= E_2 - E_1$). This gives rise to a Raman line with a frequency less than that of the incident spectral line and called Stokes line (Fig. 4.29). On the other hand, the molecule already in a higher state E_2 and transferred to state E_1 by collision, the scattered photon emerges with increased energy hv + ΔE. This gives rise to a Raman line with a frequency greater than that of incident photon, and known as anti-Stokes line. Stokes and anti-Stokes lines are symmetrically situated on either side of Rayleigh line. Thus Raman-effect probes vibrational levels of the molecule, which depend on the kinds of atom and their bond strengths and arrangements in a specific molecule. Therefore, a Raman spectrum provides a structural fingerprint of a molecule [66].

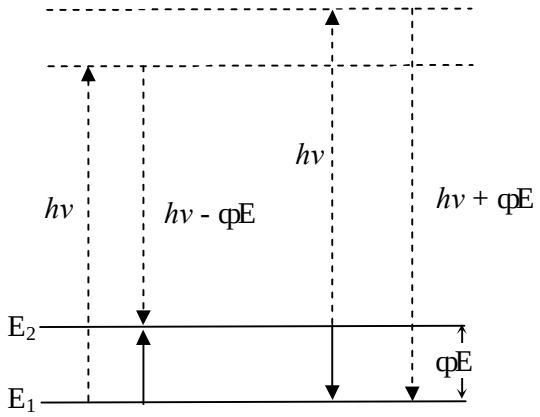

Fig. 4.29: *Quantum mechanical representation of Raman scattering.*

Now such a molecule in contact with a metal nanoparticle is illuminated with laser light in SERS process. As already discussed, a small metal sphere with dimensions smaller than the wavelength of light will sustain oscillating surface plasmon multipoles of various order induced by the time-varying electric field. When the exciting laser light is resonant with the plasmon, the metal particle will radiate light characteristic of dipolar radiation. Light intensity from a certain portion of space surrounding the particle is enhanced. In an analogous

fashion to the laser field, the scattered Stokes or anti-Stokes field will be enhanced if it is in resonance with the surface plasmons of the metal sphere, i.e. the metal particle can scatter light at the *Raman shifted* wavelength.

Conceptual diagram of SERS enhancement is shown in Fig. 4.30. The metallic nanostructure is a small sphere with the complex dielectric function $\varepsilon(\omega)$ in a surrounding medium with a dielectric constant ε_o. The diameter of the sphere $(2r)$ is small compared with the wavelength of light (Rayleigh limit). A molecule in the vicinity of the sphere (distance d) is exposed to a local field E_M, which is the superposition of the incoming field E_o and the field of a dipole E_{sp} induced in the metal sphere. The field enhancement factor $A(\omega)$ is the ratio of the field at the position of the molecule and the incoming field and is given by [48, 66]

$$A(\omega) = \frac{E_M(\omega)}{E_o(\omega)} \sim \frac{\varepsilon - \varepsilon_o}{\varepsilon + 2\varepsilon_o}\left(\frac{r}{r+d}\right)^3 \quad (4.30)$$

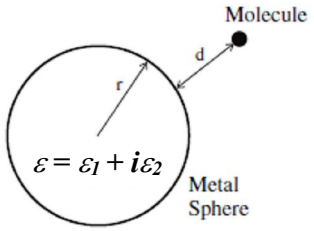

Fig. 4.30 : *Molecule sitting close to nanoparticle in SERS process.*

$A(\omega)$ is particularly strong when the real part of $\varepsilon(\omega)$ is equal to $-2\varepsilon_o$. In a purely classical treatment of electromagnetic theory Kneipp et al. [66] showed that the electromagnetic enhancement factor for the Stokes signal power $G(\omega_S)$ can be written as

$$G_{em}(\omega_S) = \left|A(\omega_L)\right|^2 \left|A(\omega_S)\right|^2 \sim \left|\frac{\varepsilon(\omega_L) - \varepsilon_o}{\varepsilon(\omega_L) + 2\varepsilon_o}\right|^2 \left|\frac{\varepsilon(\omega_S) - \varepsilon_o}{\varepsilon(\omega_S) + 2\varepsilon_o}\right|^2 \left(\frac{r}{r+d}\right)^{12} \quad (4.31)$$

$A(\omega_L)$ and $A(\omega_S)$ express enhancement factors for the laser and for the Raman scattered field, respectively, and ε_L and ε_S are corresponding dielectric functions, r is the radius of nanoparticle and d is the distance of the molecule from the particle surface. eq. 4.31 shows that the enhancement scales as the fourth power of the local field and that is particularly strong when excitation *and* scattered fields are in resonance with the surface plasmons. This is automatically the case for low-frequency Raman modes and explains that the scattering powers of different Raman bands in a spectrum fall off with increasing vibrational energy. Electromagnetic SERS enhancement does not require direct contact between molecule and

metal but it strongly decreases with growing distance described by the decay of the field of a dipole over the distance $[1/d]^3$ to the fourth power, resulting in $[1/d]^{12}$.

Four important points must be noted about SERS:

(1). The major contribution to SERS is scattering by the metal particle rather than by the molecule whose Raman spectrum is, however, reflected in the SERS spectrum of the light scattered by the metal.

(2) Although the SERS intensity (for low-wavenumber Raman modes) varies as the fourth power of the local field, the effect is a linear optical effect that depends on the first power of *Intensity*. However, the fourth power dependence is key to the inordinate enhancements that SERS provides. For silver at 400 nm, for example, field enhancement is only ~30 yet produces a Raman enhancement of $\sim 8 \times 10^5$, assuming the Raman polarizability to be unchanged from that of the isolated molecule.

(3) It is the Raman polarizability of the scatterer that includes the molecule but, when the molecule is adsorbed on the metal particleôs surface, will include contributions from the metal and may, as a result, be greatly altered in its magnitude, symmetry and resonant properties from the Raman polarizability of the isolated molecule. This will be particularly important in systems where metal-to-molecule or molecule-to-metal charge transfer occurs, altering dramatically the resonances of the system and thereby contributing to so-called chemical enhancement.

(4) SERS excitation is a near-field phenomenon. The near-field, especially near a metal surface, will have spatial components that decay more rapidly with distance than the spatial variation in the far-field (where the spatial óstructureô in the field is of the order of the wavelength). Hence, one expects to see (and indeed does see) effects such as relaxation of dipole selection rules, which causes normally forbidden vibrational modes to occur in the SERS spectrum and dipole-forbidden fluorescences to be observed.

4.4.3 SERS dependency on particle size

Surface-enhanced Raman spectroscopy is one of the few phenomena that can truly be described as nanoscience. This is because; the metal particles or metal features responsible for its operation must be small with respect to the wavelength of the exciting light. This normally means that the SERS-active systems must ideally possess structure in the 5ï 100 nm range. Likewise, the dimensions of the active structure cannot be much smaller than some lower bound that is normally larger than the average molecule. The upper dimensional bound of the

SERS-active system is determined by the wavelength. Because features of the order of the wavelength or larger are used, the optical fields no longer excite dipolar plasmons but higher order multipoles. Unlike the dipole, these modes are non-radiative and hence are not efficient in exciting Raman (or other dipole-driven) excitations. Accordingly, the SERS efficiency drops until, for large enough particles, so much of the exciting radiation is locked up in higher order plasmon multipoles that SERS is all but extinguished. Mentioned fact will be shown in experimental results of SERS using nanowires arrays.

At the other end of the dimensional scale, as the nanostructure responsible for SERS becomes too small the effective conductivity of the metal nanoparticles diminishes as a result of electronic scattering processes at the particles surface. In the previous section the dielectric properties of the nanoparticles were described and their insulating nature was demonstrated. As a result, the re-radiated field strength is reduced. With the help of simple electromagnetic theory we can understand this size effect in the SERS signal. The polarizability of a small metal sphere with radius *R* surrounded by a vacuum by combining this expression with the expression for the dielectric function of a Drude metal, slightly modified for interband transitions, is given by [48]

$$\alpha = \frac{R^3(\varepsilon_b\omega^2 - \omega_p^2) + i\omega\Gamma\varepsilon_b}{\left((\varepsilon_b + 3)\omega^2 - \omega_p^2\right) + i\omega\Gamma(\varepsilon_b + 3)} \tag{4.32}$$

where ε_b is the (generally wavelength-dependent) contribution of interband transitions to the dielectric function, ω_p is the metal plasmon resonance whose square is proportional to the electron density in the metal and Γ is the electronic scattering rate, which is inversely proportional to the electronic mean free path and therefore also inversely proportional to the metalôs DC conductivity.

The real and imaginary parts of the expression for α given in equation (4.32) have a pole when the frequency, ω, is equal to $\omega_R = \omega_p / (\varepsilon_b+3)^{1/2}$ .The width of that resonance is given by $\Gamma(\varepsilon_b+3)$. Hence, when Γ is large, either because of the inherent poor conductivity of the metal or due to the fact that the metal nano-features are so small that electronic scattering at the particles surfaces become the dominant electron-scattering process, the quality of the resonance is reduced, and with it the SERS enhancement. Likewise, for metals whose dielectric properties are greatly modified by interband transitions in the wavelength range under consideration, i.e. for which the value of the function ε_b is large, the width of the resonance is increased and the SERS enhancement decreases. This explains why, all things being equal, the SERS enhancement of silver exceeds that of gold, which in turn exceeds that

of copper. This will actually show in our experimental measurements. The participation of interband transitions in the dielectric function of those metals in the visible range of the spectrum increases in that order. Summarizing, for a given metal system the SERS intensity will depend, to first order, on the size of the nanostructure responsible for its enhancement. It will be optimal when this size is small with respect to the wavelength of exciting light as long as that size is not much smaller than the electronic mean free path of the conduction electrons. For the noble metals this optimal range will span ~10ï 100 nm.

4.4.4 Rhodamine 6 G (R6G) properties and sample preparation

R6G dye was used as a probe molecule in order to determine the enhancement in SERS signal. R6G is widely used as a laser dye, tracer dye to trace water flow, in biotechnology for fluorescence microscopy, fluorescence correlation spectroscopy [67,68]. It has remarkably high photo-stability, high quantum yield (0.95), and its lasing range (555-585 nm) close to it absorption maximum (530 nm). Rhodamine 6G usually comes in three different forms. Rhodamine 6G chloride is a bronze/red powder with the chemical formula $C_{27}H_{29}ClN_2O_3$ (Fig. 4.31). An example of fluorescence capability of Rhodamine 6G Chloride is also shown below, powder mixed with methanol, emitting yellow light under green laser illumination (Fig. 4.33). R6G is highly soluble in Methanol (400 g/l), Ethanol (80 g/l) and in water (20 g/l). Length of the longest axis of the molecule is around 1.4 nm and maximum area coverage is around 4 nm^2.

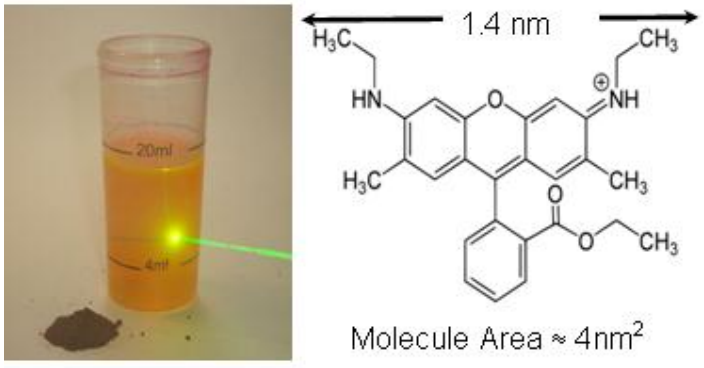

Fig. 4.31: *Fluorescence behaviour and chemical structure of R6G are shown, respectively.*

Since we aimed to observe the effect of aspect ratio, and ordering of the nanoparticles and not the molecular concentration; a fixed concentration of 10^{-6} M R6G (Radiant Dye Laser

Pvt. Ltd.) was used. Already rich literature is available, showing the effect of molecule molar concentrations on SERS signal. Dilute solution as low as 10^{-11} M can be detected using SERS method. Due to the good solubility of R6G in Ethanol, highly pure grade Ethanol solution was used. Ethanol vaporise very fast even at room temperature, therefore the same solution can not be utilise for several days, otherwise the molar concentration of the solution will changed. All the prepared samples were dipped in the solution and taken out just before the measurement and were allowed to dry in atmosphere for a few minutes.

To observe the effect of particles ordering and aspect ratio on SERS intensity fallowing sets of samples were prepared.

(i). Randomly distributed nanoparticles on Si substrate (Fig. 4.34(a))

(ii). Particles array of elongated shapes on ripple pattern Si substrate (Fig. 4.34(b)).

(iii). Self-aligned particles of spherical shapes Fig. 4.35(a).

(iv). Silver nanowire arrays of different width 10 nm and 12.5 nm (Fig. 4.36(a, b)).

(v). Gold nanowires were also prepared to compare them with silver nanowires.

4.4.5 Laser Raman spectrometer

In modern Raman spectrometers (Fig. 4.32), lasers are used as a photon source due to their highly monochromatic nature, and high beam fluxes. This is necessary as the Raman effect is very weak, typically the Stokes lines are ~10^5 times weaker than the Rayleigh scattered component. In the visible spectral range, Raman spectrometers use notch filters to cut out the signal from a very narrow range centred on the frequency corresponding to the laser radiation. Most Raman spectrometers for material characterisation use a microscope to focus the laser beam to a small spot (1-100ε m diameter). Light return from the sample passes back through the microscope optics into the spectrometer. Raman shifted radiation is detected with a CCD detector and a computer is used for data acquisition and curve fitting. These factors have helped Raman spectroscopy to become a very sensitive and accurate technique.

A Micro-Raman spectrometer (HR800 from Horiba Jobin Yvon Ltd.) was used for vibrational mode Raman measurements. A 532 nm laser with 14 mW intensity and probe beam diameter of 2.6 μm (10 x objective lens of N.A 0.25, 100μm slit width) was used in all measurements. Raman spectra were accumulated for 2 seconds in backscattering mode. All spectra were plotted on the same intensity scale in arbitrary units of the CCD detector readout signal.

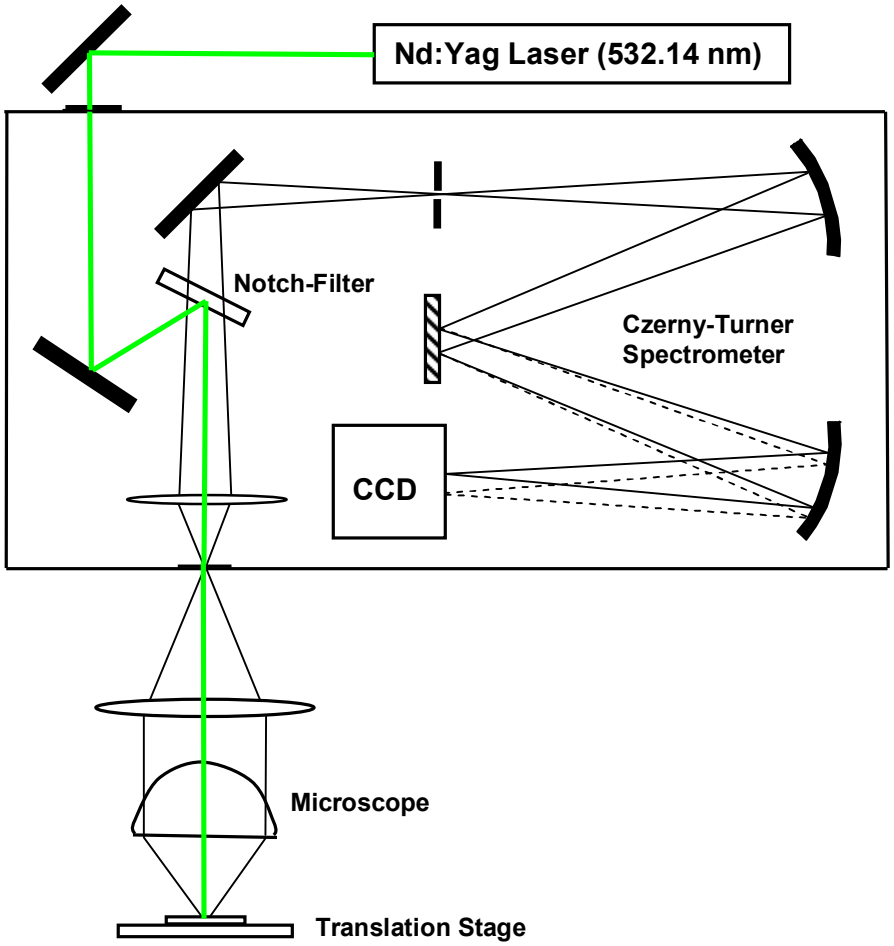

Fig. 4.32: *Schematic diagram of a micro-Raman spectrometer.*

4.4.6 Results and discussion

Fig. 4.33 shows the Raman spectra of rippled Si substrate without R6G solution (black colour) and covered with R6G solution (red colour), respectively. In first case well known Si peak (520 cm^{-1}) can be observed while in second case the fluorescence band of R6G appears together with the Si peak . It is important to note that even though Si ripple top layer is oxidised still we observe Raman spectra like crystalline Silicon not like amorphous Silicon band. In crystalline form Si-Si bonds are symmetrical and result in strong Raman scattering. Crystalline silicon has highly uniform bond angles and bond lengths and exists in a limited number of states. This results in sharp Raman peaks with a characteristic strong band at 520 $cm^{ï 1}$. Amorphous silicon is less ordered with a wider array of bond angles, bond energies, and bond lengths in addition to dangling bonds. The distribution of possible states leads to a broad Raman band centered at 480 $cm^{ï 1}$ that is readily distinguishable from that of crystalline

silicon. But we do not see any such band in our measurement as the amorphize layer is only few nm thick.

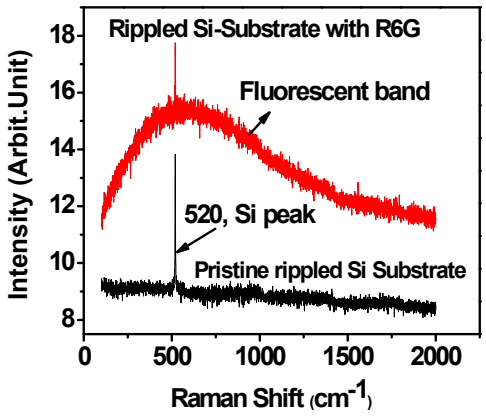

Fig. 4.33: *Raman spectra of pristine Si sample and Si sample with R6G solution. The Si peak at 520 cm^{-1} is observed in both cases. Broad florescence band of R6G appears for the covered sample.*

Following sets of SERS intensities are compared in the discussion below.

(i) SERS intensities of ordered *elongated nanoparticles* are compared with randomly arranged particles, to observed the effect of ordering and inter-particle gap (Fig. 4.34).

(ii) SERS intensities of ordered *spherical nanoparticles* are compared with randomly arranged particles to observe the effect of particle aspect ratio and interparticle gap (Fig. 4.35).

(iii) Comparison of SERS intensities of thin and thick silver nanowires, to confirm field enhancement in between the wires and effect of gap (Fig. 4.36).

(iv) Comparison between silver and gold wires (Fig. 4.37).

Vibrational Raman spectra of R6G molecules corresponding to the randomly distributed nanoparticles (Fig. 4.34(a)) and ordered elongated nanoparticles (Fig. 4.34(b)) are shown in Fig. 4.34(c). Two observations can be make based on this SERS spectra. First, when the electric field of the polarised laser light is parallel to the ripples ($E_{//}$), the obtained Raman signal intensity is higher compared to perpendicular field ($E_{\perp}$). Second, It is even higher than the SERS intensity of the particles deposited on flat Si substrate (non-ordered). Although the average interparticle gap is found to be nearly same (~ 5 nm) for the elongated nanoparticles along the ripples and for the non ordered particles on flat surface, still the enhancement is higher for the ordered elongated particles. This confirms that plasmonic coupling is stronger

for the elongated particles arranged in a chain along the ripple. For the particles arranged in a random fashion (Fig. 4.34(a)), the near field coupling will be different in different directions. Therefore effective field enhancement in the direction of polarised light field will diminish. Chen et al. [62] added a factor of $Cos^2\theta$ in the total enhancement in scattering cross-section to make it become $(E_{local}/E_{incident})^4 Cos^2\theta$. Here θ is the angle of polarised light field with particle long axis.

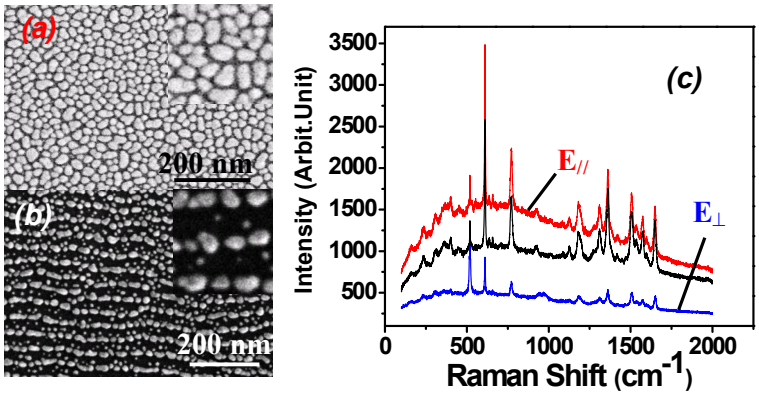

Fig. 4.34: *SEM image of non-ordered (a) and ordered (b) silver nanoparticles. Corresponding SERS spectra is shown in (c). Red and blue are along and perpendicular to the ripple direction of electric field and black corresponds to non-odered particles, respectively.*

Therefore in randomly oriented particles component of electromagnetic enhancement is reduced. The field enhancement depends strongly on interparticle gap and particle longer axis should be parallel to the field of incident light ($\theta \approx 0^o$)[39, 47, 52, 62]. Randomly distributed particles have long axis in different directions henceforth effective field enhancement is lesser. The small zoomed portion (130 x124) nm of Fig. 4.34(a, b) shown in the inset , demonstrate that even though for a given region there are more numbers of hot-spot in (Fig. 4.34(a)) but still the resultant intensity of SERS is lower .

In the perpendicular direction of the ordered elongated particles SERS intensity is reduced (Fig. 4.34(c)). Again the two possibilities arise due to this intensity reduction, particles shape is changing in this direction and also the inter-particles gap is increased from 5 nm to 35 nm. Both these fact support the reduced field coupling in the perpendicular direction. It has been shown experimentally [57] as well as theoretically [52,69] that the plasmon resonance is blue shifted if the incident light electric field move parallel to perpendicular direction with respect to particle long axis. This even more blue shifted with increasing interparticle distance. In a theoretical model it has been shown that coupling is

drastically reduced with inter-particles gap [57-58]. This is the reason we observed a reduced intensity in perpendicular direction. Anisotropy observed in SERS intensity along the ripples to across the ripple also confirms the different plasmonic coupling.

So for the hot-junction formation inter-particle gap is very important. The reflection measurement shown in previous section (Fig. 4.9(c)) also indicates the same behaviour. Plasmon resonance position is blue shifted for light field applied from parallel to perpendicular direction. We already proposed that different electromagnetic coupling along and perpendicular direction of ripples; results in this shift of plasmon resonance position. Coupling gets stronger with increase in aspect ratios of particles and produces a larger red shift in resonance. Randomly distributed particles show no anisotropy as shown in reflection measurement (Fig. 4.9(a)). Reflection results matches very well with the SERS spectra obtained in the present study.

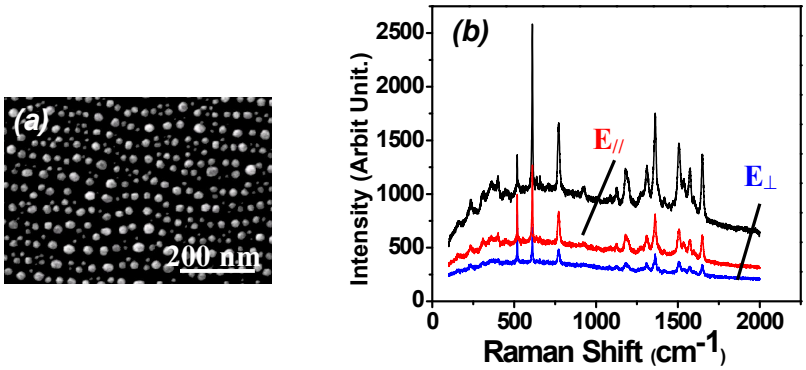

Fig. 4.35: *SEM image of low aspect ratio particle chain and corresponding SERS spectra. Black colour spectra corresponding to non-order nanoparticles shown in Fig. 4.26 (a).*

Fig. 4.35(b) compares the SERS spectra of particles shown in Fig. 4.35(a) and Fig. 4.34(a), respectively. In this case silver particles are roughly spherical in shape with lower aspect ratio. The average inter-particle distance along the ripple direction is also higher now. SERS intensity is found to be less in both parallel and perpendicular direction to the particles chain compared to randomly deposited particles. It is appreciably lower in comparison to the case discussed above. Periodicity of the particles is still the same but interparticle gap along the chain is now increased to ~21 nm and aspect ratio close to one, this results in reduction of field enhancement [51, 52]. Therefore the optimum inter-particle gap and their aspect ratios are important to get the maximum enhancement in signal. Since in this case only the aspect ratio is changed in the perpendicular direction and distance is still the same as 35 nm. SERS in the perpendicular direction is also slightly less compare to the case discussed above, *this*

also support our argument given for Gans theory violation that it is the coupling which is more effective not the size effect.

Nanowires of two different widths (10 nm and 15.5 nm) were also used for SERS and are shown in Fig. 4.36(a, b). A thicker wire gives stronger Raman signal in perpendicular direction and almost no detection along the wire long axis. This example also gives a clear indication that if the wires are closer the field enhancement is stronger due to better dipole coupling. In the parallel direction behaviour is more like bulk silver and intensity is too weak to resolve any peaks of R6G clearly. In both cases of nanowires the SERS intensity is much smaller than for the nanoparticles. This supports the formation of hot-junction in between two particles or wires. Since along the wire length there is no near field coupling (no hot-spot) there is no strong field enhancement. We already reported bulk metal like behaviour in the dielectric properties of nanowire array along the ripple. Therefore SERS study on nanowire array is a good example to observe the difference of SERS intensity on bulk metal (along wire long axis) and due to hot-junction region (in between the wires).

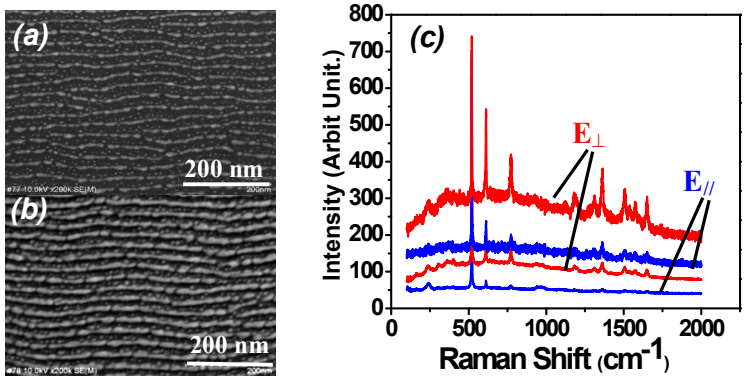

Fig. 4.36: *Nanowires of two different width 10 nm and 15 nm and their SERS spectra. Higher intensity is corresponding to the thicker nanowires.*

Similar measurements were performed for 15 nm width gold nanowires (Fig. 4.37). In this case SERS intensity of the gold nanowire is much lower compare to silver nanowires of the same thickness (Fig. 4.37(c)). It is well known that gold shows poor plasmonic strength compare to silver due to higher interband transition loss [31, 70]. The loss is higher in the visible range around 500 nm. In metals, when a bound electron absorbs an incident photon, the electron can shift from a lower energy level to the Fermi surface or from near the Fermi surface to the next higher empty energy level. Both of these processes result in high loss at optical frequencies. Due to this reason less field enhancement is expected in gold wires compare to silver for the laser light (532 nm) used in our experiment.

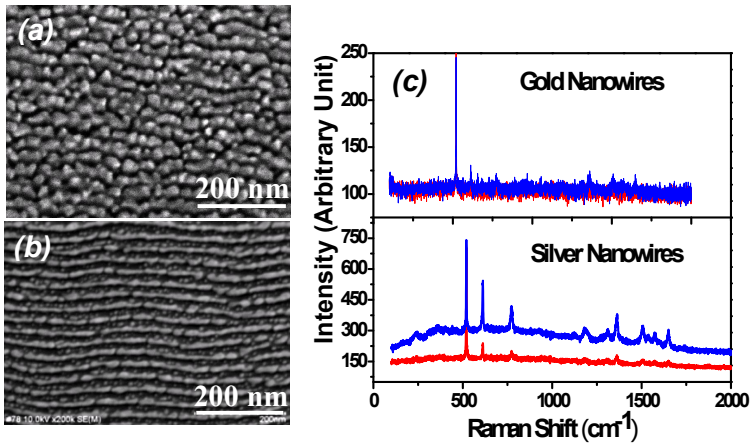

Fig. 4.37: *(a&b) SEM images of gold and silver nanowires,(c) SERS spectra of gold nanowires compared with silver nanowires. Blue colour is across the ripple and red along the ripples.*

Finally (Fig. 4.38) summary of the intensity of the R6G peak at 1509 cm^{-1} collected for all the cases discussed above and some others although theirs SEM images are not shown. Peak intensity is written along with the type of particles and wires. Maximum intensity is found to be for ordered elongated particles with a field parallel to the ripple direction and lowest for thin silver wires. Intensity of fluorescence band is also higher along the ripple for nanoparticles and perpendicular to ripples for the nanowires system, also a clear evidence of near field coupling of self-aligned nanoparticles and nanowires.

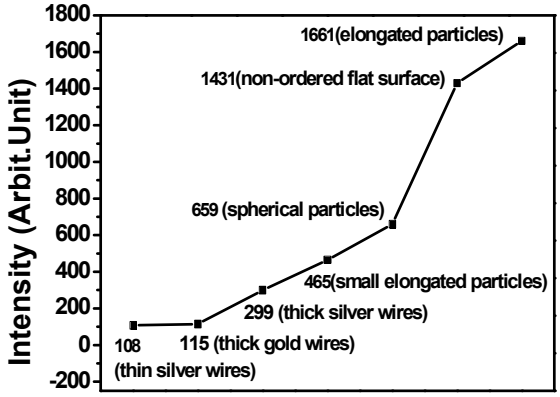

Fig. 4.38: *SERS intensities of R6G molecule for different type of sample corresponding to the peak at 610 cm^{-1}. SERS intensity is mentioned near to the type of sample.*

4.4.7 SERS enhancement factor calculation

The enhancement factor (E_f) for R6G was also calculated only for the elongated particles. Enhancement factor can be calculated using fallowing equation [47, 71, 72].

$$E_f = [I_{SERS}/I_{Raman}] \times [C_{bulk}/C_{adsorbed}] \quad (4.33)$$

I_{SERS}, I_{Raman} are Raman spectra intensities collected with (R6G + Silver nanoparticles) and without nanoparticles (only R6G), respectively. C_{bulk} and $C_{adsorbed}$ are concentrations of R6G molecule in the laser spot area and in the region of hot-junctions (between two particles), respectively. It is evident from this equation that E_f depends on molecule concentration. Various enhancement factors reported in literature should be compared at the same concentration level and laser wavelength. The methodology commonly assumed in the calculation of the enhancement factor is that one mono-layer of molecule is present at the surface and 100 % adsorption by molecules [72, 73]. Otherwise the value of $C_{adsorbed}$ will be reduced and E_f will be even higher. We have also adopted the same methodology. Using the equation

$$N_{bulk}=\pi r^2 hcN_A \quad (4.34)$$

r: radius of laser *spot, h:* Focal depth of objective, *c:* molar concentration, N_A*:* Avogadroôs number [47,75]. Number of molecules in bulk comes out to be 2 x10^6 in 10^{-6} M concentrated R6G solution for a 2.5 μm laser spot (Calculated using Rayleigh criteria with a cone angle 14^o [74]). Long axis length of R6G is 1.4 nm, in closely packed form one molecule of R6G will occupy maximum of 4 nm^2 surface area [73]. The average inter-particle gap of elongated particle is ~5 nm and their width is around ~12 nm calculated by analysing SEM images. Assuming only one sheet of molecule covered in the hot-junction region (Fig. 4.39). Average total number of molecule per hot junction would be ~15. The enhancement factor corresponding R6G peak at 610 cm^{-1} comes out to be 3.7 x10^8 for the sample (Fig. 4.34(b)) which is comparable of the work of similar nature [72]. They have reported particle chain grown on Si nano tips. Also when compared this value of non-ordered particles and to the bulk silver [72] it is one and two order of magnitude higher respectively.

We have demonstrated that self-aligned nanoparticles can be used as active SERS substrates. Hot-junctions do exists and are responsible for large enhancement in SERS signal. In a single sample the effect of the nanoparticle distance in the electric field enhancement can

be observed. The SERS signal also validates the anisotropic nature of ordered particles sitting on rippled substrate and support the reflection measurements. Enhancement is found to be more for the equally distant particles sitting in a chain compare to randomly distributed particles. Our SERS measurements confirm theoretical prediction that below 10 nm inter-particle distance enhancement is large. In elongated particle chains the enhancement factor is found to be of the order of 10^8 much higher compare to bulk silver.

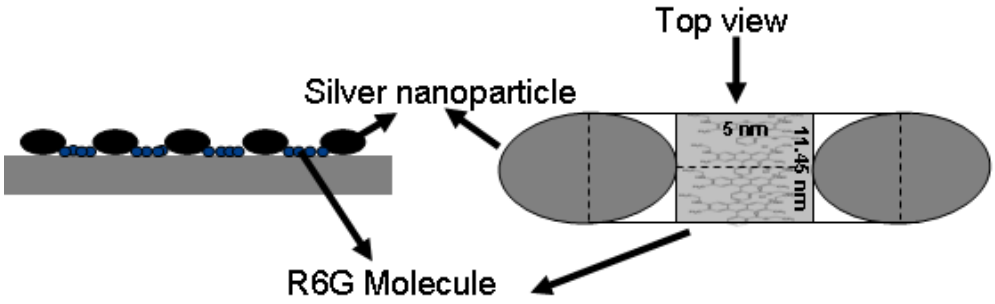

Fig. 4.39: *R6G molecules sitting in between the nanoparticles side view and the top view as assumed in the calculation of enhancement factor.*

References

[1] U. Kreibig, M.Vollmer, *Optical properties of metal clusters* (*Springer* series in material science*)*(**1993**).

[2] S. A. Maier, *Plasmonics: Fundamental and applications* (Springer) (**2007**).

[3] S. Link, M. A. El-sayed, *Int. Review Physi. Chem*. 19 (**2000**) 409.

[4] U. Kreibig, B. Schmitz, H. D. Breuer, *Phys. Rev. B* 36 (**1987**) 5027.

[5] A. Hilger, M. Teneflde, U. Kreibig, *Appl.Phys.B.*73 (**2001**) 361.

[6] B. K. Russell, J. G. Mantovani, V. E. Anderson, R. J. Warmack, T. L. Ferrell, *Phys. Rev. B* 35 (**1987**) 2151.

[7] R. K. Roy, S. K. Mandal, D. Bhattacharya, A. K. Pal, *Eur. Phys. J.* B 34 (**2003**) 25.

[8] T. W. H. Oates, A. Mücklich, *Nanotechnology* 16 (**2005**) 2606.

[9] T. W. H. Oates, *Appl. Phys. Lett.* 88 (**2006**) 213115.

[10] H. Wormeester, E. S. Kooij, *Thin Solid Films* 455 (**2004**) 323.

[11] D. D. Evanoff, G. Chumanov, *Chem. Phys. Chem.* 6 (**2005**) 1221.

[12] J. J. Mock, M. Barbic, D. R. Smith, D. A. Schultz, S. Schultz*, J. Chem. Phys.* 116 (**2002**) 6755.

[13] E. Hutter, J. H. Fendler, *Adv. Mater.* 16 (**2004**) 1685.

[14] H. Wormeester, E. S. Kooij, *J. Chem. Phys.* 124 (**2006**) 204713.

[15] R. Gupta, M. J. Dyer, W. A. Weimer, *J. Appl. Phys.* 92 (**2002**) 5264.

[16] T. W. H. Oates, A. Keller, S. Facsko, A. Mücklich, *Plasmonics* 2 (**2007**) 47.

[17] A. Toma, D. Chiappe, D. Massabo, C. Boragno, F. B. Mongeot, *Appl. Phys. Lett*. 93 (**2008**) 163104.

[18] M. Schubert, *Phys Rev B* 53 (**1996**) 4265.

[19] H. Fujiwara, *Spectroscopic Ellipsometry principles and applications* (John Wiley and sons ltd, England) (**2007**).

[20] Z. Wang, X. Cai, Q. Chen, L. Li, *Vacuum* 80 (**2006**) 438.

[21] J. R. Krenn, G. Schider, W. Rechberger, B. Lamprecht, A. Leitner, F. R. Aussenegg, *Appl. Phys. Lett*. 77 (**2002**) 3379.

[22] A. Taleb, C. Petit, M. P. Pileni**,** *J. Phys. Chem. B* 102 (**1998)** 2214.

[23] T. W. H. Oates, A. Keller, S. Facsko, A. Mücklich, *Plasmonics* 2 (**2007**) 47.

[24] A. Toma, D. Chiappe, D. Massabo, C. Boragno, F. B. Mongeot, *Appl. Phys. Lett*. 93 (**2008**) 163104.

[25] K.-H. Su, Q.-H. Wei, X. Zhang, J. J. Mock, D. R. Smith, S. Schultz, *Nano Lett.* 3

(**2003**) 1087.

[26] P. K. Jain, W. Huang, M. A. El-Sayed, *Nano Letters* 7 (**2007**) 2080.

[27] R. Chern, X. Liu, C. Chang, *Phys. Rev E* 76 (**2007**) 016609.

[28] R. L. Zong, J.Zhou, Q. Li, B. Du, B. Li, M. Fu, X. W. Qi, L. T. Li, S.Buddhudu, *J. Phys. Chem. B* 108 (**2004**) 16713.

[29] A. Azarian, A. I. Zad, A. Dolati, M. Ghorbani, *Nanotechnology* 19 (**2008**) 415705.

[30] T. M. Hsu, C. C. Chang, Y.F. Hwang, *Chinese J. of Phys.* 21 (**1983**) 26.

[31] P. B. Johnson, R.W. Christy, *Phys. Rev. B* 6 (**1972**) 4370.

[32] A. Brioude, X. C. Jiang, M. Pileni, *J. Phys. Chem. B* 109 (**2005**) 13138.

[33] B. Yan, Y. Yang, Y. Wang, *J. Phys. Chem. B* 107 (**2003**) 9159.

[34] M. Ranjan, T. W. H. Oates, S. Facsko, W. Möller, *Optics Letter* 35 (**2010**) 2576.

[35] R. Doremus, *Thin Solid Films* 326 (**1998**) 205.

[36] V. E. Ferry, L. A. Sweatlock, D. Pacifici, H. A. Atwater, *Nano Letters* **8** (**2008**) 4391.

[37] D. D. Evanoff Jr., G. Chumanov, *Chem. Phys. Chem.* 6 (**2005**) 1221.

[38] S. Henrichs, C. P. Collier, R. J. Saykally,Y. R. Shen, J. R. Heath, *J. Am. Chem. Soc.*122 (**2000**) 4077.

[39] S. Nie, S.R. Emory, *Science*, 275 (**1997**) 1102.

[40] K. Kneipp, Y. Wang, H. Kneipp, L.T. Perelman, I. Itzkan, R.R. Dasari, M.S. Feld, *Phys. Rev. Lett.* 78 (**1997**) 1667.

[41] K. Kneipp, H. Kneipp, R. Manoharan, I. Itzkan, R. R. Dasari, M. S. Feld, *Bioimagin*g. 6 (**1998**) 104.

[42] P. R. Stoddart, D. J. White, *Anal. Bioanal. Chem.*, 394 (**2009**) 1761.

[43] D. L. Stokes, T. V. Dinh, *Sensors and Actuators B* 69 (**2000**) 28.

[44] X. X. Han, B. Zhao ,Y.Ozaki, *Anal. Bioanal. Chem.* 394 (**2009**) 1719.

[45] T.V.Dinh, L.R. Allain, D.L.Stokes, *J. Raman Spectrosc.* 33 (**2002**) 511.

[46] D. L. Jeanmaire, R. P. Vanduyne, *J. Electroanal. Chem.*, 84 (**1977**) 1.

[47] K. D. Alexander, M. J. Hampton, S. Zhang, A. Dhaw-an, H. Xuc, R. Lopeza, *J. Raman Spectrosc.* 40 (**2009**) 2171.

[48] M. Moskovits**,** *J. Raman Spectrosc.* 36 (**2005**) 485.

[49] A. Otto, *J. Raman Spectrosc.* 22 (**1991)** 743.

[50] F. J. Garcē a-Vidal, J. B. Pendry, *Phys. Rev. Lett.*77 (**1996**) 1663.

[51] J. Jiang, K. Bosnick, M. Maillard, L. Brus, *J. Phys. Chem. B*, 107 (**2003**) 9964.

[52] E. Hao, G. C. Schatz, *J. Chem. Phys.* 375 (**2004**) 120.

[53] F. Song, T. Wang, X. Wang, C. Xu, L. He, J. Wan, C.V.Haesendonck, S.P. Ringer,

[54] M. Han, Z. Liu, G. Wang, *Small*, 6(3) (**2010**) 446.

[55] R. L. Chern, X. X. Liu, C. C. Chang, *Phys. Rev. E* 76 (**2007**) 016609.

[56] S. Enoch, R. Quidant, G. Badenes, *Optics Express* 12 (15) (**2004**) 3422.

[57] Z. B. Wang, B. S. Lukôyanchuk, W. Guo, S. P. Edwardson, D. J. Whitehead, L. Li, Z. Liu, K. G. Watkins, *J. Chem. Phys* 128 (**2008**) 094705.

[58] K. -H. Su, Q. -H. Wei, X. Zhang, *Nano Lett.* 3 (**2003**) 1087.

[59] P. K. Jain, W. Huang, M. A. El-Sayed, *Nano Lett*. 7 (**2007**) 2080.

[60] H. H. Wang, C. Y. Liu, S. B. Wu, N. W. Liu, C. Y. Peng, T. H. Chan, C. F. Hsu, J. K. Wang, Y. L.Wang*, Adv. Mater.*, 18 (**2006**) 491.

[61] A. Brioude, X. C. Jiang, M. P. Pileni, *J. Phys. Chem. B.* 109 (**2005**) 13138.

[62] E. S. Kooij, B. Poelsema, *Phys. Chem. Chem. Phys.* 8 (**2006**) 3349.

[63] J. Chen, T. M. Artensson, K. A. Dick, K. Deppert, H. Q. Xu, L. Samuelson, H. Xu, *Nanotechnology*. 19 (**2008**) 275712.

[64] Y. Yang, L. Xiong, J. Shi, M. Nogami, *Nanotechnology*, 17 (**2006**) 2670.

[65] M. Suzuki, Y. Niidome, N. Terasaki, K. Inoue, Y. Kuwahara, S. Yamada, *Jpn. J. Appl. Phys.* 43 (**2004)** 554.

[66] R. Kumar, *Atomic and Molecular Spectra* (Kedar Nath Ram Nath Publisher) (**1997**).

[67] K. Kneipp, H. Kneipp, I. Itzkan, R. R. Dasari, M. S .Feld, *J. Phys.: Condens. Matter* 14 (**2002**) R597.

[68] http://en.wikipedia.org/wiki/Rhodamine_6G

[69] http://omlc.ogi.edu/spectra/PhotochemCAD/html/rhodamine6G.html

[70] Brioude, X. C. Jiang, M. P. Pileni, *J. Phys. Chem. B.* 109 (**2005)** 13138.

[71] R. P. West, S. Ishii1, G. Naik, N. Emani, A. Boltasseva, *arxiv.org /pdf / 0911.2737.*

[72] A. Tao, F. Kim, C. Hess, J. Goldberger, R. He, Y. Sun, Y. Xia, P. Yang**,** *Nano Lett.* 3 (**2003**) 1229.

[73] S. Chattopadhyay, H. C. Lo, C. H. Hsu, L. C. Chen, K. H. Chen, *Chem. Mater.*17. (**2005**) 553.

[74] A. Kudelski, *Chem. Phys. Lett.* 414 (**2005)** 271.

[75] M. J. Pelletier, *Analytical application of Raman spectroscopy* (Blackwell science Limited) (**1999**).

[76] Z. Q. Tian, B. Ren, D. Y. Wu, *J. Phys. Chem. B* 106 (**2002**) 9463.

Chapter-5

Cobalt Nanoparticles Self-assembly and Properties

5.1 Introduction

The field of nanotechnology is very broad and has shown its importance in different areas, but it is most successfully employed in the field of magnetism. Size of the magnetic memories is getting down day by day while the recording bits are improving drastically [1]. In fact; the rapidly growing importance of electronic data processing was accompanied by a growing demand for bigger throughput mass storage media. Mooreôs law concerning the increase of CPU frequencies can be directly transferred to mass storage media, where an increase of storage density follows a similar empirical law. Hard disks with a capacity of more than 1 TB are already available. Hence development of new approaches and study of nanosize magnetic particles has of great importance. In particular, nanoparticles of magnetic materials have attracted considerable and increasing attention due to their potential applications in very demanding fields. Except for magnetic storage technology [2] usage of magnetic nanoparticles is possible also in drug targeting [3], refrigeration [4], printing [5] and spin-valve technology [6].

From a technological viewpoint magnetic anisotropy is one of the most important property of magnetic materials [7,8]. Depending on the application, materials with high, medium or low magnetic anisotropy will be required, for respective applications such as permanent magnets, storage media or magnetic cores in transformers and magnetic

recording heads[1,8]. The physical origin of magnetic anisotropy and its strength in ultrathin magnetic films or magnetic nanodots can be quite different from that in the bulk. This makes it possible to tune the magnetic anisotropy by using different substrates, deposition materials, and different growth conditions. The substrate symmetry, film thickness, and surface morphology, for example, influences the magnetic anisotropy.

Liedke et al. [9] demonstrated uniaxial magnetic anisotropy generated by the growth of a continuous film of $Ni_{81}Fe_{19}$ on ripple patterned substrates. Due to the film morphology a strong uniaxial anisotropy is induced in the polycrystalline $Ni_{81}Fe_{19}$ layer, which is fixed in its orientation. Oates et al. [10] demonstrated the growth of ordered cobalt nanowires on rippled substrates using a magnetron sputtering approach. F Buatier de Mongeot et al. [11, 12] produced cobalt rippled pattern using ion beam sputtering and also reported uniaxial magnetic anisotropy in such patterns. Until today, growth of magnetic nanoparticles on pre-patterned rippled surfaces and their magnetic properties is not reported. Therefore in this thesis, we also aimed to use the same approach (used for silver) to apply for cobalt nanoparticles self-assembly on pre-patterned Si substrates. Like tuning of LSPR is demonstrated using silver nanoparticles of different aspect ratios, similar tuning of magnetic anisotropy can be explored for ordered cobalt particles to nanowires. We will show that this approach is also capable for cobalt particles self-assembly, and pronounce uniaxial magnetic anisotropy was observed for ordered cobalt nanoparticles as confirmed by MOKE, and SQUID measurement.

5.2 Experimental approach and results

For this study as well e-beam evaporation was used for cobalt nanoparticles growth. Due to the higher melting point (1495^{o}C) it was hard to evaporate cobalt with the parameters optimised for silver. A special crucible with an Al_2O_3 core inside Mo was used to avoid any alloy formation (Fig. 2.8(d)). Growth of cobalt on Si (100)/SiO_2 also follows Volmer-Weber growth mode like silver. The crystal structure of cobalt is found to be fcc for the film grown at room temperature and upto a temperature of 350^{o}C. Film growth above this temperature shows hcp crystal structure [13, 14]. Diffusion of cobalt is also reported to be much lower in the temperature range 300-500^{o}C [13].

A cobalt film of around 5 nm grown on flat Si (100) substrate at room temperature is shown in Fig. 5.1(a). The film consists of small clusters, however their size is much smaller and dansly packed then silver films. It is almost like a closed film. When cobalt is deposited

at the same growth parameters on rippled surfaces no cluster ordering is observed. Growing at a higher substrate temperature of 500^{o}C, cluster size increases due to higher diffusion or temperature enhanced coalescence of clusters. In this case the film consists of big and separate clusters as shown in Fig. 5.1(b)).

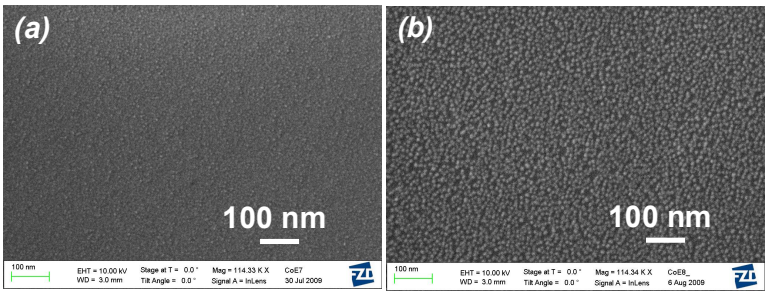

Fig. 5.1: *Cobalt film grown at room temperature (a) and at 500^{o}C (b) on flat Si (100)/SiO_2 substrate.*

Experiment shown above indicates that at a higher substrate temperature bigger cluster formation is possible. Therefore two possibilities were studied for the cobalt cluster self-assembly on rippled substrate; first higher substrate temperature during deposition and second post annealing. The same angle of incidence (70^{o} from surface normal) and deposition direction for film growth optimised for silver were used. 10 nm thick films of cobalt grown at a heated substrate of 500^{o}C and post annealed at the same temperature are shown in Fig. 5.2(a, b), respectively. It can be observed that even though well separated clusters are formed but no alignment is found. They are just randomly distributed on the rippled surface. In case of Fig. 5.2(a), it seems that even the cluster density (local flux) is still higher near the top ridge portion but due to the high temperature cobalt atom detachment seems to be higher. Cluster coalescence appears to be poor in this case therefore very small sized clusters are formed unlike for silver. On the other hand annealing shows completely different behaviour. There is no uniaxial ripening is observed (Fig. 5.2(b)), big particles of random shape or facet are formed on top of ripples and again no ordering observed. Annealing process was kept same here like for silver .i.e. cobalt film was exposed to atmosphere and then annealed inside the vacuum. Fig. 5.2(a) showed a positive sign for the possibility of cobalt particles alignment if somehow cluster coalescence can be enhanced. Therefore an experiment was planned to even increase the temperature higher than 500^{o}C.

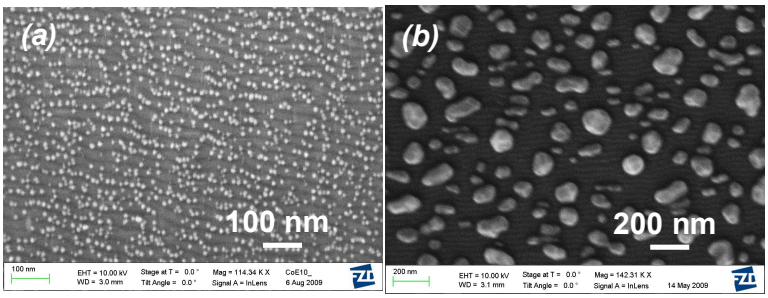

Fig. 5.2: *Co nanoparticles grown at ripple substrate: (a) during heated substrate of 500 ^{o}C and (b) sample post annealed after deposition.*

In the new experiment the temperature was increased upto 800^{o}C to promote cluster coalescence, this resulted in $CoSi_2$ formation as shown in Fig. 5.3(a, b). A zoomed view of Fig. 5.3(a) is shown in Fig. 5.3(b). These results are the same like reported (Fig. 5.1(1c)) on flat Si surface along 100 and 111 direction [15]. Cobalt silicide ($CoSi_2$) formation at a heated substrate has widely been studied [13, 15, 16]. Enough literature is available on this topic due to the fact that $CoSi_2$ has shown great potential to be used as a contact material for electronic devices owing to its high electrical conductivity, thermal stability, and good epitaxial alignment with the silicon substrate [13, 15, 16]. It has been reported that $CoSi_2$ forms at 375^{o}C on clean Si surface with no native oxide. Shi et al. [13] reported that in an annealing process of an epitaxially grown Co film, cobalt started reacting with Si and transformed into $CoSi_2$ at 500^{o}C. Carter et al. [15] reported $CoSi_2$ formation at 900^{o}C in a chemical approach of making cobalt nanoparticles. In our experiments no $CoSi_2$ formation was observed below 500^{o}C, this may be prevented due to native oxide of around 2 nm at ripple surfaces.

Belousov et al. [16] did a detail experimental and theoretical investigation of $CoSi_2$ formation. They had reported that the activation energy during the chemical reaction of silicide formation decreases from 144 to 79 kJ/mole. Even though the melting temperature of $CoSi_2$ is 1464^{o}C, this reaction takes place at much lower temperature (726^{o}C). Silicide could melt during the heating process during the fast exothermic reaction inside the defects of silicon. So even the oxide layer of 2 nm thick on ripple surface is not able to prevent the $CoSi_2$ formation. Single crystal $CoSi_2$ nanowires are formed as long as 100-200 nm range (Fig. 5.3(b)). Therefore to overcome this problem, a thermally grown oxide layer of 20 nm was developed on the rippled surface; such a thick oxide layer prevents further $CoSi_2$ formation.

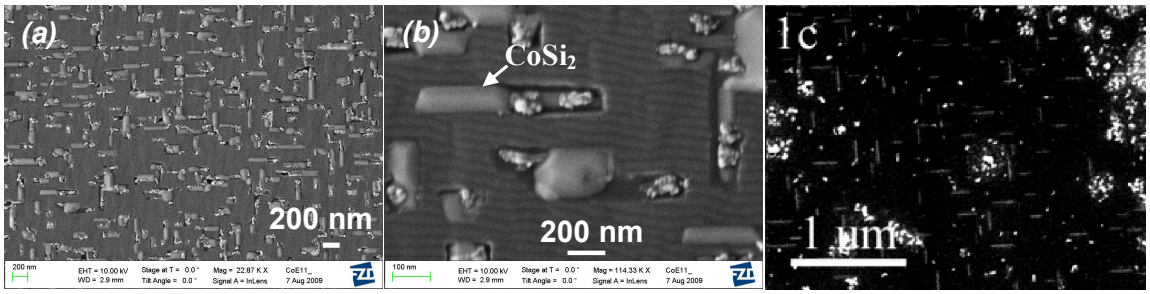

Fig. 5.3: *$CoSi_2$ formation at a high temperature of 800°C (a & b). (b) is the zoomed view of image (a). Image (1c) is from [15], Reprinted with permission from [15] copyright [2004], American Institute of Physics.*

In the next experiment we increased the amount of deposition to 20 nm and also substrate temperature of 800°C. Still a poor particle alignment was observed with particles size and density larger (Fig. 5.4(a, b)). In the Fig. 5.4(b) region of the shadow of a dirt on the sample is shown. In this low deposition region it can be seen that particles are not aligned as they appear in Fig. 5.4(b). It appears that the main problem with cobalt particles alignment is the poor coalescence with the adjacent particle unlike silver, and low adatom diffusion and higher sticking in the entire ripple ridge.

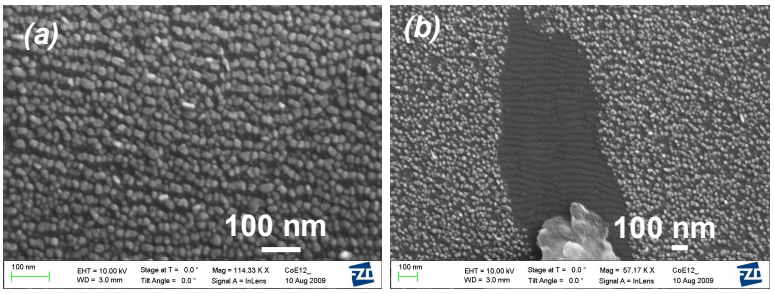

Fig. 5.4: *Co film of 20 nm grown at substrate temperature of 800°C. (a) They appeared to be poorly ordered but in some low density region on the same sample they are not ordered (b).*

In additional experiments the temperature was increased further to ~1500°C close to the melting point of cobalt. Unfortunately this temperature was also close to the melting point of our SS made sample holder (1536°C) and already out of the limit of the used Boron Nitride heater, which was realised after the experiment was over. So both sample holder and heater were destroyed after the experiment however the results were successful (Fig. 5.5). We could achieve the required self-assembly of the Co nanoparticles. In Fig. 5.5(b) it can be observed that now cobalt particles are perfectly aligned along the ripples. Black dark region shown in the image is the region of shadow of the dirt.Y. J. Oh et al. [17] also reported the high temperature annealing effects on cobalt nanoparticles, they reported that dewetting behaviour of cobalt changes at substantially high temperature similar to what observed in our

experiment. In this way one can explore several possibilities to really tune the aspect ratio of the cobalt nanoparticles.

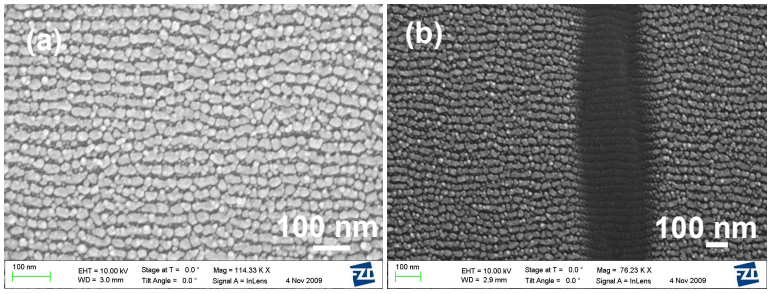

Fig. 5.5: *(a)Elongated Co nanoparticles grown at a very high substrate temperature (~1500°C).(b)region of shadow of a dirt, showing the ripple alignment with particles.*

Since the final objective of this study was to investigate the magneto-optic properties of ordered cobalt nanoparticles. Do they also possess some interesting magnetic properties like ordered silver particles optically? For this purpose two characterisation techniques, MOKE and SQUID, were used. MOKE provides the information about the magneto-optical response of the sample whereas SQUID provides the volume magnetization information. High precision rotational in-plane measurements revealing overall magnetic anisotropy behavior in-plane of the sample were performed using MOKE, whereas magnetization measurements as a function of temperature were performed using SQUID.

5.3 Some basic definitions used in magnetism

The properties of magnetic materials are typically stated in terms of the remanence and coercivity. When a ferromagnetic material is magnetized in one direction, it will not relax back to zero magnetization when the imposed magnetizing field is removed. The amount of magnetization it retains at zero driving field is called its *remanence* (Fig. 5.6). It must be driven back to zero by a field in the opposite direction; the amount of reverse driving field required to demagnetize it is called its *coercivity*. If an alternating magnetic field is applied to the material, its magnetization will trace out a loop called a *hysteresis loop*. The lack of retraceability of the magnetization curve is the property called hysteresis and it is related to the existence of magnetic domains in the material. Once the magnetic domains are reoriented, it takes some energy to turn them back again. This property of ferromagnetic materials is

useful as a magnetic "memory". Some compositions of ferromagnetic materials will retain an imposed magnetization indefinitely and are useful as "permanent magnets".

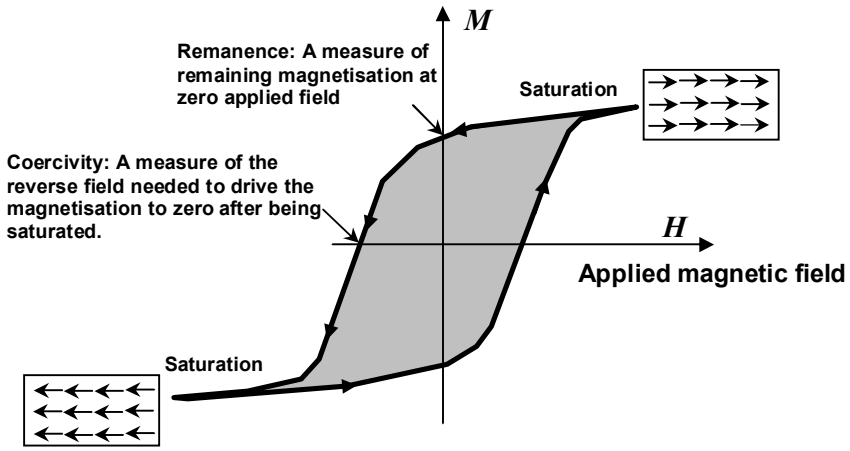

Fig. 5.6: *Generated hysteresis loop, when an alternating magnetic field applied to a magnetic material.*

In magnetic materials there are certain directions along which the magnetization prefers to orient itself, easy axis, or tries to avoid, hard axis. The magnetic anisotropy constant K_u is the energy density for which the magnetization rotates from the easy axis to the hard axis. As an example Co, hcp structure, has the magnetic anisotropy of $5x10^6$ erg/cc [21], with the easy axis aligned along the c-axis. Large values of magnetic anisotropy are required in magnetic recording media in order for the magnetization to remain in the recorded direction. In magneto-optical recording with perpendicular anisotropy, an easy axis aligned with the film normal is required whereas media with in-plane anisotropy, the easy axis is in the film plane, therefore this is the material of choice in hard disc fabrication.

5.4 Magneto-optic Kerr effect (MOKE)

In 1877 the scottish physicist John Kerr discovered an effect based on the interaction of polarised light with magnetic material. He found that the light that is reflected from a magnetized surface can change in both polarization and reflected intensity [18, 19]. This discovery gave birth to a new direction to study this Kerr effect behaviour for different magnetic materials. MOKE can be further measured in different geometries i.e. polar, longitudinal and transverse MOKE (Fig. 5.7). When the magnetization vector is perpendicular

to the reflection surface and parallel to the plane of incidence, the effect is called the *polar Kerr effect*. To simplify the analysis, near normal incidence is usually employed when doing experiments in the polar geometry. In *longitudinal MOKE,* the magnetization vector is parallel to both the reflection surface and the plane of incidence. The longitudinal setup involves light reflected at an angle from the reflection surface and not normal to it, as above in the polar MOKE case. In the same manner, linearly polarized light incident on the surface becomes elliptically polarized, with the change in polarization directly proportional to the component of magnetization that is parallel to the reflection surface and parallel to the plane of incidence. When the magnetization is perpendicular to the plane of incidence and parallel to the surface it is said to be in the *transverse* configuration. In this case, the incident light is also not normal to the reflection surface but instead of measuring the polarity of the light after reflection, the reflectivity is measured. This change in reflectivity is proportional to the component of magnetization that is perpendicular to the plane of incidence and parallel to the surface, as above.

The effect is greatest in ferromagnetic materials, is smaller in ferrites and barely observable in paramagnetic materials. MOKE was first employed as an experimental technique for the characterization of the magnetic properties of surfaces and overlayers in 1986. The fact that most of the necessary equipment can be mounted outside the Ultra-High Vacuum chamber makes this technique particularly convenient for in-situ studies of magnetism in epitaxial systems.

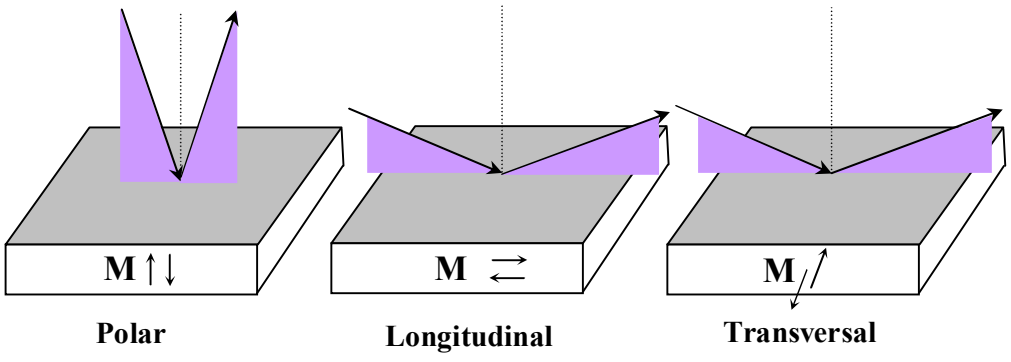

Fig. 5.7: *Schematic diagram of Polar, Longitudinal and Transversal MOKE effect.*

Fig. 5.8 shows a schematic drawing of the Kerr setup used for the measurements [20]. The setup consists of a laser (λ= 405, 635 nm), polarizers, focusing optics, two Si-photodiode detectors and four current driven core-less Helmholtz coils (magnets). The four magnets are

positioned in such a way that magnetic fields perpendicular (polar geometry) and parallel (longitudinal geometry) to the surface plane can be applied. In both Kerr geometries, the maximum magnetic field amounts upto 800 Oe. In the permanent magnets configuration the magnetic field could be increase upto 3500 Oe in our setup. An illumination angle of 45^{o} enables the effective measurement of the magnetization perpendicular and parallel to the surface (Fig. 5.8). The polarizers with a low extinction coefficient are mounted on accurate rotation units to produce s-polarised light. Finally, with a Wollaston prism the Kerr ellipticity instead of the Kerr rotation is measured using two photodiodes. Measurements of the Kerr ellipticity as a function of the external magnetic field start with a minimization of the light intensity. Two photodiodes measure the current (I_1, I_2) after Wollaston prism, which provide the in plane magnetisation information using the relation shown below.

$$(I_1 - I_2)/(I_1 + I_2) = 2\theta_{Kerr} = 2Re(r_{ps}/r_{ss}) \sim m_y \qquad (5.1)$$

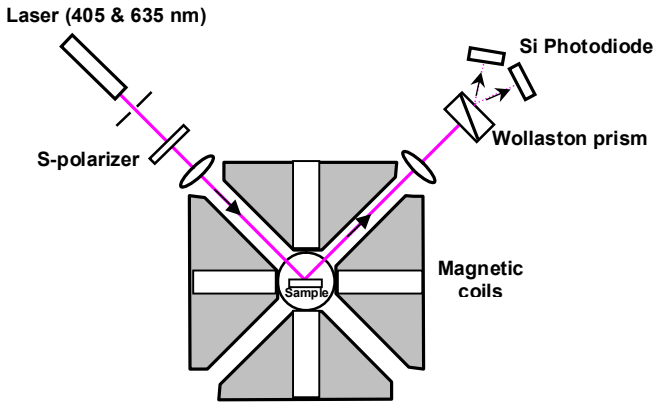

Fig. 5.8: *MOKE setup*

5.5 Superconducting QUantum Interference Device (SQUID)

SQUID is an extremely sensitive magnetic flux-to-voltage transducer. The SQUID may be the most sensitive detector of any physical quantity, with an energy resolution that approaches the quantum limit [22-25]. SQUID consists of two superconductors separated by thin insulating layers to form two parallel Josephson junctions (Fig. 5.9) [22-25]. It is possible to use in two modes rf (one junction in the loop) and dc (two junctions) SQUIDs. The device may be configured as a magnetometer to detect incredibly small magnetic fields (10^{-14} kG). The main part of the SQUID magnetometer, i.e. the SQUID unit, is shown in Fig. 5.12**.** The

unit is immersed in a He-bath at 4.2 K and contains essentially the following details: the SQUID, a magnetic flux transformer including pick-up coils, magnet coil, heat switches and magnetic shielding. The magnetic field produced by the superconducting magnet coil. Then the sample is slowly moved through the pick-up coils. The magnetic moment of the sample induces a magnetic flux change in the pick-up coils. The magnetic flux transformer exhibits a superconducting loop, thus transforming part of the total magnetic flux change from the pick-up coils into the SQUID.

There are two distinct ways to measure the magnetization with a SQUID magnetometer. The field cooling (FC) method is to apply the field far above a characteristic temperature T_f and cool the sample in a field to $T << T_f$, all the while recording the magnetization. The zero field cooling (ZFC) is to cool the sample in zero field to $T << T_f$, and at this low temperature apply the field. Then one can heat the sample while measuring M to $T >> T_f$ with the field constant. The difference between ZFC and FC magnetization indicates that the free energy has a complicated many valley structure below T_f. The remnant magnetic field of less than 3 mOe is the key to the precise measurement of FC and ZFC magnetizations. While MOKE is a measurement of magneto-optic effect, SQUID give information about volume magnetisation.

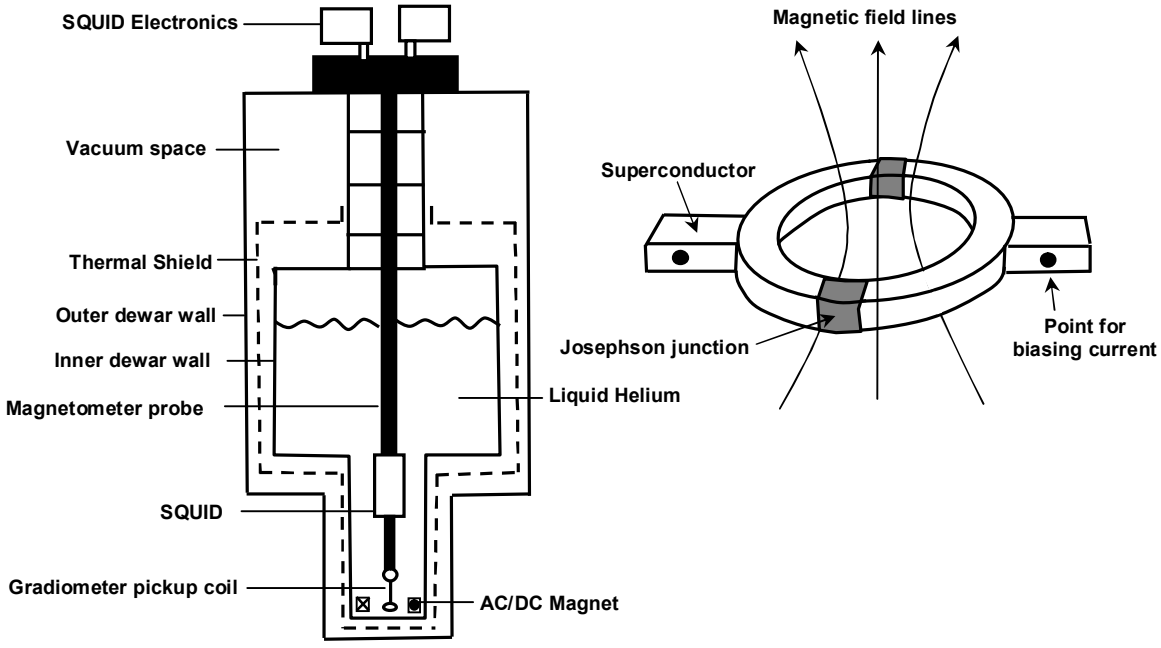

Fig. 5.9: *SQUID Magnetometer setup and Josephson junction.*

5.6 Results of MOKE measurements

Magnetization reversal (MR) curves measured for ordered cobalt nanoparticles in polar and longitudinal MOKE modes are shown in Fig. 5.10(e, c) corresponding to the samples shown in Fig. 5.10(a, b). Sample (a) and (b) are the non-ordered and ordered cobalt nanoparticles on rippled substrate, respectively. MR curves were acquired along and perpendicular to the Co wires. Along z-direction (Normal to surface) magnetization saturates at ~1 kOe as shown in polar MOKE plot, while in plane it saturates at ~0.2 kOe along the ripple in Longitudinal MOKE measurement. One can clearly distinguished an easy and hard direction of magnetization, along wires elongation and perpendicular to it, respectively. Obviously, the transition of the magnetization from positive to negative orientation is much faster in the case of measurement along wires elongation than for perpendicular direction, as well as the squerness of the loop and coercivity are larger, suggesting a strong magnetic anisotropy (Fig. 5.10(c)). Irregularity of the shape of the magnetic reversal curve along hard direction suggests that magnetization process is realized by a combination of coherent rotation of magnetization in majority with additional nucleation and slow propagation of domain walls passing through partially coupled wires. Because of the elongation of wires it is expected that the system is dominated by dipolar anisotropy contributions rather than magneto-crystalline, due to the shape of the wires and morphology given by ripples themselves, i.e., stray fields generated at the wavy surface.

Complete 360^{o} azimuthal rotation remanence measurement normalised to the saturation magnetisation is shown in Fig. 5.10(d). This plot suggests that both contributions superimpose and give a strong input to the overall magnetization picture in-plane of the sample as can be seen from the M_r/M_s ratio that is largest (close to unity) along the direction tilted by about 20° with respect to the ripples orientation (along 90° in Fig. 5.10(d), red curve). In the other words, due to a slight distribution of particle shapes and sizes, i.e. a minority of the wire shape population is actually more disk like rather than elliptical.

An intrinsic Co magneto-crystalline magnetic anisotropy exhibits uniaxial orientation that is different from shape anisotropy given by elongation of wires and the morphology contribution from ripples. The latter input is supposedly the lowest, i.e. due to not full coverage of the substrate at vales regions. In the case of non-ordered cobalt nanoparticle sample also grown on ripple substrate, the in-plane LMOKE measurement (Fig. 5.10(d), blue curve) reveals nearly complete isotropic magnetization behaviour that is expressed by close to constant

M_r/M_s = 0.6-0.7 ratio as a function of in-plane rotation angle. Only a very slight anisotropy is visible along ripples direction that originates from a petty elongation of some of the particles along ripple ridges direction.

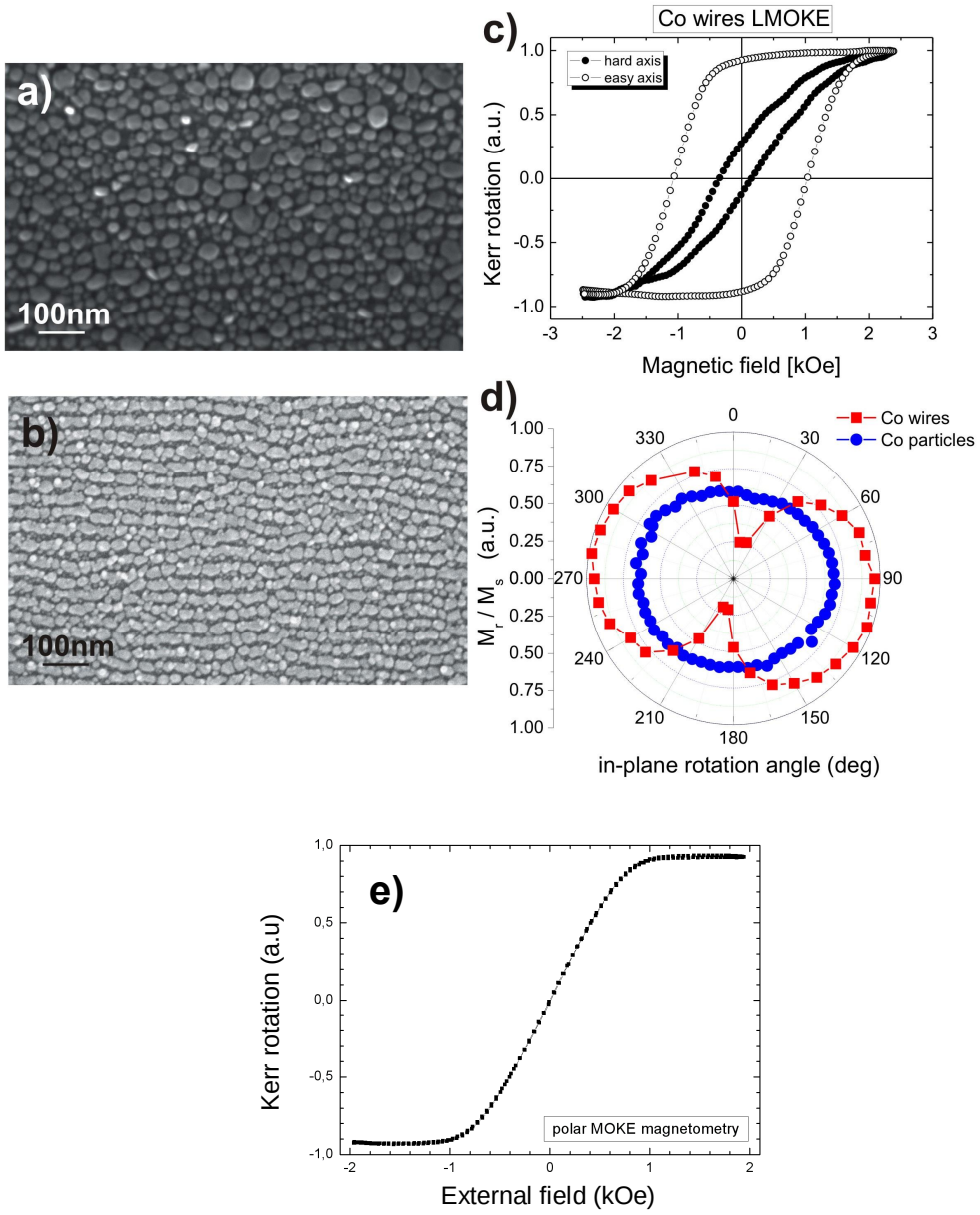

Fig. 5.10: *(a, b) sample used for MOKE and SQUID measurements.(c) LMOKE along and perpendicular to the wire array. (d) 360° rotation remanence measurement normalised to the saturation magnetisation. Red points are corresponding to sample (b) and blue corresponding to sample (a), respectively. (e)Polar MOKE*

5.7 SQUID measurement results

In the case of SQUID measurements two types of studies were performed: (i) Zero Field Cooling ï Field Cooling (ZFC-FC) dependencies in the temperature range of 4-340K and (ii)

a regular magnetization reversal curve scan acquired at several temperatures in the range of 4-300K, both taken along two distinguish directions, along and perpendicular to the ripple ridges elongation. Measurement data are plotted in Fig. 5.11 for non-ordered and Fig. 5.12 for ordered nanoparticles, respectively.

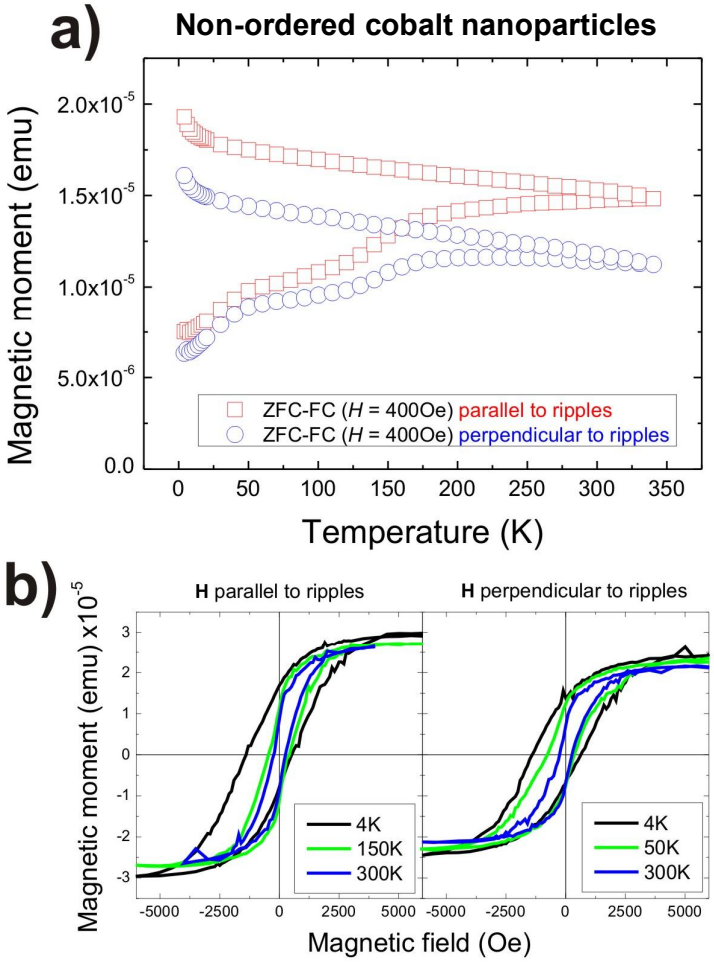

Fig. 5.11: *SQUID measurements conducted for non ordered cobalt sample shown in Fig. 5.10. (a)ZFC-FC measurement, (b) magnetization reversal curve.*

ZFC-FC dependencies and MR curves (Fig. 5.11(a, b)) clearly shows a similar responses between parallel and perpendicular measurement orientations. Slight differences correspond most probably to the elongation of particles along ripple ridges direction that is consistence with magneto-optical results, too. In addition, in all the MR curves a shift to the negative field direction is visible (Fig. 5.11(b)). This can be assessed to the so-called exchange bias effect that is a consequence of the interface coupling between Co and its oxide created at the surface of disks. Since, the direction of the unidirectional anisotropy, i.e. the

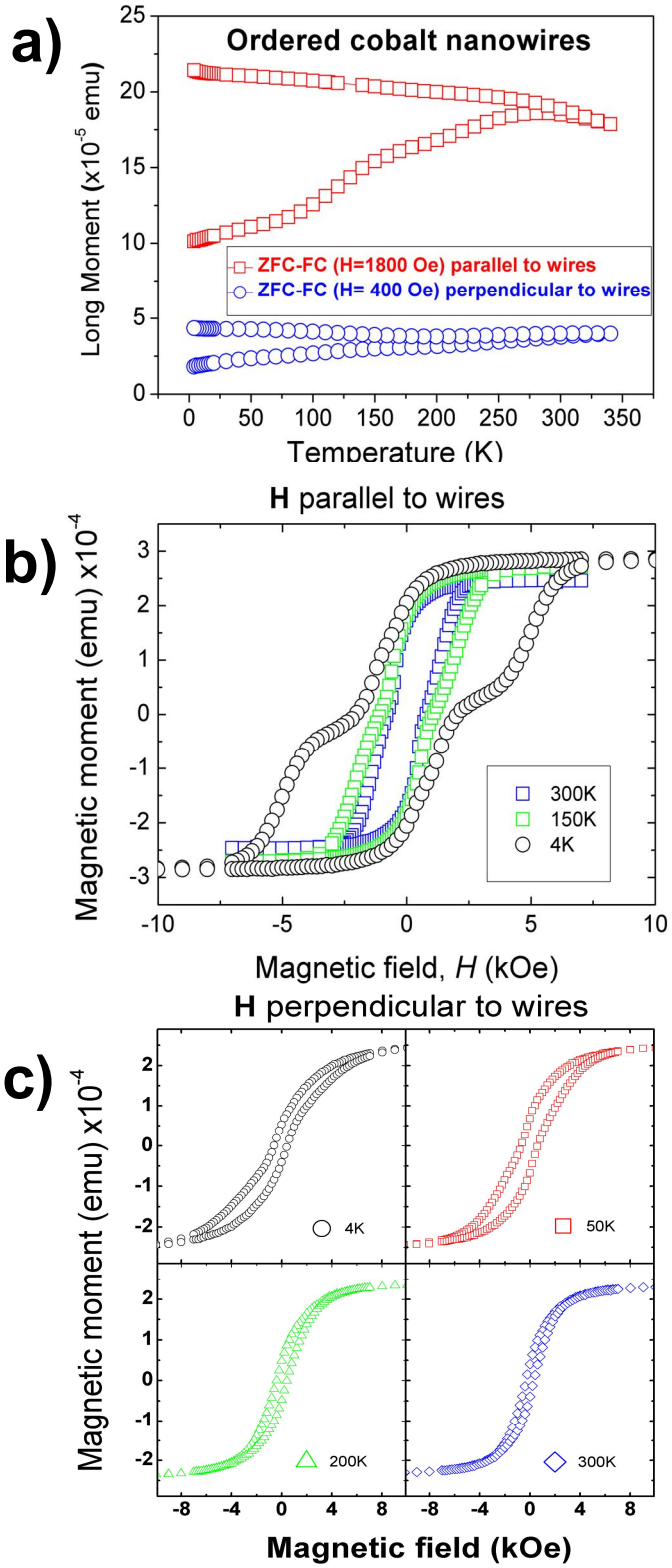

Fig. 5.12: *SQUID measurements conducted for ordered cobalt sample shown in Fig. 5.10(b).(a)Measured ZFC-FC measurement, (b) Measured magnetization reversal curve along the cobalt wires, (c) Measured magnetization reversal curve perpendicular to the cobalt wires.*

anisotropy inseparably connected to the exchange bias effect, has been never setup, the shift of MR curves is visible for both measurement directions. In addition, this offset is decreasing with increasing temperature that is a typical exchange bias property [26].

ZFC-FC dependencies in the case of ordered cobalt particles shown in Fig. 5.12(a), where one can find an increase in the long magnetic moment measured along the wires. Even it is one order higher then the randomly ordered particles (Fig. 5.11(a)). Magnetic field of 1800 and 400 kOe is needed to apply to see the ZFC-FC behaviour from parallel to perpendicular direction of the wires. Such behaviour is a quite intuitional if one looks at wires morphology, since the elongation of wires is about twice as much along ripple ridges orientation than orthogonal to it. Moreover, the local interaction field is expected to be slightly larger, concomitantly that is a consequence of a larger number of adjacent elements along perpendicular direction to the ripple ridges orientation. Thus, along wires elongation the interactions take place mostly between two single adjacent elements. That can be understood by taking a closer look at the shape of the loop and a large loop opening for all the MR curves in this particular case (Fig. 5.12(b)). MR curves analysis reveals a larger reversible contribution in the perpendicular case that is a consequence of a strong anisotropy in the system along this hard magnetization direction (Fig. 5.12(c)). This is in a good agreement with magneto-optical results. Blocking temperature is found to be close to the 300K.

References

[1] D. O'Connor, A.V. Zayats, *Nature Nanotechnology* 5 (**2010**) 482.

[2] S. Sun, C. B. Murray, *J. Appl. Phys.* 85 (**1999**) 4325.

[3] J. Kreuter, *J. Controlled Release* 16 (**1991**) 169.

[4] V.K. Pecharsky, K.A. Gschneidner, *J. Mag. Mag. Mater.* 200 (**1999**) 44.

[5] C. Kormann, E. Schwab, F.W. Raulfs, K.H. Beck, *U. S. Patent* 5, 500 (**1996**).141.

[6] J. C. Lodder, D. J. Monsma, R. Vlutters, T. Shimatsu, *J. Mag. Mag. Mater.* 119 (**1999**) 198.

[7] L. Yan, M. Przybylski, Y. Lu, W. H. Wang, J. Barthel, J. Kirschner, *Appl. Phys. Lett.* 86 **(2005)** 102503.

[8] B. D. Terris, T. Thomson, *J. Phys. D: Appl. Phys.* 38 (**2005**) 199.

[9] O. M. Liedke, B. Liedke, A. Keller, B. Hillebrands, A. Mucklich, S. Facsko, J. Fassbender, *Phys. Rev. B* 75 (**2007**) 220407.

[10] T. W. H. Oates, A. Keller, S. Noda, S. Facsko, *Appl. Phys. Lett.* 93 (**2008**) 063106.

[11] R. Moroni, D. Sekiba, F. Buatier de Mongeot, G. Gonella, C. Boragno, L. Mattera, U.Valbusa, *Phys. Rev. Lett.* 91 (**2003**) 167207.

[12] F.B. de Mongeot, U.Valbusa, *J. Phys.: Condens. Matter* 21 (**2009**) 224022.

[13] J. Shi, U.T. Irie, F. Takahashi, M. Hashimoto, *Thin Solid Films* 375 (**2000**) 37.

[14] B. X. Chung, C. P. Liu, *Materials Letters* 58 (**2004**) 1437.

[15] J. D. Carter, G. Cheng, T. Guo, *J. Phys. Chem. B* 108 (**2004**) 6902.

[16] I. Belousov, A. Grib, S. Linzen, P. Seidel, *Meth.in Phys.Res.B* 186 (2002) 61.

[17] Y. J. Oh, C. A. Ross, Y. S. Jung, Y. Wang, C.V. Thompson, *Small* 5 (**2009**) 865.

[18] http://en.wikipedia.org/wiki/Magneto-optic_Kerr_effect

[19] P. Weinberger, *Philosophical Magazine Letters* (**2008**) 1.

[20] Sebastiaan van Dijken, Pattern formation and Magnetic anisotropy in thin metal films (PhD Thesis) (**2000**).

[21] M. O. Liedke, *The role of patterning for the magnetization reversal in the exchange bias* (PhD thesis) (**2007**).

[22] http://hyperphysics.phy-astr.gsu.edu/hbase/solids/magperm.html

[23] http://www.vanderbilt.edu/lsp/abstracts/jenks-eap-1997.htm

[24] K. Gramm, L. Lundgren , O. Beckman, *Physica Scripta.* 13 (**1976**) 93.

[25] W. G. Jenks, I. M. Thomas, J. P. Wikswo, *Enc. Appl. Phys.* 19 (**1997**) 457.

[26] J. Nogués, I. K. Schuller, *J. Mag. Mag. Mater.* 192 (**1999**) 203.

Chapter-6

Conclusions and Future Scope

6.1 Conclusions

In this work growth of highly ordered silver nanoparticles/nanowires array using periodically patterned Si substrate is demonstrated. Self-organised ripple pattern produced by low energy (500 eV) ion bombardment have very low ripple modulations (2 nm). Still particles self-assembly was observed under non-shadow deposition. Therefore adatoms kinetics on ripple ridge is found to be very important for the self-assembly process. Magnetron sputtering produced adatoms with higher energy and higher flux compare to e-beam evaporation, therefore this method provides a relatively poor control on the self-assembly process. Sputtered atoms easily migrate over the ripple modulation and occupy a random position. Due to low adatom energy and flux, e-beam evaporation method had proven to be better to control the self-assembly process. Formation of long nanowires is possible in the case of very low incident flux and longer deposition time. Due to this reason sputtering process always develop nanoparticles chain not the nanowires.

Role of incident angle was also studied both experimentally and in 3D-LKMC simulation. Growth at 70^{o} angle of incidence with respect to the surface normal produces the best alignment of particles. The difference between maximum and minimum of the calculated local flux show a peak at an incidence angle of 70^{o} with respect to surface normal. This confirms the experimentally observed best self-assembly at this angle of incidence compare to others. Under similar experimental conditions deposited flux is found to be inhomogeneous on ripple

surface and homogeneous at flat Si surface. This indicates the different sticking probabilities at the two surfaces. In in-situ RBS measurements with simultaneous growth on ripple and flat surface for a given time, we have found that deposited amount is more on ripple surface indicating a higher sticking coefficient.

The direction of deposition also leads to different results due to asymmetric tilt of ripple pattern. The local flux is either concentrated on ripple top or distributed over the ridge depending on deposition from short ridge or long ridge side, respectively. Growth from shorter ridge side easily covers the ridge portion and was found to be more appropriate for nanowire growth. In this way choosing the proper incident flux and time the width of nanowires can be varied. For the growth of nanoparticles of various aspect ratios deposition from longer ridge portion is appropriate. In this case small nanoparticles follow uniaxial coalescence along the ripple leading to elongated nanoparticles.

Post annealing of silver nanoparticles exposed to atmosphere leads to spherical shaped nanoparticles. Physisorbed oxygen on silver surface reduces the surface free energy and helps the nanoparticles to gain energy minimised spherical shape during vacuum annealing. This shape change occurs around 200^{o}C temperature. Highly ordered and spherical nanoparticles array could be achieved in this way not reported so far. Since temperature enhances the atoms mobility on the surface, therefore affect the process of coalescence and Ostwald ripening. The interparticle gap can be adjusted by temperature and time of annealing. Ostwald ripening was observed on ripples with different periodicity. Ostwald ripening is found to be uniaxial for ripples of 35 nm wavelength or above. It remains uniaxial even at higher temperature. However, for the ripples of 20 nm wavelength it is found to be more like Ostwald ripening on flat surfaces.

Detailed studies of the optical properties of self-assembled nanoparticles and nanowires arrays were performed. Both nanoparticles and nanowires arrays were found to be optically anisotropic. With the help of reflection measurements and Gans theory we could show that different plasmonic coupling along and across the ripple is responsible for the strong optical anisotropy. Red shift in both longitudinal and transverse plasmon resonances with the increase in particles aspect ratio indicates that coupling is dominant over the shape anisotropy. Number of particles varied by annealing process demonstrated that more number of nanoparticles or closer particles coupled strongly and produces the red shift in LSPR. LSPR can be tuned using nanoparticles array of different periods.

Using generalised ellipsometry we have demonstrated that nanoparticles/nanowire arrays are biaxially anisotropic, i.e. all the dielectric functions along, across the ripples and perpendicular to the surface are unequal. For this purpose a biaxial layer model was developed with Drude model (bulk silver) and Lorentz model (LSPR) along different axes. Nanoparticles show predominantly insulating behaviour and strong LSPR while nanowires are like bulk silver along the ripple and show LSPR only across the ripple. It was found that there exists a critical length below which the particles or wire become insulating. Annealed particles show a sharp resonance reflecting the narrow particle distribution.

Self-aligned nanoparticles can be used as active SERS substrates. Hot-junction do exists and are responsible for large enhancement in the Raman signal of the R6G molecule. Due to anisotropy effect of distance in hot-junction field strength can be observed in a single sample. SERS signal also validates the anisotropic nature of ordered particles sitting on rippled substrate and support reflection measurement. Enhancement is found to be more for the equally distant particles sitting in a chain compare to randomly distributed particles. Elongated particle chain is the best choice compare to all other cases discussed. Enhancement factor is found to be of the order of 10^8 much higher compare to bulk silver.

Self-assembly of cobalt nanoparticles is found to be more complicated compare to silver due to higher sticking and lower adatoms mobility on ripple surface. Temperature above 1000^oC is needed to form big cobalt nanoparticle above 10 nm in size. At higher temperature $CoSi_2$ is also formed that can be prevented by growing a thick oxide layer on the ripple surface. MOKE and SQUID measurements show pronounce uniaxial magnetic anisotropy in the case of ordered cobalt particles. One can clearly distinguish an easy and hard axis of magnetization, along wires elongation and perpendicular to it, respectively.

ZFC-FC measurements show a clear different behavior for ordered and non-ordered cobalt particles, respectively. Long range moment is found to be an order higher along the aligned wires. Analysis of MR curves measured in SQUID reveals a larger reversible contribution in the perpendicular case that is a consequence of a strong anisotropy in the system along hard axis magnetization direction. This is in a good agreement with magneto-optical results.

6.2 Future scope

(1.) More detailed study of the temperature effect on silver nanoparticle is suggested. This demands more TEM, XRD, XPS and probably in-situ STM measurements. Similarly uniaxial Ostwald ripening should be studied at much higher temperature using in-situ GISAXS or STM.

(2.) A measurement of absolute sticking probability is also suggested. Also its variation with ripples of different aspect ratio will give more fundamental insight of the growing mechanism of silver on rippled surface.

(3) Experiment of in-situ ellipsometry is also suggested to observe the plasmon shift in real time with increasing nanowire width and find out at which minimum gap the plasmon resonance is lost.

(4.) SERS study can also be extended for the alignment of biological tissue along with silver or gold nanoparticles. This may have potential applications.

(5.) Growth of cobalt nanoparticles on rippled substrate demands a detail study both in terms of growth and magnetic properties. Since in this work we only reported the possibility of cobalt nanoparticles self-assembly, effect of the different particles aspect ratios and wires can be studied.

(6.) Formation of $CoSi_2$ during growth of cobalt on Si at the high temperature is also a field of more investigation. The effect of ripple wavelength, or orientation on $CoSi_2$ formation can be an interesting study.

(7.) Finally one can explore the combination of both silver and cobalt nanoparticles and investigate the magneto-plasmonic properties. It has been reported in recent years that if ferromagnetic material layer is in contact with gold or silver the magnetization effects are enhanced due to the plasmonic properties. Since ordered silver particles on ripple are strongly coupled, therefore a multilayer of silver and cobalt nanoparticles may results to unusual magnetic properties.

Acknowledgements

During my PhD work several peoples helped and supported me, many-many thanks to all of them. I ask for the apology if I miss some one to acknowledge here.

I am greatly thankful to **Prof. Wolfhard Möller** for showing faith in me and providing the opportunity to work in FZD as PhD student. He always solved all my hurdles and always very encouraging for all the students. He is such a great scientist but so down to earth person, he left a deep impact of his personality in me.

I am not sure in which words I should express my thanks to my thesis supervisor **Dr. Stefan Facsko**. I know how different ways I bothered him but he was always polite and generous to me. He not only helped to solve my scientific / technical problems but also personal problems as well. In his unique way of supervising he slowly-slowly developed the thinking of science in me. I feel so lucky to work with **Dr. Stefan Facsko**, a real scientist and gentle person. The only regret I have in my PhD is that I should have learnt more science from him. I hope he will keep supervising me where ever I am.

I want to give special thanks to my friend **Monika Fritzsche**. She also helped me a lot at different stages of my PhD. She spent her time to settle down my life in Dresden and did lots of SEM measurements for me. We almost shared every day by day activities and made lots of funny chats. I am also thankful to my friend **Alexandra**, she also helped me at several occasions. We always spent long time in office till late evening. I also enjoyed the discussion of different cultures with her.

I am also greatly thankful to **Dr. T. W. H. Oates**, he helped me so much even far away from me. He always cleared all my doubts, doesnôt matter how big email I send to him. I am thankful to **Satoshi** and **Dr. K.-H. Heinig,** who did the simulation work for me. Satoshi become my good friend and we spend some quality time together. *He always felt so happy when I told him that the best think I like in attending conferences is the breakfast given in hotels*.

I also want to thank to **Robert Aniol**, he was so prompt and perfect in any workshop related work. I am thankful to **Dr. Oskar Liedke** for useful discussions about magnetism. I can not forget the help of **Mrs. Elfi Christalle** for her several SEM measurements. She was so prompt in her work, without her help I could have never finished my work in time. I am also thankful to **Dr. Mykola Vinnichenko** for his help in ellipsometry measurement. My thank goes to **Dr. Rene Heller** for his help in RBS measurements. I am also thankful to **Dr. Adrian Keller** for his useful help at many occasions. I am also thankful to **Dr. Arndt Mücklich** and **Dr. György Kovacs** for the TEM measurements. I am also thankful to (Dr. B. Schmidt, Clean room staff, Dr. G. Abrasonis, Matthias Buhl, Thomas Strache, Dr. Georg Talut, Dr. Jörg Grenzer, Manja Kiebler, Dr. Heidemarie Schmidt, Kah Ming Mok, Erik Ritter , Entire FZD Colleagues) for their timely helps at several occasions.

I am thankful to all my friends **Jing**, Bartosz, Marina, Khalid, Varun, Avanish, Hardeep, Kanwar , Rahul, Abhishek, and others who were with me in FZD guest house and shared a quality time. I also extent my thank to all my friends in entire IPR, who were always connected with me and I never felt like alone. I am also thankful to them for giving nice company to my wife during this time.

I am thankful to **Dr. Subroto Mukherjee** who always encouraged me for the research. I am also thankful to Director IPR Prof. P. K. Kaw and academic committee of IPR for granting me leaves for pursuing PhD at Germany.

My biggest thanks go to my dear wife **Pramila**, who has shown tremendous patient during this time and sacrificed quality time of life. She always encouraged me. Without her support I could have never dreamed to come to Dresden. I am also thankful to my little daughter **Manya**, she is as old as my PhD. Ever since she started speaking she asked me each time on phone ñ*Father have you completed your study*ò . These words always inspired me to work more. I am also thankful to my mother, brother and other family members who are the reason for me to be here where I am.

In the end I want to thank **God**, without his wish or blessing nothing is possible. For me all those who helped are the persons send by God.

List of publications

Parts of this work have been or will be published

[1] *Optical properties of silver nanowire arrays with 35 nm periodicity*
M. Ranjan, T. W. H. Oates, S. Facsko, W. Möller, *Optics Letters* 35 (**2010**) 2576.

[2] *Highly anisotropic effective dielectric functions of silver nanoparticle arrays*
T. W. H. Oates, **M. Ranjan**, S. Facsko, H. Arwin, *Optics Express* 19 (**2011**) 2014.

[3] *Anisotropic Surface Enhanced Raman Scattering of R6G in a periodic chain of self aligned nanowires in a template approach.*
M. Ranjan, S. Facsko, *Nano Letters* (To be submitted)

[4] *Super short range surface adatom migration induced selective Ag nano-structure on pre patterned substrates*
S. Numazawa, **M. Ranjan**, K.-H. Heinig, S. Facsko, R. Smith, *J. Phys.: Condens. Matter* 23 (**2011**) 222203.

[5] *Growing mechanism of self-aligned silver nanoparticles and nanowires*
M. Ranjan, S. Facsko, M. Fritzsche, S. Numazawa, K.- Heinig, A. Mücklich, *Nanotechnology* (To be submitted).

[6] *Applications of ion induced patterned substrates in plasmonics*
M. Ranjan, T. W. H. Oates, S. Facsko
Book chapter contribution for the book: *Advances in Nanofabrication: From Lithography to Ion-Beam Sputtering*, by Pan Stanford Publishing (To be contribute).

Planed Publications:

[6] *Uniaxial Ostwald ripening of silver nanoparticles sitting on pattern surface*

[7] *Growth of magnetically anisotropic self-aligned cobalt nanoparticles*

[8] *Sticking probability evolution at ripple pattern substrate*

[9] *Plasmonic coupling and tuning in self-assembled nanoparticles*

[10] *Biaxial anisotropy in self-aligned nanoparticles*

Never Give Up

This story is about a farmer and his mule. The effectiveness of the story lies in the way it focuses upon adversity and how attitude determines the course of seemingly lost cause. There was this farmer in a tiny village.

He owned an old mule that used to carry grains and other farming related stuff for the farmer. During one of those days, the mule fell into a well. The well ran deep and despite trying hard many a times, mule couldnôt get himself out the well. He started to lose hope. His consistent shrieks drew attention of the farmer who came rushing to the well.

Farmer looked around and tried to come up with a rescue plan but eventually, he also lost the hope. He decided that the old mule was not worth the trouble of saving. So, he called his neighbours and asked for their help in hauling dirt to bury the old mule.

The mule got hysterical. Soon enough, the farmer and the neighbours started to shovel and fill well with the dirt. When the first bout of dirt hit muleôs back, suddenly his fast losing spirit came up with an idea. He thought every time a shovel load of dirt will land on his back, he will just shake it off and step up a bit higher. The idea filled him with a new lease of life and hope.

Old mule kept doing the same blow after blow. He would just shake the dirt off and step up a notch higher. He kept reminding himself of possibility of a brand new life. He controlled his nerves and kept stepping up. After some time, the exhausted mule managed to step over the wall of that well. He was completely tired and fatigued yet his spirit triumphed. The dirt that was meant to bury him actually helped him in remaining alive.

The story is a clear example of how our attitude towards seemingly impossible adversities determines the final outcome. Life is like this only. If we respond positively to the stream of problems faced by us and refuse to surrender, we are likely to emerge victorious.

Versicherung

Hiermit versichere ich, dass ich die vorliegende Arbeit ohne unzulässige Hilfe Dritter und ohne Benutzung anderer als der angegebenen Hilfsmittel angefertigt habe; die aus fremden Quellen direkt oder indirekt übernommenen Gedanken sind als solche kenntlich gemacht. Die Arbeit wurde bisher weder im Inland noch im Ausland in gleicher oder ähnlicher Form einer anderen Prüfungsbehörde vorgelegt.

Ich erkenne die Promotionsordnung der Technischen Universität Dresden an.

Dresden, 22.11.2010

Mukesh Ranjan

Diese Arbeit wurde am Forschungszentrum Dresden-Rossendorf e.V. und unter wissenschaftlicher Betreuung von Dr. Stefan Facsko und Prof. Dr. Wolfhard Möller angefertigt. Wolfhard Möller ist Professor im Institut für Angewandte Physik der Fakultät Mathematik und Naturwissenschaften der Technischen Universität Dresden